Unified directional parabolic-accurate lattice Boltzmann boundary schemes for grid-rotated narrow gaps and curved walls in creeping and inertial fluid flows

Irina Ginzburg [1,*] Goncalo Silva [2] Francesco Marson [3] Bastien Chopard [3] and Jonas Latt [3]
[1] *Université Paris-Saclay, INRAE, UR HYCAR, 92160 Antony, France*
[2] *IDMEC, University of Évora, 7000-671 Évora, Portugal*
[3] *University of Geneva, 1204 Geneva, Switzerland*

(Received 20 January 2022; accepted 8 January 2023; published 9 February 2023)

The goal of this work is to advance the characteristics of existing lattice Boltzmann Dirichlet velocity boundary schemes in terms of the accuracy, locality, stability, and mass conservation for arbitrarily grid-inclined straight walls, curved surfaces, and narrow fluid gaps, for both creeping and inertial flow regimes. We reach this objective with two infinite-member boundary classes: (1) the single-node "Linear Plus" (LI^+) and (2) the two-node "Extended Multireflection" (EMR). The LI^+ unifies all directional rules relying on the linear combinations of up to three pre- or postcollision populations, including their "ghost-node" interpolations and adjustable nonequilibrium approximations. On this basis, we propose three groups of LI^+ nonequilibrium local corrections: (1) the LI_1^+ is *parametrized*, meaning that its steady-state solution is physically consistent: the momentum accuracy is viscosity-independent in Stokes flow, and it is fixed by the Reynolds number (Re) in inertial flow; (2) the LI_3^+ is parametrized, exact for arbitrary grid-rotated Poiseuille force-driven Stokes flow and thus most accurate in porous flow; and (3) the LI_4^+ is parametrized, exact for pressure and inertial term gradients, and hence advantageous in very narrow porous gaps and at higher Reynolds range. The directional, two-relaxation-time collision operator plays a crucial role for all these features, but also for efficiency and robustness of the boundary schemes due to a proposed *nonequilibrium* linear stability criterion which reliably delineates their suitable coefficients and relaxation space. Our methodology allows one to improve any directional rule for Stokes or Navier-Stokes accuracy, but their parametrization is not guaranteed. In this context, the parametrized two-node EMR class enlarges the single-node schemes to match exactness in a grid-rotated linear Couette flow modeled with an equilibrium distribution designed for the Navier-Stokes equation (NSE). However, exactness of a grid-rotated Poiseuille NSE flow requires us to perform (1) the modification of the standard NSE term for exact bulk solvability and (2) the EMR extension towards the third neighbor node. A unique relaxation and equilibrium exact configuration for grid-rotated Poiseuille NSE flow allows us to classify the Galilean invariance characteristics of the boundary schemes without any bulk interference; in turn, its truncated solution suggests how, when increasing the Reynolds number, to avoid a deterioration of the mass-leakage rate and momentum accuracy due to a specific Reynolds scaling of the kinetic relaxation collision rate. The optimal schemes and strategies for creeping and inertial regimes are then singled out through a series of numerical tests, such as grid-rotated channels and rotated Couette flow with wall-normal injection, cylindrical porous array, and Couette flow between concentric cylinders, also comparing them against circular-shape fitted FEM solutions.

DOI: 10.1103/PhysRevE.107.025303

I. INTRODUCTION

The lattice Boltzmann method (LBM) [1–3] applies for fluid modeling within a wide range of engineering, biological and physical problems with complex static and moving surfaces, such as particle-laden ones [4–9], suspensions of soft particles [10], red blood cells [11] and pulsatile [12,13] flows, porous flow in materials [14], synthetic structures [15–20], or natural rocks [21–24]. These problems are essentially described by the Stokes and finite Reynolds number regimes, and characterized by a coarse grid resolution over a narrow fluid path. The uniform regular grid is one of the keystone elements of the LBM success allowing for extremely simple implementation and optimal performance on modern computational platforms [25,26]. On the reverse side, the explicit fitting of an off-lattice boundary or interface will necessarily call for a "zero cost" but accurate population reconstruction; otherwise, its intrinsic accommodation may give rise to spurious discrete layers and destroy the second-order bulk accuracy [27–31].

The existing Dirichlet-velocity boundary techniques are numerous and include different types of approaches. Considering straight-wall modeling, we find either first-order [32–35] or second-order [36] finite-difference shear-stress nonequilibrium reconstruction and on-grid moment-based method [37]. Regarding off-lattice boundary conditions, it is worth mentioning the single-node projection method for curved walls called Local Second-Order Boundary (LSOB) [28] and its recent variants, namely, the simplified degraded

*irina.ginzburg@inrae.fr

[38], no-slip [39], and slip [40] reformulations for pipe flows, and the A-LSOB extensions [41,42] for Dirichlet and Neumann conditions in advection-diffusion scalar transport. The distinctive key point is that LSOB introduces boundary condition through a wall-normal Taylor closure relation, whereas the one-point approach [43] combines the matrix projections with the lower-order directional Dirichlet prescription. In contrast, the large stencil method [44] reconstructs the lacking populations in outside (ghost) nodes from their *normally* extrapolated hydrodynamic values, based on the geometry-depending bilinear (four-point in two dimensions) interpolation for ghost-node off-grid image. Conceptionally different from the direct prescription of the Dirichlet closure relation, the partially saturated method (PSM) [45–47] is motivating for micritic grid-unresolved structures, such as carbonates [23], whereas a dissipative immersed-boundary method (IBM) [48–50] enables smooth description of the moving fronts.

This work focuses on *directional* methods: they extend the versatile but only mid-grid accurate bounce-back (BB) [4,51] to an arbitrary *linkwise* distance $\delta \in [0, 1]$ towards a solid surface, and assign an unknown population via a linear combination of the known components moving upstream and downstream the surface-cut discrete-velocity axis $\vec{c}_q$. Among the first directional rules, the single-node FH rule introduced by Filippova and Hänel [52] and the two-node MLS rule by Mei *et al.* [53] are based on the directional finite-difference velocity-gradient representation; in turn, the lower-order equilibrium interpolations [7,54] permit the reconstruction of one-node gaps. The linkwise schemes developed subsequently operate directly with the linear combinations of the postcollision (streaming) populations. Among the pioneering methods are the two-population fractional BFL interpolation introduced by Bouzidi, Firdaouss, and Lallemand [55] and the three-population uniform YLI interpolation proposed by Yu *et al.* [56].

The BFL and YLI rules belong to the Linear (LI) family [57,58], which freely combines the two opposite outgoing populations with the incoming one; an intrinsic Dirichlet Taylor closure expansion [59,60] then develops *directionally*, and it scales with an arbitrary prefactor, say, $\alpha^{(u)}(\delta)$; this last property explains why LI contains an infinite number of formally equivalent *second-order accurate* schemes. Moreover, this prefactor $\alpha^{(u)}(\delta)$ uniquely determines the three interpolation coefficients by prescribing a value to their sum. To give one example, the Central Linear (CLI) scheme [57] prescribes $\alpha^{(u)}(\delta)$ from the physical consistency *parametrization* condition, without restoring the corresponding interpolation. We will show that the interpolations with an adjustable length l, such as ZLI and CHLI recently introduced by Zhao *et al.* [61] and Chen *et al.* [62], can be transformed into specific dependencies $\alpha^{(u)}(\delta, l)$; they reduce to YLI-type schemes [22,56,63] when $l = \delta$, and to the Second-Order Single-Node (SSN) rule [64] when $l = 2\delta$.

There is a general misunderstanding that the BFL, YLI, or CLI are *non-single-node* rules. However, the whole LI family turns into a local scheme if (1) one performs the streaming step *prior* to the boundary update or (2) one employs the *precollision* population solution in the boundary node. The first technique was proposed [59] for all links with the upstream fluid neighbor; we call these algorithms *single-node* methods. The second technique was adopted [59] when an upstream neighbor is missing; more recent three-population interpolations [22,61–65] adopt this approach for all cut links and allow one to update unknown populations already in *a modified collision* step. This last property is shared by the *local-single-node* methods, which employ only local *outgoing populations* and nonequilibrium corrections. The Enhanced Linear (ELI) infinite family [66] belongs to this last group; it is conceived with two outgoing and two reconstructed virtual wall-located (ghost) populations, where NELI employs the *nonequilibrium bounce-back* wall approximation of the antisymmetric postcollision local component, say $\hat{n}_q^-$, while *symmetric* SELI copies $\hat{n}_q^-$ and *central* CELI prescribes their mean value $\hat{n}_q^- = 0$. We will reinterpret ELI as a modified collision ELI_0^+, without any ghost-wall reconstruction, due to a specific *symmetric postcollision* correction $\hat{F}_q = K_{ELI}^+ \hat{n}_q^+$, where an adjustable combination of NELI and SELI then covers the uniform linear ULT and LLI schemes introduced by Tao *et al.* [67] and Liu *et al.* [68], respectively. To generalize these ideas, we introduce a wider three-population LI^+ class dropping all "convex" constraints, and derive its generic coefficients in the presence of an arbitrary local correction $\hat{F}_q = \hat{K}^+ \hat{n}_q^+ + \hat{K}^- \hat{n}_q^-$. Additionally, the LI^+ is equipped with a temporal flag $I^{(t)} \in [0, 1]$, optionally varying between the aforementioned implementation via "poststreaming" [$I^{(t)} = 1$] and "precollision" [$I^{(t)} = 0$]. Thus, the LI^+ unifies the single- and local-single-node rules and extends their available degrees of freedom.

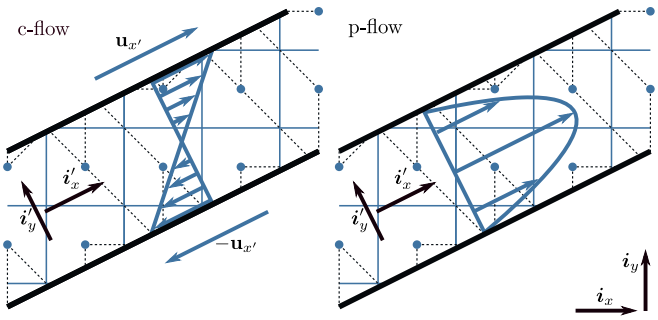

FIG. 1. Sketch of the linear Couette *c-flow* and the parabolic Poiseuille *p-flow* in a narrow grid-rotated channel.

Our second objective is to propose the linear stability criteria for LI^+. Indeed, up to now, either a "convex-interpolation" argument [55,56,61,62] or semiheuristic multireflection stability condition [57,59] was used to restrict the boundary coefficients, respectively, to intervals [0,1] or $[-1, 1]$, knowing that their sum is one. In contrast, based on the modified-collision arguments, our nonequilibrium constraints will delineate the admissible Taylor scale factors $\alpha^{(u)}(\delta)$ and reliably predict the stable relaxation space when LI^+ is amended by the explicit nonequilibrium correction $\hat{F}_q$.

Third, a central criterion for the boundary conditions proposed in this article is to match the exact solutions (down to machine precision) for reference flows in arbitrarily inclined channels, as illustrated in Fig. 1. A grid-rotated steady-state Couette Stokes flow is described by a linear profile and

a linear population solution, and hence we require from a boundary condition to deliver an exact solution for this flow to deserve a categorization as a second-order accurate method. Hereafter, this property is referred to as *c-flow* exactness or *linear* accuracy, and accordingly, *c-nse-flow* exactness for Couette flow modeled with equilibrium distribution designed for the Navier-Stokes equation (NSE). However, the linear flow does not capture shear (curvature) effects, emblematically mimicked by a steady-state grid-rotated Poiseuille channel flow, where a quadratic polynomial population solution satisfies any linear collision operator with the Stokes equilibrium. Hereafter, exactness with respect to the force-driven inclined Poiseuille Stokes profile is referred to as *p-flow*, and accordingly *p-nse-flow* exactness applying the NSE equilibrium. The key point is that all linear schemes neglect (1) the second-order momentum gradient and (2) the first-order gradients of the pressure and inertial equilibrium term contained in $\hat{n}_q^-$. Due to this first feature, they all are inexact even for a straight and diagonal grid-aligned Poiseuille Stokes profile, except for specific values $\Lambda(\delta)$ assigned to free-tunable combination of relaxation rates $\Lambda = (\tau^+ - \frac{1}{2})(\tau^- - \frac{1}{2})$, also known as the "magic parameter," giving a kinematic viscosity $\nu = \frac{1}{3}(\tau^+ - \frac{1}{2})$ and an adjustable rate τ^- for $\hat{n}_q^-$. Namely, this is the property of the Λ-parametrized schemes, such as BB [51], the Magic Linear (MGLI) subfamily [17,58], which includes the recent MSSN parametrization [65], or else $K_1^- - \mathrm{ELI}$ and $K_2^- - \mathrm{ELI}$ [66]. We will introduce the parametrized subclass $\mathrm{LI}_1^+ \in \mathrm{LI}^+$ based on the recent revision [69], which makes the directional closure relation force-independent, and then the dependency $\Lambda(\delta)$ the same in the straight and diagonal channels.

Another interesting exception is the three-population interpolation by Wang *et al.* [70], fitted here to $\mathrm{WLI} \in \mathrm{LI}$: we will show that it cancels the parabolic truncation error in a straight channel due to its specific prefactor $\alpha^{(u)}(\delta, \tau^\pm)$. However, our attempt to extend WLI to the *p-flow* accuracy makes $\alpha^{(u)}(\delta, \tau^\pm)$ channel-inclination-dependent. We then replace WLI by the single-node *isotropic Poiseuille* (IPLI) and the local-single-node Central-ELI (CELI-IP), which are isotropic *p-flow* schemes. Still, like WLI, both these schemes approach the relaxation stability limit as $\delta \to 0$. To this end, we amend the whole LI^+ class with one of the two nonequilibrium corrections: (1) $\hat{K}_3^- \hat{n}_q^-$ which ensures the *p-flow* exactness within LI_3^+ and (2) $\hat{K}_4^- \hat{n}_q^-$ which cancels the first gradients of the pressure and inertial equilibrium term from closure relation and ensures the *p-pressure* accuracy within LI_4^+; these two properties then hold for any $\alpha^{(u)}(\delta)$ and Λ. A distinguished property is that LI_3^+ and LI_4^+ are parametrized and we demonstrate how sufficient conditions [57,69] verify whether a given directional scheme obeys this property.

The *parametrization* means that when combined with the proper collision operator and *linear force implementation* [71], the steady-state Stokes flow error estimate and adjacent permeability measurements are viscosity-independent, whereas the NSE incompressible steady-state momentum solution is set by the grid Reynolds number $\mathrm{Re}_g = \mathcal{U}/\nu$, [8,22,72–74]. The *directional two-relaxation-time* TRT collision operator [57,60] plays a crucial role in the *parametrization* and accuracy, in both bulk and boundary. The TRT solution is parametrized by prescribing any fixed value to its free collision number Λ; the multiple-relaxation-time MRT collisions [75] achieve such an exact parametrization either within their TRT subclass $\tau_i^\pm = \tau^\pm$, or when scaling their additional symmetric rates $(\tau_i^+ - \frac{1}{2})$ in proportion with ν, [8,17]. When compressible effects are negligible, the MRT boundary effects remain practically controlled by Λ alone [16,17]. In turn, the regularized models [7,76–78] with $\tau^- = 1$, as well as the single-relaxation-time BGK model [62,81,82] with $\tau^- = \tau^+$, scale, respectively Λ linearly and quadratically with ν, so that such models cannot make their steady-state solutions physically parametrized, whatever the boundary scheme is.

The *p-flow* accuracy appears to be crucial in porous flow, whereas the *p-pressure* feature is essential in inertial flow. However, we will show that the LI^+ class cannot combine both LI_3^+ and LI_4^+ properties within one family. We then reconsider nonlocal methods. Unlike it might be expected, the *five-population*-based quadratic interpolations, such as BFL-QI [55] and YLI-QI [56,79], are not even *p-flow* accurate in grid-aligned setups. The $\mathrm{BFL\text{-}QI}_3$ and MLS_3 will illustrate that the proper $\hat{K}_3^- \hat{n}_q^-$ corrections make two-node schemes *p-flow* accurate, although not necessarily ensuring their parametrization.

In contrast, the two-node five-population Multireflection (MR1) scheme [59] and an infinite-member MR families [57,69] combine *p-flow* and *p-pressure* exactness with the parametrization, whereas the two-node MLI [57,58] operates with the LI coefficients and reaches *p-flow* accuracy with the help of the directional finite-difference Taylor correction. Numerically, it is observed [17,19,31,54,57,59,80] that MR1 and MLI reach a quasianalytical accuracy in regular porous arrays, where they gain in accuracy over the equilibrium, linear and quadratic interpolations, but also over PSM and IBM [16]. Moreover, the BGK-based PSM gets especially penalized by viscosity dependence [16,83] and, although the coupling with the TRT/MRT reduces [49] the IBM numerical slip error equally, the full consistency is not achieved automatically. In this work, advanced and extended (AVMR/EMR) *c-nse-p-flow* families combine the *p-flow*, *p-pressure*, and *c-nse-flow* exactness; we compare them with the LI^+ in different regimes.

The reverse side of the advanced accuracy is the loss of local mass conservation. However, *an enforcement of local mass conservation* tends to degrade [5,28,84–86] accuracy and convergence; indeed, an exact *c-flow* or *p-flow* population solution conserves an outgoing mass quantity only over the whole periodic grid-inclined solid fragment, [28,84]. Otherwise, the directional rules establish *a quasisteady solution* [54,59], which combines a stationary momentum field with a space-time uniform mass leakage rate $\partial_t \rho$; accordingly, the *steady-state linear* S-TRT solver [42,69] accounts for that via an uniform mass-source variable. We will show that the same *global mass-leakage mechanism* originates from the mass and momentum *local bulk* solvability condition of the quartic-polynomial Navier-Stokes equilibrium in the grid-rotated Poiseuille profile, which becomes exact [87] only making the third-order momentum truncation vanish with

$\Lambda = \frac{1}{12}$ and adjusting the fourth-order NSE equilibrium projection. This exact bulk flow configuration enables us to purely verify the respective Galilean invariance properties of the boundary schemes on the static walls and the *p-nse-flow* three-node family. More generally, the *p-nse-flow* solvability conditions give us ideas on how to reduce the Reynolds number increase of the mass-leakage rate. Based on that, we delineate those parametrized schemes which make their accuracy Re-independent due to $\Lambda(\mathrm{Re})$. These dependencies are then confronted with a grid-rotated Couette NSE flow subject to wall-normal injection.

In what follows, Sec. II presents the TRT, an extended NSE equilibrium and S-TRT, provides effective solutions of the grid-rotated Poiseuille NSE model. Section III formulates the directional boundary rule, its closure relation and conditions of the (1) parametrization, (2) stability, and (3) *c-flow*, *p-flow*, *c-nse-p-flow*, and *p-nse-flow* exactness. Section IV defines LI^{+}, specifies LI_1, LI_3, LI_4 and their counterparts ELI^{+}_k, together with their stability conditions. Section V extends the two-node MR. Section VI addresses the numerical simulations in grid-rotated Couette and Poiseuille flows, also including the Couette NSE flow subject to wall-normal injection. Section VII performs TRT and FEM computations in an array of solid cylinders and a cylindrical Couette flow. Section VIII concludes the paper. Appendix A builds truncation corrections and the MR_{nse}. Appendix B addresses the MRT model and closure relations. Appendix C recasts single-node schemes: (1) YLI [56], GLI [63], ZLI [61], CHLI [62], SSN [64], and MSSN [65] to LI_0; (2) scheme [70] to $\mathrm{WLI} \in \mathrm{APLI}$; and (3) ELI [66], ULT [67], and LLI [68] to ELI^{+}. Appendix D 1 builds the TRT BFL-QI_3 and $\mathrm{MLS}_3/\mathrm{FH}_3$; Appendix D 2 provides EMR families. Appendix E complements the stability analysis. Table I specifies the acronyms and classifies all involved boundary schemes.

II. THE TRT SOLVABILITY CONDITIONS

We first recall the standard TRT model and its recent steady-state S-TRT reformulation [69]. The quasi-steady-state solution is then defined: it couples the stationary momentum field with the space-time uniform permanent density update. Then follow the TRT solvability conditions of the rotated NSE Poiseuille flow.

A. TRT collision

We keep in mind the standard LBM operating on the d-dimensional equidistant computational grid $\vec{r} \in V_p$ with the discrete velocity sets $\{\vec{c}_0 = 0\} \cup_{q=1}^{Q_m} \vec{c}_q$ [as d2q9, d3q15, or d3q19]; the space and time stepping is set equal to 1 l.u., and the translation into the physical units is performed through the governing dimensionless numbers, such as the Reynolds number. We numerate the one-half of the nonzero discrete velocities with the positive numbers $q \in Q_{\frac{1}{2}}$ [$\mathrm{sgn}_q = 1$] and their opposite vectors with the negative numbers $-q \in Q_{-\frac{1}{2}}$ [$\mathrm{sgn}_{-q} = -1$]. Giving an equilibrium distribution $e^{\pm}_q(\vec{r}, t)$, the TRT collision operator decomposes the internal real variables, which are the "populations" $\{f_q, f_{-q}\}$, into their symmetric ("+") and antisymmetric ("−") components $f^{\pm}_q(\vec{r}, t) := \frac{1}{2}(f_q \pm f_{-q})$, and updates them according to the following rule:

$$
\begin{aligned}
&f_j(\vec{r} + \mathrm{sgn}_j \vec{c}_q, t+1) = \hat{f}_j(\vec{r}, t),\\
&\hat{f}_j(\vec{r}, t) = f_j(\vec{r}, t) + \hat{n}^{+}_q(\vec{r}, t) + \mathrm{sgn}_j \hat{n}^{-}_q(\vec{r}, t),\\
&\hat{n}^{\pm}_q = -\frac{1}{\tau^{\pm}}(f^{\pm}_q - e^{\pm}_q), \quad \hat{n}^{+}_0 = -2\sum_{q=1}^{Q_m/2} \hat{n}^{+}_q, \quad \hat{n}^{-}_0 = 0,\\
&q = j\mathrm{sgn}_j \in Q_{\frac{1}{2}}, \quad \forall\, \{\vec{r}, \vec{r} + \mathrm{sgn}_j \vec{c}_q\} \in V_p, \quad \forall\, j. \qquad (1)
\end{aligned}
$$

The two relaxation rates $\tau^{\pm}(\vec{r}, t) > \frac{1}{2}$ determine the two positive combinations $\Lambda^{\pm}(\vec{r}, t)$ and their product $\Lambda(\vec{r}, t)$:

$$
\Lambda^{\pm}(\vec{r}, t) := \left[\tau^{\pm}(\vec{r}, t) - \tfrac{1}{2}\right], \quad \Lambda(\vec{r}, t) := \Lambda^{+}\Lambda^{-}. \qquad (2)
$$

The symmetric equilibrium component $e^{+}_q(\vec{r}, t)$ optionally incorporates the incompressible Navier-Stokes equation (NSE hereafter) term $I_{nse}\mathcal{E}^{(u)}_q(\vec{r}, t)$; the Stokes flow is modeled with $I_{nse} = 0$; the antisymmetric component $e^{-}_q(\vec{r}, t)$ includes the forcing term $\mathcal{E}^{(f)}_q(\vec{r}, t)$ giving an external force $\vec{F}(\vec{r}, t)$:

$$
e^{+}_q(\vec{r}, t) = t^{\star}_q P(\vec{r}, t) + I_{nse}\mathcal{E}^{(u)}_q(\vec{r}, t), \quad P = c_s^2 \rho, \qquad (3a)
$$

$$
\mathcal{E}^{(u)}_q(\vec{r}, t) = t^{\star}_q \frac{3j_q^2 - ||\vec{j}||^2}{2\rho_0} - \frac{||\vec{j}||^2}{\rho_0} a_\varepsilon \varepsilon_q, \qquad (3b)
$$

$$
e^{-}_q(\vec{r}, t) = t^{\star}_q \vec{j} \cdot \vec{c}_q + \mathcal{E}^{(f)}_q(\vec{r}, t), \quad \vec{j} = \sum_{q=1}^{Q_m} f_q \vec{c}_q + \frac{1}{2}\vec{F},
$$

$$
\mathcal{E}^{(f)}_q(\vec{r}, t) = t^{\star}_q \Lambda^{-} \vec{F} \cdot \vec{c}_q. \qquad (3c)
$$

The square sound speed $c_s^2 \in]0, 1[$ relates the pressure $P(\vec{r}, t)$ to the local mass quantity $\rho(\vec{r}, t) = \sum_{q=0}^{Q_m} f_q(\vec{r}, t)$, and it is kept adjustable inside its discrete-velocity-dependent stability interval following [17,21,59]. The macroscopic momentum $\vec{j}(\vec{r}, t)$ adds the half-forcing to local population momentum $\vec{J} = \sum_{q=1}^{Q_m} f_q \vec{c}_q$; the macroscopic velocity $\vec{u}(\vec{r}, t)$ is to be defined given a reference density value ρ_0: $\vec{u} = \vec{j}/\rho_0$. When the forcing term $\mathcal{E}^{(f)}_q$ is added to e^{-}_q, its variation is automatically accounted by the boundary analysis; we discuss in Appendix B 1 how the MRT collision adapts for this. The hydrodynamic weights $t^{\star}_q$ are fixed by two isotropic conditions:

$$
\sum_{q=1}^{Q_m} t^{\star}_q c_{q\alpha} c_{q\beta} = \delta_{\alpha\beta}, \quad \forall \alpha, \beta, \quad \sum_{q=1}^{Q_m} t^{\star}_q c^2_{q\alpha} c^2_{q\beta} = \frac{1}{3}, \quad \alpha \neq \beta. \qquad (4)
$$

The term $\mathcal{E}^{(u)}_q(\vec{r}, t)$ in Eq. (3b) adopts Eq. (B1) [87] with an adjustable equilibrium projection a_ε on the fourth-order polynomial vector ε_q(which obeys $\sum_{q=0}^{Q_m} \varepsilon_q = 0$, $\sum_{q=1}^{Q_m} \varepsilon_q c_{q\alpha} c_{q\beta} = 0, \forall \alpha, \beta$); the coordinate and diagonal populations then apply respectively:

$$
\begin{aligned}
&\text{d2q9: } t^{\star}_q = \left\{\tfrac{1}{3}, \tfrac{1}{12}\right\}, \quad \varepsilon_q = \{-2, 1\},\\
&\text{d3q15: } t^{\star}_q = \left\{\tfrac{1}{3}, \tfrac{1}{24}\right\}, \quad \varepsilon_q = \{-2, \tfrac{1}{2}\},\\
&\text{d3q19: } t^{\star}_q = \left\{\tfrac{1}{6}, \tfrac{1}{12}\right\}, \quad \varepsilon_q = \{-4, 1\}. \qquad (5)
\end{aligned}
$$

TABLE I. This table summarizes the boundary schemes and infinite families controled by $\alpha^{(u)}(\infty)$. Second column: "N" is the minimal number of nodes operating in Eq. (21) with the post-streaming $[I^{(t)}=1]$ or pre-collision $[I^{(t)}=0]$ populations. Columns 3-6: exactness in a grid-rotated channel, where all schemes are *c-flow* exact in Couette Stokes flow; (a) *p-flow*: *force-driven* Poiseuille Stokes flow, Eq. (34); (b) *parabolic* = *p-flow* ∪ *p-pressure*: Poiseuille Stokes flow, Eq. (36); (c) *c-nse-p-flow*: Couette NSE flow ∪ *parabolic*, Eq. (37); (d) *p-nse-flow*: Poiseuille NSE flow, Eq. (39). The single-node LI^+ and the local-single-node ELI^+ both impose $\gamma=\hat{\gamma}=0$, but ELI^+_k enforces $\beta=0$ and $\hat{K}^+=K^+_{ELI}$; the LI_k, MR1, AVMR and MR_{nse} enforce $\hat{K}^+=0$ in Eq. (22) and $\alpha^{(p)}=0$ in Eq. (28); $\mathrm{MR1}^+$ holds $\alpha^{(p)}=0$.

Acronym	N	*p-flow*	*p-pressure*	*c-nse-p-flow*	*p-nse-flow*	Name	Ref.	Eq., Sec., Table
Parametrized three-nodes *p-nse-flow* family								
$\mathrm{MR}_{nse}(\infty)$	3	✓	✓	✓	✓	MR NSE		Sec. A 2, Table VII
Parametrized two-nodes parabolic (velocity) VMR families and schemes								
$\mathrm{MR1}\in\mathrm{MR1}^+$	2	✓	✓			Multireflection MR	[59]	Sec. V A
$\mathrm{MR1}^+\in\mathrm{VMR}\,(\infty)$	2	✓	✓			MR1 *Plus*		Sec. V A
$\mathrm{MR1\text{-}BB}\in\mathrm{MR1}^+$	2	✓	✓			MR1 + BB		Eq. (70)
$\mathrm{AVMR}\in\mathrm{EMR}\,(\infty)$	2	✓	✓	✓		Advanced velocity + MR	[69]	Sec. V B
$\mathrm{EMR}\in\mathrm{VMR}\,(\infty)$	2	✓	✓	✓		Extended + MR		Secs. V B, D 2
Parametrized single-node *p-flow* families using $I_b=0$ in Eq. (33)								
$\mathrm{LI}^+_3\in\mathrm{LI}^+\,(\infty)$	1	✓				$\mathrm{LI}^+_3=\mathrm{LI}^+_0+\hat{K}^-_3\hat{n}^-_q$		Eqs. (42), (44b)
$\mathrm{LI}_3\in\mathrm{LI}^+_3\,(\infty)$	1	✓				$\mathrm{LI}_3=\mathrm{LI}_0+\hat{K}^-_3\hat{n}^-_q$		Eqs. (46), (51)
$\mathrm{BB}_3\in\mathrm{LI}_3$	1	$\delta=\frac{1}{2}$				Bounce-back+$\hat{K}^-_3\hat{n}^-_q$		Eqs. (46), (51)
$\mathrm{ELI}^+_3\in\mathrm{LI}^+_3\,(\infty)$	1	✓				$\mathrm{ELI}^+_3=\mathrm{ELI}^+$+$\hat{K}^-_3\hat{n}^-_q$		Eqs. (53), (54), (57d)
Parametrized isotropic single-node *p-flow* schemes without corrections using $I_b=0$ in Eq. (33)								
$\mathrm{IPLI}\in\mathrm{LI}_0\cap\mathrm{LI}_3$	1	✓				Isotropic Poiseuille (IP) + LI		Eq. (50), Table (III)
$\mathrm{CELI\text{-}IP}\in\mathrm{ELI}^+_3$	1	✓				Central + ELI + IP		Eq. (60), Table (IV)
Parametrized anisotropic single-node *p-flow* schemes without corrections using $I_b=1$ in Eq. (33)								
$\mathrm{APLI}\in\mathrm{LI}_0$	1	✓				Anisotropic Poiseuille + LI		Sec. (C4)
$\mathrm{WLI}\in\mathrm{APLI}$	1	Straight				Wang + LI	[70]	Eqs. (C5)-(C8)
Parametrized single-node *p*-pressure families								
$\mathrm{LI}^+_4\in\mathrm{LI}^+\,(\infty)$	1		✓			$\mathrm{LI}^+_4=\mathrm{LI}^+_0+\hat{K}^-_4\hat{n}^-_q$		Eqs. (42), (44c)
$\mathrm{LI}_4\in\mathrm{LI}^+_4\,(\infty)$	1		✓			$\mathrm{LI}_4=\mathrm{LI}_0+\hat{K}^-_4\hat{n}^-_q$		Eqs. (46), (52)
$\mathrm{ELI}^+_4\in\mathrm{LI}^+_4\,(\infty)$	1		✓			$\mathrm{ELI}^+_4=\mathrm{ELI}^+\hat{K}^-_4\hat{n}^-_q$		Eqs. (53), (54), (57e)
Parametrized single-node families								
$\mathrm{MGLI}\in\mathrm{LI}^+\,(\infty)$	1					$\mathrm{LI}_1=\mathrm{LI}_0(I_b=1)+\hat{K}^-_1\hat{n}^-_q$	[57]	Eqs. (46), (48), (49a)
$\mathrm{MSSN}\in\mathrm{MGLI}$	1					Magic + SSN	[65]	Sec. C 1
$\mathrm{LI}^+_1\in\mathrm{LI}^+\,(\infty)$	1					$\mathrm{LI}^+_1=\mathrm{LI}^+(I_b=0)+\hat{K}^-_1\hat{n}^-_q$		Eqs. (42), (44a)
$\mathrm{LI}_1\in\mathrm{LI}^+_1\,(\infty)$	1					$\mathrm{LI}_1=\mathrm{LI}_0(I_b=0)+\hat{K}^-_1\hat{n}^-_q$	[69]	Eqs. (46), (48)
$\mathrm{ELI}^+_1\in\mathrm{LI}^+_1\,(\infty)$	1					$\mathrm{ELI}^+_1=\mathrm{ELI}^+\hat{K}^-_1\hat{n}^-_q$		Eqs. (53), (54), (57c)
Parametrized single-node schemes without corrections								
$\mathrm{CLI}\in\mathrm{LI}_0\cap\mathrm{LI}_1$	1					Central + LI	[57]	Table III
$\mathrm{BB}\in\mathrm{LI}_0(\delta=\frac{1}{2})$	1					Bounce-back	[4,51]	Table III
$\mathrm{CELI\text{-}UQ}\in\mathrm{ELI}^+_1$	1					CELI+ uniform quadratic	[66]	Table IV
Nonparametrized single-node families and schemes								
$\mathrm{LI}_0\in\mathrm{LI}^+\,(\infty)$	1					Linear	[57]	Eq. (46)
$\mathrm{BFL}\in\mathrm{LI}_0$	1					Bouzidi-Firdaouss-Lallemand	[55]	Table III
$\mathrm{YLI}\in\mathrm{ZLI}$	1					Yu + LI	[56]	Table III, Sec. C 1
$\mathrm{GLI}\sim\mathrm{YLI}$	1					Geier + LI	[63]	Sec. C 1
$\mathrm{SSN}\in\mathrm{ZLI}$	1					Second-order single-node	[64]	Sec. C 1
$\mathrm{ZLI}\in\mathrm{LI}_0\,(\infty)$	1					Zhao + LI	[61]	Table III, Sec. C 1
$\mathrm{CHLI}\sim\mathrm{ZLI}\,(\infty)$	1					Chen + LI	[62]	Sec. C 1
Nonparametrized local-single-node XELI = {NELI, CELI, SELI}								
$\mathrm{ELI}^+_0\in\mathrm{ELI}^+\,(\infty)$	1					$\mathrm{ELI}^+_0=\mathrm{ELI}^+-I_{ncs}K^-_{ELI_0}\hat{n}^-_q$		Eqs. (53)-(55), (57b)
$\mathrm{XELI}\sim\mathrm{ELI}^+_0(\infty)$	1					$X=\{\mathrm{N},\mathrm{C},\mathrm{S}\}:I_{ncs}=\{-1,0,1\}$	[66]	
XELI-UQ	1					Uniform quadratic	[66]	Table IV, Eqs. (58)-(59)
XELI-UL	1					Uniform linear	[66]	Table IV, Eqs. (58)-(59)
XELI-ULT	1					Uniform linear + Tao	[66,67]	Table IV, Eqs. (58)-(59)
XELI-FL	1					Fractional linear	[66]	Table IV, Eqs. (58)-(59)
Nonparametrized local-single-node $\mathrm{LLI}(\gamma^-)$ schemes except for particular γ^-								
$\mathrm{LLI}(\gamma^-)\in\mathrm{ELI}^+$	1					Liu + LI	[68]	Eq. (C15)

TABLE I. (*Continued.*)

Acronym	N	*p-flow*	*p-pressure*	*c-nse-p-flow*	*p-nse-flow*	Name	Ref.	Eq., Sec., Table
Nonparametrized two-node quadratic-interpolation based schemes								
BFL-QI	2					BFL + Quadratic Interpol.	[55]	Sec. D 1 a
BFL-QI$_3$	2	✓				BFL-QI + $\hat{K}_3^- \hat{n}_q^-$		Sec. D 1 a
Nonparametrized two-node equilibrium-interpolation based schemes								
FH	1					Filippova-Hänel	[52]	Sec. D 1 b
MLS	2					Mei-Luo-Shyy	[53]	Sec. D 1 b
MLS$_3$/FH$_3$	2	✓				MLS/FH + $\hat{K}_3^- \hat{n}_q^-$		Sec. D 1 b

The "standard" equilibrium [81] corresponds to $a_\varepsilon = 0$ and $c_s^2 = \frac{1}{3}$. In principle, Eq. (1) does not need to prescribe e_0^+; nevertheless, one may compute an immobile population update equivalently with $\hat{n}_0^+ = -\frac{1}{\tau^+}(f_0 - e_0^+)$ giving $e_0^+(\vec{r},t) = \rho - 2\sum_{q=1}^{Q_m/2} e_q^+$. The macroscopic equations are derived with the help of the Chapman-Enskog nonequilibrium expansion or its discrete recurrence solution from the linear solvability conditions, e.g., [57,87,88],

$$\hat{n}_0^+(\vec{r},t) + 2\sum_{q=1}^{Q_m/2} \hat{n}_q^+(\vec{r},t) = 0, \tag{6a}$$

$$2\sum_{q=1}^{Q_m/2} \hat{n}_q^-(\vec{r},t)\vec{c}_q = \vec{F}(\vec{r},t). \tag{6b}$$

The momentum equation in Eq. (6b) is then defined with the kinematic viscosity $\nu = \frac{1}{3}\Lambda^+$. For steady-state solutions at least, an arbitrarily given value $\Lambda > 0$ in Eq. (2) should remain fixed when ν and characteristic velocity $\mathcal{U}$ vary either in a series of Stokes or NSE computations within the same grid geometry where, in the NSE case, grid Reynolds number $\mathrm{Re}_g = \mathcal{U}/\nu$ should also remain fixed. In bulk, the specific Λ values, such as $\Lambda = \frac{1}{12}$ (third order) and $\Lambda = \frac{1}{6}$ (fourth-order), make the spatial truncation corrections in Eq. (A1) vanish, and improve their anisotropy in transition (see, for example, [39,42,87,89–95]), whereas $\Lambda = \frac{1}{4}$ improves linear stability (see [92] and references herein); they also determine the most accurate boundary [17,51,58,96] and interface location [69,73], or attenuate the spurious accommodation [29,97]. Additionally, in this work, Λ will explicitly determine the stable viscosity range with the parabolic-accurate single-node schemes, whereas the suitable dependencies $\Lambda(\mathrm{Re}_g)$ will diminish the error dependency upon Re_g.

B. Steady-state S-TRT linear-flow model

When an equilibrium distribution is linear with respect to the macroscopic variables, pressure $P(\vec{r})$ and momentum $\vec{j}(\vec{r})$, the steady-state S-TRT formulation [69] may replace the transient update in Eq. (1) by a global linear system composed from two equations per every internal link connecting $\vec{r} \in V_p$ and $\vec{r} + \vec{c}_q \in V_p$, $q \in Q_{\frac{1}{2}}$, such as

$$S_q(\vec{r}) = S_{-q}(\vec{r} + \vec{c}_q), \tag{7a}$$

$$G_q(\vec{r}) = -G_{-q}(\vec{r} + \vec{c}_q), \tag{7b}$$

with

$$\begin{aligned} S_q(\vec{r}) &= \left(e_q^+ + \tfrac{1}{2}\hat{n}_q^- - \Lambda^+\hat{n}_q^+\right)(\vec{r}), \\ S_{-q}(\vec{r}+\vec{c}_q) &= \left(e_q^+ - \tfrac{1}{2}\hat{n}_q^- - \Lambda^+\hat{n}_q^+\right)(\vec{r}+\vec{c}_q), \\ G_q(\vec{r}) &= \left(e_q^- + \tfrac{1}{2}\hat{n}_q^+ - \Lambda^-\hat{n}_q^-\right)(\vec{r}), \\ -G_{-q}(\vec{r}+\vec{c}_q) &= \left(e_q^- - \tfrac{1}{2}\hat{n}_q^+ - \Lambda^-\hat{n}_q^-\right)(\vec{r}+\vec{c}_q). \end{aligned} \tag{8}$$

This system is complemented with the local mass and momentum conservation equations given by

$$2\sum_{q=1}^{Q_m/2} \hat{n}_q^+(\vec{r}) = M_0, \tag{9a}$$

$$2\sum_{q=1}^{Q_m/2} \hat{n}_q^-(\vec{r})\vec{c}_q = \vec{F}(\vec{r}), \quad \vec{r} \in V_p. \tag{9b}$$

The global set of the unknowns *Var* in the linear system formed by Eqs. (7)–(9) reads

$$Var = M_0 \cup_{\vec{r}\in V_p} [P(\vec{r}) \cup \vec{j}(\vec{r}) \cup_{q\in Q_{\frac{1}{2}}} \hat{n}_q^\pm(\vec{r})]. \tag{10}$$

When the d-dimensional grid is composed of N_p nodes, the set *Var* contains $N_p(Q_m + (1+d)) + 1$ variables. A single unknown variable M_0 is introduced to ensure the solvability condition, typically $M_0 \neq 0$ when the boundary conditions do not conserve the global mass. Since the pressure is defined to an additive constant, P is fixed in one grid node to an arbitrary value, the normalizing procedure applies *a posteriori*, e.g., $P \to P - \bar{P}$. In principle, the pressure-momentum formulation allows for a nonlinear underlying dependency $P(\rho)$; we apply here the standard "ideal gas" relation $P = c_s^2\rho$ in Eq. (3) where $\{P, \vec{j}\}$ and $\{\rho, \vec{j}\}$ linear formulations are equivalent. This global system is complemented [69] with the set of the boundary rules for incoming populations; in the present work, they are restricted to directional rules in Eq. (B8) which are all expressed through $e_q^\pm(P, \vec{j})$ and $\hat{n}_q^\pm$ from *Var*; an extension to nodal rules is straightforward; see [42]. The S-TRT is robust for any physical and model parameter range, and it allows for an efficient validation of boundary rules.

C. Quasi-steady state due to mass balance

The steady state is reached when an immobile population is at an equilibrium: $\hat{n}_0^+(\vec{r},t) = 0$ in Eq. (1). However, it has been recognized [54,59,69,84] that when the boundary condition does not allow one to reach the steady-state, the

LBM self-activates a time-space uniform update $\partial_t\rho$ of the density solution:

$$\rho(\vec{r},t+1)=\rho(\vec{r},t)+\partial_t\rho,\quad \partial_t\rho=\frac{\delta M(t)}{N_p},\tag{11}$$

giving a total mass variation $\delta M(t)=M(t+1)-M(t)=\sum_{r\in V_p}[\rho(t+1)-\rho(t)]$ per time step over N_p grid nodes. Internally, $\partial_t\rho$ is operated by the mass-conserving postcollision correction $\delta\hat{n}_q^+$:

$$\text{TRT: } \hat{n}_q^+(\vec{r},t)=\hat{n}_q^+(\vec{r})+\delta\hat{n}_q^+,\quad \delta\hat{n}_q^+=-\partial_t\rho\varepsilon_q^{(im)},$$
$$\varepsilon_0^{(im)}=2c_s^2\sum_{q=1}^{Q_m/2}t_q^\star-1,\quad \varepsilon_q^{(im)}=t_q^\star\frac{||\vec{c}_q||^2}{d}-t_q^\star c_s^2,\quad q\neq 0,$$
$$\sum_{q=1}^{Q_m}t_q^\star\frac{||\vec{c}_q||^2}{d}=1,\quad \text{then}\quad \sum_{q=0}^{Q_m}\delta\hat{n}_q^+=0.\tag{12}$$

Indeed, $\delta\hat{n}_q^+$ is projected on the same vector $\varepsilon_q^{(im)}$ as $\vec{\nabla}\cdot\vec{j}$ in weakly compressible flow solutions [e.g., Eqs. (11)–(13) of [98]], and $\varepsilon_q^{(im)}$ represents a linear combination of the isotropic second-order and fourth-order basis vectors in the standard MRT basis. Hereafter, we refer to such a solution as *a quasi-steady state*; its distinguished feature is that an immobile postcollision solution is not at rest but its distribution is uniform in space and constant in time: $\hat{n}_0^+(\vec{r},t)=-\partial_t\rho\varepsilon_0^{(im)}$; its steady-state average value provides us a mass-leakage rate estimate $\partial_t\rho$:

$$\partial_t\rho:=-\frac{\sum_{r\in V_p}\hat{n}_0^+(\vec{r})}{\varepsilon_0^{(im)}N_p}.\tag{13}$$

In turn, since the S-TRT operates without immobile population, the artificial mass source M_0 in Eq. (9a) adjusts the mass balance to solvability condition:

$$\text{S-TRT: }\delta\hat{n}_q^{+,s}=M_0t_q^\star\frac{||\vec{c}_q||^2}{d},\quad \sum_{q=1}^{Q_m}\delta\hat{n}_q^{+,s}=M_0.\tag{14}$$

We will delineate those boundary rules where $M_0\equiv-\partial_t\rho$ and the S-TRT can efficiently serve to access their mass balance characteristics following [42], with an advantage to be free from the transient stability issue and robust for any boundary rules.

D. Solvability of the Couette and Poiseuille flows in inclined channels

We will classify all boundary schemes with respect to their exactness in the linear (Couette) and parabolic (Poiseuille) flow modeled in an arbitrary rotated and grid-placed channel either with the Stokes or Navier-Stokes equilibrium. In this section we derive the solvability conditions, when these classical stationary flow solutions satisfy the TRT bulk model. The reference momentum solution $\vec{j}=\rho_0\vec{u}=\{j_{x'}(y'),0\}$ is parallel with the x' axis in a wall-aligned coordinate system (x',y') $[\{x'=x\cos[\varphi]+y\sin[\varphi],y'=y\cos[\varphi]-x\sin[\varphi]\}]$. The profile $j_{x'}(y')$ obeys the Stokes equation because the inertial term vanishes in a laminar channel flow:

$$\vec{\nabla}\cdot\vec{j}=0,\quad j_{y'}=0,\quad -F_{x'}=\nu\partial_{y'}^2j_{x'}.\tag{15}$$

The density solution is uniform in a periodic channel; the constant pressure-gradient driven Poiseuille flow replaces $F_{x'}$ by $-\partial_{x'}P(x')$ and the exact inlet-outlet pressure boundary schemes have been introduced for this system [58,69]. Although our analysis matches the two configurations, we focus primarily on the force-driven Poiseuille flow in a periodic channel. In theory, a linear or parabolic channel profile is expected to remain the same in the presence of the NSE term in Eq. (3b). However, numerically, these two solutions may differ because of the discretization (truncation) and boundary corrections. The bulk solvability conditions have been first established [87]; Sec. A extends them in Eq. (A6) and, in the dimensionless form in Eq. (A7); this analysis shows that the rotated profile can be matched exactly at the cost of introducing a nonuniform density distribution $\rho(y')$, which adjusts the truncation corrections to Eq. (15). We resume here the principal results.

Assuming a linear (Couette) momentum profile, the population solution is represented by either a linear (Stokes) or a quadratic (NSE) polynomial, and its nonequilibrium component satisfies the steady-state solvability conditions in Eq. (6) in an arbitrary rotated channel. However, the population solution becomes represented either by a quadratic (Stokes) or a quartic (NSE) polynomial in space on the parabolic (Poiseuille) profile $j_{x'}(y')$. The nonequilibrium Stokes component obeys the solvability conditions in Eq. (6) with *time-independent* uniform density field in an arbitrary rotated channel. In contrast, the NSE equilibrium allows for that only provided that the two free parameters: (collision) Λ in Eq. (2) and (equilibrium) a_ε in Eq. (3b) take particular values except in grid-aligned channels:

$$\text{NSE: }\vec{j}=j_{x'}(y'),\quad \rho(\vec{r},t)=\text{const when}$$
$$\sin[2\varphi]=0\text{: }\forall\ \Lambda,\ \forall a_\varepsilon,\tag{16a}$$
$$\sin[4\varphi]=0\text{: if }\ a_\varepsilon=-k_\varepsilon^{-1},\tag{16b}$$
$$\forall\ \varphi\text{: if }\Lambda=\tfrac{1}{12}\text{ and }a_\varepsilon=-k_\varepsilon^{-1},\quad k_\varepsilon=24.\tag{16c}$$

Equation (16a) says that no parameter restriction is required in a straight channel; Eq. (16b) indicates that Λ remains free in a diagonal flow provided that a_ε takes a particular value; Eq. (16c) means that $\Lambda=\frac{1}{12}$ shall be additionally fixed for an arbitrary rotation. In the case of the standard NSE equilibrium $a_\varepsilon=0$, or when $\Lambda=\frac{1}{12}$, $\rho(y',t)$ obeys in lattice units:

$$\text{NSE}:(1)\ a_\varepsilon=0,\quad \forall\Lambda,\ \forall\varphi,\ \text{or }(2)\ \Lambda=\frac{1}{12},\ \forall\ a_\varepsilon,\quad \forall\varphi,$$
$$c_s^2\partial_{y'}^2\rho=216(1+k_\varepsilon a_\varepsilon)\sin^2(2\varphi)\rho_0\frac{\left(\Lambda-\frac{1}{12}\right)\nu^2\text{Re}_g^2}{h^4},\tag{17a}$$
$$\partial_t\rho=6(1+k_\varepsilon a_\varepsilon)\sin^2(2\varphi)\rho_0\frac{\Lambda\nu\text{Re}_g^2}{h^4},\tag{17b}$$
$$\text{Re}_g=\frac{\mathcal{U}}{\nu}=\frac{\text{Re}}{h}.\tag{17c}$$

In these two cases, $\vec{j}=\{j_{x'}(y')=\rho_0u_{x'}(y'),0\}$ is exact but, as explained in more detail in Eqs. (A6a)–(A9), the parabolic distribution $\rho(y')$ adjusts the linear truncation dependency $E_{y'}(y')$

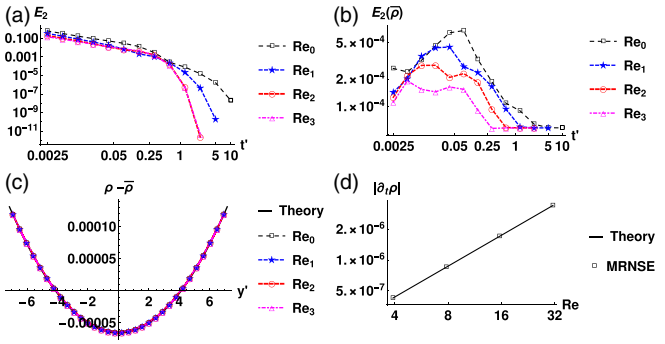

FIG. 2. The Poiseuille NSE flow solution in a grid-rotated channel is modeled with the standard equilibrium $a_\varepsilon = 0$ in Eq. (3b) and the exact MR$_{nse}$ no-slip scheme (symbols): (a) $E_2(t' = \frac{\nu t}{h^2})$; (b) $E_2(\bar{\rho})$; (c) $\rho(y') - \bar{\rho}$; (d) $|\partial_t\rho(\mathrm{Re})|$. Data: $\varphi = \arctan(\frac{1}{2})$, $H = 16$, $h = H\cos(\varphi)$, $\mathcal{U} \approx 0.136533$, $\Lambda = \frac{1}{8}$, $\nu_n = 2^{-n}\nu_0$, $\nu_0 = \frac{1}{2}$, $F_{x',n} = 2^{-n}F_{x',0}$, $F_{x',0} = 4\times10^{-3}$, $\mathrm{Re}_n = \frac{\mathcal{U}h}{\nu_n} \in 2^n\mathrm{Re}_0 \in [3.91, 31.2625]$, $n \in [0, 3]$.

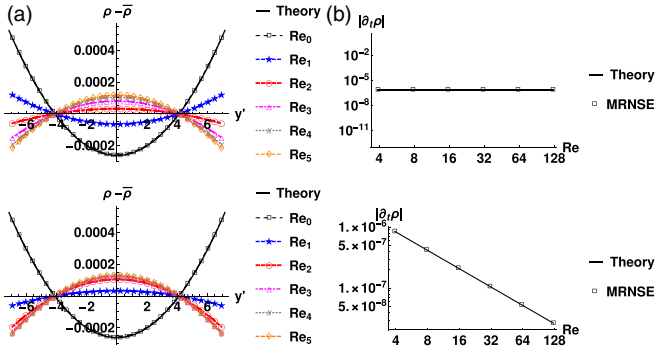

FIG. 3. The momentum profile $j_{x'}(y')$ is exact, but the density distribution (a) $\rho(y') - \bar{\rho}$ is parabolic in the presence of the mass-leakage rate (b) $|\partial_t\rho(\mathrm{Re})|$. These results are in exact agreement with the solvability prediction in Eq. (17). Data are similar as in Fig. 2 with $\nu_n = \frac{1}{2}\times2^{-n}$, $\mathrm{Re}_n \in [3.91, 125.05]$ but $\Lambda_n = \frac{1}{8}\times2^{-n}$ (top row) and $\Lambda_n = \frac{1}{4}\times2^{-2n}$ (bottom row).

in the y'-momentum equation when $\Lambda \neq \frac{1}{12}$; in turn, an uniform update $\partial_t\rho$ adjusts the right-hand-side term $\Lambda^- c_s^2\partial^2_{y'}\rho - E_m$ in the mass-conservation equation. These predictions are confirmed exactly with the help of the *p-nse-flow* exact scheme MR$_{nse}$ from Table VII; the key point is that MR$_{nse}$ supports directionally a quartic polynomial distribution $e_q^+(\rho, \mathcal{E}_q^{(u)})$ and the parabolic velocity profile. We apply the standard equilibrium $a_\varepsilon = 0$ in a fixed rotated channel, prescribe $\nu_n = 2^{-n}\nu_0$, and consider an increasing series of the Reynolds values $\mathrm{Re}_n = 2^n\mathrm{Re}_0$ at a fixed mean velocity $\mathcal{U}$; hence $\nu_n\mathrm{Re}_n$ remain constant in these simulations. Figure 2 confirms that the error estimate $E_2(j_{x'})$ converges to a zero solution and hence the steady-state profile $j_{x'}(y')$ remains exact, whereas the corrective term $\rho(y') - \bar{\rho}$ and $|\partial_t\rho|$ exactly agree with their predictions in Eq. (17). First, $\Lambda = \frac{1}{8}$ is arbitrary fixed in Fig. 2, the pressure curvature is then ν_n Re$_n$-independent in Eq. (17a) and all density distributions converge to the same value $E_2(\bar{\rho})$, computed with respect to the uniform solution $\rho = \bar{\rho}$. At the same time, $|\partial_t\rho|$ linearly increases with Re$_g$, as $2^n\Lambda\mathcal{U}^2/\nu_0$ in Eq. (17b). Prescribing again $\nu_n = 2^{-n}\nu_0$, Fig. 3 addresses the two situations, when $\Lambda_n = 2^{-n}\Lambda_0$ and $\Lambda_n = 2^{-2n}\Lambda_0$; the pressure curvature then varies with Re$_n$ whereas $|\partial_t\rho|$ is either Re$_n$-independent or decreases with it, accordingly.

Hence, $\partial_t\rho$ scales as $\Lambda^-\nu^2\mathrm{Re}_g^2 \propto \Lambda\nu\mathrm{Re}_g^2$ according to Eq. (17b) on a fixed grid, and its dimensionless counterpart scales as $\partial_{t'}\rho \propto \Lambda\mathrm{Re}h^{-4}$ giving $t' = t/T$, $T = h/\mathcal{U}$, and accordingly as $\partial_{t'}\rho \propto \Lambda\mathrm{Re}^2h^{-4}$ when $t' = t\nu/h^2 = t/(T\mathrm{Re})$; hence, $\partial_{t'}\rho$ is parametrized by Re and Λ, and it depends upon a_ε. The linear reduction $\Lambda \propto \mathrm{Re}_g^{-1}$, and hence $\Lambda \propto \nu$ at a fixed mean velocity $\mathcal{U}$, keeps the mass leakage rate $\partial_t\rho$ and, accordingly $\partial_t\rho/\mathcal{U}$, constant. The TRT/MRT ensures this Λ scaling due to the (freely) fixed value Λ^-, whereas the regularized models fix $\Lambda^- = \frac{1}{2}$. In turn, the TRT/MRT provides any quadratic scaling $\Lambda \propto \mathrm{Re}_g^{-2}$, and hence $\Lambda \propto \nu^2$ at a fixed $\mathcal{U}$, by reducing freely Λ^- with ν, whereas the BGK model [81] fixes $\Lambda = 9\nu^2$. It is recalled that the linear scaling of all nonhydrodynamic symmetric and antisymmetric rates $\Lambda_i^\pm \propto \nu$ at fixed $\mathcal{U}$ and h also corresponds to the consistent incompressible scaling [99], $\Lambda_i^\pm \propto \sqrt{3}\mathrm{Ma}\,h/\mathrm{Re}_i$, given the Mach number $\mathrm{Ma} = \mathcal{U}/c_s$ and the ghost Reynolds scale $\mathrm{Re}_i \propto \mathrm{Re}_g$.

In summary, the grid-rotated Poiseuille profile satisfies the TRT NSE bulk system in a time-space uniform density field only when $\Lambda = \frac{1}{12}$ and $a_\varepsilon = -k_\varepsilon^{-1}$ in Eq. (3b); otherwise, when $\Lambda \neq \frac{1}{12}$, the momentum and density solutions become x'-dependent, and this is also the case of any boundary scheme which is not *p-nse-flow*-exact, such as all commonly used and novel schemes, with the exception of MR$_{nse}$. The dimensionless truncation corrections in Eq. (A11) extend this analysis to the exponential grid-rotated Couette flow in the presence of wall-normal fluid injection; they suggest that the TRT cannot solve this NSE solution exactly, although $\Lambda = \frac{1}{12}$ still makes the third-order momentum corrections vanish and $a_\varepsilon = -k_\varepsilon^{-1}$ improves for the y' momentum and density distribution. In the general case, $a_\varepsilon = -k_\varepsilon^{-1}$ probably should not apply when $\Lambda \neq \frac{1}{12}$, because it then worsens the accuracy of the x' momentum according to Eqs. (A7a) and (A11a). Nevertheless, the exact parabolic grid-rotated NSE flow configuration $\Lambda = \frac{1}{12}$ and $a_\varepsilon = -k_\varepsilon^{-1}$ will allow us to examine the Galilean invariant characteristics of the proposed boundary classes in Sec. VI E without any bulk interference.

III. BOUNDARY SCHEMES: GUIDELINES

We first formulate the directional Taylor closure relation suitable for any link-wise boundary scheme. We then (1) define the *single-node* LI$^+$ and *the two-node* MR multireflection type rules; (2) provide the coefficients of their approximate closure relation; (3) formulate forcing boundary configuration; (4) derive the necessary conditions for *c-flow*, *p-flow*, *p-pressure*, parabolic, *c-nse-p-flow* and *p-nse-flow* accuracy; (5) discuss steady-state exact closure relations and parametrization conditions; (6) provide an expression for the temporal boundary step; and (7) introduce linear stability condition.

A. Directional closure relation

We construct boundary rules and develop their analysis in the frame of the TRT collision operator where they are independent of the discrete velocity set and problem dimension. Assuming the diffusive timescale, the population solution to Eq. (1) is approximated with the second-order accurate directional Chapman-Enskog expansion [57]:

$$\begin{aligned} f_q^{\pm} &= e_q^{\pm} - \tau^{-}\hat{n}_q^{\pm}, \\ \hat{n}_q^{\pm} &\approx \partial_t e_q^{\pm} + \partial_q e_q^{\mp} - \Lambda^{\mp}\partial_q^2 e_q^{\pm}, \ \forall\, \vec{r}, \quad \forall\, t. \end{aligned} \tag{18}$$

Equation (18) is expressed through the directional derivatives $\partial_q\psi = \vec{\nabla}\psi\cdot\vec{c}_q$ and $\partial_q^2\psi = \vec{\nabla}[\partial_q\psi]\cdot\vec{c}_q$. Combining the population decomposition in Eq. (18) with the second-order accurate directional Taylor relations between the neighbor nodes, the effective closure relation of a given linkwise boundary rule is fitted to the following Taylor expansion along the cut link $\vec{c}_q$:

$$\begin{aligned} \mathrm{CL}_q(\vec{r}_\mathrm{b},t) &= -w_q(\vec{r}_q,\tilde{t}), \quad \vec{r}_q = \vec{r}_\mathrm{b}+\vec{c}_q, \quad \tilde{t} = t+\delta_t, \\ \mathrm{CL}_q(\vec{r}_\mathrm{b},t) &:= (\alpha^{(p)}e_q^{+} + \alpha^{(u)}e_q^{-} \\ &\quad + \beta^{(p)}\partial_q e_q^{+} + \beta^{(u)}\partial_q e_q^{-} \\ &\quad + \gamma^{(p)}\partial_q^2 e_q^{+} + \gamma^{(u)}\partial_q^2 e_q^{-} \\ &\quad + \tau^{(p)}\partial_t e_q^{+} + \tau^{(u)}\partial_t e_q^{-})(\vec{r}_\mathrm{b},t). \end{aligned} \tag{19}$$

Hereafter, $\delta = \delta_q$ is the relative distance from the boundary node $\vec{r}_\mathrm{b}$ to the wall surface point $\vec{r}_q$ along $\vec{c}_q$ and all spatial coefficients $\alpha_q^{(p)} - \gamma_q^{(u)}$ are determined per link; for the sake of the simplicity, the index q is dropped unless indicated (see Fig. 4). The Dirichlet velocity boundary rule shall fit Eq. (19) to the directional Taylor expansion, which is prescribed with a free scale factor $\alpha^{(u)} = \alpha_q^{(u)}$:

$$\alpha^{(u)}\left(e_q^{-} + \delta\partial_q e_q^{-} + \frac{\delta^2}{2}\partial_q^2 e_q^{-} + \delta_t\partial_t e_q^{-}\right)\Big|_{\vec{r}_\mathrm{b}}^{t} = \alpha^{(u)}e_q^{-}\Big|_{\vec{r}_q}^{\tilde{t}}. \tag{20}$$

Hence, ideally, the coefficients in the left column in Eq. (19) should all vanish in the Dirichlet velocity rule, and vice versa in the Dirichlet scalar or pressure rule following [57,60,69].

B. The single-node and two-node multireflection

When the population $f_q(\vec{r}_\mathrm{b},t+1)$ leaves the computational domain at the boundary node $\vec{r}_\mathrm{b}$, the opposite (incoming) population $f_{-q}(\vec{r}_\mathrm{b},t+1)$ is prescribed by the boundary rule. The *multireflection* boundary rule computes $f_{-q}(\vec{r}_\mathrm{b},t+1)$ from the known or already updated solution components (populations, their postcollision, equilibrium, and nonequilibrium) moving along the same link $(\vec{c}_q,\vec{c}_{-q})$ (see Fig. 4):

$$\begin{aligned} f_{-q}(\vec{r}_\mathrm{b},t+1) &= \mathrm{MR}_q(\vec{r}_\mathrm{b}) + \mathcal{W}_q(\vec{r}_q,\tilde{t}), \\ \mathrm{MR}_q(\vec{r}_\mathrm{b}) &= \hat{\alpha}\widehat{f_q}(\vec{r}_\mathrm{b},t) + \hat{\beta}\widehat{f_{-q}}(\vec{r}_\mathrm{b},t) \\ &\quad + \beta[I^{(t)}f_q(\vec{r}_\mathrm{b},t+1) + (1-I^{(t)})f_q(\vec{r}_\mathrm{b},t)] \\ &\quad + \gamma[I^{(t)}f_q(\vec{r}_\mathrm{b}-\vec{c}_q,t+1) \\ &\quad + (1-I^{(t)})f_q(\vec{r}_\mathrm{b}-\vec{c}_q,t)] \\ &\quad + \hat{\gamma}\widehat{f_{-q}}(\vec{r}_\mathrm{b}-\vec{c}_q,t) \\ &\quad + \hat{F}_q(\vec{r}_\mathrm{b},t). \end{aligned} \tag{21}$$

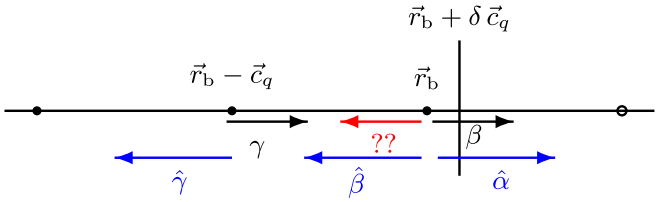

FIG. 4. The cut link $\vec{c}_q(\vec{r}_\mathrm{b})$ bisects the boundary surface at $\vec{r}_q = \vec{r}_\mathrm{b}+\delta\vec{c}_q$. A directional boundary scheme in Eq. (21) applies the postcollision populations with the coefficients $\{\hat{\alpha},\hat{\beta},\hat{\gamma}\}$, and either the poststreaming ($I^{(t)}=1$), precollision ($I^{(t)}=0$), or their combination ($I^{(t)}\in[0,1]$) with the coefficients $\{\beta,\gamma\}$.

The postcollision correction $\hat{F}_q$ is computed locally:

$$\hat{F}_q(\vec{r}_\mathrm{b},t) = \hat{K}^{+}\hat{n}_q^{+}(\vec{r}_\mathrm{b},t) + \hat{K}^{-}\hat{n}_q^{-}(\vec{r}_\mathrm{b},t). \tag{22}$$

The Dirichlet velocity term $\mathcal{W}_q(\vec{r}_q,\tilde{t})$ is prescribed in the form

$$\mathcal{W}_q(\vec{r}_q,\tilde{t}) = -\mathcal{A}_w^{(p)}e_q^{+}(\vec{r}_\mathrm{b},t) - \mathcal{A}_w^{(u)}e_q^{-}(\vec{r}_q,\tilde{t}). \tag{23}$$

Plugging Eq. (18) into Eq. (21), and interconnecting $e_q^{\pm}$ and $\hat{n}_q^{\pm}$ in neighbor nodes with the consistent second-order in space and first-order in time Taylor expansion, the second-order directional approximation to Eq. (21) becomes expressed by Eq. (19). The coefficients of the spatial component are provided in Eqs. (24)–(26), and the temporal coefficients are given in Eq. (41); their derivation is provided by Sec. B 2. The term of $\mathcal{A}_w^{(p)}e_q^{+}(\vec{r}_\mathrm{b},t)$ will cancel an unwanted contribution $\alpha^{(p)}e_q^{+}$ in Eq. (19); the term of $\mathcal{A}_w^{(u)}$ prescribes $e_q^{-}(\vec{r}_q,\tilde{t})$ on the wall surface from the given Dirichlet velocity value.

Definition: We refer any scheme obeying Eq. (21) with $\gamma = \hat{\gamma} = 0$ as *single-node LI*$^{+}$, otherwise it is referred to as *two-node MR*.

The original multireflection operates the population of β (LI and MR), and the one of γ (MR) after the propagation step from $\vec{r}_\mathrm{b}-\vec{c}_q$ to $\vec{r}_\mathrm{b}$, i.e., at time $t+1$ in Eq. (21) giving $I^{(t)}=1$, unless in the specific corner situations where the precollsion time t solution is employed in Eq. (21) with $I^{(t)}=0$. In order to make an automatic switch between t and $t+1$, Eq. (21) includes an optional flag $I^{(t)}\in[0,1]$. We then consider LI^{+} as a *single-node* class because the streaming may supply $\beta I^{(t)}f_q(\vec{r}_\mathrm{b},t+1)$ prior to the boundary update. In principle, this assumes that $\vec{r}_\mathrm{b}-\vec{c}_q$ is the fluid node unless when $I^{(t)}=0$ or, *in local-single-node schemes* $\beta = 0$. Similarly, the *two-node* MR sums $\gamma I^{(t)}f_q(\vec{r}_\mathrm{b}-\vec{c}_q,t+1)$ and $\gamma(1-I^{(t)})f_q(\vec{r}_\mathrm{b}-\vec{c}_q,t)$. The spatial approximation and steady-state solutions are independent of $I^{(t)}$ but the boundary time stepping δ_t in Eq. (19) may depend upon it.

C. Coefficients of the closure relation

The second-order directional approximation of Eq. (21) is presented by Eq. (19). The two equilibrium coefficients $\alpha^{(p)}$ and $\alpha^{(u)}$ in Eq. (19) read as

$$\alpha^{(p)} = -1 + \hat{\alpha} + \beta + \gamma + \hat{\beta} + \hat{\gamma}, \tag{24a}$$

$$\alpha^{(u)} = 1 + \hat{\alpha} + \beta + \gamma - \hat{\beta} - \hat{\gamma}. \tag{24b}$$

These two combinations are free-tunable; $\alpha^{(u)}$ defines the scale factor in Taylor relation in Eq. (20). The first-order

directional gradient terms of $\beta^{(p)}\partial_q e_q^+$ and $\beta^{(u)}\partial_q e_q^-$ in Eq. (19) read with

$$\beta^{(p)} = \tfrac{1}{2}(\hat{\alpha} - \hat{\beta} - \beta - 1) + \hat{K}^- - \alpha^{(u)}\Lambda^- + \tilde{\beta}^{(p)},$$
$$\tilde{\beta}^{(p)} = -\tfrac{3}{2}(\gamma + \hat{\gamma}), \tag{25a}$$
$$\beta^{(u)} = \tfrac{1}{2}(\hat{\alpha} + \hat{\beta} - \beta + 1) + \hat{K}^+ - \alpha^{(p)}\Lambda^+ + \tilde{\beta}^{(u)},$$
$$\tilde{\beta}^{(u)} = -\tfrac{3}{2}(\gamma - \hat{\gamma}). \tag{25b}$$

In turn, the second-order directional gradients $\gamma^{(p)}\partial_q^2 e_q^+$ and $\gamma^{(u)}\partial_q^2 e_q^-$ read with

$$\gamma^{(p)} = -\beta^{(u)}\Lambda^- + \tilde{\gamma}^{(p)}, \quad \tilde{\gamma}^{(p)} = \gamma + \hat{\gamma}, \tag{26a}$$
$$\gamma^{(u)} = -\beta^{(p)}\Lambda^+ + \tilde{\gamma}^{(u)}, \quad \tilde{\gamma}^{(u)} = \gamma - \hat{\gamma}. \tag{26b}$$

Since the coefficients $\tilde{\beta}^{(p)}$, $\tilde{\beta}^{(u)}$ and $\tilde{\gamma}^{(p)}$, $\tilde{\gamma}^{(u)}$ are nonzero only in two-node MR in Eq. (21), $\gamma^{(u)}$ and $\gamma^{(p)}$ are set by $\beta^{(p)}$ and $\beta^{(u)}$, respectively, in their single-node LI$^+$ counterpart:

$$\text{LI}^+\text{:}\ \gamma^{(u)} = -\beta^{(p)}\Lambda^+, \tag{27a}$$
$$\text{LI}^+\text{:}\gamma^{(p)} = -\beta^{(u)}\Lambda^-. \tag{27b}$$

This means that the closure relation in Eq. (19) needs two nodes to prescribe $\gamma^{(u)}$ and $\beta^{(p)}$, or $\gamma^{(p)}$ and $\beta^{(u)}$, independently.

D. Necessary conditions for linear accuracy

The first necessary condition, referred to as $CN^{(\alpha^{(p)})}$, is to make the term of $\alpha^{(p)}e_q^+(\vec{r}_b, t)$ vanish from Eq. (19) with the help of the $\mathcal{A}_w^{(p)}$ in Eq. (23):

$$CN^{(\alpha^{(p)})}\text{:}\ \ \mathcal{A}_w^{(p)} = \alpha^{(p)}. \tag{28}$$

The majority of the considered schemes, like LI$_k$, MR1$^+$, BFL-QI$_k$, and FH$_k$, will enforce $\alpha^{(p)} = 0$ with no need to compute the term of $e_q^+(\vec{r}_b, t)$ in Eq. (23).

The second necessary condition $CN^{(\alpha^{(u)})}$ equates the scaling factors $\alpha^{(u)}$ and $\mathcal{A}_w^{(u)}$ in Eq. (23) according to Eq. (19):

$$CN^{(\alpha^{(u)})}\text{:}\ \ \mathcal{A}_w^{(u)} = \alpha^{(u)}. \tag{29}$$

Accordingly, the r.h.s. term w_q in Eq. (19) gets the solution

$$w_q(\vec{r}_q, \tilde{t}) = -\alpha^{(p)}e_q^+(\vec{r}_b, t) - \alpha^{(u)}e_q^-(\vec{r}_q, \tilde{t}). \tag{30}$$

The third necessary condition ensures the linear accuracy for e_q^- in Eq. (20) via the term of $\beta^{(u)}\partial_q e_q^-(\vec{r}_b, t)$ in Eq. (19):

$$CN^{(\beta^{(u)})}\text{:}\ \beta^{(u)} = \alpha^{(u)}\delta. \tag{31}$$

The three necessary conditions are to be respected by all schemes. In particular, the exact *steady-state* closure relation is given in Eq. (B8), and it reads in LI$^+$ as

$$\text{LI}^+\text{:}\ \alpha^{(p)}e_q^+ + \alpha^{(u)}e_q^- + \beta^{(u)}\hat{n}_q^+ + \beta^{(p)}\hat{n}_q^-|_{\vec{r}_b}$$
$$= \alpha^{(p)}e_q^+|_{\vec{r}_b} + \alpha^{(u)}e_q^-|_{\vec{r}_q}. \tag{32}$$

Using Eqs. (28)–(31), any two LI$^+$ members will produce the same *steady-state* solutions when Eq. (32) is equivalent in them up to a scale factor $\alpha^{(u)}$. Nevertheless, the stability and transient accuracy may then differ and depend upon $\alpha^{(u)}$.

E. Forcing in the Dirichlet equilibrium

The forcing term is commonly considered as the parabolic effect, and it is then neglected in second-order (linear) accurate schemes. Following [69] we prescribe boundary equilibrium value in Eq. (23) with the optional flag $I_b = \{0, 1\}$:

$$e_q^-|_{\vec{r}_q}^{\tilde{t}} = t_q^\star \vec{j}(\vec{r}_q, \tilde{t}) \cdot \vec{c}_q + (1 - I_b)\mathcal{E}_q^{(f)}(\vec{r}_q, \tilde{t}),$$
$$I_b = \{0, 1\}, \quad I_b = 0 \text{ unless indicated.} \tag{33}$$

The common choice is $I_b = 1$ where $e_q^-(\vec{r}_q)$ is forcing independent and this term is set equal to zero on the no-slip wall. Alternatively, when $I_b = 0$, both the bulk and boundary equilibrium is computed with Eq. (3c). Using this choice, a constant, space-linear or parabolic forcing term will automatically vanish from the closure relation in Eq. (20). Moreover, only $I_b = 0$ will allow for the *isotropic* single-node *p-flow* schemes.

F. The *p-flow*, *p-pressure*, and parabolic accuracy

The parabolic term $\gamma^{(u)}\partial_q^2 e_q^-(\vec{r}_b, t)$ in Eq. (19) should match $\frac{1}{2}\delta^2\partial_q^2 e_q^-(\vec{r}_b, t)$ in Eq. (20); this defines the necessary *p-flow* condition $CN^{(\gamma^{(u)})}$:

$$\textit{p-flow}\text{:}\ \ CN^{(\gamma^{(u)})}\text{:}\ \ \gamma^{(u)} = \tfrac{1}{2}\alpha^{(u)}\delta^2 \ \text{ if } \ I_b = 0. \tag{34}$$

Equation (34) complements the three necessary conditions. In principle, the term of $\beta^{(p)}\partial_q e_q^+$, which sums the pressure-gradient and the inertial-term gradient (in the NSE case), shall vanish from Eq. (19); we call this "pressure-gradient accurate" *p-pressure* solution:

$$\textit{p-pressure}\text{:}\ CN^{(\beta^{(p)})}\text{:}\ \beta^{(p)} = 0. \tag{35}$$

A *parabolic*-accurate scheme combines two conditions:

$$\textit{parabolic} = \ \textit{p-flow} \cup \textit{p-pressure}. \tag{36}$$

The *p-flow* schemes are exact for grid-rotated force-driven Poiseuille Stokes flow; the two-node parabolic MR families will all obey Eq. (36) and extend this property to pressure-driven flow. However, the single-node LI$^+$ obeys Eq. (27), and hence, it cannot satisfy both Eqs. (34) and (35). To this end, we will introduce two corrections, referred to as $\hat{K}_3^-$ and $\hat{K}_4^-$, where LI$_k^+$ matches either Eq. (34) or Eq. (35), respectively.

G. The *c-nse-p-flow* accuracy

The symmetric equilibrium component $e_q^+(\vec{r})$ has a parabolic shape in a linear Couette flow modeled with the NSE equilibrium in Eq. (3b). The directional variation of this term is matched exactly only provided that the terms of $\beta^{(p)}\partial_q e_q^+$ and $\gamma^{(p)}\partial_q^2 e_q^+$ vanish in Eq. (19). Hence, the *c-nse-flow* exact scheme shall combine the linear accuracy with the two additional conditions:

$$\textit{c-nse-flow}\text{:}\ \ \textit{c-flow} \cup \{\beta^{(p)} = 0,\ \gamma^{(p)} = 0\}. \tag{37}$$

In this work, we construct the *c-nse-p-flow* Extended Multireflection (EMR) families, which combine the *c-nse-flow* and parabolic accuracy obeying the stronger conditions, as

$$\textit{c-nse-p-flow}\text{:}\ \textit{p-flow} \cup \{\beta^{(p)} = 0,\ \gamma^{(p)} = 0\}. \tag{38}$$

The EMR then extends the Pressure-Parabolic Multireflection (PM) family [69] by dropping its constraint $\alpha^{(p)} = 0$. The

EMR is exact for grid-rotated (1) Couette flow either with the Stokes or NSE equilibrium and (2) for Poiseuille Stokes flow.

H. The *p-nse-flow* accuracy

The $e_q^+(\vec{r})$ becomes quartic in Poiseuille profile modeled with the NSE term in Eq. (3b), and this academic flow model satisfies bulk solvability condition only in the restricted parameter space given in Eqs. (16) and (17). It is then matched in an arbitrarily rotated flow only provided that the additional (truncation) terms to Eq. (19), $\delta^{(p)}\partial_q^3 e_q^+$ and $\varepsilon^{(p)}\partial_q^4 e_q^+$, vanish from the closure relation:

$$p\text{-}nse\text{-}flow\text{: }c\text{-}nse\text{-}p\text{-}flow \cup \{\delta^{(p)} = \varepsilon^{(p)} = 0\}. \tag{39}$$

The three-node MR_{nse} family from Table VII enforces these two last additional conditions with respect to Eq. (38) due to the two second-neighbor populations: $\kappa f_q(\vec{r}_\mathrm{b} - 2\vec{c}_q, t+1)$ and $\hat{\kappa}\,\widehat{f}_{-q}(\vec{r}_\mathrm{b} - 2\vec{c}_q, t)$. This scheme is helpful for the exact benchmarking of the NSE equilibrium in a grid-rotated channel flow.

I. Grid-aligned channel flow

A straight channel, aligned with the coordinate axis, presents an exception where the Stokes and NSE equilibrium produce the same solution due to *an exponential nonequilibrium accommodation* [29,58] which remains invisible to $j_x(y)$ due to the symmetry of the cut links. Hence, the single-node LI^+ is sufficient to match the Couette flow, and the single-node LI_3^+ is sufficient to match the force-driven straight Poiseuille profile over the full relaxation parameter range, with either Stokes or NSE equilibrium. Otherwise, when the grid-aligned (straight or diagonal) walls are placed symmetrically, the single-node parametrized families $\mathrm{MGLI}(I_b = 1)$ and $\mathrm{LI}_1(I_b = 0)$ are able to locate them exactly due to specific, anisotropic and isotropic, respectively, solutions $\Lambda(\delta)$ in Eq. (49). Further, we show in Eqs. (C5)–(C8) that the single-node scheme [70] extends the *p-flow* property to an arbitrarily location of the straight channel due to its specific dependency $\alpha^{(u)}(\delta, \Lambda^\pm)$. On the contrary, Eqs. (D1) and (D5) show that $\Lambda(\delta, \Lambda^+)$ solutions do not exist with the two-node BFL-QI scheme [55] and FH/MLS schemes [52,53], which remain inexact even in a straight, force-driven Poiseuille Stokes flow. However, the $\mathrm{BFL\text{-}QI}_3$ and $\mathrm{FH}_3/\mathrm{MLS}_3$ are *p-flow* schemes in a rotated channel due to LI_3-type local nonequilibrium corrections built in Eqs. (D2) and (D6).

J. Bulk and boundary parametrization

The *parametrization* means that the dimensionless numerical steady-state solution obeys the physical scaling on a given grid. In bulk, the TRT and S-TRT schemes obey this condition when Λ is fixed. In the Stokes flow, the error estimate $E_2(\vec{j})$, or the Darcy's law permeability measurement, is then the same for any applied forcing and viscosity values. In the NSE flow, $\vec{j}$ and $E_2(\vec{j})$ is fixed by the grid Reynolds number Re_g and Λ. However, the numerical solutions do not necessarily obey the bulk parametrization condition because the boundary schemes may not support it. The sufficient parametrization conditions are formulated [57,69,72] with respect to the coefficients of the steady-state closure relation in Eq. (B8), and they can be applied to verify the parametrization of any directional boundary rule. These conditions are recalled in Eq. (B9).

It has been shown that the linear CLI and MR1 schemes [57,59] but also the recent MR extensions [69], including the *c-nse-p-flow* PM family, are parametrized. The original linear schemes, such as BFL_0 [55] and YLI_0 [56], do not respect this property, but they are parametrized within MGLI family [57]. Among the recent ELI schemes [66], the CELI-UQ counterpart of CLI is parametrized; otherwise, the two parametrization corrections, hereafter referred to as $\hat{K}_1^-$ and $\hat{K}_2^-$ in Eq. (22) are proposed [66]. In the present work, LI_1^+ generalizes MGLI uniformly for LI^+ with the help of $\hat{K}_1^-$. The two alternative corrections, $\hat{K}_3^-$ for *p-flow* and $\hat{K}_4^-$ for *p-pressure*, automatically parametrize LI_3^+ and LI_4^+ due to Eq. (27). The FH_k and $\mathrm{BFL\text{-}QI}_k$, $k = \{0, 1, 3, 4\}$, remain unparametrized, however, except when they are exact, such as FH_3 and $\mathrm{BFL\text{-}QI}_3$ in *p-flow*.

We emphasize that, although the parametrization does not imply the Galilean invariance, a parametrized numerical solution remains the same at fixed Re provided that the Dirichlet momentum value in Eq. (33) scales with the characteristic velocity $\mathcal{U}$.

K. Galilean invariance (GI)

The violation of the Galilean invariance (VGI) of the LBM velocity solution is attributed either to (1) third-order momentum truncation [100]; (2) incorrect viscous stress [101,102] due to absence of its cubic-velocity correction by the quadratic NSE term $\mathcal{E}_q^{(u)}$ in Eq. (3b); (3) inaccuracy of the boundary scheme on a static solid surface subject to the tangential motion [103]; and (4) deficient reconstruction on the moving solid-fluid interface due to (i) mass-flux [8,79,83], (ii) "refill" of the new-born nodes [82,83,104], and (iii) momentum-exchange algorithm [105], and also a combination of all these effects, where it has been understood [59] that the drag measured on the cylinder surface shows a much better agreement between the static and moving frames when the multireflection-based "refill" combines with the same accuracy-order modified momentum-exchange [59], which improves the standard force computation [2,4,55] for the stress approximation from the middle of the cut link towards the solid surface.

In bulk, the free relaxation rate MRT solution for VGI improvement is derived [100] from the third-order wave analysis in an uniform streaming flow, and it is equivalent to the TRT choice $\Lambda = \frac{1}{12}$ [see their Eq. (53), $s_5 = 3(2 - s_8)/(3 - s_8)$ giving $\Lambda^+ = \frac{1}{2} - \frac{1}{s_5}$ and $\Lambda^- = \frac{1}{2} - \frac{1}{s_8}$]. So far, the numerical confirmations [101] of the VGI bulk improvement have been carried out in a fully periodic time-dependent flow by combining the cubic velocity equilibria, able to correct the off-diagonal terms in the viscous momentum flux tensor, with the anisotropic relaxation stress-mode rates for its diagonal components. Arguably, in the presence of the solid wall, one needs first to confirm that the gradient of the cubic-velocity terms, contained in the symmetric postcollision $\hat{n}_q^+$, does not modify the linear boundary accuracy in Eq. (31). Provided that this necessary condition is satisfied, and since the linear boundary accuracy is independent of the collision rates, it might cope with the anisotropic relaxation stress rates.

TABLE II. Time stepping $\delta_t = \frac{1}{2}$ or $\delta_t = 1$ in the Dirichlet term $w_q(\vec{r}_q, t+\delta_t)$ in Eq. (19) is available due to specific $\alpha^{(u)}(\delta_t, I^{(t)})$ based on Eq. (41b). The ELI_k^+ corresponds to $I^{(t)} = 0$. Availability or stability restrictions are established as following: (a, b) $\Lambda^- \to 0$; (c) CLI_4; (d) $\Lambda^+ \leqslant 2$; (e) $\Lambda^- \leqslant \frac{1}{2}$; (f) $\Lambda^- \leqslant \frac{1}{6}$; (g) $\Lambda^- \leqslant \frac{1}{2}$.

	LI_0	ELI_0	LI_4	ELI_4	LI_3	$\mathrm{MR1}^+$	$\mathrm{MR1\text{-}BB} = \mathrm{MR1}^+(\alpha^{(u)}=2)$	AVMR	EMR
$\delta_t = \frac{1}{2}$	$I^{(t)} = 1^{(a)}$	$I^{(t)} = 0^{(b)}$	$I^{(t)} = 1^{(c)}$	ELI-UQ$_4$	$I^{(t)} \in [0,1]^{(d)}$	$I^{(t)} = 1, \forall\, \alpha^{(u)}$	$I^{(t)} \in [0,1]$		$I^{(t)} = 0^{(f)}$
$\delta_t = 1$			$I^{(t)} \in [0,1]$	ELI-UL$_4$	$I^{(t)} \in [0,1]$	$I^{(t)} \in [0,1]$		$I^{(t)} = 1^{(e)}$,	$I^{(t)} = 0^{(g)}$

Alternatively, the velocity-gradient ($\hat{n}_q^+$-based) equilibrium corrections [102] might need to verify whether their gradient interferes with the parabolic accuracy in the closure relations. For these reasons, before undertaking a coupling with the VGI bulk corrections, one shall preselect the most GI-compatible boundary schemes.

We then examine in Sec. VI E the GI property of the boundary schemes on the static walls following [103], but in the context of *an exact, Galilean invariant grid-rotated bulk solution* (16c). This study will show that the closure relation independence of the NSE term gradient $\partial_q \mathcal{E}_q^{(u)}$ is crucial for the mass-leakage reduction and the solution equivalence in the moving and static frames, when the Reynolds number grows with the tangential wall velocity. The established GI classification of the boundary schemes remains also valid for an inexact grid-rotated Poiseuille NSE flow bulk solution, confirming the GI suitability not only for two-node parabolic MR and AVMR, but also for single-node *p-pressure* LI_4^+ family. The next research step could, on the one hand, replace MR1 algorithms [59] with a more stable LI_4- or AVMR-based moving boundary techniques and, on the other hand, examine whether these boundary schemes retain their accuracy in the presence of the VGI bulk corrections.

L. Linear stability of boundary schemes

The semiheuristic stability condition [59] constrains the coefficients $\{\hat{\alpha}, \beta, \hat{\beta}, \gamma, \hat{\gamma}\}$ in Eq. (21) to interval $[-1, 1]$ given that their sum is equal to 1. This, however, guarantees the stability condition only for two coefficients, e.g., $\hat{\alpha}x + \hat{\beta}y \in [-1, 1]$ provided that $\{\hat{\alpha}, \hat{\beta} = 1 - \hat{\alpha}, x, y\} \in [-1, 1]$. The "convex linear interpolations" enforce stronger conditions $\{\hat{\alpha}, \beta, \hat{\beta}\} \in [0, 1]$ and $\hat{\alpha} + \beta + \hat{\beta} = 1$, thus giving $\alpha^{(p)} = 0$ in Eq. (24a), e.g., BFL [55], YLI [56], SSN [64], ZLI [61], and CHLI [62]. However, the $\hat{F}_q$ term in Eq. (22) modifies the nonequilibrium. We then propose an additional nonequilibrium stability criterion, which is inspired by the linear stability condition of the collision matrix. Recall that the TRT collision sums $n_q^\pm$ with its postcollision value $-n_q^\pm/\tau^\pm$, and the necessary linear stability condition prescribes $(1 - 1/\tau^\pm) \in [-1, 1]$, or $\tau^\pm \geqslant \frac{1}{2}$. Dropping the time, $-\beta^{(u)}/\tau^+$ and $-\beta^{(p)}/\tau^-$ present the coefficients of $n_q^\pm(\vec{r}_b)$ in *the exact* single-node closure relation in Eq. (32). Subtracting there the term $\mp n_q^\pm$ [which comes from the incoming population $-f_{-q}(\vec{r}_b)$ in Eq. (21)], we suggest two following linear stability conditions in single-node boundary schemes:

$$b^{(u)} = |-\beta^{(u)}/\tau^+ + 1| \leqslant 1, \tag{40a}$$

$$b^{(p)} = |-\beta^{(p)}/\tau^- - 1| \leqslant 1. \tag{40b}$$

We will show that Eq. (40) is satisfied by the three-population schemes obtained as the "convex linear interpolations," and this property remains valid with their $\hat{K}_1^-$ and $\hat{K}_4^-$ parametrizations. In contrast, the *p-flow* $\hat{K}_3^-$ parametrization narrows the stable small-viscosity space $\Lambda^+(\alpha^{(u)}, \Lambda)$ unless using the specific $\alpha^{(u)}(\Lambda, \delta)$, in agreement with the numerical computations.

M. Temporal accuracy

We substitute Eq. (18) into Eq. (21), replace $e_q^\pm(t+1)$ by $[e_q^\pm + \partial_t e_q^\pm](t)$ and express the coefficients of $\tau^{(p)}$ and $\tau^{(u)}$ in Eq. (19) through $\beta^{(p)}$ and $\beta^{(u)}$ from Eqs. (25a) and (25b):

$$\begin{aligned}
\tau^{(p)}(I^{(t)}) &= \tau^{(p)}|_{I^{(t)}=0} + (\beta+\gamma)I^{(t)},\\
\tau^{(p)}|_{I^{(t)}=0} &= (\beta^{(u)} - 1) - (\hat{\gamma} - \gamma),\\
\tau^{(u)}(I^{(t)}) &= \tau^{(u)}|_{I^{(t)}=0} + (\beta+\gamma)I^{(t)},\\
\tau^{(u)}|_{I^{(t)}=0} &= (\beta^{(p)} + 1) + (\hat{\gamma} + \gamma),
\end{aligned} \tag{41a}$$

$$\delta_t(I^{(t)}) = \frac{\tau^{(u)}(I^{(t)})}{\alpha^{(u)}}. \tag{41b}$$

The time stepping $\delta_t(I^{(t)})$ in Eq. (41b) formally defines $\tilde{t} = t + \delta_t$ for time-dependent Dirichlet value $e_q^-|_{\vec{r}_q}^{\tilde{t}}$ in Eq. (41b). Giving $\tilde{t}$, e.g., $\tilde{t} \in \{t, t+\frac{1}{2}, t+1\}$, one may solve Eq. (41b) with respect to $\alpha^{(u)}(I^{(t)})$, or with respect to $I^{(t)} \in [0, 1]$ unless when $\beta + \gamma = 0$, such as in ELI^+ where $\beta = \gamma = 0$. Table II summarizes conditions corresponding to the boundary stepping $\delta_t(\alpha^{(u)}, I^{(t)}) = \{\frac{1}{2}, 1\}$ in Eq. (20). According to these results, $\delta_t = 1$ is easier to achieve with LI_3^+, LI_4^+ and *c-nse-p-flow* $\mathrm{VMR}(\alpha^{(u)}, \hat{K}^\pm)$, whereas $\delta_t = \frac{1}{2}$ is the solution with CLI_4, ELI-UQ$_4$, $\mathrm{MR1}(I^{(t)} = 1)$, and MR1-BB (see Table I). Our simulations will be restricted to the time-independent boundary conditions; however, LI_0 and MR have been examined [58] for $I^{(t)} = 1$ in the pulsatile, force-driven, and pressure gradient-driven, Womerslay flow along the same lines. Further, Eq. (41a) can be fitted similarly for either the Dirichlet pressure boundary condition [57,69] with $\delta_t(I^{(t)}) = \frac{\tau^{(p)}(I^{(t)})}{\alpha^{(p)}}$, or when one aims to remove the temporal pressure fluctuation from Eq. (19).

IV. THE SINGLE-NODE CLASS LI^+

In what follows, Sec. IV A specifies the single-node large class $\mathrm{LI}^+ = \{\mathrm{LI}_k^+\}$ and states its parametrization relations. Section IV B defines its subclass $\mathrm{LI} = \{\mathrm{LI}_k\}$, $k \in [0, 4]$. Section IV C defines another subclass $\mathrm{ELI}^+ = \{\mathrm{ELI}_k^+\}$, $k \in [0, 4]$. Section IV D builds LI_0 and ELI_0^+ counterparts. Section IV E develops the LI^+ linear stability analysis.

Section IV F verifies it numerically. Section IV G summarizes the findings.

A. The LI$^+$: coefficients

The LI$^+$ operates with $\gamma = \hat{\gamma} = 0$ in Eq. (21) but allows for $\hat{K}^\pm \neq 0$ in Eq. (22). Its coefficients $\alpha^{(p)}$ in Eq. (24a) and $\alpha^{(u)}$ in Eq. (24b) are freely adjustable. The LI$^+$ satisfies the two necessary linear conditions given in Eqs. (28) and (29) through Eq. (30), and the third condition in Eq. (31) substituting there $\beta^{(u)}$ from Eq. (25b). Equations (24), (30), and (31) then allow us to express $\{\hat{\alpha}, \beta, \hat{\beta}\}$ and $\{\mathcal{A}_w^{(p)}, \mathcal{A}_w^{(u)}\}$ through three adjustable coefficients $\alpha^{(u)}$, $\alpha^{(p)}$, and $\hat{K}^+$:

$$\begin{aligned}
\text{LI}^+\text{: } \hat{\alpha} &= -1 + \alpha^{(u)}\left(\tfrac{1}{2} + \delta\right) - \hat{K}^+ + \alpha^{(p)}\Lambda^+,\\
\beta &= 1 - \alpha^{(u)}\delta + \alpha^{(p)}\left(\tfrac{1}{2} - \Lambda^+\right) + \hat{K}^+,\\
\hat{\beta} &= 1 + \tfrac{1}{2}(\alpha^{(p)} - \alpha^{(u)}), \quad \gamma = \hat{\gamma} = 0,\\
\mathcal{A}_w^{(p)} &= \alpha^{(p)}, \quad \mathcal{A}_w^{(u)} = \alpha^{(u)}.
\end{aligned} \tag{42}$$

The last relation defines the Dirichlet term $\mathcal{W}_q$ in Eq. (23). We substitute Eq. (42) into Eq. (25) to obtain $\beta^{(p)}$, and express $\gamma^{(u)}$ and $\gamma^{(p)}$ with Eq. (27). The LI$^+$ closure relation in Eq. (19) then reads with the following coefficients:

$$\text{LI}^+\text{: } \beta^{(u)} = \alpha^{(u)}\delta, \quad \gamma^{(p)} = -\beta^{(u)}\Lambda^-, \tag{43a}$$

$$\begin{aligned}
\beta^{(p)} &= -2 + \alpha^{(u)}\left(\tfrac{1}{2} + \delta - \Lambda^-\right) + \alpha^{(p)}\left(\Lambda^+ - \tfrac{1}{2}\right)\\
&\quad + \hat{K}^- - \hat{K}^+, \quad \gamma^{(u)} = -\beta^{(p)}\Lambda^+.
\end{aligned} \tag{43b}$$

The coefficient $\hat{K}^-$ of the antisymmetric correction $\hat{K}^-\hat{n}_q^-$ in Eq. (22) modifies $\beta^{(p)}$ and $\gamma^{(u)}$ in Eq. (43b), but Eq. (42) remains the same. We introduce (1) $\hat{K}_1^-$ for the steady-state parametrization following MGLI [57], (2) $\hat{K}_3^-$ for the *p-flow* condition in Eq. (34), and (3) $\hat{K}_4^-$ for the *p-pressure* accuracy in Eq. (35). These corrections adjust $\gamma^{(u)}$ in Eq. (43b) as, accordingly,

$$\text{LI}_1^+ \text{ with } \hat{K}_1^-\text{: } \gamma^{(u)}(\hat{K}_1^-) = \alpha^{(u)}\Lambda, \tag{44a}$$

$$\text{LI}_3^+ \text{ with } \hat{K}_3^-\text{:} \gamma^{(u)}(\hat{K}_3^-) = \alpha^{(u)}\frac{\delta^2}{2}, \quad I_b = 0, \tag{44b}$$

$$\text{LI}_4^+ \text{ with } \hat{K}_4^-\text{:} \gamma^{(u)}(\hat{K}_4^-) = \beta^{(p)}(\hat{K}_4^-) = 0. \tag{44c}$$

The parametrization procedure with $\hat{K}_1^-$ is not unique; for example, ELI$_2$ [66] is derived with the condition $\partial_{\Lambda^+}\gamma^{(u)}(\hat{K}_2^-) = 0$. Noticeably, when $\alpha^{(p)} = 0$, the coefficients $\{\hat{\alpha}, \beta, \hat{\beta}\}$ in Eq. (42), $\hat{K}_1^-$ and $\hat{K}_4^-$ in Eq. (44), do not depend upon Λ^+ explicitly plugging there $\gamma^{(u)}$ from Eq. (43). Hence, the TRT and MRT collisions with the same rate Λ^- for all antisymmetric modes are expected to apply LI$_1^+$ and LI$_4^+$ similarly, provided that $\hat{K}^+$ is prescribed Λ^+-independent. This is not the case of *p-flow* LI$_3^+$ unless when MRT collision builds $\hat{n}_q^+$ from the kinematic viscosity modes and computes $\hat{K}_3^-$ with $\Lambda^+ = 3\nu$ (see also Sec. B 1)

The exact LI$^+$ *steady-state* closure relation is given in Eq. (32) with $\beta^{(u)} = \alpha^{(u)}\delta$ and $\beta^{(p)} = -\frac{\gamma^{(u)}}{\Lambda^+}$. The sufficient parametrization condition is fulfilled when the coefficients $m_3' = \frac{\beta^{(u)}}{\alpha^{(u)}}$ and $m_4' = -\frac{\gamma^{(u)}}{\alpha^{(u)}\Lambda}$ depend upon $\Lambda^\pm$ only through Λ [see Eqs. (37)–(40) in [69] and Eq. (B9)]. The LI$_k^+$ families with $k = \{1, 3, 4\}$ are then all parametrized with $m_3' = \delta$ and, plugging Eq. (44) for $m_4'(\hat{K}_k^-) = -\gamma^{(u)}(\hat{K}_k^-)/(\alpha^{(u)}\Lambda)$:

$$m_4'(\hat{K}_1^-) = -1, \quad m_4'(\hat{K}_3^-) = -\frac{\delta^2}{2\Lambda}, \quad m_4'(\hat{K}_4^-) = 0. \tag{45}$$

Additionally, the ratio $e_q^-(\vec{r}_q, \tilde{t})/\mathcal{U}$ in Eq. (32) should remain fixed giving a characteristic velocity $\mathcal{U}$, meaning that the Dirichlet velocity value should scale with $\mathcal{U}$ to ensure the same dimensionless solution. This procedure assumes $I_b = 0$ in Eq. (33); otherwise the dimensionless force form should be additionally respected by the closure relation following [69,72]. The parametrization condition with Eq. (45) applies for any single-node directional boundary rule provided that it fits Eq. (32) at the steady state.

Finally, according to Eq. (32), any two LI$^+$ members with the same ratio $\beta^{(p)}/\alpha^{(u)}$ produce equivalent *steady-state* closure relations. Since all members of one family LI$_k^+$, $k = \{1, 3, 4\}$, hold $\beta^{(p)} = -\gamma^{(u)}(\hat{K}^-)/\Lambda^+$, they obey this condition and produce the same *stationary momentum solution*. However, their quasisteady state solutions in the presence of the mass leakage $\partial_t\rho \neq 0$ may slightly differ when $\alpha^{(p)} \neq 0$ or $\hat{K}^+ \neq 0$ (see Sec. VI A 1).

B. The subclass LI = {LI$_k$}

Originally, the infinite LI($\alpha^{(u)}$) family [57] gathers the two- and three-population linear combinations in Eq. (21), their MGLI parametrization [57] is then performed with $\hat{K}_1^-$ condition in Eq. (44a). Hereafter, we consider LI$_k$ as the LI$_k^+$ subfamily with $\alpha^{(p)} = \hat{K}^+ = 0$. Sec. IV B 1 specifies LI$_k$ coefficients; Sec. IV B 2 extends MGLI to force-independent (isotropic) LI$_1$; Sec. IV B 3 introduces the *isotropic* scheme IPLI which is *p-flow* accurate due to a specific $\alpha^{(u)}$ dependency; IPLI extends the *anisotropic* WLI scheme [70] from the straight channel to an arbitrary rotation. Sections IV B 4 and IV B 5 construct two parametrized subfamilies LI$_3^+$ and LI$_4^+$ according to Eq. (44).

1. *The LI : Coefficients*

When $\alpha^{(p)} = \hat{K}^+ = 0$, the set $\{\hat{\alpha}, \beta, \hat{\beta}\}$ in Eq. (42) becomes fixed by $\alpha^{(u)}$ and δ:

$$\begin{aligned}
\text{LI: } \hat{\alpha} &= \alpha^{(u)}\left(\frac{1}{2} + \delta\right) - 1, \quad \hat{\beta} = 1 - \frac{1}{2}\alpha^{(u)},\\
\beta &= 1 - (\hat{\alpha} + \hat{\beta}) = 1 - \alpha^{(u)}\delta,\\
\mathcal{A}_w^{(p)} &= \alpha^{(p)} = 0, \quad \mathcal{A}_w^{(u)} = \alpha^{(u)}
\end{aligned} \tag{46a}$$

$$\{\hat{\alpha}, \beta, \hat{\beta}\} \in [-1, 1] \quad \text{if } \alpha^{(u)} \in \left[0, \alpha_{\text{CLI}}^{(u)} = \frac{4}{1 + 2\delta}\right]. \tag{46b}$$

Accordingly, Eq. (43b) gives

$$\gamma^{(u)} = 2\Lambda^+ - \alpha^{(u)}\left[\left(\delta + \tfrac{1}{2}\right)\Lambda^+ - \Lambda\right] - \hat{K}^-\Lambda^+. \tag{47}$$

The LI$_0$ operates with $\hat{K}^\pm = 0$; the well-known LI$_0$ members are (bounce-back) BB($\delta = \frac{1}{2}$), BFL$_0$ [55], YLI$_0$ [56] and CLI$_0$ [57]; their coefficients are gathered in Table III. The LI$_0$ does not necessarily reduce to BB when $\delta = \frac{1}{2}$, e.g., BFL$_0$ and CLI$_0$ reduce to it but not YLI$_0$. Moreover, CLI$_0$ copes with $\hat{\alpha} = 1$, like the BB, and its coefficient $\alpha^{(u)}$ determines the heuristic stability limit $\alpha_{\text{CLI}}^{(u)}$ in Eq. (46b). Section C 1 shows

TABLE III. The LI applies with $\alpha^{(p)} = \hat{K}^+ = 0$, and its coefficients $\{\hat{\alpha}, \beta, \hat{\beta}\}$ are set by $\alpha^{(u)}$ and δ in Eq. (46). Several LI_0 members are specified, where ZLI [61] and CHLI [62] families belong to LI_0 according to Eq. (C2); CHLI is equivalent to $\mathrm{ZLI}|_{l->\gamma-2\delta}$; YLI $\in$ ZLI with $l = \delta$ and ZLI reduces to the SSN scheme [64] when $l = 2\delta$. The LI_0 applies with $\hat{K}_1^- = 0$; LI_1 with $\hat{K}_1^-$ in Eq. (48); LI_3 with $\hat{K}_3^-$ in Eq. (51); and LI_4 with $\hat{K}_4^-$ in Eq. (52); IPLI is *p-flow* scheme with $\hat{K}^\pm = 0$. The $\mathrm{LI}_3(\alpha^{(u)})$ performs a switch to $\alpha_0^{(u)}$ from Eq. (65) for those links where $\Lambda < \frac{\alpha^{(u)}(\delta)\delta^2}{4}$ or to IPLI when $\Lambda \leqslant \frac{\delta^2}{2}$; otherwise the small viscosity range $\Lambda^+ \geqslant \Lambda^+_{\min}$ in Eq. (64) improves $\mathrm{LI}_3(\alpha^{(u)})$ stability for any Λ when $\alpha^{(u)} \to 0$.

$\mathrm{LI}_0 \in \mathrm{LI}^+$ with $\hat{K}^\pm = 0, \alpha^{(p)} = 0, \beta = 1 - (\hat{\alpha} + \hat{\beta})$					
Eq. (46)	δ	$\alpha^{(u)}$	$\hat{\alpha}$	$\hat{\beta}$	$\{\hat{\alpha}, \beta, \hat{\beta}\}$
Parametrized scheme					
BB	$\frac{1}{2}$	2	1	0	[0,1]
CLI	[0,1]	$\alpha^{(u)}_{\mathrm{CLI}} = \frac{4}{1+2\delta}$	1	$-\frac{1-2\delta}{1+2\delta}$	$[-1, 1]$
Parametrized *p-flow* scheme					
IPLI	]0,1]	$\alpha^{(u)} = \frac{4\Lambda^+}{\delta^2+\Lambda^+ +2\delta\Lambda^+ -2\Lambda}$, $\Lambda < \frac{\delta^2}{2}$			$[-1, 1]$
"Convex-interpolation based" schemes					
BFL(1)	$[0, \frac{1}{2}]$	2	2δ	0	[0,1]
BFL(2)	$[\frac{1}{2}, 1]$	$\frac{1}{\delta}$	$\frac{1}{2\delta}$	$1 - \hat{\alpha}$	[0,1]
YLI	[0,1]	$\frac{2}{1+\delta}$	$\frac{\delta}{1+\delta}$	$\frac{\delta}{1+\delta}$	[0,1]
ZLI	$[0, \frac{1}{2}]$	$\frac{2}{1+l}$, $l \in [0, 2\delta]$	$\frac{2\delta-l}{1+l}$	$\frac{l}{1+l}$	[0,1]
ZLI	$[\frac{1}{2}, 1]$	$\frac{2}{1+l}$, $l \in [2\delta - 1, 2\delta]$	$\frac{2\delta-l}{1+l}$	$\frac{l}{1+l}$	[0,1]

that ZLI [61] and CHLI [62] belong to $\mathrm{LI}_0^+(I^{(t)} = 0)$ with the specific adjustable dependency $\alpha^{(u)}(\delta, l)$, where they match YLI_0 for $l = \delta$ and SSN [64] for $l = 2\delta$.

2. *The MGLI/LI$_1$: Parametrization and grid-aligned p-flow*

Originally, the LI family [57,58] operates with $I_b = 1$ in Eq. (33). The idea of the (Λ-parametrized) MGLI family [57,58] is to replace the coefficient $\beta^{(p)}$ by its BB solution $\beta^{(p)} = -\alpha^{(u)}\Lambda^-$, or equivalently $\gamma^{(u)} = \alpha^{(u)}\Lambda$. According to Eq. (45), this condition is sufficient for LI^+ parametrization, and it is equivalent to the condition $\partial_{\Lambda^+}\gamma^{(u)}(\hat{K}_2^-) = 0$ in LI family. The LI_1 adopts the MGLI parametrization condition but applies $I_b = 0$. The two schemes then produce the same solution $\hat{K}_1^-$:

$$\begin{aligned} &\mathrm{MGLI/LI}_1\colon \hat{K}^- = \hat{K}_1^-\colon \gamma^{(u)}(\hat{K}_1^-) = \alpha^{(u)}\Lambda, \\ &\text{with } \hat{K}_1^- = 1 - \hat{\alpha} = \tfrac{1}{2}[4 - \alpha^{(u)}(1 + 2\delta)], \\ &\mathrm{BB},\ \mathrm{CLI}_0 = \mathrm{CLI}_1\colon \quad \hat{\alpha} = 1\colon \hat{K}_1^- = 0. \end{aligned} \tag{48}$$

The BB and CLI_0 are automatically parametrized, but this is not the case for BFL_0 and YLI_0, as has been shown in [57,59]. The stationary solutions are identical inside MGLI and LI_1, but MGLI and LI_1 solutions differ in the presence of forcing. Namely, MGLI and LI_1 solutions coincide, respectively, with the ones of $\mathrm{BB}(I_b = 1)$ and $\mathrm{BB}(I_b = 0)$ on the midway straight wall $\delta = \frac{1}{2}$. These schemes, however, do not satisfy the *p-flow* condition (34) unless under a particular Λ for a straight *symmetric channel*, giving the same distance $\delta \in]0, 1]$ for the two walls:

$$\mathrm{MGLI}, \quad I_b = 1\colon \Lambda = \frac{3\delta^2}{4}, \quad \mathrm{BB}\colon \Lambda|_{\delta=\frac{1}{2}} = \frac{3}{16}, \tag{49a}$$

$$\mathrm{LI}_1, \quad I_b = 0\colon \Lambda = \frac{\delta^2}{2}, \quad \Lambda|_{\delta=\frac{1}{2}} = \frac{1}{8}. \tag{49b}$$

Equation (49a) is derived [58] using the (anisotropic) directional projection of the Stokes flow equation (C3) to express $\alpha^{(u)}\mathcal{E}_q^{(f)}$ in Eq. (3c) with $\partial_q^2 e_q^-$, and this term then sums with $\gamma^{(u)}(\hat{K}_1^-)\partial_q^2 e_q^- = \alpha^{(u)}\Lambda\partial_q^2 e_q^-$ in Eq. (19). The MGLI then reproduces the BB solution [51]: $\Lambda|_{\delta=\frac{1}{2}} = \frac{3}{16}$, on the midway wall. It is shown [58] that the MGLI solutions are equivalent in the force- and pressure-gradient driven channel flow (see Sec. 2.4 in [58] with their notations $p_q = \hat{n}_q^+$, $m_q^{(F)} = \hat{n}_q^-$, $\alpha^{(u)}\beta^{p\star} = \beta^{(p)}$, $\Lambda_e = \Lambda^+$, $\Lambda_o = \Lambda^-$, $\Lambda_{eo} = \Lambda$). In turn, Eq. (49b) is isotropic, it is obtained by equating $\gamma^{(u)}(\hat{K}_1^-) = \alpha^{(u)}\Lambda$ to the correct Taylor term $\alpha^{(u)}\frac{\delta^2}{2}$ in Eq. (20), because the forcing term vanishes from Eq. (20) when $I_b = 0$. These solutions are also extended [17,65,69] over a diagonal flow: Eq. (49a) then changes to $\Lambda = \frac{3\delta^2}{2}$ but Eq. (49b) remains the same.

To sum up, the particular optimal solutions established with $\mathrm{MGLI}(I_b = 1)$ are also valid in the pressure-gradient driven flow; however, they are anisotropic and depend upon the forcing weight in Eq. (3c); e.g., Eq. (49a) is valid provided that momentum term $t_q^\star \vec{j}\cdot\vec{c}_q$ and $\mathcal{E}_q^{(f)} = t_q^\star \Lambda^- \vec{F}\cdot\vec{c}_q$ apply the same weight $t_q^\star$ (see also [96]). On the other hand, the $\mathrm{LI}_1(I_b = 0)$ closure relation is force-independent, and its optimal Λ solution is isotropic.

3. *Isotropic single-node p-flow IPLI with $\hat{K}^\pm = 0$*

We first explore the idea to enforce the *p-flow* accuracy with the help of a particular solution $\alpha^{(u)}$. We prescribe $\gamma^{(u)}$ with Eq. (47), substitute $\hat{K}^\pm = 0$ and compute $\alpha^{(u)}$ from the LI_3^+ condition in Eq. (44):

$$\begin{aligned} &\mathrm{IPLI} = \mathrm{LI}_0 \cap \mathrm{LI}_3\colon \alpha^{(u)} = \frac{4\Lambda^+}{\delta^2 + \Lambda^+ + 2\delta\Lambda^+ - 2\Lambda}, \\ &\hat{K}^\pm = 0, \quad I_b = 0, \quad \gamma^{(u)} = \alpha^{(u)}\frac{\delta^2}{2}, \\ &\{\hat{\alpha}, \beta, \hat{\beta}\} \in [-1, 1] \quad \text{if} \quad \Lambda \in \left[0, \frac{\delta^2}{2}\right], \quad \delta \in [0, 1]. \end{aligned} \tag{50}$$

The *inclined Poiseuille* IPLI is then exact in a force-driven grid-rotated Poiseuille flow for any Λ using $I_b = 0$ in Eq. (33) and, operating without corrections, it is a common member of LI_0 and LI_3; hence, this scheme is parametrized according to Eq. (45) and *p-flow* accurate. However, giving $\alpha^{(u)}$ from Eq. (50) in Eq. (46b), IPLI constraints Λ to the interval $[0, \frac{\delta^2}{2}]$. The nonequilibrium stability conditions in Eq. (40) produce slightly more strict conditions. Practically, we find that condition $\Lambda \leqslant \frac{1}{2}\min\delta^2$ is necessary and sufficient. When $\Lambda = \frac{\delta^2}{2}$ in a straight channel, IPLI reduces to $\mathrm{CLI}(\alpha^{(u)}_{\mathrm{CLI}})$, giving the stability limit in Eq. (46b) and *p-flow* accuracy in Eq. (49b). It follows that the IPLI stability condition becomes too much restrictive when $\delta \to 0$.

The APLI counterpart of IPLI in Sec. C 2 switches $I_b = 0$ to $I_b = 1$; the obtained solution $\alpha^{(u)}$ then depends upon the flow inclination, and it is equivalent to WLI [70] in a straight flow. In contrast to IPLI and APLI, WLI is exact only in a straight flow, and whereas WLI is extended [107] for a pure diffusion in a straight slab, IPLI is extended [42] to an isotropic PPLI, which is exact on the parabolic diffusion profile in an arbitrarily inclined channel.

4. LI_3: A generic p-flow approach via $\hat{K}_3^-$

We consider now an alternative *p-flow* approach, when $\alpha^{(u)}$ remains free but $\hat{K}^-$ solves LI_3^+ condition $\gamma^{(u)}(\hat{K}^-) = \alpha^{(u)}\frac{\delta^2}{2}$ giving $\gamma^{(u)}(\hat{K}^-)$ from Eq. (47):

$$\begin{aligned}\mathrm{LI}_3 \quad \text{with } \hat{K}^- = \hat{K}_3^- \ &: \gamma^{(u)}(\hat{K}_3^-) = \alpha^{(u)}\frac{\delta^2}{2}, \quad I_b = 0,\\ \hat{K}_3^- &= 2 + \alpha^{(u)}\Lambda^- - \frac{\alpha^{(u)}[\delta^2 + \Lambda^+(1+2\delta)]}{2\Lambda^+},\\ \hat{K}_3^- &= 0 \quad \text{if } \alpha^{(u)} = \alpha^{(u)}_{IPLI}. \end{aligned} \tag{51}$$

The $\mathrm{BB}_3(I_b = 0)$ applies with $\hat{K}_3^-(\alpha^{(u)} = 2, \delta = \frac{1}{2})$, and it is then *p-flow*-exact in a straight channel with midway wall. The coefficient $\hat{K}_3^-$ vanishes either giving $\alpha^{(u)}$ from IPLI in Eq. (50), or $\alpha^{(u)}_{\mathrm{CLI}}$ from Eq. (46b) together with $\Lambda = \frac{\delta^2}{2}$ from Eq. (49b). Replacing $I_b = 0$ by $I_b = 1$, $\hat{K}_3^-$ becomes anisotropic summing $\gamma^{(u)}(I_b = 0)$ with $-\frac{\alpha^{(u)}\Lambda}{3\Theta_q^2}$ according to Eq. (C3).

To sum up, the *p-flow* LI_3 is exact for a parabolic profile in a force-driven grid-inclined flow. The $\hat{K}_3^-$ postcollision correction can be built-in into any linkwise scheme giving its coefficient $\gamma^{(u)}$ in Eq. (19). We will specify $\hat{K}_3^-$ with $\mathrm{ELI}_3^+ \in \mathrm{LI}_3^+$, the two-node BFL-$\mathrm{QI}_3$ obeying Eq. (21) and the two-node $\mathrm{FH}_3/\mathrm{MLS}_3$ which do not fit Eq. (21). The LI_3^+ members all produce equivalent *steady-state density and momentum* solution due to the equivalence of their closure in Eq. (32), and they satisfy the parametrization condition according to Eq. (45). However, the stationary profiles may differ between LI_3^+, BFL-QI_3, and $\mathrm{FH}_3/\mathrm{MLS}_3$, because $\beta^{(p)}$ does not obey Eq. (27a) with these two last schemes, and then they remain nonparametrized even in the presence of $\hat{K}_3^-$.

5. LI_4: A generic p-pressure approach via $\hat{K}_4^-$

Since the single-node schemes cannot satisfy the two parabolic conditions in Eq. (36) simultaneously, we introduce LI_4 which satisfies only the *p-pressure* condition in Eq. (35) with $\beta^{(p)} = -\gamma^{(u)}/\Lambda^+$ giving $\gamma^{(u)}$ from Eq. (47):

$$\begin{aligned}\mathrm{LI}_4 \quad \text{with } \hat{K}^- = \hat{K}_4^- &: \ \beta^{(p)} = 0,\\ \hat{K}_4^- &= 2 + \alpha^{(u)}\big(\Lambda^- - \tfrac{1}{2} - \delta\big). \end{aligned} \tag{52}$$

The coefficient $\hat{K}_4^-$ reduces to $\hat{K}_1^-$ when $\Lambda^- \to 0$ in agreement with the parametrization conditions $\gamma^{(u)} = 0$ (LI_4) and $\gamma^{(u)} = \alpha^{(u)}\Lambda$ (LI_1), accordingly. The $\hat{K}_4^-$ is parametrized in agreement with Eq. (45), and it lies on the stability boundary to Eq. (40b); hence Eq. (40a) alone determines the LI_4^+ nonequilibrium stability condition. The *p-pressure* schemes are only exact on linear velocity and pressure solutions; hence, they match for the pressure-gradient and the leading order inertial term $\partial_q \mathcal{E}_q^{(u)}$ in Eq. (3b).

C. The subclass $\mathrm{ELI}^+ = \{\mathrm{ELI}_k^+\}$

The *local single-node* XELI family [66] is based on the construction of the virtual ("ghost") wall populations and the generalized interpolations for incoming populations. In this work, XELI is first represented in Eq. (C10) by ELI_0, which operates with $\beta = \gamma = \hat{\gamma} = 0$ but complements Eq. (21) with the additional local ("ghost") term ME_q. Here we introduce ELI_0^+: it replaces the nonequilibrium component of the ME_q via the specific $\hat{F}_q$ in Eq. (22), without need to reconstruct the ghost populations, and then ELI_0^+ belongs to LI^+; its counterparts ELI_k^+ will be built with Eq. (44). Plugging β from Eq. (42) into condition $\beta = 0$, we derive solution for $\hat{K}^+$ in Eq. (22) which is used by all ELI^+ members:

$$\mathrm{ELI}^+: \quad \hat{K}^+ = K^+_{ELI} := \alpha^{(u)}\delta + \alpha^{(p)}\big(\Lambda^+ - \tfrac{1}{2}\big) - 1. \tag{53}$$

We substitute Eq. (53) for $\hat{K}^+$ in Eq. (42) and define the coefficients of ELI^+:

$$\begin{aligned}\mathrm{ELI}^+: \ \hat{\alpha} &= \tfrac{1}{2}(\alpha^{(p)} + \alpha^{(u)}), \quad \hat{\beta} = 1 + \tfrac{1}{2}(\alpha^{(p)} - \alpha^{(u)}),\\ \beta = \gamma = \hat{\gamma} &= 0, \quad \mathcal{A}_w^{(p)} = \alpha^{(p)}, \quad \mathcal{A}_w^{(u)} = \alpha^{(u)}. \end{aligned} \tag{54}$$

Hence, whereas the coefficients of LI_0 are fixed with $\alpha^{(p)} = 0$ and $\alpha^{(u)}$ in Eq. (46), those of ELI_0^+ are expressed through the two adjustable parameters, $\alpha^{(u)}$ and $\alpha^{(p)}$; their solutions for particular ghost interpolations [66] are specified in Table IV. The ELI_0^+ then reproduces $\mathrm{ELI}_0 = \mathrm{XELI}$ with the help of the specific correction $K^-_{ELI_0}\hat{n}_q^-$ derived in Eq. (C14):

$$\mathrm{ELI}_0^+: \hat{F}_q = K^+_{ELI}\hat{n}_q^+ - I_{ncs}K^-_{ELI_0}\hat{n}_q^-, \tag{55a}$$

$$K^-_{ELI_0} = -1 + \alpha^{(u)}\delta + \alpha^{(p)}\big(\Lambda^- - \tfrac{1}{2}\big), \tag{55b}$$

$$X = \{\mathrm{N}, \mathrm{C}, \mathrm{S}\}: \ I_{ncs} = \{-1, 0, 1\}. \tag{55c}$$

An optional value I_{ncs} reflects that, originally, the ghost population $f_{-q}(\vec{r}_q, \tilde{t})$ in Eq. (C10) is built with one of the three approximations: $\mathrm{XELI} = \{\mathrm{NELI}, \mathrm{CELI}, \mathrm{SELI}\}$ [*non-symmetric*, *central*, and *symmetric*] for the ghost component $\hat{n}_q^-(\vec{r}_q, t+1)$; The ELI_0^+ can be extended to the continuous parameter $I_{ncs} \in [-1, 1]$ with the idea of LLI scheme [68] recast to $\mathrm{ELI}^+ - \mathrm{ULT}$ in Eq. (C15).

Plugging K^+_{ELI} into Eq. (43b), ELI_k^+ copes with

$$\mathrm{ELI}_k^+: \quad \gamma^{(u)}(\hat{K}_k^-) = \Lambda^+ - \alpha^{(u)}\left(\frac{\Lambda^+}{2} - \Lambda\right) - \hat{K}_k^-\Lambda^+. \tag{56}$$

We derive solution $\hat{K}_k^-$ when $k = \{1, 3, 4\}$ from Eq. (44) by substituting there Eq. (56) for $\gamma^{(u)}(\hat{K}_k^-)$:

$$\mathrm{ELI}_k^+: \ \hat{F}_q = K^+_{ELI}\hat{n}_q^+ + \hat{K}_k^-\hat{n}_q^-, \quad k = \{0, 1, 3, 4\}, \tag{57a}$$

$$\mathrm{ELI}_0^+: \hat{K}_0^- = -I_{ncs}K^-_{ELI_0}, \tag{57b}$$

$$\mathrm{ELI}_1^+: \hat{K}_1^- = 1 - \frac{\alpha^{(u)}}{2}, \tag{57c}$$

$$\mathrm{ELI}_3^+: \hat{K}_3^- = 1 + \alpha^{(u)}\Lambda^- - \frac{\alpha^{(u)}(\delta^2 + \Lambda^+)}{2\Lambda^+}, \tag{57d}$$

$$\mathrm{ELI}_4^+: \hat{K}_4^- = 1 + \alpha^{(u)}\left(\Lambda^- - \frac{1}{2}\right). \tag{57e}$$

TABLE IV. The ELI_k^+ applies K_{ELI}^+ from Eq. (53) and $\{\hat{\alpha}, \beta, \hat{\beta}\}$ from Eq. (54); they are determined by $\alpha^{(p)}$ and $\alpha^{(u)}$. The $\text{ELI}_0^+ = \{\text{NELI}, \text{CELI}, \text{SELI}\}$ applies $\hat{F}_q = K_{ELI}^+ \hat{n}_q^+ - I_{ncs} K_{ELI_0}^- \hat{n}_q^-$ from Eq. (55) with $I_{ncs} = \{-1, 0, 1\}$, accordingly. The ELI_k^+, $k = \{1, 3, 4\}$, applies $\hat{F}_q = K_{ELI}^+ \hat{n}_q^+ + \hat{K}_k^- \hat{n}_q^-$ with $\hat{K}_k^-$ from Eq. (57). The parameters $\alpha^{(u)}$ and $\alpha^{(p)}$ are specified in interpolation-based XELI schemes [66] and the *p-flow* CELI-IP from Eq. (60); the LLI [67,68] copes with the XELI-ULT coefficients and $\hat{K}^-$ given in Eq. (C15). The last column lists the LI_0 counterparts of CELI according to Eq. (59), where CELI-UQ from Eq. (59a) is parametrized.

	$\text{ELI}^+ \in \text{LI}^+$ with $\hat{K}^+ = K_{ELI}^+$, $\beta = 0$			
Eq. (54)	δ	$\alpha^{(p)}$	$\alpha^{(u)}$	$\text{LI}_0 \sim$ CELI, Eq. (58b)
	Parametrized *p-flow* scheme with $\hat{K}^- = 0$			
CELI-IP	[0,1]	0	$\frac{2\Lambda^+}{\delta^2+\Lambda^+-2\Lambda}$	IPLI ∼ CELI-IP
	Ghost-interpolation-based coefficients			
ELI-UQ	[0,1]	0	2	CLI ∼ CELI-UQ
ELI-UL	[0,1]	−1	1	YLI ∼ CELI-UL
ELI-ULT	[0,1]	$\frac{-1}{1+\delta}$	$\frac{1}{1+\delta}$	SSN ∼ CELI-ULT
ELI-FL(1)	$[0, \frac{1}{2}]$	$\frac{2\delta-1}{1-\delta}$	$\frac{1}{1-\delta}$	BFL(1) ∼ CELI-FL(1)
ELI-FL(2)	$[\frac{1}{2}, 1]$	$\frac{1-2\delta}{\delta}$	$\frac{1}{\delta}$	BFL(2) ∼ CELI-FL(2)

We stress that when $k \neq 0$, (1) an original $\hat{n}_q^-$-approximation is dropped, and ELI_k^+ does not need to distinguish between $\{N, C, S\}$, and (2) ELI_k^+ steady-state solutions are then all parametrized. When $\alpha^{(p)} = 0$, K_{ELI}^+ in Eq. (53) does not depend upon Λ^+ explicitly, and then ELI_0^+, ELI_1^+, and ELI_4^+ apply similarly with the TRT and the MRT operators giving Λ^- for all antisymmetric modes and summing all postcollision symmetric modes in $\hat{n}_q^+$, provided that $\alpha^{(u)}$ is set Λ^+-independent. In contrast, the *p-flow* ELI_3^+ in Eq. (57d) depends upon Λ^+ and the MRT implementation shall then adapt its different symmetric modes (see in Sec. B 1).

D. The LI_0 and $\text{ELI}_0^+ \sim \text{ELI}_0 = \text{XELI}$

We construct the equivalent members between the *non-parametrized* classes LI_0 and ELI_0^+ keeping in mind that ELI_0^+ produces the same solutions as the original $\text{XELI} = \text{ELI}_0$. We give $\gamma^{(u)}$ with $\hat{K}^- = 0$ for LI_0 in Eq. (47), and $\gamma^{(u)}$ with $\hat{K}^- = -I_{ncs} K_{ELI_0}^-$ in Eq. (56), where $I_{ncs} = \{-1, 0, 1\}$ accordingly in $\text{XELI} = \{\text{NELI}, \text{CELI}, \text{SELI}\}$. The LI_0 and ELI_0^+ steady-state solutions are the same provided that their coefficients $\beta^{(p)}/\alpha^{(u)}$, or equivalently $\gamma^{(u)}/\alpha^{(u)}$, are the same in Eq. (32). The counterparts $\text{LI}_0(\alpha^{(p)} = 0, \alpha^{(u)})$ and $\text{ELI}_0^+(\tilde{\alpha}^{(p)}, \tilde{\alpha}^{(u)})$ then obey:

$$\text{NELI} \sim \text{LI}_0 \quad \text{if } \tilde{\alpha}^{(u)} = \alpha^{(u)} + \frac{1}{2}\tilde{\alpha}^{(p)}\left(\frac{1}{2} - \Lambda^-\right), \tag{58a}$$

$$\text{CELI} \sim \text{LI}_0 \quad \text{if } \tilde{\alpha}^{(u)} = -\frac{\alpha^{(u)}}{\alpha^{(u)}\delta - 2}, \tag{58b}$$

$$\text{SELI} \sim \text{LI}_0 \quad \text{if } \tilde{\alpha}^{(u)} = -\frac{\tilde{\alpha}^{(p)}\alpha^{(u)}(1 - 2\Lambda^-)}{4(\alpha^{(u)}\delta - 1)}. \tag{58c}$$

It is noticeable that $\text{NELI} \sim \text{LI}_0$ in Eq. (58a) for equal prefactors $\tilde{\alpha}^{(u)} = \alpha^{(u)}$ when $\tilde{\alpha}^{(p)} = \alpha^{(p)} = 0$; in particular, this allows us to build local NELI counterparts with $\beta = 0$ of the three-population interpolations; in contrast, there are no SELI equivalents when $\tilde{\alpha}^{(p)} = 0$ in Eq. (58c). In turn, Eq. (58b) delineates the "central" basic counterparts which scale Eq. (32) with the scale factor $k = \frac{\alpha^{(u)}}{\tilde{\alpha}^{(u)}}$:

$$\text{CELI-UQ} \sim \text{CLI}, \quad k = \frac{2}{1 + 2\delta}, \tag{59a}$$

$$\text{CELI-UL} \sim \text{YLI}, \quad k = \frac{2}{1 + \delta}, \tag{59b}$$

$$\text{CELI-ULT} \sim \text{SSN}, \quad k = \frac{2(1 + \delta)}{1 + 2\delta}, \tag{59c}$$

$$\text{CELI-FL(1)} \sim \text{BFL(1)}, \quad k = 2(1 - \delta),$$

$$\text{CELI-FL(2)} \sim \text{BFL(2)}, \quad k = 1. \tag{59d}$$

Equation (59a) predicts the steady-state equivalent solutions for CELI-UQ and CLI, both operating with $\alpha^{(p)} = 0$, $\hat{\alpha} = 1$ and both parametrized automatically, $\hat{K}_1^- = 0$; we will find, however, that CLI is much more stable than CELI-UQ. Eq. (59b) delineates CELI-UL and YLI counterparts; these two schemes apply uniformly through $\delta \in [0, 1]$ and they perform very similarly, robustly, and rapidly converging to steady state; Eq. (59c) indicates another uniform couple CELI-ULT and SSN which is expected to behave even more stably due to the smaller coefficients $\alpha^{(u)}$. Equation (59d) assigns BFL and CELI-FL: these two schemes are fractional at $\delta = \frac{1}{2}$ and CELI-FL(2) with $K_{ELI_0}^- = 0$ is a common member of three classes: NELI/CELI/SELI; additionally, since it operates with $\alpha^{(p)} = 0$ and $\alpha^{(u)} = \delta^{-1}$, it holds $\hat{K}^+ = 0$ and then coincides with BFL(2). The BFL and CELI-FL behave very similarly between them and with YLI/CELI-UL in terms of stability. Finally, the XELI counterparts of ZLI and CHLI can be constructed giving $\alpha^{(u)} = \alpha^{(u)}(\delta, l)$ from Table III and $\alpha^{(p)} = 0$ in Eq. (58).

We build now the counterpart $\text{CELI-IP} \in \text{ELI}_0^+ \cap \text{ELI}_3^+$ of IPLI from Eq. (50) giving $\alpha^{(u)}(\text{IPLI})$ in Eq. (58b); the CELI-IP then also becomes a parametrized *p-flow* scheme, where we additionally prescribe $\alpha^{(p)} = 0$:

$$\text{CELI-IP} = \text{CELI}_0^+ \cap \text{ELI}_3^+ \text{: } \alpha^{(u)} = \frac{2\Lambda^+}{\delta^2 + \Lambda^+ - 2\Lambda},$$

$$\hat{K}^+ = K_{ELI}^+, \quad \alpha^{(p)} = \hat{K}^- = 0, \; I_b = 0, \quad \gamma^{(u)} = \alpha^{(u)}\frac{\delta^2}{2},$$

$$\{\hat{\alpha}, \beta, \hat{\beta}\} \in [0, 1] \quad \text{if} \quad \Lambda \in \left]0, \frac{\delta^2}{2}\right]. \tag{60}$$

The stability condition $\Lambda \in]0, \frac{\delta^2}{2}]$ holds $\{\hat{\alpha}, \beta, \hat{\beta}\} \in [0, 1]$, and it is sufficient to satisfy the nonequilibrium stability condition in Eq. (40) when $\delta \in [0, \frac{1}{2}]$; otherwise the Λ^+-independent condition slightly narrows the Λ range, e.g., from $\Lambda^{\max}(\delta^2 = 1) = \frac{1}{2}$ to $\Lambda^{\max}(\delta = 1) \approx 0.457$. In principle, Eq. (40) gives some advantage to CELI-IP over IPLI, whereas numerically the two schemes perform very similarly.

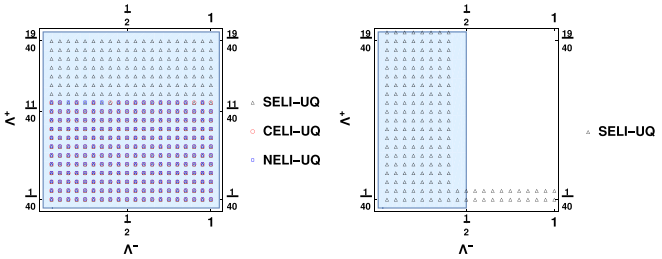

FIG. 5. Unstable numerical subdomains (symbols) in the Couette Stokes channel flow with a three-node width closed by XELI-UQ; the code is run through 20^2 points $\Lambda^+\times\Lambda^- \in [\frac{1}{40}, \frac{1}{2}]^2$. (a) $\delta = \{1, 1\}$, Eq. (E1a) predicts XELI-UQ as unstable when $\Lambda^+ \leqslant \frac{1}{2}$, $\forall\Lambda^-$. (b) $\delta = \{0, 0\}$, Eq. (E2a) predicts SELI-UQ as unstable when $\Lambda^- \leqslant \frac{1}{2}, \forall\Lambda^+$.

E. Stability

The LI$^+$ linear stability analysis is based on the nonequilibrium estimate proposed by Eq. (40). The key point is that $\beta^{(u)} = \alpha^{(u)}\delta$ in all schemes, and then condition $|b^{(u)}| \leqslant 1$ in Eq. (40a) is satisfied when either $\delta = 0$ or when $\alpha^{(u)} \in]0, \frac{1+2\Lambda^+}{\delta}]$, $\delta \in]0, 1]$. The sufficient, *viscosity-independent* condition then reads

$$\delta = 0 \;\text{ or }\; \alpha^{(u)}(\delta) \in \left]0, \frac{1}{\delta}\right], \;\forall\,\Lambda^+, \quad \forall\,\delta \in]0, 1]. \tag{61}$$

The BB($\delta = \frac{1}{2}, \alpha^{(u)} = 2$) and the convex-interpolation-based schemes as YLI, BFL, SSN, and ZLI in Table III, but also their local-single-node counterparts ELI-UL, ELI-FL, ELI-ULT in Table IV and LLI in Eq. (C15) obey this condition [see also after Eq. (C2)]. This is then valid for all their counterparts, such as XELI $\in$ ELI$_0^+$ in Eq. (55), and parametrizations with $\hat{K}^-$, $k = \{1, 3, 4\}$, because these post-collision manipulations do not modify $\alpha^{(u)}$. However, neither CLI$_k$ with $\alpha^{(u)} = \frac{4}{1+2\delta}$ nor XELI-UQ$_k$ with $\alpha^{(u)} = 2$ obey Eq. (61) when $\delta \in]\frac{1}{2}, 1]$, and they then satisfy Eq. (40a) within a very restricted viscosity range given in Eq. (E1); recall, these schemes operate with $\{\hat{\alpha}, \beta, \hat{\beta}\} \in [-1, 1]$. Figure 5 displays in the first diagram the results of the numerical stability study with the three schemes XELI-UQ giving the same distance $\delta = \{1, 1\}$ towards the two channel walls; Eq. (E1a) then predicts the whole domain $\Lambda^+ \leqslant \frac{1}{2}$ as *unstable*. The NELI-UQ and CELI-UQ display almost an identical unstable region $\Lambda^+ \leqslant \frac{11}{40}$; the SELI-UQ is the most unstable and uniformly covers the predicted interval $\Lambda^+ < \frac{1}{2}$ independently of Λ^-, in agreement with Eq. (40a).

The second stability condition in Eq. (40b), $|b^{(p)}| \leqslant 1$, reads with

$$\text{LI}_k^+, \quad \beta^{(p)} = -\frac{\gamma_k^{(u)}}{\Lambda^+}: \quad b^{(p)} = \frac{2\gamma_k^{(u)}}{\Lambda^+(1+2\Lambda^-)} - 1, \tag{62a}$$

$$\text{LI}_1^+, \quad \beta^{(p)} = -\alpha^{(u)}\Lambda^-: \quad b^{(p)} = \frac{2\alpha^{(u)}\Lambda^-}{1+2\Lambda^-} - 1, \tag{62b}$$

$$\text{LI}_3^+, \quad \beta^{(p)} = -\frac{\alpha^{(u)}\delta^2}{2\Lambda^+}: \quad b^{(p)} = \frac{2\alpha^{(u)}\delta^2}{\Lambda^+(1+2\Lambda^-)} - 1, \tag{62c}$$

$$\text{LI}_4^+, \quad \beta^{(p)} = 0: \quad b^{(p)} = 1. \tag{62d}$$

The convex-interpolation-based schemes YLI/BFL, SSN, and ZLI, but also their counterparts ELI-UL/ELI-FL and ELI-ULT satisfy Eq. (62a) when $k = 0$ and then both conditions in Eq. (40) in full parameter range $\Lambda^\pm > 0$; this property is also shared by LLI(γ^-) schemes from Eq. (C15) when $\gamma^- \in [0, 2]$. In contrast, Eq. (62a) ($k = 0$) restricts SELI-UQ to Eq. (E2a) in the second half-interval $\delta \in [0, \frac{1}{2}]$. Figure 5 demonstrates in the second diagram that SELI-UQ matches the predicted unstable region $\Lambda^-|_{\delta=0} \leqslant \frac{1}{2}$ in Eq. (E2a) within the whole examined viscosity range; in addition, the small viscosity range $\Lambda^+ \leqslant \frac{1}{20}$ is unstable with all Λ^-. Hence, the SELI-UQ, which copies $\hat{n}_q^-$ from $\vec{r}_b$ to $\vec{r}_q$, is less stable than the "central" approximation $\hat{n}_q^-(\vec{r}_q) = 0$ (CELI-UQ) or the nonequilibrium bounce-back $\hat{n}_q^-(\vec{r}_q) = -\hat{n}_q^-(\vec{r}_b)$ (NELI-UQ). In fact, SELI-UQ is the least stable among the "standard" schemes in Tables III and IV. The CELI-UQ counterpart is CLI; CLI$|_{\delta=1}$ and CLI$|_{\delta=0}$ is predicted to be unstable when $\Lambda^+ < \frac{1}{6}$ or $\Lambda^- \geqslant \frac{1}{2}$, respectively in Eqs. (E1b) and (E2c) but it remains stable inside the predicted regions in simulations shown in Fig. 5. In practice, the CLI$_k$ behaves overall much more robustly than predicted.

Further, using Eqs. (62b) and (62d), the YLI/BFL, SSN, ZLI, ELI-UL/ELI-FL, and ELI-ULT$_k$ = LLI$_k$ satisfy Eq. (40b) with their $\hat{K}_1^-$ and $\hat{K}_4^-$ parametrizations, $k = 1$ and $k = 4$ [see also after Eq. (C15)]. Indeed, (1) $\hat{K}_1^-$ in Eq. (62b) does not restrict Λ^- when $\alpha^{(u)} \in]0, 2]$, $\forall\delta \in [0, \frac{1}{2}]$ and $\alpha^{(u)} \in]0, \delta^{-1}]$, $\forall\delta \in]\frac{1}{2}, 1]$; (2) $b^{(p)}$ in Eq. (62d) lies on the stability boundary, and hence $\hat{K}_4^-$ does not impose any additional limitation; and (3) $\hat{K}_1^-$ and $\hat{K}_3^-$ obey the stability conditions when $\alpha^{(u)} \to 0$, i.e., when the role of the boundary constraint diminishes and two bulk constraints $\Lambda^\pm > 0$ become sufficient. The most restrictive is $\hat{K}_3^-$ in Eq. (62c), and its stability is addressed in the next section.

F. Stability of *p-flow* schemes

1. *Predicted p-flow stability*

Plugging Eq. (62c) into Eq. (40b), the $\hat{K}_3^-$ stable viscosity range reads

$$\text{LI}_3^+\text{: } \Lambda^+ \geqslant \Lambda_{\min}^+ = \frac{\alpha^{(u)}\delta^2}{2(1+2\Lambda^-)}, \quad \delta \in [0, 1]. \tag{63}$$

Equation (63) says that (1) $\delta = 0$ is stable and (2) the small viscosity range becomes available when $\alpha^{(u)} \to 0$ or Λ^- grows. In terms of Λ, Eq. (63) predicts the following stable viscosity range:

$$\text{LI}_3^+\text{:}\Lambda^+ \geqslant \Lambda_{\min}^+ = \frac{1}{2}(\alpha^{(u)}\delta^2 - 4\Lambda),$$

$$\text{when } \;\Lambda \in]0, \Lambda_{\min}], \quad \Lambda_{\min} = \frac{\alpha^{(u)}\delta^2}{4}, \tag{64a}$$

$$\text{or } \;\forall\Lambda^+ \quad \text{if } \;\Lambda > \Lambda_{\min},\; \delta \in [0, 1]. \tag{64b}$$

Figure 6 displays the predicted stability bounds (a) $\Lambda_{\min}^+(\Lambda^-)$ and (b) $\Lambda_{\min}^+(\Lambda)$ in the worst case $\delta = 1$. Equation (64a) says that the whole viscosity range becomes available when $\alpha^{(u)}$ is set equal to $\alpha_0^{(u)}$; Eq. (61) is then satisfied provided that

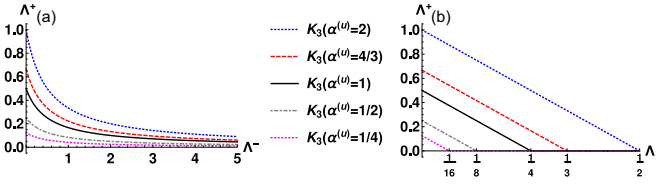

FIG. 6. A predicted *p-flow* stability boundary due to $\hat{K}_3^- \hat{n}_q^-$ when $\delta = 1$: (a) $\Lambda^+_{\min}(\Lambda^-)$ in Eq. (63) and (b) $\Lambda^+_{\min}(\Lambda)$ in Eq. (64a); the unstable domain is below the line.

$\Lambda \leqslant \frac{\delta}{4}$:

$$\mathrm{LI}_3^+\big(\alpha_0^{(u)}\big): \quad \alpha^{(u)} \to \alpha_0^{(u)}(\delta,\Lambda) := \frac{4\Lambda}{\delta^2} \quad \text{if} \quad \Lambda \leqslant \frac{\alpha^{(u)}(\delta)\delta^2}{4},$$
$$\text{then} \quad \alpha_0^{(u)} \in]0, \delta^{-1}] \quad \text{if} \quad \Lambda \leqslant \frac{\delta}{4}, \quad \delta \neq 0. \tag{65}$$

We propose to (optionally) apply a directional switch to $\alpha_0^{(u)}(\delta,\Lambda)$ when first condition in Eq. (65) is met, by replacing a given link value $\alpha^{(u)}(\delta)$ by $\alpha_0^{(u)}$; this strategy is expected to provide full viscosity range with the schemes obeying Eq. (61). The ELI_3^+ shall preselect its second governing parameter $\alpha^{(p)}$ in Eq. (54): for example, $\alpha^{(u)} = \alpha_0^{(u)}$ combined with $\alpha^{(p)} = 0$ satisfies condition $\{\hat{\alpha}, \hat{\beta}\} \in [-1, 1]$ when $\Lambda < \frac{\delta^2}{2}$, $\delta \in [0, \frac{1}{2}]$ or $\Lambda < \frac{\delta}{4}$, $\delta \in]\frac{1}{2}, 1]$. Alternatively, the *p-flow* IPLI and CELI-IP operate with $\hat{K}_3^- = 0$ and the same stability restriction $\Lambda < \min[\frac{\delta^2}{2}]$ in Eqs. (50) and (60); IPLI then holds $\{\hat{\alpha}, \beta, \hat{\beta}\} \in [-1, 1]$ and CELI-IP in more stable interval $\{\hat{\alpha}, \beta, \hat{\beta}\} \in [0, 1]$. In turn, IPLI and CELI-IP converge faster than $\mathrm{LI}_3^+(\alpha_0^{(u)})$ to the steady state applying these schemes uniformly for all links when Λ is very small. Alternatively, since all these schemes reduce Λ towards its stability limit when $\delta \to 0$, the most robust strategy is to apply $\hat{K}_3^-$ with the sufficiently large $\Lambda > \Lambda_{\min}$ when viscosity is small and possible in terms of the accuracy.

2. *Numerical p-flow stability*

In principle, one should not expect that Eq. (40) provides the effective stability conditions exactly, because it only concerns the boundary populations. The numerical validation is then run in a small, three node width straight channel, where all examined schemes are exact for a steady-state Stokes Couette flow for any distances between the two walls. The Poiseuille flow produces very similar stability diagrams in this system. The simulations are terminated when either the exact solution is reached with (1) a given precision $E_2 < \varepsilon \approx 10^{-8}$ or (2) the global mass conservation is violated. Our numerical analysis first confirmed the robustness of the interpolation-based schemes YLI/BFL and ELI-UL/ELI-FL, as well as their parametrized counterparts $\hat{K}_1^-$ and $\hat{K}_4^-$ close to the stability limit $\Lambda^\pm > 0$. Concerning the single-node LI_3^+ but also the two-node *p-flow* scheme BFL-QI_3 and FH_3 which are built in Sec. D 1, our numerical analysis confirms that $\delta = 0$ is stable with these schemes, except of the MLS and MLS_3 where Eq. (D7a) predicts that the most restrictive condition $\Lambda^+ \leqslant 1$ is set by $\delta = 0$. Figure 7 confirms that the linear Couette system $\delta = \{0, 0\}$ closed by the MLS becomes unstable when $\Lambda^+ > 1$ and $\Lambda <\approx 0.2$, and then rapidly the whole region

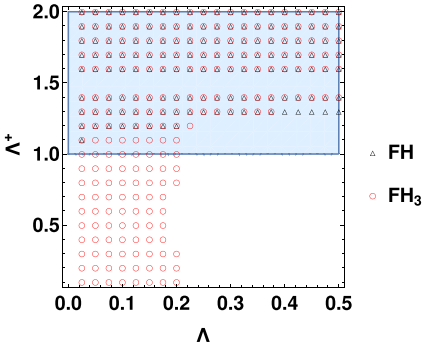

FIG. 7. The unstable domain with MLS and MLS_3 components $\delta \in [0, \frac{1}{2}]$ of FH and FH_3, respectively, in the minimal Couette system $\delta = \{0, 0\}$ when $\Lambda^+ \times \Lambda \in [\frac{1}{10}, 2] \times [\frac{1}{20}, \frac{1}{2}]$ is run through 20^2 points. The predicted MLS stable domain in Eq. (D7a) is $\Lambda^+ \leqslant 1 + \delta$; the MLS_3 enlarges unstable zone towards the whole zone $\{\Lambda^+ < 1, \Lambda <\approx \frac{1}{5}\}$.

$\Lambda^+ \geqslant \approx 1.3$ becomes unstable with any Λ. In turn, the MLS_3 in Fig. 7 combines the MLS− and *p-flow* restrictions, and it additionally uniformly forbids the small viscosity range when $\Lambda < \approx \frac{1}{5}$ and $\delta = 0$. We then examine whether the triangular domain $\{\Lambda^+ < \Lambda^+_{\min}, \Lambda < \Lambda_{\min}\}$ in Fig. 6 is *unstable* with the LI_3^+ as predicted by Eq. (64a). When $\delta = \frac{1}{2}$, CLI_3, BFL_3, $\mathrm{ELI\text{-}UQ}_3$, and $\mathrm{ELI\text{-}FL}_3$ on the one hand, and the BFL-QI_3 and FH_3 on the other hand, all reduce to $\mathrm{BB}_3(\alpha^{(u)} = 2)$. Numerical simulations confirm that their unstable diagrams have a very similar triangular shape $\Lambda^+ < \Lambda^+_{\min}(\Lambda)$ when $\Lambda < \Lambda_{\min} = \frac{1}{8}$ according to Eq. (64a). The $\mathrm{YLI}_3(\alpha^{(u)} = \frac{4}{3})$, and especially $\mathrm{ELI\text{-}UL}_3$ with $\alpha^{(u)}(\delta = \frac{1}{2}) = 1$, show smaller unstable domains with $\Lambda_{\min} = \frac{1}{12}$ and $\Lambda_{\min} = \frac{1}{16}$, respectively (these results are not shown). Table V gives $\{\alpha^{(u)}, \Lambda_{\min}\}$ for the reference interpolation schemes in the "worst" case $\delta = 1$.

Figure 8 then displays unstable diagrams obtained with the different values $\delta = \{1, \frac{1}{2}\}$ on the two walls; these unstable regions are the same (or very similar) as when $\delta = \{1, 1\}$. In agreement with the prediction for $\Lambda^+_{\min}(\alpha^{(u)})$ in Eqs. (63) and (64a), the four schemes with $\alpha^{(u)}(\delta = 1) = 1$: YLI_3, BFL_3, $\mathrm{ELI\text{-}UL}_3$, and $\mathrm{ELI\text{-}FL}_3$, produce identical diagrams, whereas the BFL-$\mathrm{QI}_3(\alpha^{(u)} = \frac{2}{3})$ allows for a larger stable viscosity range.

However, the case $\delta = 1$ is principally different between FH_3, on the one hand, LI_3^+ and BFL-QI_3 on the other hand,

TABLE V. Equation (64a) predicts *unstable* domain $\Lambda^+ < \Lambda^+_{\min}(\alpha)$ when $\Lambda < \Lambda_{\min} = \frac{\alpha^{(u)}\delta^2}{4}$. The additional constraints may apply with CLI_3 and $\mathrm{ELI\text{-}UQ}_3$ according to Eq. (E1). The most unstable case $\delta = 1$ is addressed.

Scheme	$\alpha^{(u)}$	$\Lambda_{\min}$	Unstable
SSN_3, BFL-QI_3	$\frac{2}{3}$	$\frac{1}{6}$	Eq. (64a)
YLI_3, $\mathrm{ELI\text{-}UL}_3$			Eq. (64a)
BFL_3, $\mathrm{ELI\text{-}FL}_3$	1	$\frac{1}{4}$	Eq. (64a)
CLI_3	$\frac{4}{3}$	$\frac{1}{3}$	Eq. (64a) when $\Lambda^+ \leqslant \Lambda^+_c = \frac{1}{6}$
$\mathrm{ELI\text{-}UQ}_3$	2	$\frac{1}{2}$	Eq. (64a) when $\Lambda^+ \leqslant \Lambda^+_c = \frac{1}{2}$

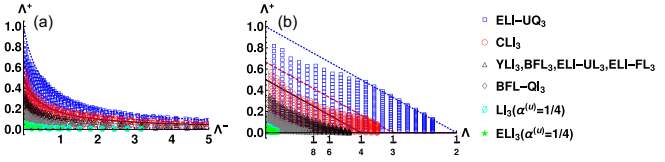

FIG. 8. The predicted *p-flow* $\hat{K}_3^-$ stability boundary when δ=1 (solid lines) and the unstable numerical diagram (symbols) (a) $\Lambda^+(\Lambda^-)$ and (b) $\Lambda^+(\Lambda)$ in a three-node straight Stokes Couette flow with the distance $\delta = \{1, \frac{1}{2}\}$ on the two walls. The computations are run by decreasing Λ^+ from $\Lambda^+(\Lambda)$ in Eq. (64a) when $\Lambda \in [\Lambda_{\min}\times(1-\delta')/20, \Lambda_{\min}\times(1-\delta')]$, $\delta' = \frac{1}{8}$ is set arbitrarily. The MR1 remains stable with $\delta = \{0, \frac{1}{2}, 1\}$ towards $\Lambda^+_{lim} = 1.25\times10^{-3}$ at least.

because FH_3 then remains stable close to the stability limit $\Lambda^\pm > 0$; for example, it does not produce unstable points in simulations shown in Fig. 8. This suggests that the limit $\delta \to 1$ dominates the FH_3 effective stability, much like the LI_3^+, and the FH_3 is stable in this limit in agreement with Eq. (D7b).

Figure 9 then focuses on LI_3 and ELI_3 with smaller values $\alpha^{(u)} = \{\frac{1}{4}, \frac{1}{2}\}$ where, in agreement with the predictions, the unstable domain narrows when $\alpha^{(u)}$ diminishes, and the whole bulk stability condition $\Lambda^+>0$ becomes available as $\alpha^{(u)}\to0$. The ELI_3 is slightly more stable than LI_3 in this example but their (common) predicted boundary is sufficient in the two cases. Finally, it is confirmed that applying $\alpha_0^{(u)}$ from Eq. (65), LI_3 and ELI_3 both remain stable up to the smallest examined values, e.g., $\Lambda^+_{lim} = \frac{1}{4}\times10^{-2}$ ($\tau^+ = 0.5025$, $\nu = \frac{1}{12}\times10^{-2}$). The schemes examined above obey Eq. (61), and they are more stable in Figs. 8 and 9 than the prescribed (sufficient) stability line. The ELI-UQ_3 and CLI_3 do not respect Eq. (61) and Eq. (E1) predicts that the unstable domain is additionally limited to $\Lambda^+ < \Lambda_c^+$ (see Λ_c^+ in Table V).

Figure 10 reports the results of the simulations above the stability line in Eq. (64a). The results confirm that ELI-UQ_3 combines the unstable CELI-UQ area in Fig. 5, which is predicted by Eq. (E1), with the $\hat{K}_3^-$ prediction diagram from Fig. 8. Accordingly, in agreement with CLI results, CLI_3 is only very slightly unstable above $\Lambda^-_{\min}(\Lambda^-)$, and it shows very similar results in Figs. 8 and 10. The predicted CLI stability condition $\Lambda^+ \geqslant \Lambda_c^- = \frac{1}{6}$ is too much restrictive and CLI_3 is mostly governed by the *p-flow* condition due to Eq. (40b).

G. Summary

The single-node class LI^+ operates Eq. (21) with the three coefficients $\{\hat{\alpha}, \beta, \hat{\beta}\}$ from Eq. (42); they are defined giving the relative distance δ, two adjustable scale factors $\alpha^{(u)}$ and

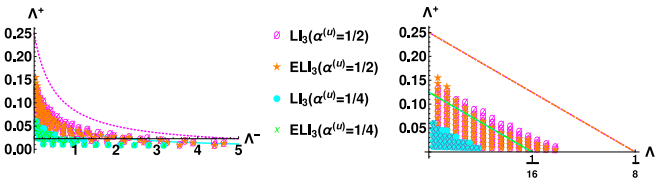

FIG. 9. Zoom in $LI_3(\alpha^{(u)})$ and $ELI_3(\alpha^{(u)}, \alpha^{(p)}=0)$ with the smallest values $\alpha^{(u)}$ from Fig. 8; their predicted stability boundaries are the same (solid lines).

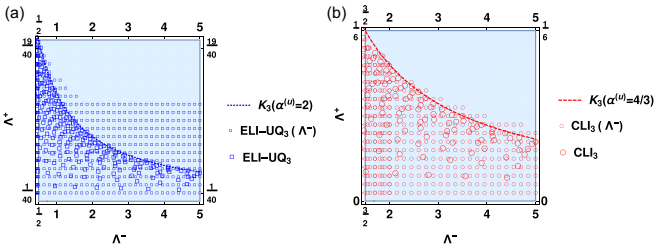

FIG. 10. In addition to Eq. (64a) [below the lines $\hat{K}_3^-(\alpha^{(u)})$], (a) ELI-$UQ_3$ and (b) CLI_3 are predicted in Table V to be unstable when $\Lambda^+ < \Lambda_c^+$ with (a) $\Lambda_c^+ = \frac{1}{2}$ and (b) $\Lambda_c^+ = \frac{1}{6}$. The computations are run with $\delta = \{1, 1\}$, $\Lambda^+ \in [\Lambda_c^+/20, \Lambda_c^+]$, the unstable results (symbols) are displayed together with those from Fig. 8 (large symbols).

$\alpha^{(p)}$, and free-tunable coefficient $\hat{K}^+$ of the term $\hat{F}_q$. The upstream population of β is included with the optional time flag $I^{(t)} \in [0, 1]$; the LI^+ operates a single boundary node locally when $\beta = 0$ or $I^{(t)} = 0$, and this setup applies for cut link with no upstream fluid neighbor; otherwise we apply $I^{(t)} = 1$ and the postcollision population of β propagates into the boundary node before the boundary step with Eq. (21).

The LI subclass enforces the optional condition $\alpha^{(p)} = \hat{K}^+ = 0$. Its subclass LI_0 operates without any postcollision term $\hat{F}_q$, and then matches the convex-interpolation-based schemes specified in Table III, such as BFL [55], YLI [56], GLI [63], ZLI [61], CHLI [62], and SSN [64], but also the parametrized CLI and *p-flow* IPLI. The ELI^+ subclass operates with free tunable $\alpha^{(p)}$ and enforces $\beta = 0$ due to $\hat{K}^+ = K^+_{ELI}$ in Eq. (53), where K^+_{ELI} becomes Λ^+-independent when $\alpha^{(p)} = 0$; the ELI^+ coefficients are exemplified in Table IV. The LI_0 and ELI_0^+ steady-state counterparts are built with Eqs. (58). We note that $LI_0 \cup ELI_0^+$ does not cover the whole LI_0^+ class, e.g., $\alpha^{(p)}$ may else remain free for $\beta \neq 0$. Also, following the idea of $LLI(\gamma^-) \in ELI^+$ schemes [68] in Eq. (C15), ELI_0^+ can be extended to $I_{ncs} = \gamma^- - 1 \in [-1, 1]$.

The antisymmetric postcollision corrections $\hat{F}_q = \hat{K}_k^- \hat{n}_q^-$, defined in Eq. (44) with $k = \{1, 3, 4\}$, make LI^+ steady-state solutions parametrized by the nondimensional governing numbers; additionally, $\hat{K}_3^-$ makes them *p-flow* accurate, whereas $\hat{K}_4^-$ removes the gradients of pressure and inertial equilibrium terms from the Dirichlet velocity closure relation. The counterparts CLI and CELI-UQ are parametrized without $\hat{K}_1^-$, whereas IPLI and CELI-IP are *p-flow*-accurate without $\hat{K}_3^-$. The *steady-state* solutions are expected to be the same for any two members of the same LI_k^+ class when $k = \{1, 3, 4\}$.

The convex-interpolation-based schemes with $\{\hat{\alpha}, \beta, \hat{\beta}\} \in [0, 1]$ obey stability condition proposed in Eq. (40) together with their $\hat{K}_1^-$ and $\hat{K}_4^-$ counterparts. The CLI_k behaves less stably than the convex interpolations, but much more robustly than CELI-UQ_k and, especially, nonparametrized SELI-UQ. Indeed, among the three ghost nonequilibrium XELI approximations, the commonly used bounce-back ($X = N$) and the simplest zero approximation ($X = C$) are much more stable than the bulk-node "copy" variant ($X = S$). In turn, the two-population local-single-node subclass $NELI(\alpha^{(u)}, \alpha^{(p)} = 0)$ produces identical steady-state momentum solutions with the three-population class $LI_0(\alpha^{(u)}, \alpha^{(p)} = 0)$, which includes

all standard convex interpolations. Besides, we observe that CLI_k and $\mathrm{CELI\text{-}UQ}_k$ converge much slower than the basic interpolation schemes, perhaps because these two schemes support staggered invariants owing to their coefficient $\hat{\alpha} = 1$ (see Sec. VI A 4).

The LI_3^+ forbids the small viscosity range $\Lambda^+ \leqslant \Lambda^+_{\min}(\delta, \alpha^{(u)}, \Lambda^-)$ when $\Lambda < \frac{\alpha^{(u)}\delta^2}{4}$ according to Eqs. (63) and (64); the choice $\alpha^{(u)} = \alpha_0^{(u)}$ from Eq. (65) avoids this limitation when $\Lambda < \frac{\delta}{4}$, at least. Alternatively, IPLI and CELI-IP operate over the whole viscosity range robustly when $\Lambda < \frac{\delta^2}{2}$. Finally, although the relatively high values $\Lambda > \Lambda_{\min} \geqslant \frac{\alpha^{(u)}}{4}$ are typically not accurate enough in Stokes flow, they behave more robustly with LI_3^+ in small viscosity range nonlinear flow according to Eq. (64b). Another possibility is to use small values of $\alpha^{(u)}$, because $\alpha^{(u)} \to 0$ progressively increases the stable small-viscosity range; in particular, among the ZLI_3 members, the uniform subclass SSN_3 formed from the SSN scheme [64] is expected to be the most stable due to its smallest factor $\alpha^{(u)}(\delta)$. However, very small $\alpha^{(u)}$ values retard the convergence to the steady state and worsen the transient accuracy.

In turn, the *p-flow* two-node schemes, $\mathrm{BFL\text{-}QI}_3$ and $\mathrm{MLS}_3/\mathrm{FH}_3$ become exact for grid-aligned or inclined stationary Poiseuille Stokes flow. However, beyond these exact solutions, neither FH, BFL-QI nor FH_3, $\mathrm{BFL\text{-}QI}_3$ are parametrized and their steady-state error estimates will remain viscosity-dependent in Stokes and Navier-Stokes flow simulations at given Re_g. The $\mathrm{BFL\text{-}QI}_3$ shares a similar stability diagram with the convex interpolation coefficient-based LI_3 schemes. In principle, the single-node FH_3 component might substitute the LI_3^+ for those links where $\delta \to 1$ when both ν and Λ are small. All in all, giving that the stationary LI_3^+ solutions are parametrized, they can be produced for relatively large viscosity values in Stokes and very low Reynolds number flows. In contrast, the stability conditions do not constrain the viscosity range with the *p-pressure* LI_4, which suits the higher Re range.

V. TWO-POINT PARABOLIC CLASSES: VMR AND *c-nse-p-flow* EMR

The Velocity-Multireflection [$\mathrm{VMR}(\alpha^{(u)}, \hat{K}^{\pm})$] family [69] solves the linear system of five equations composed from the *c-flow* condition $CN^{(\beta^{(u)})}$ in Eq. (31), two parabolic conditions in Eq. (36), an optional condition $\alpha^{(p)} = 0$ with Eq. (24a) and $\alpha^{(u)}$ definition in Eq. (24b). The five coefficients $\{\hat{\alpha}, \beta, \hat{\beta}, \gamma, \hat{\gamma}\}$ are then expressed through $\alpha^{(u)}$ and $\hat{K}^{\pm}$; they are reviewed in Table VI. Since they yield $\beta^{(u)} = \alpha^{(u)}\delta$, $\gamma^{(u)} = \alpha^{(u)}\frac{\delta^2}{2}$, $\alpha^{(p)} = \beta^{(p)} = 0$, the VMR is "parabolic" for e_q^- and "linear" for e_q^+. The remaining term $\gamma^{(p)}\partial_q^2 e_q^+$ in Eq. (19) reads

$$\mathrm{VMR}(\alpha^{(u)}, \hat{K}^{\pm}), \quad \alpha^{(p)} = 0: \\ \gamma^{(p)} = \hat{K}^- - \hat{K}^+ - 2 + \frac{\alpha^{(u)}}{2}(1+\delta) \times (1+\delta-2\Lambda^-). \tag{66}$$

TABLE VI. Coefficients of the two-node parabolic family VMR with the three adjustable parameters per cut link: $\alpha^{(u)}$ and $\hat{K}^{\pm}$ [see also Table A.5 [69]]. The VMR is parametrized within its particular subclasses, such as $\mathrm{MR1}^+(\alpha^{(u)})$ or $\mathrm{AVMR}(\alpha^{(u)})$; the EMR extends AVMR to the case $\alpha^{(p)} \neq 0$ and $\hat{K}^+ \neq 0$ in Sec. D 2; the $\mathrm{MR1}^+(\alpha^{(u)})$ and AVMR/EMR stability bounds are suggested by Eqs. (69) and (71), respectively.

	$\mathrm{VMR}(\alpha^{(u)}, \hat{K}^{\pm})$ parabolic Dirichlet velocity family, $\alpha^{(p)} = 0$
$\hat{\alpha}$	$\frac{1}{2}(-2 - 2\hat{K}^+ + \alpha^{(u)}(1+\delta)^2)$
β	$\frac{1}{4}(8 - 2\hat{K}^- + 6\hat{K}^+ - \alpha^{(u)}(1 + 6\delta + 4\delta^2 - 2\Lambda^-))$
$\hat{\beta}$	$\frac{1}{4}(8 - 2\hat{K}^- + 2\hat{K}^+ + \alpha^{(u)}(-3 - 2\delta + 2\Lambda^-))$
γ	$\frac{1}{4}(-4 + 2\hat{K}^- - 2\hat{K}^+ + \alpha^{(u)}(1 + 2\delta(1+\delta) - 2\Lambda^-))$
$\hat{\gamma}$	$\frac{1}{4}(-4 + 2\hat{K}^- - 2\hat{K}^+ + \alpha^{(u)}(1 + 2\delta - 2\Lambda^-))$
	Parametrized members with $\hat{K}^- = \alpha^{(u)}\Lambda^-$
$\mathrm{MR1} \in \mathrm{MR1}^+$	$\hat{K}^+ = 0, \hat{K}^- = \alpha^{(u)}\Lambda^-, \alpha^{(u)} = \frac{4}{(1+\delta)^2}$
$\mathrm{MR1}^+$	$\hat{K}^+ = \frac{1}{2}(\alpha^{(u)}(1+\delta)^2 - 4), \hat{K}^- = \alpha^{(u)}\Lambda^-, \forall\alpha^{(u)}$
	Parametrized *c-nse-p-flow* member with $\hat{K}^+ = 0$
AVMR	$\hat{K}^+ = 0, \hat{K}^- = 2 - \frac{1}{2}\alpha^{(u)}(1+\delta)(1+\delta-2\Lambda^-), \forall\alpha^{(u)}$

The MR1 scheme [59] is the VMR member with the specific prefactor $\alpha^{(u)}(\delta)$, $\hat{K}^- = \alpha^{(u)}\Lambda^-$ and $\hat{K}^+ = 0$; its extension $\mathrm{MR1}^+(\alpha^{(u)})$ will operate with the free-tunable $\alpha^{(u)}$ and specific $\hat{K}^+(\alpha^{(u)})$ (see Table VI).

In turn, the so-called PM VMR subclass [Table (A.8) [69]] enforces the *c-nse-p-flow* condition $\gamma^{(p)} = 0$ in Eq. (66), and hence it obeys Eq. (38); its three subfamilies [69]: (1) VMR2, (2) $\mathrm{SVMR}(\alpha^{(u)})$, and (3) $\mathrm{AVMR}(\alpha^{(u)})$ operate with (1) $\hat{K}^{\pm} = 0$ and specific $\alpha^{(u)}$, (2) $\hat{K}^- = 0$, and (3) $\hat{K}^+ = 0$ [see Tables (A.6)–(A.7) in Ref. [69]]. Here the focus is put on $\mathrm{AVMR}(\alpha^{(u)})$ from Table VI for its better stability; further, the two AVMR constraints $\alpha^{(p)} = \hat{K}^+ = 0$ are relaxed within the larger *c-nse-p-flow* EMR family. Our aim is to understand whether these additional adjustable parameters may help to improve the stability of the two-point schemes, especially in an inertial regime.

Concerning stability, recall that Eq. (40) originates from the exact single-node closure relation in Eq. (32), which is different in the single-node *p-flow* LI_3^+ and the two-node parabolic MR, where it is given by Eq. (B8). In fact, in contrast with the two-node $\mathrm{BFL\text{-}QI}_3$, the MR does not apply the $\hat{K}_3^-$ correction and we find that Eq. (40) does not apply with it. To this end, we neglect a nonequilibrium variation between the two neighbor nodes and sum their coefficients in Eq. (B8): (1) m_3 and m_7 of $-\tau^+\hat{n}_q^+$ and (2) m_4 and m_8 of $-\tau^-\hat{n}_q^-$, then propose to consider the following approximate stability estimate:

$$B^{(u)} := |-(m_3+m_7)/\tau^+ + 1| \leqslant B_s, \tag{67a}$$

$$B^{(p)} := |-(m_4+m_8)/\tau^- - 1| \leqslant B_s, \tag{67b}$$

$$B_s \in [1, \approx (1+\alpha^{(u)})] \quad \text{when } \alpha^{(u)} \in]0, 2], \tag{67c}$$

$$\text{and } \{\hat{\alpha}, \beta, \hat{\beta}, \gamma, \hat{\gamma}\} \in [-1, 1]. \tag{67d}$$

Giving $B_s = 1$ and Eq. (32), Eqs. (67a) and (67b) reduce to Eq. (40) in single-node schemes. The coefficients in all

VMR($\alpha^{(u)}, \hat{K}^{\pm}$) schemes are restricted to the heuristic condition in Eq. (67d).

A. From MR1 to MR1$^+$

Like the BB and CLI, the MR1 in Table VI operates with $\hat{\alpha} = 1$, $\beta = -\hat{\beta}$, $\gamma = -\hat{\gamma}$, where $\{\hat{\alpha}, \beta, \hat{\beta}, \gamma, \hat{\gamma}\} \in [-1, 1]$. Another key point is that the specific choice $\hat{K}^- = \alpha^{(u)}\Lambda^-$ makes the sum of the coefficients $m_4 + m_8$ for two neighbor terms $\hat{n}_q^-(\vec{r}_b)$ and $\hat{n}_q^-(\vec{r}_b - \vec{c}_q)$ vanish in Eq. (B8); the pressure-gradient term $\beta^{(p)}\partial_q e_q^+$ and the momentum term $\gamma^{(u)}\partial_q^2 e_q^-$ in Eq. (19) are then held solely by the Taylor relations between $e_q^{\pm}(\vec{r}_b)$ and $e_q^{\pm}(\vec{r}_b - \vec{c}_q)$, obeying the parabolic accuracy $\beta^{(p)} = 0$ and $\gamma^{(u)} = \alpha^{(u)}\delta^2/2$.

The MR1$^+$ retains the following conditions: $\hat{\alpha} = 1$, $\hat{K}^- = \alpha^{(u)}\Lambda^-$ and $m_4 + m_8 = 0$ in Eq. (B8), but it relaxes $\alpha^{(u)}$ due to $\hat{K}^+(\alpha^{(u)})$:

$$\begin{aligned} \text{MR1}^+\text{: } \hat{\alpha} = 1, \quad \beta = -\hat{\beta} = -1 - \tfrac{1}{4}\alpha^{(u)}(-2 + \delta^2), \\ \gamma = -\hat{\gamma} = \tfrac{1}{4}\alpha^{(u)}\delta^2, \quad \alpha^{(p)} = 0, \quad \hat{K}^- = \alpha^{(u)}\Lambda^-, \\ \hat{K}^+(\alpha^{(u)}, \delta) = \tfrac{1}{2}[\alpha^{(u)}(1+\delta)^2 - 4]. \end{aligned} \tag{68}$$

The MR1$^+$ cannot make $\gamma^{(p)}$ in Eq. (19) vanish unless with $\hat{K}^+ = -2$ where $\alpha^{(u)} = 0$; the MR1$^+$ then is expected to be exact for a pressure- or force-driven rotated Poiseuille Stokes flow, but it does not satisfy the *c-nse-p-flow* condition. The MR1$^+$ reduces to MR1 when $\hat{K}^+ = 0$ and it satisfies heuristic condition $\{\hat{\alpha}, \beta, \hat{\beta}, \gamma, \hat{\gamma}\} \in [-1, 1]$ provided that

$$\begin{aligned} \text{MR1}^+\text{: } \alpha^{(u)} \in \left]0, \frac{8}{2-\delta^2}\right], \quad \delta \in \left[0, \frac{\sqrt{2}}{3}\right], \\ \text{and } \alpha^{(u)} \in \left]0, \frac{4}{\delta^2}\right], \quad \delta \in \left[\frac{\sqrt{2}}{3}, 1\right]. \end{aligned} \tag{69}$$

These heuristic *linkwise* stability conditions restrict $\hat{K}^+$ in Eq. (68) to the intervals $[-2, \frac{2\delta(4+3\delta)}{2-\delta^2}]$ and $[-2, \frac{2(1+2\delta)}{\delta^2}]$, respectively.

One interesting member called MR1-BB operates with $\alpha^{(u)} \equiv 2$, ELI-UQ$_k$, and FH$_k$ alike:

$$\begin{aligned} \text{MR1-BB}: \alpha^{(u)} = 2, \quad \hat{K}^+ = -1 + \delta(2+\delta) \in [-1, 2], \\ \hat{\alpha} = 1, \quad \beta = -\hat{\beta} = \hat{\gamma} = -\gamma \\ = -\frac{\delta^2}{2} \in \left[-\tfrac{1}{2}, \tfrac{1}{2}\right], \\ \text{then } \delta_t = \tfrac{1}{2}, \quad \forall I^{(t)} \in [0, 1[. \end{aligned} \tag{70}$$

The MR1-BB holds the mid-time stepping $\delta_t = \frac{1}{2}$ in Eq. (20) for any $I^{(t)} \in [0, 1[$, whereas the MR1$^+$ regularly holds $\delta_t = \frac{1}{2}$ applying the "implicit" configuration $I^{(t)} = 1$ in Eq. (21).

Concerning the two-node stability estimate, an approximate MR1$^+$ condition is solely determined by Eq. (67a) because $m_4 + m_8 = 0$ and then $B^{(p)} = 1$ obeys Eq. (67b). Eq. (67a) then predicts the stable viscosity range $\Lambda^+ > \Lambda^+_{\min}(\delta, \hat{K}^+)$, or equivalently $\Lambda^+ > \Lambda^+_{\min}(\delta, \alpha^{(u)})$ plugging there $\hat{K}^+(\alpha^{(u)}, \delta)$ from Eq. (68). In particular, $\delta = 0$ lies on the stability boundary $B_s = 1$; next, Eq. (67a) with $B_s = 1$ is satisfied in the whole relaxation range $\Lambda^{\pm} > 0$ and for any distance only in the narrow interval $\hat{K}^+ \in [-2, -\frac{2}{3}]$,

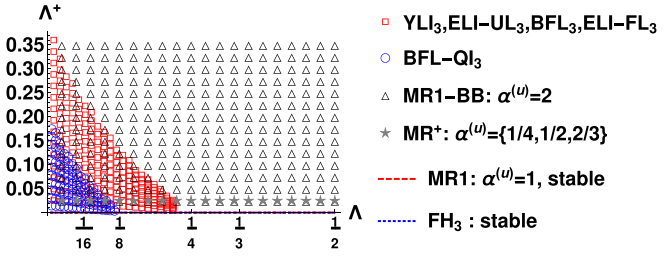

FIG. 11. The unstable regions at the distance $\delta = \{1, \frac{1}{2}\}$ to the two walls with (1) MR1-BB($\alpha^{(u)} = 2$), (2) MR1, and (3) MR1$^+$($\alpha^{(u)}$), $\alpha^{(u)} = \{\frac{1}{4}, \frac{1}{2}, \frac{2}{3}\}$ [$\hat{K}^+ = \{-\frac{3}{2}, -1, -\frac{2}{3}\}$, accordingly] are examined when $\Lambda^+ \times \Lambda \in [0.025, 0.5]^2$ and compared to YLI$_3$, ELI-UL$_3$, BFL$_3$, ELI-FL$_3$, and BFL-QI$_3$ from Fig. 8. The MR1 and FH$_3$ remain stable up to $\Lambda^+_{lim} = 1.25\times10^{-3}$ at least.

when $\alpha^{(u)} \in]0, \frac{2}{3}]$; these conditions exclude MR1($\hat{K}^+ = 0$) and MR1-BB($\alpha^{(u)} = 2$), and they define their most strong conditions when $\delta = 1$ with $\Lambda^+_{\min} = \frac{1}{4}$ and $\Lambda^+_{\min} = 1$, respectively. In general, it is predicted that $\Lambda^+_{\min}(\delta, \hat{K}^+)$ diminishes, and hence the stable viscosity range enlarges, when $\hat{K}^+$ and $\alpha^{(u)}$ take smaller values inside their stability range in Eq. (69). Remarkably, the stability boundary $\Lambda^+_{\min}$ is independent of Λ^- and Λ provided that $\alpha^{(u)}$ and $\hat{K}^+$ are independent of these parameters.

The results of the numerical computations are presented in Fig. 11 prescribing two different distances $\delta = \{1, \frac{1}{2}\}$ on the upper and bottom walls. They confirm that (1) $\Lambda^+_{\min}$ is independent of Λ, and (2) $\Lambda^+_{\min}$ drastically diminishes with $\hat{K}^+$ and $\alpha^{(u)}$ comparing to MR1-BB($\alpha^{(u)} = 2$). In these two diagrams, MR1-BB numerical bounds $\Lambda^+_{\min}(\delta = \frac{1}{2}) \approx 0.05$ and $\Lambda^+_{\min}(\delta = 1) \approx 0.35$ lie between their predictions with $\{B_s = 1 + \alpha^{(u)}, B_s = 1\}$ in Eq. (67). In turn, MR1($\hat{K}^+ = 0$) is stable in these examples up to the minimal examined value, $\Lambda^+ \geqslant \Lambda^+_{lim}$, in agreement with its unconstrained linear stability condition $\Lambda^{\pm} > 0$ predicted with $B_s = 1 + \alpha^{(u)}$ in Eq. (67). Hence, $B_s = 1$ is much stronger than practically necessary with these two schemes. At the same time, Eq. (67) with $B_s = 1$ is not completely sufficient because it predicts $\Lambda^+ > 0$ to be stable when $\alpha^{(u)} \leqslant \frac{2}{3}$, but $\alpha^{(u)} = \{\frac{1}{4}, \frac{1}{2}, \frac{2}{3}\}$ become all unstable for the smallest viscosity in Fig. 11. Hence, these examples indicate only a qualitative validity of the approximate *two-node* criteria in Eq. (67).

To sum up, MR1$^+$ with $\hat{K}^+ \in [-2, -1]$ is stable with much smaller viscosity values in the whole interval $\Lambda^- > 0$ than the *p-flow* interpolation-based schemes, like BFL-QI$_3$, ZLI$_3$, YLI$_3$/BFL$_3$, and ELI-UL$_3$/ELI-FL$_3$. The *p-flow* families, such as LI$_3^+(\alpha^{(u)})$ and MR1$^+(\alpha^{(u)})$, are generally more stable when $\alpha^{(u)} \to 0$, and they tolerate well the limit $\delta = 0$ where, in contrast, MLS$_3$ is unstable. Surprisingly, MR1 overpasses all schemes in these linear flow numerical experiments; we relate this property to its zero symmetric correction $\hat{K}^+ = 0$, as might be also suggested for CLI. On the other hand, both CLI and MR1 operate with $\hat{\alpha} = 1$ and converge slower than other schemes to the steady state; this might explain why no unstable region is detected with them for a given control time point. Finally, the steady-state stable solutions without mass leakage are equivalently for all MR1$^+$ members; otherwise,

they are very slightly different due to $\hat{K}^+ \neq 0$ in Eq. (68) [see Eq. (72)].

B. The *c-nse-p-flow* EMR

The EMR class relaxes the condition $\alpha^{(p)} = 0$ and operates with the free tunable coefficients $\alpha^{(p)}$, $\alpha^{(u)}$ and $\hat{K}^+$, where $\hat{K}^-(\alpha^{(u)}, \hat{K}^+, \Lambda^\pm, \delta)$ is then fixed from the *c-nse-p-flow* condition $\gamma^{(p)} = 0$. We consider four EMR families: the known one AVMR and three alternative ones: {EMR-1, EMR-2, EMR-3}, which collectively we refer to EMR for brevity. These EMR schemes obey Eq. (38) and produce the same steady-state coefficients $m_2 - m_8$ in Eq. (B8), which are parametrized according to Eq. (B9). The AVMR is specified in Table VI; it operates with $\alpha^{(p)} = \hat{K}^+ = 0$ and yields all five coefficients $\{\hat{\alpha}, \beta, \hat{\beta}, \gamma, \hat{\gamma}\}$ inside $[-1, 1]$ when either $\delta = 0$, $\alpha^{(u)} \in]0, 4]$ or provided that Λ^- is limited to $\Lambda^-_{\max}(\alpha^{(u)})$ when $\delta \in]0, 1]$:

$$\text{AVMR, most stable condition :}$$

$$\Lambda^- \leqslant \Lambda^-_{\max}(\alpha^{(u)}) = \frac{4-\alpha^{(u)}}{2\alpha^{(u)}}, \quad \alpha^{(u)} \in \left]0, \frac{2}{3}\right], \tag{71a}$$

$$\Lambda^- \leqslant \Lambda^-_{\max}(\alpha^{(u)}) = \frac{8-7\alpha^{(u)}}{2\alpha^{(u)}}, \quad \alpha^{(u)} \in \left]\frac{2}{3}, 1\right]. \tag{71b}$$

$$\text{EMR, most stable condition :}$$

$$\Lambda^- \leqslant \Lambda^-_{\max}(\alpha^{(u)}) = \frac{4-\alpha^{(u)}}{2\alpha^{(u)}}, \quad \alpha^{(u)} \in]0, 1]. \tag{71c}$$

Hence, $\alpha^{(u)}$ is restricted to]0,1] where the stable interval $\Lambda^- \in]0, \Lambda^-_{\max}]$ increases as $\alpha^{(u)} \to 0$, and it narrows to $\Lambda^-_{\max} = \frac{1}{2}$ when $\alpha^{(u)} \to 1$.

Equations (D8) and (D9) specify the three subfamilies EMR-1, EMR-2, and EMR-3 with the common solution for $\hat{K}^-$ and $\{\gamma, \hat{\gamma}\}$, where the two of the three remaining coefficients $\{\hat{\alpha}, \beta, \hat{\beta}\}$ vanish and all five coefficients have the same amplitude. The heuristic stability condition $\{\hat{\alpha}, \beta, \hat{\beta}, \gamma, \hat{\gamma}\} \in [-1, 1]$ when $\delta = 1$ is sufficient for $\delta \in [0, 1]$, and giving $\alpha^{(u)} \in]0, 1]$ it reads with Eq. (71c). Equations (71a) and (71c) are the same but EMR applies this criterion through the whole interval, and then enlarges $\Lambda^-_{\max} = \frac{1}{2}$ [AVMR] to $\Lambda^-_{\max} = \frac{3}{2}$ [EMR]. At the same time, Eq. (67) is the same in the *c-nse-p-flow* schemes. Giving $\Lambda^- < \min_\delta \Lambda^-_{\max} = \frac{1}{2}$ and $\alpha^{(u)} > 0$, Eq. (67) with $B_s = 1$ predicts that only $\delta = 0$ is stable. In contrast, when replacing B_s by $B_s = 1 + \alpha^{(u)}$ and (1) enforcing $\alpha^{(u)} \in]0, 1]$, Eq. (67) becomes satisfied for any $\Lambda^\pm$, whereas (2) prescribing $\Lambda^- < \frac{1}{2}$, reduces to $\alpha^{(u)} \in]0, 1]$ when $\delta = 1$. This analysis suggests that the heuristic conditions in Eqs. (71) provide a reasonable, although not strictly sufficient stability estimate, because the condition $B_s = 1 + \alpha^{(u)}$ is usually a bit weaker than necessarily. Figure 12 (first diagram) confirms these predictions: it displays the unstable (numerical) regions $\Lambda^+(\Lambda^-)$ and compares them with the prediction $\Lambda^- > \Lambda^-_{\max}(\alpha^{(u)})$ in Eqs. (71a) and (71c). These results confirm that the unstable subdomains $\Lambda^- > \Lambda^{-(num)}_{\max}$ are (practically) viscosity-independent and lie inside of the prediction. Hence Eq. (71a) is numerically sufficient with the AVMR when $\alpha^{(u)} \leqslant \frac{1}{2}$, at least. Figure 12 (second diagram) displays the unstable domains vs $\Lambda^+(\Lambda)$; since the computations are run in the parameter space $\Lambda^+ \times \Lambda^-$, the unstable domain reads as $\Lambda(\Lambda^+) \geqslant \Lambda^+\Lambda^{-(num)}_{\max}(\alpha^{(u)})$. The AVMR, EMR-1 and EMR-2 (nonshown) show practically the same results; however, EMR-3 is less stable than both the prediction and the other schemes. The EMR example is interesting because its three schemes operate with the same coefficient range but apply different values $\hat{K}^\pm$; they keep then the same type of relationship, such as $\Lambda^- > \Lambda^{-(num)}_{\max}(\alpha^{(u)})$, but may display different values $\Lambda^{-(num)}_{\max}(\alpha^{(u)})$. This confirms that $\hat{K}^\pm$ impacts stability, on top of the coefficient range. Finally, we have verified that other specified *c-nse-p-flow* schemes [69], such as VMR2, SVMR, and MGMR2, not respecting condition $\{\hat{\alpha}, \beta, \hat{\beta}, \gamma, \hat{\gamma}\} \notin [-1, 1]$, show a complicated unstable behavior in the parameter space $\{\Lambda^+, \Lambda\}$ and behave less stably than AVMR/EMR. These numerical observations agree with Eq. (67) which predicts them as unstable even giving $B_s = 1 + \alpha^{(u)}$.

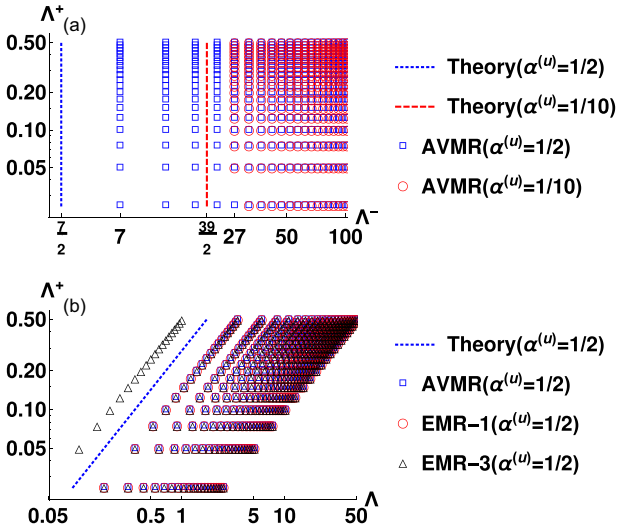

FIG. 12. Unstable domains [log-log] (a) $\Lambda^+(\Lambda^-)$ and (b) $\Lambda^+(\Lambda)$ with the AVMR and EMR when $\alpha^{(u)} = \frac{1}{2}$ and $\alpha^{(u)} = \frac{1}{10}$; the computations are run through 20^2 points $\Lambda^+ \times \Lambda^- = [2.5\times10^{-2}, 5\times10^{-1}]\times[2, 100]$. The unstable domain is predicted in Eqs. (71a) and (71c) as (a) $\Lambda^- > \Lambda^-_{\max}(\alpha^{(u)} = \frac{1}{2}) = \frac{7}{2}$ and $\Lambda^- > \Lambda^-_{\max}(\alpha^{(u)} = \frac{1}{10}) = \frac{39}{2}$, and (b) $\Lambda > \Lambda^+\Lambda^-_{\max}(\alpha^{(u)})$. Numerical results with the AVMR and EMR-1 give $\Lambda^{-(num)}_{\max}(\alpha^{(u)} = \frac{1}{2}) = 7$, $\Lambda^{-(num)}_{\max}(\alpha^{(u)} = \frac{1}{10}) = 27$, and hence Eqs. (71a) and (71c) provide sufficient bound $\Lambda^{-(num)}_{\max}(\alpha^{(u)}) > \Lambda^-_{\max}(\alpha^{(u)})$; EMR-3: $\Lambda^{-(num)}_{\max}(\alpha^{(u)} = \frac{1}{2}) = 2$, $\Lambda^{-(num)}_{\max}(\alpha^{(u)} = \frac{1}{10}) = 7$, then $\Lambda^{-(num)}_{\max} < \Lambda^-_{\max}$ and Eq. (71c) is slightly insufficient.

C. Summary

We extended the MR1 and *c-nse-p-flow* families to the $\text{MR1}^+(\alpha^{(u)})$ and $\text{EMR}(\alpha^{(u)})$, and examined their linear stability against (1) the heuristic prediction based on the coefficient range $\{\hat{\alpha}, \beta, \hat{\beta}, \gamma, \hat{\gamma}\} \in [-1, 1]$, (2) the approximate condition in Eq. (67), and (3) the numerical simulations. Equation (67) allows one to qualitatively prioritize different schemes with respect to stability, but it is not accurate enough for the precise prediction of their unstable parameter space. Figure 13 demonstrates that the AVMR/EMR stability conditions are complimentary with the LI^+_3 and BFL-QI_3 in their

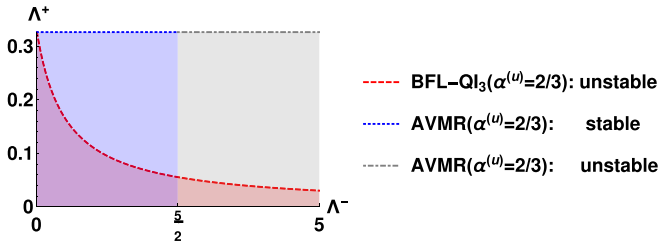

FIG. 13. Stability diagrams are schematized in the worst case $\delta = 1$ for BFL-QI$_3$($\alpha^{(u)} = \frac{2}{3}$) according to Eq. (63) and AVMR [with $\Lambda^-_{\max}(\alpha^{(u)} = \frac{2}{3}) = \frac{5}{2}$ according to Eq. (71)]. The BFL-QI$_3$ is unstable below the displayed stability line (red dashed), whereas AVMR is stable left to the vertical bound $\Lambda^- = \Lambda^-_{\max}$ (blue region) and unstable on its right (gray region) [see also Tables V and VIII and Figs. 6 and 8].

similar $\alpha^{(u)}$ range; the AVMR/EMR allow one to *uniformly* match the small $\Lambda^\pm$ and Λ range by easily satisfying an adjustable condition $\Lambda^- \leqslant \Lambda^-_{\max}(\alpha^{(u)})$ in Eqs. (71) and (71c). In Stokes flow, the stable viscosity range is almost Λ^- and Λ independent with the MR1$^+$ family, where MR1 is numerically found to be the most linearly stable in the full parameter range $\Lambda^\pm > 0$ and $\delta \in [0, 1]$. However, we will show that in the presence of the NSE term in Eq. (3a), AVMR gains over MR1, because Eq. (71) automatically adjusts the accuracy and stability when the grid Reynolds number Re$_g$ increases but Λ diminishes together with Λ^+. We will find that the interpolation-based LI$_k^+$ schemes show similar transient accuracy level with BFL-QI, MR1, MR1-BB, and AVMR/EMR when $\alpha^{(u)} \in [\frac{1}{2}, 1]$. The LI$_k^+$, MR1$^+$, and AVMR/EMR are commonly more stable with small $\alpha^{(u)}$ range, but we will find that the transient accuracy worsens when $\alpha^{(u)}$ reduces to zero. The stationary solutions are independent of $\alpha^{(u)}$, the AVMR($\alpha^{(u)}$) *quasisteady* solutions retain this property (because $\alpha^{(p)} = \hat{K}^+ = 0$) but those of MR1$^+$ and EMR are slightly $\alpha^{(u)}$-dependent (see Sec. VI A 1). Finally, the MR1 and AVMR apply equally with the TRT and standard MRT operators employing the same antisymmetric rate Λ^-, whereas EMR depends upon the implementation of the symmetric collision component through its term $\hat{K}^+\hat{n}_q^+$ and its coefficient $\hat{K}^-$ in Eq. (D8), which depends upon Λ^+.

VI. ROTATED CHANNEL FLOW

According to Sec. II D, the Couette and Poiseuille steady-state profiles satisfy the TRT-Stokes scheme for any channel inclination and Λ. Hence, all developed schemes can be first validated in a streamline-periodic, grid-rotated force-driven channel flow. Their predicted classification with respect to the exact modeling of the Couette and Poiseuille, Stokes and NSE flow is gathered in Table I. We validate this analysis and examine how the steady-state momentum error and the mass leakage rate $\partial_t \rho$ depend upon the governing parameters, such as Re$_g$ and Λ, with the inexact schemes. In addition, the GI property of the different boundary classes is examined in the grid-rotated parabolic flow subject to tangential wall motion. In turn, the Couette NSE flow subject to wall-normal injection extends these studies to discrete-exponential numerical solutions. Sec. VI A provides the numerical aspects; Secs. VI B, VI C, VI D, and VI E analyze the numerical results in the grid-rotated Poiseuille Stokes flow and Couette and Poiseuille NSE flows, respectively. Section VI F extends this study to the presence of wall-normal flow injection.

A. Numerical aspects

In what follows, Sec. VI A 1 discusses steady- and quasi-steady-state solutions in TRT and S-TRT; Sec. VI A 2 resumes the developed schemes; Sec. VI A 3 describes the benchmark geometry; and Sec. VI A 4 discusses the possibility of staggered solutions.

1. Mass balance, TRT, and S-TRT (any geometry)

It has been suggested that all members of the same family LI$_k^+$, giving $k = 1, 3, 4$, produce the same steady-state solutions, which are also equivalent between the TRT and S-TRT. The same has been suggested for LI$_0$ and its ELI$_0^+$ counterparts obeying Eq. (58) and exemplified in Table IV, We recognize now that these predictions are exact only provided that *the steady state* is reached for the momentum $\vec{j}$ but also for *the density* ρ. Otherwise, when the momentum is stationary but $\rho(t)$ undergoes a time-space uniform update, the resulting quasi-steady-state solution is operated by the additional post-collision correction $\delta\hat{n}_q^+$ in Eq. (12). Accordingly, the S-TRT produces an uniform mass source correction M_0 in Eq. (9a) operated by $\delta\hat{n}_q^{+,s}$ in Eq. (14). The steady-state closure relation in Eq. (B8) then gets an additional term δ_{lhs} in its left-hand side:

$$\begin{aligned}\delta_{\text{lhs}} &= (\beta + \gamma - 1)t_q^\star c_s^2 \partial_t \rho + (\hat{\alpha} + \hat{\beta} + \hat{\gamma})\delta\hat{n}_q^+ + \hat{K}^+\delta\hat{n}_q^+ \\ &= |_{\alpha^{(p)}=0}(\hat{\alpha} + \hat{\beta} + \hat{\gamma})\left(\delta\hat{n}_q^+ - t_q^\star c_s^2 \partial_t \rho\right) + \hat{K}^+\delta\hat{n}_q^+ \\ &= |_{\hat{K}^+=0}(\hat{\alpha} + \hat{\beta} + \hat{\gamma})\delta\hat{n}_q^{+,s}. \end{aligned} \tag{72}$$

Equation (72) assumes $I^{(t)} = 1$ where it takes into account that an unknown population and the postcollision populations of β and γ carry the next step solution $e_q^+(t+1) = e_q^+(t) + t_q^\star c_s^2 \partial_t \rho$. Equation (72) suggests that the boundary schemes (21) with $\alpha^{(p)} = \hat{K}^+ = 0$ produce identical TRT and S-TRT closure relations in Eq. (B8). The quasisteady parametrized solutions are then $\alpha^{(u)}$-independent provided that steady-state closure in Eq. (B8) are equivalent. The LI$_k$ with $k = \{1, 3, 4\}$ and AVMR($\alpha^{(u)}$) satisfy these conditions, in agreement with their numerical results. In contrast, since ELI$_k^+$ operates with $\hat{K}^+ \neq 0$, and possibly with $\alpha^{(p)} \neq 0$, the LI$_k$ and ELI$_k^+$ quasis-teady solutions very slightly differ when $\partial_t \rho \neq 0$. This is also true within the MR1$^+$($\alpha^{(u)}$) and EMR($\alpha^{(u)}$) families. We are not yet able to predict $\partial_t \rho$ for a given scheme, and examine its parameter behavior numerically using the S-TRT in Stokes flow and the transient simulations with the NSE equilibrium, where Eq. (17b) provides the reference $\partial_t \rho$ bulk scaling in a grid-rotated Poiseuille NSE flow.

2. Summary on the schemes (any geometry)

We perform the streaming step in Eq. (1) after collision and prior to the boundary update. During the streaming, the outgoing populations $\hat{f}_q$ can first apply the bounce-back to avoid the allocation of the ghost solid nodes. We prescribe

$I^{(t)} = 1$ in Eq. (21) and substitute the *poststream* (updated) solution $\beta f_q(\vec{r}_b, t+1)$ and $\gamma f_q(\vec{r}_b - \vec{c}_q, t+1)$. The LI_k^+ then computes Eq. (21) in the boundary node $\vec{r}_b$ where it prescribes for every cut link: (1) the relative distance $\delta \in [0, 1]$ such that $\vec{r}_b + \delta\vec{c}_q$ bisects the solid; (2) the adjustable parameters $\alpha^{(p)}$ and $\alpha^{(u)}$ in Eq. (24), where $\alpha^{(u)} \in]0, \delta^{-1}]$ is recommended by stability arguments, whereas $\alpha^{(p)} = 0$ simplifies the implementation; (3) the two coefficients $\hat{K}^{\pm}$ for postcollision correction in Eq. (22); and then (4) the three coefficients $\{\hat{\alpha}, \beta, \hat{\beta}\}$ in Eq. (42). The two-node MR in Eq. (21) adds two coefficients $\{\gamma, \hat{\gamma}\}$ for the upstream neighbor $\vec{r}_b - \vec{c}_q$. Unless indicated, we apply $I_b = 0$ in Eq. (33).

The $\mathrm{LI}_k \in \mathrm{LI}_k^+$ subclass is defined with $\alpha^{(p)} = \hat{K}^+ = 0$ prescribing $\alpha^{(u)}$ in Eq. (46); its subclass LI_0 applies without corrections, $\hat{K}^{\pm} = 0$. Table III lists the interpolation-based LI_0 members, but also the self-parametrized schemes, like CLI and *p-flow* IPLI. Otherwise, $\hat{F}_q = \hat{K}_k^- \hat{n}_q^-$ applies with one of the three corrections in Eq. (44), given there $k = 1$ (physical parametrization only), $k = 3$ (the parametrization and *p-flow*), or else $k = 4$ (parametrization and *p-pressure* accuracy).

The $\mathrm{ELI}_k^+ \in \mathrm{LI}_k^+$ applies with $\beta = 0$; two remaining coefficients $\hat{\alpha}$ and $\hat{\beta}$ are computed given $\alpha^{(p)}$ and $\alpha^{(u)}$ in Eq. (54). The ELI_k^+ sums the two corrections, $K_{ELI}^+ \hat{n}_q^+$ and $\hat{K}^- \hat{n}_q^-$, where K_{ELI}^+ is defined in Eq. (53), and $\hat{K}^-$ is proposed in Eqs. (57b)–(57e) for $k = 0, 1, 3, 4$, respectively. Hence, ELI_k^+ is able to update the incoming population during the propagation step applying *a modified-collision step*, and it then especially suitable for one-cell gaps or for corner links with no fluid neighbor. The generalized-interpolation-based members ELI_0^+, but also the parametrized CELI-UQ $\sim$ CLI and *p-flow* CELI-IP $\sim$ IPLI, are specified in Table IV. Their LI_0 counterparts have equivalent steady-state closure relations in Eq. (32); they are built by Eq. (58) and exemplified in Table IV.

The two-node BFL-QI and FH apply with Eq. (21) and Eqs. (D3) and (D4), respectively, without postcollision corrections. In turn, the *p-flow* $\mathrm{BFL\text{-}QI}_3$ and FH_3 apply $\hat{F}_q = \hat{K}_3^- \hat{n}_q^-$ with Eqs. (D2) and (D6), respectively. The necessary MLS constraint in Eq. (D7a) excludes the couple MLS-FH from the larger viscosity half-interval in the limit $\delta \to 0$; the couple MLS_3-FH_3 is then further restricted within the small-viscosity range. However, the FH and FH_3 is expected to apply well when $\delta \to 1$, where the $\mathrm{LI}_3^+(\alpha^{(u)})$ and $\mathrm{BFL\text{-}QI}_3$ should respect the directional stability condition in Eqs. (61) and (64) with respect to $\{\alpha^{(u)}(\delta), \Lambda^+, \Lambda\}$. When the cut link does not respect these conditions, $\alpha^{(u)}$ is recommended to be directionally replaced by $\alpha_0^{(u)}$ from Eq. (65). Alternatively, IPLI or CELI-IP may substitute $\mathrm{LI}_3^+(\alpha_0^{(u)})$ provided that their stability condition $\Lambda < \frac{\delta^2}{2}$ is satisfied by the cut link.

The two-node parabolic $\mathrm{VMR}(\alpha^{(u)}, \hat{K}^{\pm})$ is mainly represented by $\mathrm{MR1} \in \mathrm{MR1}^+(\alpha^{(u)})$ and *c-nse-p-flow* $\mathrm{AVMR}(\alpha^{(u)})$; they are specified in Eqs. (68) and Table VI, respectively; both MR1 and AVMR prescribe $\hat{K}^+ = \alpha^{(p)} = 0$, and AVMR provides $\alpha^{(u)}$-independent steady-state solutions. Although $\mathrm{AVMR}(\alpha^{(u)})$ shall prescribe $\Lambda^-(\alpha^{(u)})$ according to Eq. (71), where we basically apply $\alpha^{(u)} \in [\frac{1}{2}, 1]$ with $\Lambda^- < \frac{1}{2}$, it will be observed that AVMR is much more suitable than the MR1 in the nonlinear NSE regime. Finally, we note that $\mathrm{LI}^+(\alpha^{(u)})$, $\mathrm{MR1}^+(\alpha^{(u)})$ and $\mathrm{AVMR}(\alpha^{(u)})$ are more stable when $\alpha^{(u)} \to 0$, however, we will show that this choice slows the convergence to steady state and deteriorates transient accuracy.

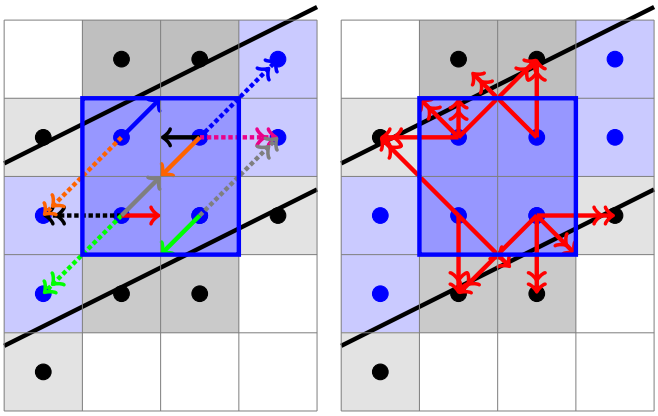

FIG. 14. Sketch of d2q9 periodic channel $\varphi = \arctan[\frac{m}{n}]$ [$m = 1$, $n = 2$] modeled inside the 2×2 (central, blue) grid box; the allocated box is $n\times(m+H) = 2\times4$ [$H = 3$]; the two walls are placed nonsymmetrically [offset $(x_0, y_0) = (0, \frac{1}{3})$ with respect to the left corner (0,0) on the bottom, the top wall is shifted by $(x, y) = (0, -\frac{1}{3})$ from (0,4)]; the effective width is $h = (H - \frac{2}{3})\cos(\varphi)$. Left: the outgoing links (dashed arrow) and their periodic incoming solution (solid arrow of the same color). Right: the cut-wall links. Other links perform the standard propagation between the four fluid nodes.

3. Discretized rotated channel

Our d2q9 computations are performed within a single allocated grid block of size $n\times(m+H)$ or $n\times(m+H+1)$, where integer $\{n, m\}$ feature an inclined channel $\arctan(\varphi) = \frac{m}{n}$ of the width $h \leqslant H\cos(\varphi)$, closed by *the stairwise periodic boundary condition* sketched in Fig. 14. The key point is that this single-box periodic configuration following [28] is much more computationally efficient than the decomposition of the rectangular box into series of the adjacent channels, e.g., [84], because only the box length H increases with the space resolution.

Giving the Stokes equilibrium in Eq. (3a), all schemes: LI_k, ELI_k^+, $\mathrm{BFL\text{-}QI}_k$, and FH_k for any $k = \{0, 1, 3, 4\}$, and the $\mathrm{VMR}(\alpha^{(u)}, \hat{K}^{\pm})$, shall be exact for a stationary grid-rotated Couette profile in a uniform density field $\rho(\vec{r}, t) = \bar{\rho}$, e.g., $j_{x'}(y') = \rho_0(a + by')$, $j_{x'}|_{\pm h/2} = \rho_0 u_0^{\pm}$, $a = \frac{u_0^+ + u_0^-}{2}$, $b = \frac{u_0^+ - u_0^-}{h}$ given arbitrary reference value ρ_0. Hence, the grid-rotated Stokes Couette profile gives perhaps a trivial but the necessary first benchmark validation.

4. Staggered invariants

We emphasize that the LI^+ schemes in Eq. (21) with $\hat{\alpha} = 1$, $\beta = -\hat{\beta}$, such as BB, CLI and CELI-UQ, support staggered invariants. This feature also affects the $\mathrm{MR1}^+$ where, additionally, $\gamma = -\hat{\gamma}$, including the MR1. The staggered momentum switches its sign every two subsequent iterations and sums with the steady-state physical solution. Several staggered solutions are specified [57] in a straight channel. When modeling the Stokes Couette flow in an inclined channel, e.g., with two grid columns along x when $\varphi = \arctan(\frac{1}{2})$, we observe the momentum component $\pm j_x^{\mathrm{stag}}$, which changes its

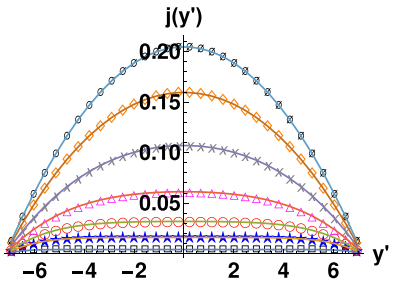

FIG. 15. Exact (lines) and numerical (symbols) solution in the rotated transient Poiseuille flow at $\mathrm{Re}_5 \approx 125.05$ applying AVMR($\alpha^{(u)} = \frac{1}{2}$) with $\Lambda_n = 2^{-2n}\Lambda_0$, $\Lambda_0 = \frac{1}{2}$. Data: $\varphi = \arctan(\frac{1}{2})$, $h = H\cos(\varphi)$, $H = 16$, $\mathcal{U} = 0.136533$, $\nu_n = 2^{-n}\nu_0$, $\nu_0 = \frac{1}{2}$, $F_{x',n} = 2^{-n}F_{x',0}$, $F_{x',0} = 4\times10^{-3}$. The results are output at $t'(k) = t(n,k)\nu_n/h^2$ when $t(n,k) = 2^n\times 2^k$ steps; in this figure $n = 5$ and $k = 0, 2, 3, 4, 5, 6, 11$ from the lowest to the highest profile.

sign between the two x columns and oscillates in time. This spurious solution is induced by the cut links parallel with the x axis, where $e_q^-(\pm j_x^{\mathrm{stag}})$ satisfies Eq. (21) when $\hat{\alpha} = 1$, $\beta = -\hat{\beta}$, $\gamma = -\hat{\gamma}$. An averaging over every two time steps makes the unwanted staggered contributions vanish.

B. Rotated Poiseuille Stokes flow

An unsteady Poiseuille momentum profile $j_{x'}(y',t) = \rho_0 u_{x'}(Y',t')$ obeying the no-slip conditions $u_{x'}(y' = \pm h/2) = 0$ sums the stationary parabolic solution to Eq. (15) with the time-dependent correction and reads as

$$j_{x'}(y',t) = -\frac{F_{x'}h^2}{8\nu}\left\{(4Y'^2-1) + \frac{32}{\pi^3}\sum_{n=0}^{\infty}\frac{(-1)^n}{(2n+1)^3} \times \exp[-\pi^2(2n+1)^2 t']\cos[\pi(2n+1)Y']\right\},$$

$$\text{with} \quad Y' = \frac{y'}{h}, \quad t' = \frac{\nu t}{h^2}, \quad y' \in \left[-\frac{h}{2}, \frac{h}{2}\right]. \tag{73}$$

Figure 15 displays analytical and numerical transient solutions at $\mathrm{Re} \approx 125$ in a small inclined channel. Although the Stokes and NSE macroscopic solutions are the same in Eq. (73) for any channel rotation, their Stokes and NSE *bulk* solutions differ except for particular configurations in Eq. (16). We first address the Stokes equilibrium in Eq. (3a) where the steady-state parabolic profile satisfies the scheme for any rotation and then (1) the two *p-flow* schemes without corrections, IPLI in Eq. (50) and CELI-IP in Eq. (60), (2) all LI_3^+ members, (3) BFL-QI$_3$, (4) FH$_3$, and (5) all VMR($\alpha^{(u)}, \hat{K}^{\pm}$) members shall (a) be exact, (b) conserve the global mass over each of two solid surfaces, and (c) produce a space-time uniform density distribution $\rho = \bar{\rho}$. In contrast, LI_0, ELI_0, LI_0^+, LI_1^+, LI_4^+, but also the two node BFL-QI and FH, are expected to produce inexact solutions either in a grid-aligned or grid-rotated Poiseiulle Stokes flow, unless in the straight or diagonal MGLI/LI_1^+ configurations with the specific $\Lambda(\delta)$ solutions in Eq. (49). In turn, BFL-QI and FH can adjust the straight flow with the help of the $\Lambda(\delta)$

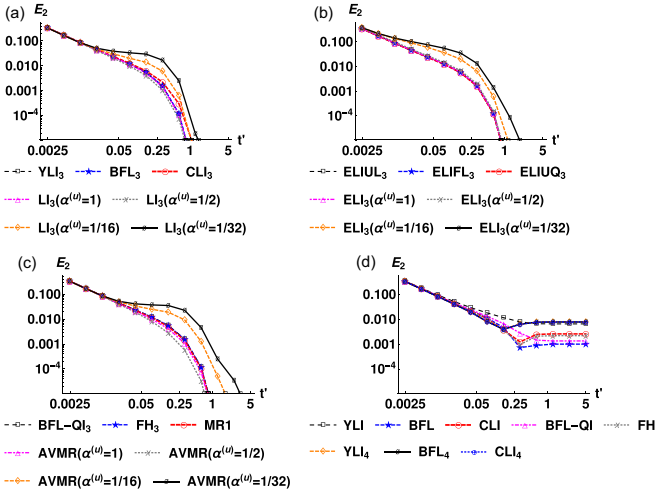

FIG. 16. The error estimate $E_2(j_{x'})$ with respect to Eq. (73) in the rotated transient Poiseuille Stokes flow is output vs the dimensionless time $t' = t(k)\nu/h^2$ when $t(k) = 2^k$ steps, $k = 1, 2, \ldots$ in log-log scale. (a) LI$_3(\alpha^{(u)})$, (b) ELI$_3(\alpha^{(u)})$, (c) BFL-QI$_3$, FH$_3$, MR1, and AVMR($\alpha^{(u)}$), (d) the standard YLI, BFL, BFL-QI, FH and the LI$_4(\alpha^{(u)})$. Panels (a), (b), and (c) converge to the exact solution up to machine accuracy, output is $E_2 > 10^{-5}$; (d) all schemes converge to finite error. Data: $\varphi = \arctan(\frac{1}{2})$, $h = H\cos(\varphi)$, $H = 16$, $\Lambda = \frac{1}{8}$, $\mathcal{U} = 0.136533$, $\nu = \frac{1}{4}$, $F_{x'} = 2\times10^{-3}$.

only asymptotically, when $\Lambda^+ \to 0$ in Eqs. (D1) and (D5), otherwise their optimal solutions are viscosity-dependent.

Figure 16 displays in the first three diagrams the temporal evolution towards the exact steady-state solution with the *p-flow* schemes: (a) YLI$_3$, BFL$_3$, CLI$_3$ and LI$_3(\alpha^{(u)})$; (b) their counterparts ELI-UL$_3$, ELI-FL$_3$, ELI-UQ$_3$, and $\mathrm{ELI}_3^+(\alpha^{(u)}, \alpha^{(p)} = 0)$; and (c) BFL-QI$_3$, FH$_3$, MR1, and AVMR($\alpha^{(u)}$), for an arbitrarily prescribed $\alpha^{(u)}$. Although the transition period is slightly different, all these schemes converge to $E_2 \approx 0$ up to the machine accuracy at a longer time. The interpolation-based coefficients typically yield $\alpha^{(u)} \in [1, 2]$ and show similar transient results; $\alpha^{(u)} = \frac{1}{2}$ is slightly more accurate in these computations with LI$_3$, ELI$_3$ and AVMR. However, when $\alpha^{(u)}$ further reduces towards zero, the transient accuracy and convergence worsens, most noticeably with the AVMR. The last diagram in Fig. 16 shows that the "standard" LI$_0$: YLI, BFL, and CLI, but also FH and BFL-QI, converge to a different E_2. The *p-pressure* LI$_4$ is represented by YLI$_4$, BFL$_4$, and CLI$_4$, these schemes are inexact in *p-flow* by construction but all LI$_4$ members converge to the same E_2. It is difficult to efficiently compare even the steady-state accuracy between these schemes because, whereas it is set by Λ with the parametrized schemes CLI/CELI-UQ, which correspond to $\Lambda \to 0$ in also parametrized LI$_4$, E_2 also depends upon ν with all other schemes. There is no mass loss in these Stokes flow simulations because the channel is placed symmetrically with respect to the grid and whereas the *p-flow* schemes return the total outgoing mass back individually for each of the two walls, the mass leakage changes sign between them with the inexact schemes.

When the rotated channel is not grid-symmetric, we additionally observed that $\partial_t \rho$ scales exactly in proportion to

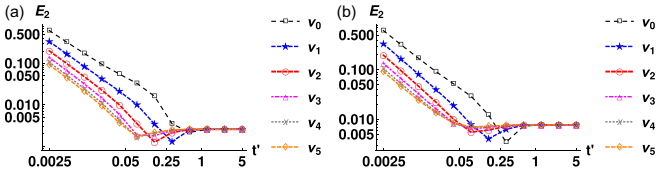

FIG. 17. Rotated transient Poiseuille Stokes flow is modeled by the parametrized inexact schemes when kinematic viscosity varies: (a) LI_1; (b) LI_4. The $E_2(j_{x'})$ is output at $t(n,k) = 2^n \times 2^k$ steps towards $t'(k) = t(n,k)\nu_n/h^2 = 2^k \nu_0/h^2$, $k \leqslant 12$ (log-log). Data: $\varphi = \arctan(\frac{1}{2})$, $h = H\cos(\varphi)$, $H = 16$, $\Lambda = \frac{1}{8}$, $\mathcal{U} = 0.136533$, $\nu_n = 2^{-n}\nu_0$, $\nu_0 = \frac{1}{2}$, $F_{x',n} = 2^{-n}F_{x',0}$, $F_{x',0} = 4\times 10^{-2}$.

$\mathcal{U}\mathrm{Re}_g$ at fixed Λ within the inexact parametrized schemes as CLI, CELI-UQ or NELI, which is the counterpart of CLI in Eq. (58a); this scaling agrees with Eq. (17b); the non-parametrized inexact schemes do not respect this property. It is also confirmed that the momentum stationary solutions are slightly different between TRT and S-TRT for ELI^+ and FH in agreement with Eq. (72).

In the transient stage, all schemes, either parametrized or not, do not respect the dimensionless timescale $t' = t\nu/h^2$ because of the truncation and boundary dependencies upon ν. Figure 17 allows one to observe this effect with LI_1^+ and LI_4^+: in the two cases, $E_2(t')$ is ν-dependent, but it converges towards the same steady-state value within each parametrized class. On the whole, we recognize that although the *p-flow* schemes are exact for steady-state, they are not necessarily the most accurate in the transient regime.

C. Rotated Couette flow with NSE equilibrium

A transient Couette velocity profile $u_{x'}(y',t)$ obeying wall conditions $u_{x'}(y' = -h/2) = u_0$, $u_{x'}(y' = h/2) = 0$ in a grid-rotated channel can be expressed through the dimensionless coordinate $\eta = \frac{y'}{2\sqrt{\nu t}}$ using $\alpha_n(\eta) = \sqrt{2n\eta_0 + \eta}$, $\beta_n(\eta) = \sqrt{2(n+1)\eta_0 - \eta}$, $\eta_0 = \frac{h}{2\sqrt{\nu t}}$:

$$\frac{u_{x'}(\eta)}{u_0} = \sum_{n=0}^{\infty} \mathrm{erfc}(\alpha_n) - \sum_{n=0}^{\infty} \mathrm{erfc}(\beta_n), \quad \eta = \frac{y'}{2\sqrt{\nu t}}. \tag{74}$$

The linear rotated Couette profile corresponds to the limit $t \to \infty$ in Eq. (74), and it is exact with all schemes using the Stokes equilibrium in Eq. (3). However, this differs either in the transient regime or in the presence of the NSE equilibrium term $\mathcal{E}_q^{(u)}$. In fact, a stationary NSE numerical profile remains exact with all schemes only in a straight channel, or in a diagonal channel provided that $\mathcal{E}_q^{(u)}$ is not projected on the diagonal cut links due to a_ε in Eq. (16b). Otherwise, with the exception of the *c-nse-p-flow* VMR($\alpha^{(u)}, \hat{K}^{\pm}$), (a) the steady-state momentum profile is not exact, (b) the density distribution is not uniform in space, and (c) only a quasisteady solution is established with a time-space uniform mean-density update rate $\partial_t \rho$ according to Eq. (11).

Figure 18 displays the analytical and numerical Couette momentum profiles $j_{x'} = \rho_0 u_{x'}(y',t')$ simulated at $\mathrm{Re} = \frac{u_0 h}{\nu} \approx 45.8$ in a rotated, symmetrically placed channel using the NSE equilibrium and the *c-nse-p-flow* AVMR($\alpha^{(u)} = \frac{1}{2}$). Figure 19 displays an evolution of the corresponding momentum error estimate $E_2(t')$ and the mass-leakage rate $\partial_t \rho(t')$, increasing the Re. These results confirm that, although the temporal evolution is not self-similar with respect to t', the AVMR numerical solution converges towards the exact, Re-independent stationary profile. Recall, AVMR($\alpha^{(u)}$) stability condition in Eq. (71) imposes at least a linear reduction $\Lambda_n \propto \nu_n$; we decrease here Λ_n in proportion to ν_n^2, then Λ_n reduces as Re_n^{-2} at a fixed wall velocity value u_0. The transient analysis shows that AVMR($\alpha^{(u)} = \frac{1}{2}$) typically outperforms other schemes in the transient stage, similarly to the Poiseuille flow in Fig. 16, and it is mainly followed here by YLI_4.

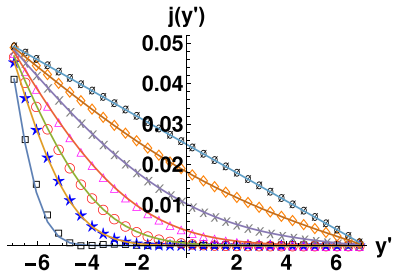

FIG. 18. Exact (lines) and numerical (symbols) transient rotated Couette NSE profile $j_{x'} = \rho_0 u_{x'}(y',t')$ computed with the *c-nse-p-flow* AVMR($\alpha^{(u)} = \frac{1}{2}$) when $\mathrm{Re} \approx 45.8$; the corresponding error estimate is displayed in Fig. 19. The results are output at $t'(k) = t(n,k)\nu_n/h^2$ when $t(n,k) = 2^n \times 2^k$, $n = 5$, $k = 0, 2, 3, 4, 5, 6, 10$ from the lowest to the highest line. Data: $\varphi = \arctan(\frac{1}{2})$, $h = H\cos(\varphi)$, $H = 16$, $u_{x'}(-h/2) = u_0 = 0.05$, $u_{x'}(h/2) = 0$, $\rho_0 = 1$, $\nu_n = 2^{-n}\nu_0$, $\nu_0 = \frac{1}{2}$, $\Lambda_n = 2^{-2n}\Lambda_0$, $\Lambda_0 = \frac{1}{6}$, $\mathrm{Re}_n = \frac{u_0 h}{\nu_n} \in [1.43, 45.7947]$ when $n \in [0,5]$.

Figure 20 displays the temporal evolution of the two metrics with YLI_4 either using (1) a constant value $\Lambda_n = \Lambda_0$ or reducing Λ_n with Re_n (2) linearly and (3) quadratically. The two last diagrams put together the steady-state results of these three computations: they show that although E_2 grows almost linearly with Re_n at a fixed $\Lambda_n = \Lambda_0$, $E_2(\mathrm{Re})$ reduces its slope when $\Lambda_n \propto \mathrm{Re}_n^{-1}$, and then E_2 becomes practically Re-independent when $\Lambda_n \propto \mathrm{Re}_n^{-2}$. At the same time, whereas $|\partial_t \rho|$ also grows linearly with Re at fixed Λ, $|\partial_t \rho|$ becomes almost Re-independent when $\Lambda \propto \mathrm{Re}^{-1}$, and $|\partial_t \rho|$ *decays* linearly with Re when $\Lambda \propto \mathrm{Re}^{-2}$. Figure 21 confirms that LI_1^+, LI_3^+ and LI_4^+ velocity error-estimate is the same for any two different parameter configurations $(u_{0,n}, \nu_n)$ with the same Re_g and Λ, and they scale then $|\partial_t \rho|$ exactly with $u_{0,n}$, such

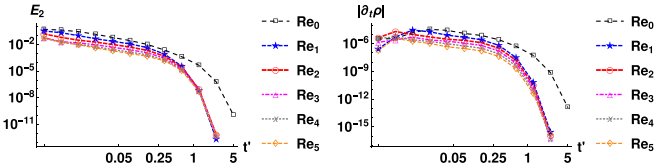

FIG. 19. The transient rotated Couette NSE flow with AVMR($\alpha^{(u)} = \frac{1}{2}$) using the standard NSE equilibrium and reducing $\Lambda_n = 2^{-2n}\Lambda_0$ as Re_n^{-2} from $\Lambda_0 = \frac{2}{3}$, $\mathrm{Re}_n \in [1.43, 45.7947]$, $n \in [0,5]$. The error estimate $E_2(j_{x'})$ with respect to Eq. (74) [giving $j_{x'} = \rho_0 u_{x'}$, $\rho_0 = 1$] and the mass-leakage rate $|\partial_t \rho|$ are output in log-log scale at $t'(k)$ according to Fig. 18. The AVMR is exact at steady state.

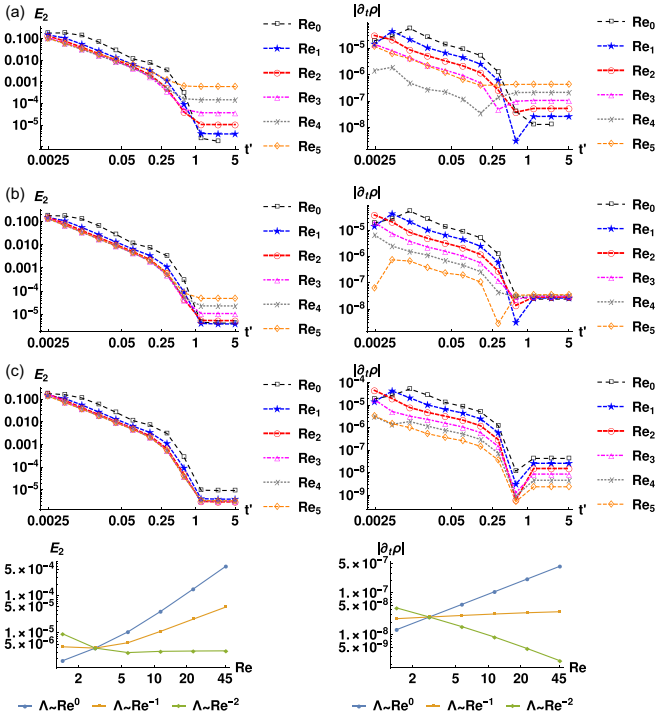

FIG. 20. The transient-rotated Couette NSE flow (log-log scale) with YLI$_4$ at $\mathrm{Re}_n = 2^n\mathrm{Re}_0$ using (a) $\Lambda = \Lambda_0 = \frac{1}{6}$; (b) $\Lambda_n = 2^{-n}\Lambda_0$; (c) $\Lambda_n = 2^{-2n}\Lambda_0$ (from the top to the bottom). The two last diagrams display together (a), (b), and (c) at the steady state. The same data as in Fig. 18.

that their dimensionless values $\partial_{t'}\rho = T_n\partial_t\rho_n$, $T_n = h/u_{0,n}$, are fixed in a given channel. These properties are also shared by the parametrized ELI$_k^+$, $k = 1, 3, 4$, and the parametrized VMR$(\alpha^{(u)}, \hat{K}^{\pm})$, such as MR1$^+$, AVMR, and EMR. At the same time, the BFL-QI and the *p-flow* BFL$_3$ both suffer from the lack of the parametrization in Couette NSE flow because of the spatial density variation; we confirmed that FH$_3$ shares the same deficiency in agreement with the predictions in Tables IX and XI. Moreover, FH and FH$_3$ are unstable here at $\Lambda_0^+ = 2$ in agreement with the stability condition in Eq. (D7a).

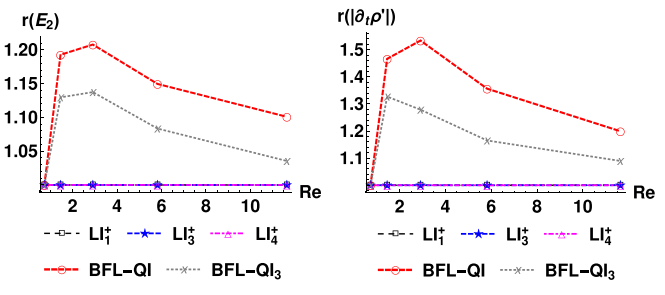

FIG. 21. The parametrization property in the steady-state rotated Couette NSE flow using the two parameter sets $\{\nu, u_0\}$ at fixed Re and grid: (1) $\nu = 2^{-n}\nu_0$, $u_0 = 0.05$; (2) $\nu = 4^{-n}\nu_0$, $u_0 = 0.05\times 2^{-n}$. Output: $r(E_2) = E_2^{(2)}/E_2^{(1)}$ and $r(|\partial_t\rho'|) = |\partial_t\rho'^{(2)}|/|\partial_t\rho'^{(1)}|$ with $\partial_t\rho' = \partial_t\rho/(u_0\mathrm{Re})$ vs Re. Data: $\varphi = \arctan[\frac{1}{4}]$, $h = 10\cos(\varphi)$, $\Lambda = \frac{1}{4}$, $j_{x'}(\pm h/2) = \pm\rho_0 u_0$, $\nu_0 = \frac{2}{3}$, $\mathrm{Re} = 2^n\mathrm{Re}_0 \in\approx [0.73, 11.46]$, $n \in [0, 4]$.

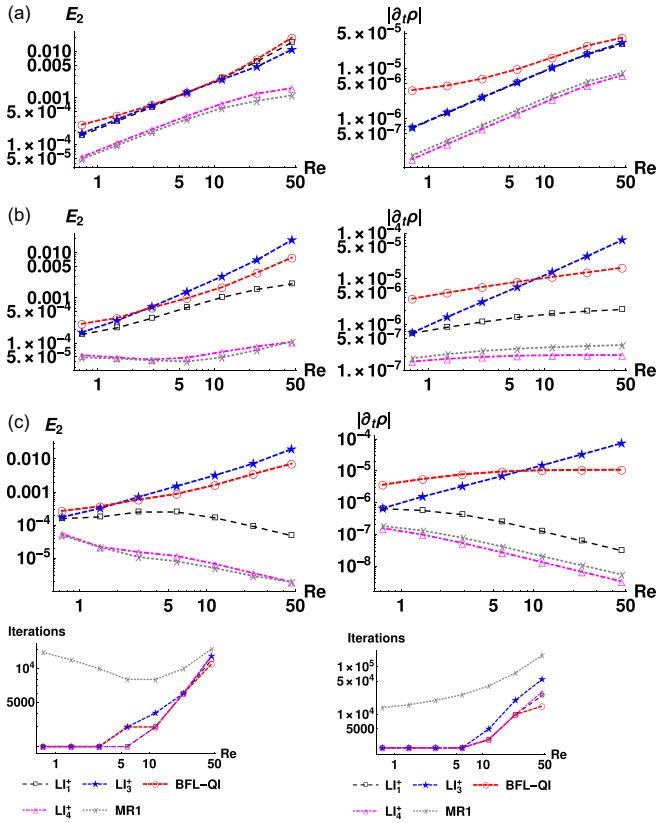

FIG. 22. The steady-state rotated Couette NSE flow is modeled with $\mathrm{Re} = 2^n\mathrm{Re}_0$ applying: (a) $\Lambda = \Lambda_0$; (b) $\Lambda_n = 2^{-n}\Lambda_0$; (c) $\Lambda_n = 2^{-2n}\Lambda_0$ [from the top to the bottom, log-log] and using LI$_1^+$, LI$_3^+$, LI$_4^+$, BFL-QI, and MR1; the LI$_k^+$ is represented by YLI$_k$, AVMR/EMR is exact. Iterations to reach steady-state criterion are displayed in the case (a) (left) and (c) (right); log-log scale. Data: $\varphi = \arctan[\frac{1}{4}]$, $(x_0, y_0) = \vec{0}$, $h = 10\cos(\varphi)$, $\Lambda_0 = \frac{1}{4}$, $u_0(y' = \pm h/2) = \pm 0.05$, $\nu = 2^{-n}\nu_0$, $\nu_0 = \frac{2}{3}$, $\mathrm{Re} \in\approx [0.73, 46.57]$, $n \in [0, 6]$. In this geometry, $\delta \in \{\frac{1}{10}, \frac{1}{8}, \frac{1}{6}, \frac{3}{10}, \frac{3}{8}, \frac{1}{2}, \frac{5}{8}, \frac{7}{10}, \frac{5}{6}, \frac{7}{8}, \frac{9}{10}\}$.

Figure 22 displays the steady-state $E_2(\mathrm{Re})$ and $|\partial_t\rho(\mathrm{Re})|$ with different schemes using the same three scalings $\Lambda(\mathrm{Re}^{-k})$, $k = 0, 1, 2$, such as with LI$_4$ in Fig. 20. When Λ_n is fixed ($k = 0$ in the top row), all schemes grow E_2 and $|\partial_t\rho|$ with Re: LI$_1^+$ and LI$_3^+$ on the one hand, and LI$_4^+$ and MR1 on the other hand, behave very similarly, whereas the (nonparametrized) BFL-QI behaves the worst. The deviation from the liner steady-state velocity profile is due to the two extra nonzero NSE terms $\beta^{(p)}\partial_q\mathcal{E}_q^{(u)}$ and $\gamma^{(p)}\partial_q^2\mathcal{E}_q^{(u)}$ in Eq. (19), which read with the following coefficients:

$$\begin{aligned}
\mathrm{LI}_1^+\text{: } \beta^{(p)} &= -\alpha^{(u)}\Lambda^-,\\
\mathrm{LI}_3^+\text{: } \beta^{(p)} &= -\frac{\delta^2\alpha^{(u)}}{2\Lambda^+},\\
\mathrm{LI}_4,\ \mathrm{VMR}(\alpha^{(u)}, \hat{K}^{\pm})\text{: } \beta^{(p)} &= 0. \qquad (75a)\\
\mathrm{LI}_k^+\text{: } \gamma^{(p)} &= -\beta^{(u)}\Lambda^- = -\alpha^{(u)}\Lambda^-\delta,\\
\mathrm{MR1}^+\text{: } \gamma^{(p)} &= -\alpha^{(u)}\Lambda^-,\\
\mathrm{AVMR, EMR}\text{: } \beta^{(p)} &= \gamma^{(p)} = 0. \qquad (75b)
\end{aligned}$$

The dimensionless truncation deviations $\beta^{(p)}\partial_q\mathcal{E}_q^{(u)}/\mathcal{U}$ and $\gamma^{(p)}\partial_q^2\mathcal{E}_q^{(u)}/\mathcal{U}$ with the coefficients from Eq. (75) are all predicted to scale in proportion with $\Lambda\mathrm{Re}$ except for LI_3^+. Figure 22 confirms that LI_3^+ does not reduce E_2 when Λ diminishes and even increases the two dependencies, whereas the BFL-QI is insensitive to Λ. In agreement with the predictions, since $\beta^{(p)}$ vanishes with LI_4^+ and MR1, these two schemes are the most accurate in Fig. 22 with the three Λ scalings. Moreover, LI_4^+ and MR1 make their two dependencies, $E_2(\mathrm{Re})$ and $|\partial_t\rho(\mathrm{Re})|$ almost Re-independent when $\Lambda_n \propto \mathrm{Re}_n^{-1}$, and these two dependencies then become *decreasing* when $\Lambda_n \propto \mathrm{Re}_n^{-2}$. Interestingly, these results follow the grid-rotated Poiseuille NSE flow bulk scaling in Eq. (17b), where $\partial_t\rho$ scales in proportion with $\Lambda\nu\mathrm{Re}^2$ on the fixed grid, and hence $\partial_t\rho$ becomes Re-independent when Λ reduces linearly with ν at fixed wall velocity value u_0. This happens because in the Couette NSE flow, the leading LI_4 and MR1 error in their closure relations is proportional to *an uniform value* $\Lambda^-\partial_q^2\mathcal{E}_q^{(u)}$, which is similar with the fourth-order *uniform truncation correction* $\Lambda^-\partial_q^4\mathcal{E}_q^{(u)}$ in rotated Poiseuille flow solvability condition in Eqs. (A6c) and (A7c). More generally, the $\partial_t\rho$ independence upon Re_g is then expected to be achieved when $\Lambda \propto \frac{\nu}{u_0^2}$.

Further, in agreement with Eq. (75), LI_1^+ behaves similarly to LI_3^+ when Λ is fixed, then it reduces the two slopes when Λ reduces linearly with Re, and finally, when $\Lambda \propto \mathrm{Re}^{-2}$, LI_1^+ shows the larger amplitude but the same shape dependencies $E_2(\mathrm{Re})$ and $\partial_t\rho(\mathrm{Re})$ as LI_4^+ and MR1, because when $\Lambda \to 0$, LI_1^+ approaches LI_4^+. The last diagram in Fig. 22 shows that the convergence to steady state slows with Re and when $\Lambda(\mathrm{Re})$ decreases, but the Λ effect is relatively weak, except with the MR1, which typically is the longest to converge. Finally, concerning stability, the simulations performed in Fig. 22 confirm that, according to Eq. (64a), YLI_3 becomes unstable at smaller ν_n. However, when Λ_n reduces linearly or quadratically with ν_n, LI_3 remains stable in the whole range by performing *a directional switch* from YLI_3 to $\mathrm{LI}_3(\alpha_0^{(u)})$ when $n \geqslant 4$ according to Eq. (65). Alternatively, IPLI produces the same results when its stability condition in Eq. (50) is satisfied (here $n \geqslant 5$ with linear Λ decrease, and $n \geqslant 4$ with Λ quadratic decrease).

D. Rotated Poiseuille flow with NSE equilibrium

A force-driven rotated Poiseuille flow obeying Eq. (15) is modeled now with the standard NSE equilibrium term $\mathcal{E}_q^{(u)}(a_\varepsilon = 0)$ in Eq. (3b). The solvability condition then combines the exact profile $j_{x'}(y')$ with the parabolic profile $\rho(y', t)$ obeying Eq. (17a) in space and Eq. (17b) in time, where $\partial_t\rho$ scales with $\frac{\Lambda\nu\mathrm{Re}_g^2}{h^4}\sin^2(2\varphi)$. Figures 2 and 3 confirm with the help of the MR_{nse} boundary scheme that $j_{x'}(y')$ and $\rho(y', t)$ agree exactly with these predictions using the same three scalings $\Lambda_n \propto \mathrm{Re}_n^{-k}$, $k = 0, 1, 2$, as has been examined for Couette NSE flow. With the exception of the MR_{nse}, all other examined schemes produce inexact solutions which also differ from their Stokes flow results, except in a straight channel, or otherwise in a diagonal channel when a_ε obeys Eq. (16b). This deviation is mainly because of the leading-order corrections in their steady-state closure relations with the coefficients

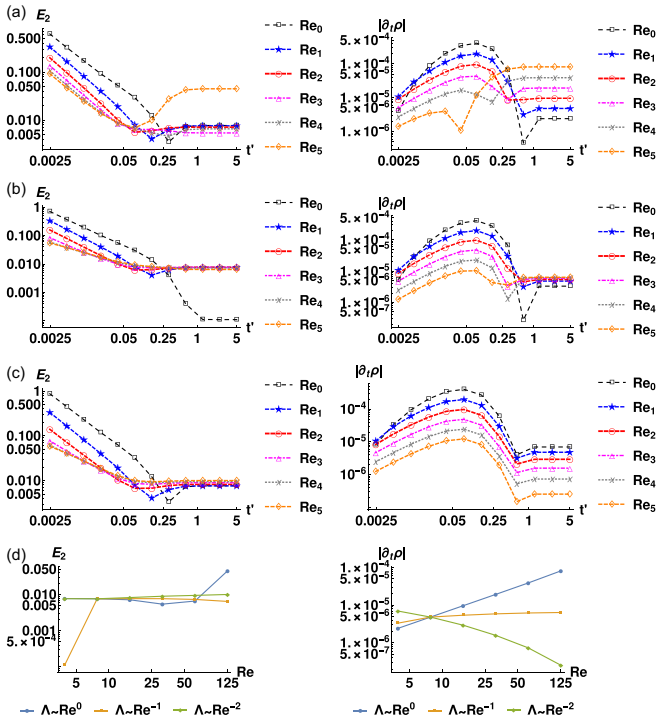

FIG. 23. The error estimate $E_2(j_{x'})$ with respect to Eq. (73) and $|\partial_t\rho|$ in the transient rotated Poiseuille NSE flow closed with the YLI_4 are output (log-log scale) at $\mathrm{Re}_n = 2^n\mathrm{Re}_0$, $n \in [0, 5]$, $\mathrm{Re}_0 \approx 3.9$: (a) $\Lambda = \Lambda_0 = \frac{1}{8}$; (b) $\Lambda \propto \mathrm{Re}^{-1}$: $\Lambda_n = 2^{-n}\Lambda_0$, $\Lambda_0 = \frac{1}{4}$; (c) $\Lambda \propto \mathrm{Re}^{-2}$: $\Lambda_n = 2^{-2n}\Lambda_0$, $\Lambda_0 = \frac{1}{2}$. (d) Panels (a), (b), and (c) together at the steady state. Data are in Fig. 15. These results can be compared with the Couette NSE flow in Fig. 20.

from Eq. (75); the additional higher-order corrections due to $\delta^{(p)}\partial_q^3\mathcal{E}_q^{(u)}$ and $\varepsilon^{(p)}\partial_q^4\mathcal{E}_q^{(u)}$ are only made to vanish with the MR_{nse} [cf. Eq. (39)]. We address the parametrized schemes LI_1^+, LI_3^+, LI_4^+, and AVMR, as well as the nonparametrized BFL-QI and $\mathrm{BFL\text{-}QI}_3$, FH and FH_3 when $\mathcal{U}$ is fixed and both viscosity and force amplitude decrease as Re_n increases. As predicted, the parametrized results are fixed by Re_g and Λ; in contrast, the nonparametrized schemes typically increase E_2 with $\mathcal{U}$. Unlike the rotated grid-symmetric Stokes channel flow in Figs. 16 and 17, the mass leakage $\partial_t\rho$ is presented in all NSE solutions.

Figure 23 displays the YLI_4 transient results with the same three $\Lambda_n(\mathrm{Re}_n^{-k})$ scalings as with the Couette NSE flow in Fig. 20. These results show that $|\partial_t\rho(\mathrm{Re})|$ behaves similarly to the Couette NSE flow and bulk Poiseuille predictions, and it becomes Re-independent with $\Lambda \propto \mathrm{Re}^{-1}$. Accordingly, the $E_2(\mathrm{Re})$ becomes then Re-independent with the quadratic scaling $\Lambda \propto \mathrm{Re}^{-2}$.

Figure 24 summarizes the most relevant steady-state results obtained with the different schemes. Following prediction in Eq. (75), the *p-flow* YLI_3 grows the two metrics with Re, and $\mathrm{BFL\text{-}QI}_3$ also shares this property; their results are almost Λ-independent and they are displayed here with a fixed Λ, where these schemes are most robust. Hence, although YLI_3 shows the smallest momentum error when Re is small, and even surpasses AVMR in this limit, it progressively loses against all schemes towards $\mathrm{Re} > 50$. In contrast, YLI_4 and AVMR

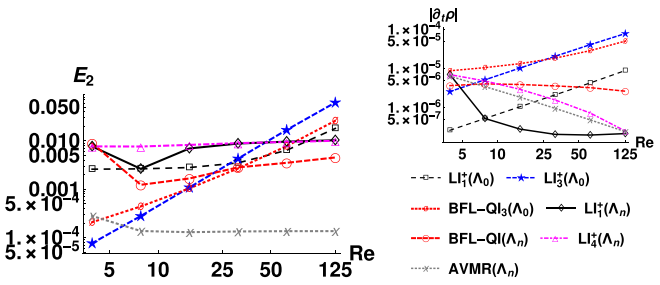

FIG. 24. The error estimate $E_2(j_{x'})$ and $|\partial_t\rho|$ in the steady-state rotated Poiseuille NSE flow are output (log-log scale) vs Re using (i) YLI$_1$, YLI$_3$, and BFL-QI$_3$ with $\Lambda=\Lambda_0=\frac{1}{8}$ and (ii) YLI$_1$, BFL-QI, YLI$_4$, and AVMR with $\Lambda_n=2^{-2n}\Lambda_0$, $\Lambda_0=\frac{1}{2}$; YLI$_k$ presents LI$_k^+$. Data are in Fig. 15: $\varphi=\arctan(\frac{1}{2})$, $h=H\cos(\varphi)$, $H=16$, $\mathcal{U}=0.136533$, $\nu_n=2^{-n}\nu_0$, $\nu_0=\frac{1}{2}$, $F_{x',n}=2^{-n}F_{x',0}$, $F_{x',0}=4\times10^{-3}$. The exact MR$_{nse}$ results are displayed in Figs. 2 and 3; the transient YLI$_4$ results in Fig. 23.

make the E_2 dependency upon Re vanish when $\Lambda_n\propto \mathrm{Re}_n^{-2}$; however, since YLI$_4$ is not *p-flow* exact, AVMR is about one to two orders of magnitude more accurate within the whole Re range. Thus, this example shows that the *p-flow* accuracy remains still relevant in the intermediate Re range, at least. Similar to the Couette NSE flow and Eq. (17b), YLI$_4$ and AVMR *decay* the mass leakage amplitude $|\partial_t\rho|$ with Re using the quadratic decay $\Lambda_n\propto \mathrm{Re}_n^{-2}$, where BFL-QI shows a weakly increasing $E_2(\mathrm{Re})$ and weakly decreasing $|\partial_t\rho(\mathrm{Re})|$. Finally, YLI$_1$ results are interesting: when Λ is constant, E_2 is dominated by the *p-flow* accuracy, and it does not depend upon Re unless when $\mathrm{Re}>\approx 50$. At the same time, YLI$_1$ shows the smallest amplitude, although linearly increasing, mass leakage $|\partial_t\rho(\mathrm{Re})|$. When using the quadratic decay $\Lambda_n\propto \mathrm{Re}_n^{-2}$, LI$_1$ and LI$_4$ produce nearly the same velocity results when Re increases and Λ converges rapidly to zero in Eq. (75a); however, LI$_1$ then shows the smallest and Re-independent mass leakage behavior.

When $k\neq 0$, we confirmed that YLI$_k$ and BFL$_k$ steady-state results are strictly the same, and they are quasi-identical with the ELI-UL$_k$ and ELI-FL$_k$, although very small difference exists between the (common) LI$_k$ solution and slightly (different) ELI$_k^+$ steady-state solutions, which depend upon $\{\alpha^{(p)},\alpha^{(u)}\}$ in agreement with Eq. (72) when $\partial_t\rho\neq 0$. The *c-nse-p-flow* AVMR$(\alpha^{(u)})$ and EMR$(\alpha^{(u)})$ show almost Re-independent momentum error behavior with the quadratic scaling strategy. In agreement with Eq. (72), AVMR$(\alpha^{(u)})$ produces $\alpha^{(u)}$-independent results, whereas they are $\alpha^{(u)}$-dependent with EMR-1/EMR-2, and smaller $\alpha^{(u)}$ improves their precision, the EMR then becomes slightly more accurate than AVMR.

Concerning stability, YLI$_k$ applies robustly for the very small viscosity range within the whole Λ range, except of YLI$_3$ which applies the stabilization according to Eq. (61). The ELI-UL$_4$ and ELI-FL$_4$ are stable, but ELI-UQ$_4$ remains stable only for the two smallest Re_n numbers according to its stability predictions (see Table IV and Eq. (E1a)). In turn, CLI$_4$ and MR1 may not converge to reliable solutions in the intermediate and higher Reynolds range; it is not impossible that CLI$_k$ and MR1 are delayed because of their staggered solutions (see Sec. VI A 4).

E. Galilean invariance in rotated Poiseuille flow

We prescribe now a tangential velocity $u_{x'}(y'=\pm h/2)=u_{w'}$ on the two channel walls and examine the Galilean invariance (GI) property for different boundary schemes. Following [103], the center-line velocity $u_{c'}=u_{x'}(y'=0)$ is fixed, the steady-state velocity profile $u_{x'}(y',u_{w'})$ and its mean value $\mathcal{U}=h^{-1}\int_{-h/2}^{h/2}u_{x'}dy'$ then read

$$u_{x'}(y',u_{w'})=u_{c'}\left(1-\frac{4y'^2}{h^2}\right)+u_{w'},\quad F_{x'}=\frac{8\nu\rho_0 u_{c'}}{h^2},$$
$$\mathcal{U}=u_{c'}\left(\frac{2}{3}+r_w\right),\quad r_w=\frac{u_{w'}}{u_{c'}},\quad \mathrm{Re}=\frac{|\mathcal{U}|h}{\nu}. \tag{76}$$

A boundary scheme is considered to better satisfy the GI property when its accuracy in the wall-moving reference frame is less dependent on the wall velocity, i.e., when the velocity error-estimate takes nearly the same value in the static and moving coordinate system x'-$u_{w'}$. Unlike in work [103], we then measure the error estimate in the moving frame for $u_{x'}(\vec{r})$-$u_{w'}$ with respect to the same no-slip solution $u_{x',0}(y')=u_{x'}(y',u_{w'}=0)$:

$$E_2(u_{x'}-u_{w'})=\sqrt{\frac{\sum_{\vec{r}}(u_{x'}^{\mathrm{num}}-u_{w'}-u_{x',0})^2}{\sum_{\vec{r}}u_{x',0}^2(y')}}. \tag{77}$$

When the Stokes equilibrium is prescribed in Eq. (3a), Eq. (76) satisfies the TRT bulk system in the full parameter range according to Eqs. (A7a)–(A7c) giving there $I_{nse}=0$. Hence, the $u_{x'}^{\mathrm{num}}(\vec{r})$ deviation from Eq. (76) happens only due to an inexact wall location coming from the parabolic term $\gamma^{(u)}\partial_q^2 e_q^-+\alpha^{(u)}I_b\mathcal{E}_q^{(f)}$ in Eq. (19), with $\mathcal{E}_q^{(f)}=t_q^\star\Lambda^- F_{x'}c_{q,x'}$ according to Eq. (33). Figure 25 confirms in the first diagram that $E_2(u_{x'}-u_{w'})$ is independent of $u_{w'}$ in an inclined channel for all principal non-*p-flow* boundary schemes, which are the members of the parametrized LI$_1$ and LI$_4$ families operating with $I_b=0$, and the original nonparametrized YLI, BFL and BFL-QI schemes, applying $I_b=1$ in Eq. (33). The *p-flow* schemes are exact for any inclination and wall velocity value $u_{w'}$ within their stability range.

However, the NSE term $\mathcal{E}_q^{(u)}$ in Eq. (3b) allows for this exact property only with the *p-nse-flow* MR$_{nse}$ family from Table VII, which is typically stable when $\Lambda<\nu$. We then prescribe the $\mathcal{E}_q^{(u)}$ with $a_\varepsilon=-k_\varepsilon^{-1}$ and apply $\Lambda=\frac{1}{12}$ according to Eq. (16c) and, in contrast to the study [103], examine the GI property of the boundary schemes when Eq. (76) satisfies the TRT bulk system exactly for any inclination. Otherwise, since the LBM operates in a static coordinate system, the truncation moments and density errors in Eqs. (A7a)–(A7c) grow together with $|u_{w'}|$ and $\mathrm{Re}(\mathcal{U})$ in Eq. (76), and in principle alone, they may interfere with the deficient mass flux and VGI property of the boundary scheme.

According to Fig. 24, we expect the term $\beta^{(p)}\partial_q\mathcal{E}_q^{(u)}$ to rapidly tend to dominate over the *p-flow* accuracy when Re grows; hence, since the *p-pressure* and *c-nse-p-flow* boundary classes operate with $\beta^{(p)}=0$ in Eq. (35), they are expected to obey best the GI property. Figure 25 shows in the three last diagrams that YLI$_4\in$ LI$_4$ and AVMR$(\alpha^{(u)})\in$ EMR deliver practically $u_{w'}$-independent solutions for (1) error estimate $E_2(u_{x'}-u_{w'})$ in Eq. (77), (2) velocity profile $u_{x'}(y')-u_{w'}$, and

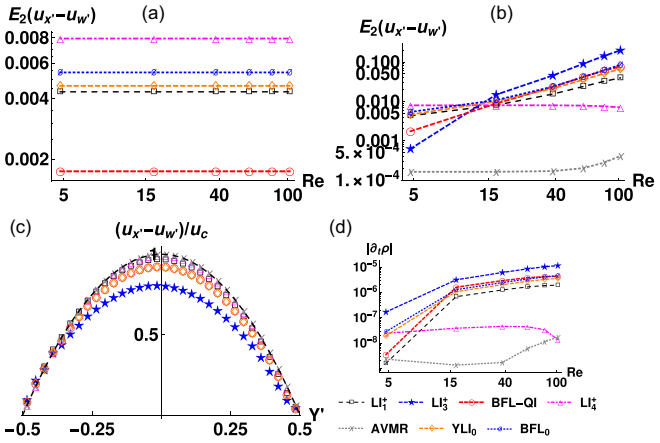

FIG. 25. The GI is examined in the grid-symmetric inclined force-driven channel subject to tangential wall velocity $u_{x'}(y' = \pm h/2) = u_{w'}$ when $|u_{w'}| = |r_w u_{c'}|$ grows with respect to the centerline velocity $u_{c'}$, with $r_w = -3n, n = 0, 1, \ldots, 5$, and $u_{x'}(y')$ satisfies the TRT in bulk with $\Lambda = \frac{1}{12}$, $a_\varepsilon = -k_\varepsilon^{-1}$ due to Eq. (16c). The error estimate is computed with Eq. (77). (a) $E_2(u_{x'} - u_{w'})$ with the Stokes equilibrium and the non-*p-flow* schemes; the LI_3^+ and AVMR are exact (not shown); $\partial_t \rho \equiv 0$ due to the symmetry. (b) $E_2(u_{x'} - u_{w'})$ with the NSE equilibrium and the non-*p-nse-flow* schemes. (c) the exact no-slip (line) and numerical (symbol) NSE profiles $u_{c'}^{-1}(u_{x'}^{\mathrm{num}} - u_{w'})$ vs $Y' = y'/h$ when $n = 5$, $u_{w'} = -15u_{c'}$, $\mathrm{Re} = 102.561$. (d) $|\partial_t \rho|$ in the NSE case (b). Data: $u_{c'} = 0.01$, $\nu = 0.02$, $h = 16\cos(\varphi)$, $\varphi = \arctan(\frac{1}{2})$, $F_{x'} = \frac{8\nu\rho_0 u_{c'}}{h^2}$, $\rho_0 = 1$, $\mathcal{U} = u_{c'}(\frac{2}{3} + r_w)$, $\mathrm{Re} = \frac{|\mathcal{U}|h}{\nu} \in [4.77, 102.561]$.

(3) mass-leakage rate $|\partial_t \rho|$. The simulations are performed here with $\Lambda = \frac{1}{12}$, and their accuracy lies at the same range as one of their no-slip counterparts in Fig. 24 using $\Lambda \propto \mathrm{Re}^{-2}$. Namely, the AVMR remains more accurate than LI_4 by about two orders of magnitude due to its correct coefficients of the second-order gradients, $\gamma^{(u)}\partial_q^2 e_q^-$ and $\gamma^{(p)}\partial_q^2 e_q^+$ in Eq. (19). In contrast, the parametrized classes LI_1 and LI_3, but also the nonparametrized schemes BFL, YLI, and BFL-QI, do not obey the *p-pressure* condition, and they all increase

TABLE VII. Coefficients of the three-point MR_{nse} scheme: $\{\hat{\alpha}, \beta, \hat{\beta}, \gamma, \hat{\gamma}\}$, $\hat{K}^{\pm}$ in Eq. (21) and two additional coefficients κ and $\hat{\kappa}$ of the second upstream neighbor: $\kappa f_q(\vec{r}_b - 2\vec{c}_q, t+1)$ and $\hat{\kappa}\hat{f}_{-q}(\vec{r}_b - 2\vec{c}_q, t)$; all of them are to be divided by the prefactors given in the first column; $\alpha^{(p)} = 0$; $\alpha^{(u)}$ is adjustable. The computations are mostly run with $\alpha^{(u)}(\delta, k) = \frac{8}{k(2+3\delta+\delta^2)}$ giving $k = 2$ where all seven coefficients are found in the interval $[-1, 1]$ $\forall \delta \in [0, 1]$ when $\Lambda^+ > 2\Lambda$; otherwise $\Lambda^+ > 8\Lambda$ is sufficient to satisfy this condition for any $k > 1$.

$4\times\hat{\alpha}$	$[-4 + \alpha^{(u)}(1+\delta)(2+\delta)]$
$4\Lambda^+\times\beta$	$[4 - \alpha^{(u)}\delta(2+\delta)]\Lambda^+ - 2\alpha^{(u)}\delta(2+\delta)\Lambda$
$4\Lambda^+\times\hat{\beta}$	$[4 - \alpha^{(u)}(2+\delta)]\Lambda^+ - 2\alpha^{(u)}\delta(2+\delta)\Lambda$
$8\Lambda^+\times\gamma$	$\alpha^{(u)}\delta[-(3+\delta)\Lambda^+ + 2(5+3\delta)\Lambda]$
$8\Lambda^+\times\hat{\gamma}$	$\alpha^{(u)}\delta[(3+\delta)\Lambda^+ + 2(5+3\delta)\Lambda]$
$8\Lambda^+\times\kappa$	$\alpha^{(u)}\delta(1+\delta)(\Lambda^+ - 2\Lambda)$
$8\Lambda^+\times\hat{\kappa}$	$-\alpha^{(u)}\delta(1+\delta)(\Lambda^+ + 2\Lambda)$
$\hat{K}^+$	0
$4\Lambda^+\times\hat{K}^-$	$[8 - \alpha^{(u)}(1+\delta)(2+\delta)]\Lambda^+ + 2\alpha^{(u)}(1+\delta)(2+\delta)\Lambda$

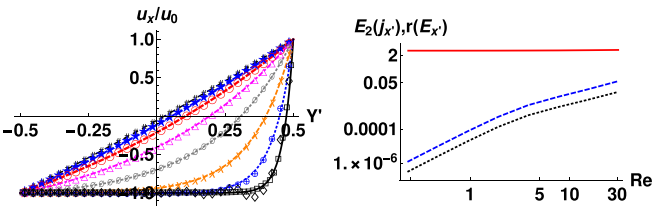

FIG. 26. Left: Analytical solution from Eq. (78) and AVMR results in steady-state Couette NSE flow with wall-normal injection over varying Re when $v_0(\pm h/2) = 0.01$, $r_{xy} = 1$. Data: $\varphi = \arctan(\frac{1}{2})$, $(x_0, y_0) = \vec{0}$, $\mathrm{Re} \in\approx [0.21, 27.5]$ on coarse grid $h = 16\cos(\varphi)$, $\nu = 2^{-n}\nu_0$, $\nu_0 = \frac{2}{3}$, $\Lambda = \frac{1}{4}\times 2^{-2n}$, $n \in [0, 7]$. Coarse grid: $n = 7$ is displayed with symbol "◇". Fine grid: $n = 7$ is displayed with symbol "□" using $h = 32\cos(\varphi)$, $\nu = 2\times 2^{-n}\nu_0$, $\Lambda = 2\Lambda_0\times 2^{-2n}$. Right: Error estimate $E_{x'} = E_2(j_{x'})$ is computed in the straight channel with Eq. (79) when $h = 16$ (dashed blue), $h = 32$ (dotted black) and their rate $r(E_{x'})$ (solid red) in log-log scale.

their velocity error estimate with Re. Next, comparing with Fig. 24 where $\mathcal{U}$ is fixed, $|\partial_t \rho|$ increases here with $\mathrm{Re}(\mathcal{U})$ but $|\partial_{t'}\rho| \propto |\partial_t \rho|/\mathcal{U}$ slightly decreases with all schemes when Re is sufficiently high, and especially with the LI_4, whereas $\mathrm{AVMR}(\alpha^{(u)})$ shows even a smaller mass leakage-rate than in Fig. 24. Most likely, these results indicate that the $\partial_t \rho(\mathrm{Re})$ dependency becomes modified in the absence of its bulk source from Eq. (17b).

To summarize, the *p-pressure* LI_4 and *c-nse-p-flow* $\mathrm{AVMR}(\alpha^{(u)}) \in \mathrm{EMR}$ naturally follow the GI property due to the vanishing of the NSE term gradient from their closure relation. At the same time, the VGI defect is especially striking with the *p-flow* LI_3 family, which is exact at zero Re number in force-driven inclined Poiseuille flow, and then in a straight NSE channel, but it fails in an inclined NSE channel by completely neglecting the $\beta^{(p)}\partial_q \mathcal{E}_q^{(u)}$ term in its parabolic correction $\hat{K}_3^- \hat{n}_q^-$ in Eq. (44b). According to our additional computations, the results with the standard equilibrium and different $\Lambda(\mathrm{Re})$ strategies confirm the same hierarchy of boundary schemes with respect to the GI property.

F. Rotated Couette flow with wall-normal injection

We consider now a velocity profile $\vec{u}(y') = \{u_{x'}, u_{y'}\}$ in a grid-rotated channel of width h driven by the tangential motion of upper and bottom walls, $u_{x'}(y' = \pm h/2) = \pm u_0$, subject to wall-normal injection $u_{y'}(y' = \pm h/2) = v_0$. Giving the characteristic velocity $\mathcal{U} = v_0$, we parametrize the dimensionless exponential solution $\mathcal{U}^{-1}\vec{u}(y')$ to the steady-state Navier-Stokes 2D equation by Re and wall-velocity ratio $r_{xy} = \frac{u_0}{v_0}$:

$$\frac{u_{x'}(Y')}{v_0} = \frac{1 + e^{\mathrm{Re}} - 2e^{\mathrm{Re}(Y'+1/2)}}{1 - e^{\mathrm{Re}}} r_{xy}, \quad \frac{u_{y'}}{v_0} \equiv 1, \quad \rho \equiv \rho_0,$$
$$\mathrm{Re} = \frac{v_0 h}{\nu}, \quad r_{xy} = \frac{u_0}{v_0}, \quad Y' = \frac{y'}{h} \in \left[-\frac{1}{2}, \frac{1}{2}\right]. \tag{78}$$

Hence, $u_{x'}$ scales with u_0 at fixed Re, and the limit $\mathrm{Re}\to 0$ corresponds to the linear Couette profile $u_{x'}(Y') = 2Y'u_0$, $v_0 \equiv 0$. Figure 26 displays in its left diagram the exact profile in a grid-rotated channel over varying Reynolds numbers

Re ∈ [0.21, 27.5] and AVMR numerical solution. However, before undertaking the analysis of the inclined channels, we address their straight counterparts for a similar resolution and Re-range.

In a straight channel, the numerical solution obeying the Dirichlet condition in grid boundary points combines an uniform vertical velocity $u_{y'}(j) \equiv v_0$ with the discrete-exponential solution $u_{x'}^{\rm num}(j)$ in grid points $Y'(j) = -\frac{1}{2} + j/h$, $j = 0, 1, \ldots, h,$:

$$\frac{u_{x'}^{\rm num}(j)}{u_0} = \frac{1+\xi^h-2\xi^j}{1-\xi^h}, \quad \left.\frac{u_{x'}^{\rm num}}{u_0}\right|_{j=0,h} = \mp 1,$$
$$\xi = \frac{1+R}{1-R}, \quad R(\nu_{\rm num}) = \frac{v_0}{2\nu_{\rm num}}, \quad R_0 = R(\nu) = \frac{\rm Re}{2h}. \tag{79}$$

The right diagram in Fig. 26 indicates that the error estimate $E_2(u_{x'}^{\rm num})$ of this numerical solution with respect to Eq. (78) monotonously increases with Re, towards $E_2 \approx 6.3\%$ on the fixed mesh $h = 16$, and converges with the second-order rate $r_{x'} = \log_2[\frac{E_{x'}(h)}{E_{x'}(2h)}] \in [1.94, 2.08]$ when Re ∈ [0.24, 30.72]. The LI$^+$, MR1, and EMR reproduce this solution exactly prescribing $\delta = 0$ on the top and bottom walls. Notably, $u_{x'}^{\rm num}$ is Λ-independent in Eq. (79) at least for the in-node grid location $\delta = 0$; its extension to any distance δ can be built following [31,87] for a given boundary scheme. The discrete solution in Eq. (79) exactly matches its continuous counterpart in Eq. (78) following [98] and prescribing $\nu_{\rm num} \neq \nu$:

$$u_{x'}^{\rm num}(j) = u_{x'}(j)\ \forall\ j \ \text{ if } \ \xi(\nu_{\rm num}) = e^{\frac{\rm Re}{h}}, \ \text{ with } \tag{80a}$$
$$\frac{\nu_{\rm num}}{\nu} = \frac{R_0}{\tanh[R_0]} \approx \left(1 + \frac{\rm Re^2}{12h^2}\right). \tag{80b}$$

Equation (80b) predicts the Re^2 increase of $\nu_{\rm num}$ on a fixed mesh, and its second-order convergence to ν at fixed Re, in agreement with the second-order error estimate in Fig. 26. This follows the idea of the so-called "optimal rule" originally proposed in the ADE context where *a positive difference* between numerical and "physical" diffusion coefficients compensates the negative numerical diffusion, either in the finite difference [106] or, equivalently, the LBM bulk solution [60].

However, the discrete-exponential form in Eq. (79) is not valid in inclined channels, where the numerical solution solves the TRT system of the steady-state directional recurrence equations (7)-(8), and it may give rise to accommodation layers [29]. Unlike in a grid-inclined parabolic profile, the truncation analysis does not deliver exact solvability conditions on an exponential profile, but it may provide ideas for the leading-order error dependency upon (1) Re, (2) h, (3) Λ, and (4) free equilibrium parameter a_ε in Eq. (3b). Giving the exact velocity profile from Eq. (78), we examine the third-order truncation corrections $E'_{X'}(Y')$ and $E'_{Y'}(Y')$ in Eqs. (A11a) and (A11b) to dimensionless X'- and Y'-momentum equations, respectively, where $E'_{Y'}(Y')$ gives rise to the exponential pressure distribution $\rho(Y')$. The fourth-order correction $E'_m(Y')$ in the mass-conservation equation and the average mass-leakage rate $\langle\partial_{t'}\rho\rangle$ are then respectively provided by Eqs. (A11c) and (A12). Although

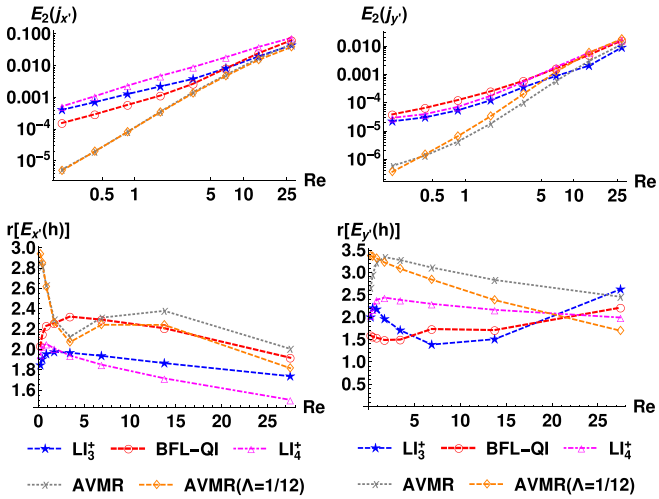

FIG. 27. The error estimates for tangential ($E_2(j_{x'})$) and wall-normal ($E_2(j_{y'})$) velocity components with respect to Eq. (78) over varying Re ∈≈ [0.21, 27.5] on the coarse grid $h = 16\cos(\varphi)$, and their convergence rate to the finer grid $h = 32\cos(\varphi)$ using $\{\text{YLI}_3, \text{LI}_3(\alpha_0^{(u)}), \text{IPLI}\} \in \text{LI}_3^+$, $\text{YLI}_4 \in \text{LI}_4^+$, BFL-QI, and AVMR($\alpha^{(u)} = \frac{1}{2}$). Additionally, AVMR($\alpha^{(u)} = \frac{1}{2}$) is applied with $\Lambda = \frac{1}{12}$. Coarse grid: $\nu = 2^{-n}\nu_0$, $\nu_0 = \frac{2}{3}$, $\Lambda = \Lambda_0 \times 2^{-2n}$, $\Lambda_0 = \frac{1}{4}$, $n \in [0, 7]$. Fine grid: $\nu = 2\times 2^{-n}\nu_0$, $\Lambda = \frac{1}{2}\times 2^{-2n}$, $\Lambda_0 = \frac{1}{2}$, $n \in [0, 7]$.

the third-order steady-state TRT corrections all vanish when $\Lambda = \frac{1}{12}$, whereas their fourth-order counterparts all vanish when $\Lambda = \frac{1}{6}$, the exact Poiseuille NSE flow solution $\partial_t\rho$ in Eq. (17b), and the approximation $\langle\partial_{t'}\rho\rangle$ in Eq. (A12), only vanish asymptotically in the limit $\Lambda \to 0$.

These dimensionless terms are all parametrized by Re, Λ and r_{xy}, and they depend upon a_ε. Recall that, in a grid-rotated parabolic velocity profile, $a_\varepsilon = -k_\varepsilon^{-1}$ makes $E'_{Y'}$ and E'_m vanish in Eqs. (A7b) and (A7c), leading then to $\partial_t\rho = 0$ in Eq. (17b), whereas $a_\varepsilon = 0$ vanishes $E'_{X'}$ in Eq. (A7a). In the presence of wall-normal fluid injection, the $E'_{X'}$ only simplifies its expression when $a_\varepsilon = 0$ and then depends linearly on r_{xy}, supporting the exact linear scaling $u_{x'} \propto u_0$ in Eq. (78). In turn, $E_{y'}(Y')$, $E'_m(Y')$ and $\langle\partial_{t'}\rho\rangle$ simplify their expressions and depend linearly on r_{xy} when $a_\varepsilon = -k_\varepsilon^{-1}$. In this last case, $\langle\partial_{t'}\rho\rangle$ becomes Re-independent provided that $\Lambda \propto \text{Re}^{-4}/\sinh(\text{Re}/2)$, where Λ then reduces much faster to zero than when $\Lambda \propto \text{Re}^{-1}$ in Eq. (17b).

Figure 27 compares the error estimates $E_{x'} = E_2(j_{x'})$ and $E_{y'} = E_2(j_{y'})$ in a small grid rotated channel, and their respective convergence rates $r(E_{x'})$ and $r(E_{y'})$, between the parametrized families LI$_3$, LI$_4$, AVMR, and also with the nonparametrized two-node BFL-QI scheme. We first confirm that the parametrized schemes fix $E_2(u_{x'})$ and $E_2(u_{y'})$ by Re$_g$, Λ and r_{xy} on a given grid, whereas $\partial_t\rho$ scales linearly with v_0 in agreement with the truncation prediction in Eq. (A12) for $\langle\partial_t\rho\rangle = v_0/h\langle\partial_{t'}\rho\rangle$. We have also observed that the standard equilibrium with $a_\varepsilon = 0$ applied here produces better $u_{x'}$ accuracy and more linear u_0 scaling than $a_\varepsilon = -k_\varepsilon^{-1}$, in agreement with prediction in Eq. (A11a).

Note that $E_2(j_{x'})$ becomes nearly Re-independent in a grid-rotated parabolic profile closed by the LI$_4$ and AVMR when $\Lambda \propto \text{Re}^{-2}$ decays quadratically with Re in Fig. 24.

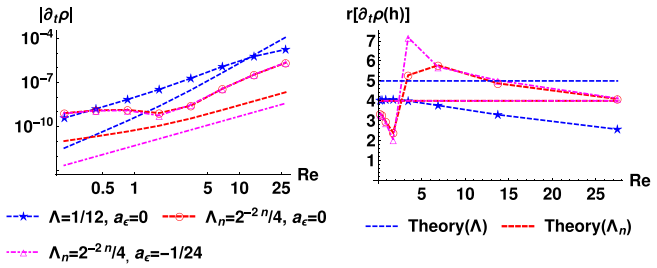

FIG. 28. The mass-leakage rate $|\partial_t\rho|$ [log-log] and its convergence rate $r[\partial_t\rho(h)] = \log_2[|\frac{\partial_t\rho(h)}{\partial_t\rho(2h)}|]$ using the AVMR with (a) $\Lambda(h) = \Lambda(2h) = \frac{1}{12}$, $a_\varepsilon = 0$; (b), (c) $\Lambda_n(h) = \frac{1}{2}\Lambda_n(2h) = \frac{1}{4}\times 2^{-2n}$, (b) $a_\varepsilon = 0$ and (c) $a_\varepsilon = -k_\varepsilon^{-1}$. Continuous lines ("Theory") display the approximation $|\langle\partial_t\rho\rangle| = \frac{h}{v_0}|\langle\partial_{t'}\rho\rangle|$ with Eq. (A12) and its rate. Data are from Fig. 27.

Figure 27 addresses the quadratic scaling $\Lambda_n(\mathrm{Re}_n) = \Lambda_0(h)\times 2^{-2n}$ with all schemes, and also displays AVMR($\Lambda = \frac{1}{12}$). Using these two Λ strategies, the AVMR is about two orders of magnitude more accurate than the three other schemes when Re is small but, probably following closer the bulk Re scaling, it grows its error estimate faster with Re than other schemes, and all schemes reach about 3%–7% discrepancy at $\mathrm{Re} \approx 27$, within the accuracy range of the straight channel in Fig. 26(b). The largest errors at $\mathrm{Re} \approx 27$ reflect an oscillation over the sharpest velocity gradient, which attenuates with the grid refinement for all examined schemes [cf. "diamond" and "square" symbols in Fig. 26(a)]. Unlike the Couette NSE flow in Fig. 22(c), the LI_3 is more accurate than LI_4 over the whole Re range and, unlike in the parabolic NSE flow, the MR_{nse} family does not improve the quality of the LI_3 and AVMR solutions, most likely because it also copes with the third-order momentum errors in its closure relation and manifests faster $|\partial_t\rho(\mathrm{Re})|$ increase. The $E_2(j_{y'})$ follows the same trend as $E_2(j_{x'})$ but with one order smaller magnitude, where BFL-QI behaves less accurately. Further, Fig. 27 confirms that the AVMR with $\Lambda \propto \mathrm{Re}^{-2}$ converges best for both velocity components, with a rate between 2 and 3, which diminishes less rapidly with Re than for other schemes.

Figure 28(a) compares the associated AVMR mass-leakage rate $|\partial_t\rho|$ between $\Lambda = \frac{1}{12}$ and $\Lambda_n = \Lambda_0(h)\times 2^{-2n}$, using the standard equilibrium $a_\varepsilon = 0$ but also $a_\varepsilon = -k_\varepsilon^{-1}$, and displays the fourth-order accurate bulk prediction $|\langle\partial_t\rho\rangle| = T|\langle\partial_{t'}\rho\rangle|$, with $T = h/v_0$. In agreement with this prediction, $\Lambda = \frac{1}{12}$ produces the largest amplitude, monotonously increasing dependency $|\partial_t\rho(\mathrm{Re})|$, where, however, the numerical slope $|\partial_t\rho(\mathrm{Re})|$ differs from the predicted dependency $|\langle\partial_t\rho(\mathrm{Re})\rangle|$. We have also observed that applying $\Lambda \propto \mathrm{Re}^{-4}/\sinh[\mathrm{Re}/2]$ (when Re is sufficiently high), the results remain nearly the same as with the quadratic $\Lambda \propto \mathrm{Re}^{-2}$ decay. Further, Eq. (A12) indicates that $|\langle\partial_t\rho\rangle|$ is (slightly) more accurate when $a_\varepsilon = -k_\varepsilon^{-1}$, however, numerically, $|\partial_t\rho|$ is less sensitive to a_ε in Fig. 28(a). According to Eq. (A12), $|\langle\partial_t\rho\rangle|$ converges as h^{-5} at fixed Λ, and hence as h^{-4} when $\Lambda_0(2h) = 2\Lambda_0(h)$ increases by 2 with the second Λ strategy applied here; these two predictions are displayed in Fig. 28(b), such as $r[\partial_t\rho] = 5$ and $r[\partial_t\rho] = 4$, respectively. Numerically, the convergence rate $r[\partial_t\rho]$ decays with Re from $r = 4$ when $\Lambda = \frac{1}{12}$, and it oscillates around the predicted value $r = 4$ with the second Λ strategy.

Thus, unlike in the grid-rotated Poiseuille NSE flow, the numerical dependency $|\partial_t\rho(\mathrm{Re}, \Lambda, a_\varepsilon)|$ does not fit exactly the fourth-order result. This observation can be explained as follows. First, the fourth-order analysis does not provide exact solvability conditions for grid-rotated exponential solutions, namely, it predicts the bulk rate $\partial_t\rho$ as the y'-dependent, whereas the numerical quasisteady solution operates with a space-uniform rate and, on the heuristic arguments, we compare it with the predicted approximation for the averaged value $|\langle\partial_t\rho\rangle|$. Second, the effective mass-leakage rate most likely combines all its truncation bulk contributions with the Λ- and Re-dependent discrete boundary accommodation, which is not described by the bulk and boundary Chapman-Enskog analysis, but known to modify their scaling predictions, e.g., [29]. We suggest that once the momentum accuracy becomes boundary-scheme-independent, it is set by the bulk truncation and accommodation terms, indicating the necessity of grid refinement in the higher Re range.

G. Summary

In this section we validated the developed bulk and boundary analysis with respect to the solvability conditions and effective accuracy of the directional boundary schemes in the Couette and Poiseuille grid-rotated flows with the Stokes and Naiver-Stokes equilibrium. We address these steady-state canonical benchmark solutions in the grid-rotated channels, where we confirm that (1) all schemes are exact in Couette Stokes flow, (2) the *p-flow* schemes extend this property to the Poiseuille Stokes flow, and (3) the *c-nse-p-flow* and *p-nse-flow* are then respectively exact in the presence of the NSE equilibrium term in Eq. (3). In contrast, the interpolation-based schemes, such as BFL, YLI, XELI, FH, or BFL-QI, and more generally LI_0^+, LI_1^+, and LI_4^+, are not even exact in a grid-aligned *p-flow* channel, except when $\mathrm{BB}/\mathrm{LI}_1^+$ adopt their particular solutions $\Lambda(\delta)$. When the stationary momentum profile is not exact, it comes with a permanent, space-time uniform density update $\partial_t\rho$ according to Eqs. (11) and (13) in the grid-asymmetric rotated Poiseuille Stokes flow; the NSE term produces mass leakage in both the Couette and Poiseuille, grid-symmetric or asymmetric, channel. During the transition period towards the steady-state, no scheme supports exactly the dimensionless solution dependency upon $t' = \nu t/h^2$ in Eqs. (73) and (74). This happens because the temporal higher-order truncation corrections are viscosity-dependent and not parametrized by Re and Λ. We suggest that in future this issue shall be examined in the frame of the time-dependent boundary values, which is beyond the scope of this work.

Our focus is put here on the momentum error estimate E_2 and mass-leakage rate $|\partial_t\rho|$ dependencies upon Re_g and Λ. We have first confirmed our predictions, that the parametrized schemes, such as CLI/CELI-UQ, IPLI/CELI-IP, or LI_k^+ for $k = 1, 3, 4$, $\mathrm{MR1}^+$ and *c-nse-p-flow* AVMR and EMR, get E_2 fixed by Re_g and Λ [or $\Lambda(\mathrm{Re}_g)$] when the space resolution is fixed. In contrast, the FH, FH_3, BFL-QI, and $\mathrm{BFL\text{-}QI}_3$ do not share this property, e.g., in inclined NSE channel with all these schemes, and since their results depend on the parameter

choice $(\nu, \mathcal{U})$, they cannot compete with other schemes in a equal manner.

Numerical simulations confirm the stability criteria established for LI_1^+, LI_3^+, LI_4^+, and AVMR families. Namely, the $\mathrm{LI}_k/\mathrm{ELI}_k^+$ counterparts, such as $\mathrm{YLI}_k/\mathrm{ELI\text{-}UL}_k$ and $\mathrm{BFL}_k/\mathrm{ELI\text{-}FL}_k$, behave equally robust whereas $\mathrm{ELI\text{-}UQ}_k$, but also CLI_k, are much less reliable in the NSE regime. In general, the smaller values of $\alpha^{(u)}(\delta)$ and the convex-interpolation-based coefficients behave more robustly (see also Tables III and V). The LI_k and AVMR steady-state results are independent of $\alpha^{(u)}$ in contrast to the (very small) $\alpha^{(u)}$ dependency in ELI_k^+ and EMR when the mass leakage is present, at least. In particular, the $\mathrm{LI}_3(\alpha^{(u)})$ steady-state solution is $\alpha^{(u)}$-independent, and hence the same with either $\mathrm{LI}_3(\alpha_0^{(u)})$ or IPLI directional stabilizations which obey respectively Eqs. (65) and (50). Indeed, the *p-flow* LI_3^+ with a constant value $\Lambda \in [\frac{1}{8}, \frac{1}{4}]$ gains over all schemes for flow accuracy only in the Stokes and low Reynolds limit $\mathrm{Re} <\approx 5-10$, where its parabolic accuracy is crucial. Hence, the limited LI_3^+ stability in small ν range is not so important.

Then, complementarily to LI_3^+, the *p-pressure* LI_4^+ and *c-nse-p-flow* AVMR/EMR apply robustly at intermediate Re regimes. The LI_1^+ behaves very similar to LI_4^+ when $\Lambda(\mathrm{Re})$ decays and takes very small values. For polynomial grid-rotated channel flow, the LI_4 and AVMR scale $|\partial_t \rho|/\mathcal{U}$ in proportion to $\Lambda \mathrm{Re}_g$ at a fixed $\mathcal{U}$, similarly with the bulk Poiseuille flow solvability condition in Eq. (17b). Hence, when $\mathcal{U}$ is fixed, these schemes make (1) the mass-leakage rate Re_g-independent when Λ varies as ν^{-1} and (2) Re_g-decaying when $\Lambda \propto \nu^{-2}$. Using this last quadratic scaling $\Lambda \propto \mathrm{Re}_g^{-2}$ at a fixed $\mathcal{U}$, the AVMR and EMR-1 − EMR-3 produce a practically Re_g-independent and the smallest amplitude error estimates $E_2(\mathrm{Re}_g)$. Moreover, these scalings tolerate well their stability conditions in Eq. (71) where these families shall select $\Lambda^- < \Lambda^-_{\max}(\alpha^{(u)})$. Since these families are all parametrized, the use of a different value $\mathcal{U}$ will produce the same error estimate at fixed Re_g and $\Lambda(\mathrm{Re}_g)$.

The GI study extends this analysis to the error dependency upon Re when the tangential wall-velocity amplitude $|u_{w'}|$ increases. It is confirmed that the LI_4 and AVMR produce an almost $|u_{w'}|$-independent error-estimate $E_2(u_{x'} - u_{w'})$ and mass-leakage rate $\partial_t \rho$, due to their removal of the NSE term gradient $\beta^{(p)} \partial_q \mathcal{E}_q^{(u)}$ from the closure relation with the *p-pressure* condition in Eq. (35). These results confirm a natural suitability of the LI_4 and AVMR families to the GI property, with no need for any explicit shifting [103] of the $\mathcal{E}_q^{(u)}$ term from the static to moving frame on the static solid surface, at least. These two classes then extend the observed [59] advanced GI property of the MR schemes to more stable implementations, including a single-node LI_4 algorithm.

Further, an extension to the grid-rotated Couette flow in the presence of the wall-normal injection has confirmed the AVMR superiority for both velocity components but only when Re is small, such as $\mathrm{Re} <\approx 10$ in a small channel. Moreover, the $\Lambda \propto \mathrm{Re}_g{}^{-2}$ strategy does not suffice here to make the Re dependency from $E_2(\vec{j})$ and $\partial_t \rho$ vanish. The straight-channel discrete solution in Eq. (79) and the rotated-flow truncation analysis in Eq. (A11) both suggest that the reason for that lies in the bulk approximation where, opposite

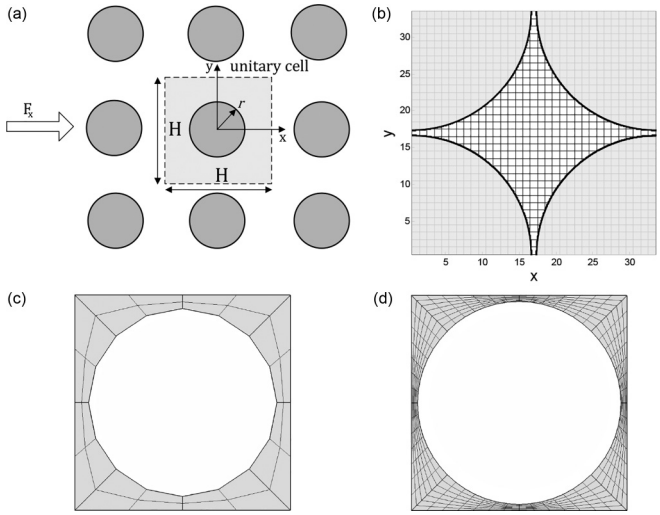

FIG. 29. (a) Unit periodic cell in a square $H \times H$ array of cylinders. (b) solid concentration $c = 0.75$, half-gap length $l \approx 0.376$ l.u, TRT square grid with no element per gap, $n_l = 0$; (c) $c = 0.6$, $l \approx 2.078$ l.u, FEM-G with two elements per gap, $e_l = 2$; (d) $c = 0.7$, FEM-N with total element number $E_l = 288$.

to the parabolic flow, the third- and fourth-order solvability conditions are, first, not exact, and second, they cannot be satisfied simultaneously, although $\Lambda = \frac{1}{12}$ still makes the $u_{x'}$ and $u_{y'}$ corrections vanish, whereas $a_\varepsilon = -k_\varepsilon^{-1}$ improves the $u_{y'}$ and mass conservation equations for the parametrization with the wall-velocity ratio r_{xy}. The boundary schemes demonstrate grid convergence rates consistent with their formal accuracy, e.g., the AVMR converges with second to third order, but these convergence rates decay with Re. Additional work is required to understand the boundary accommodation effect and to reduce the Re-dependent deviations in discrete-exponential solutions.

VII. SIMULATIONS WITH CIRCULAR BOUNDARY

We address the d2q9 Stokes flow permeability measurement in a square array of cylinders in Sec. VII A, and both the Stokes and NSE modeling of the circular Couette flow in Sec. VII B. In addition, we follow a comparative analysis [87,111,112] with respect to the finite element solver COMSOL Multiphysics [113] operating on body-fitted grids (see Fig. 29). We distinguish between (1) FEM-N where the number of elements E_l is approximately equal to the number of TRT fluid nodes N_l and (2) FEM-G where the number of elements e_l per minimal half-gap length l is the same (or larger) than the number of TRT fluid nodes n_l inside the gap: note, n_l and e_l are not equivalent because the TRT boundary cell is partly solid.

A. Stokes flow in an array of cylinders

We consider the force-driven Stokes flow past periodic square array of solid cylinders; it is modeled in a periodic unit cell $H \times H$ as depicted in Fig. 29. A *mean momentum* value $\langle j_\alpha \rangle$ along the forcing direction is evaluated a posteriori; an isotropic permeability value $k = k_\alpha$ is derived with the help of

the Darcy's law: $k = \frac{\langle j_\alpha \rangle \nu}{F_\alpha}$ and compared to the reference value $k_{\rm th}$ using the error estimate $E_k = |k/k_{\rm th} - 1|$. The dimensionless permeability value $k^\star(c) = 4\pi k_{\rm th}/H^2$ is tabulated [59] for solid volume fraction $c \in [0.2, 0.75]$ based on the pioneering works [108–110]. The BB, BFL, BFL-QI, and MR1 are examined [59] for $c \in [0.2, 0.7]$ with $H = \{33, 99\}$ applying $\Lambda = \frac{3}{16}$, $\Lambda^+ = 0.375$, but E_k is viscosity-independent only with BB and MR1. These simulations are extended to cubic and BCC/FCC regular arrays of spheres [17,57] using the parametrized schemes: BB, CLI, MR1, and MCLI [MCLI complements CLI with the Dirichlet-value-based noncentral directional approximation $\gamma^{(u)}\partial_q^2 e_q^-$ [see Eqs.(5.13) and (5.14) in Ref. [57] and Eq. (53) in Ref. [17]] and MCLI delivers the MR1 accuracy level]. The TRT flow simulations around circular obstacles with CLI and MR1/MCLI have been extended to porous Brinkman flow [31,111,112], where the TRT Stokes-Brinkman-Darcy model controls the numerical permeability estimate with Λ.

We consider four volume fractions: $c = \{0.2, 0.6, 0.7, 0.75\}$; the touching limit is $c = \frac{\pi}{4} \approx 0.785$. The TRT is applied with the Stokes equilibrium in Eq. (3); the no-slip condition on the solid surface is prescribed with the five parametrized families: LI_1^+, *p-flow* LI_3^+, *p-pressure* LI_4^+, MR1 and *c-nse-p-flow* AVMR($\alpha^{(u)} = \frac{1}{2}$); Eq. (33) is applied with $I_b = 0$; recall, this choice shifts the optimal BB value $\Lambda = \frac{3}{16}$ to $\Lambda = \frac{1}{8}$ in Eq. (49), and the $k(\Lambda)$ dependency is examined here for $\Lambda \in]\frac{1}{512}, 2]$. Here LI_k^+ is represented by CLI_k but, since there is no mass leakage in these simulations due to the symmetry and linear flow, any LI_k and ELI_k members produce the same error estimate E_k to a given accuracy (typically, when the relative momentum change is less than 10^{-12} per 100 iterations). Recall, an advantage is that $\mathrm{CLI}_0 = \mathrm{CLI}_1$ is naturally parametrized without correction but our subsequent computations suggest that YLI_k/ELI-UL$_k$ and BFL_k/ELI-FL$_k$ converge faster (we apply $F_x = 10^{-3}$ and a large viscosity value $\Lambda^+ = 10$ to accelerate the steady-state convergence). The ELI_k^+ is also preferable for cut links with no upstream fluid neighbor, where LI_k resorts to the help of the previous step solution $\beta f_q(\vec{r}_{\rm b}, t)$ in Eq. (21). The examined boundary schemes do not meet stability or nonconvergence problems in the high-viscosity range, except AVMR when $\Lambda \geqslant 1$: indeed, when increasing Λ, this scheme needs to adjust Λ^- to meet the stability condition in Eq. (71), but even when this condition is satisfied, AVMR is more reliable in the intermediate and very small viscosity ranges.

Figure 30 displays E_k in a dilute array setting $c = 0.2$, resolved with $H = 33$ and $H = 99$ cells per unit edge. The results show that LI_3^+ overpasses MR1 and AVMR for both resolutions in the most suitable interval $\Lambda \leqslant \frac{1}{4}$. In this Λ interval, LI_3^+ also gains one to two orders of magnitude over LI_1^+ and LI_4^+; these two schemes behave in a very similar manner when $\Lambda \leqslant 10^{-2}$ because $\gamma^{(u)}(\hat{K}_1^-) = \alpha^{(u)}\Lambda^-$ approaches zero. These results confirm the principal role of the parabolic velocity term on the boundary accuracy in these simulations. Here and in other examples, we observe that MR1 and *c-nse-p-flow* AVMR behave very similarly when Λ is small and $\gamma^{(p)}|_{\rm MR1} \to 0$. The LI_1^+, LI_3^+ and MR1 show a strong Λ dependency with the suitable optimal $\Lambda \in [\frac{1}{12}, \frac{1}{4}]$ where E_k is minimal; their error ratio between $H = 33$ and $H = 99$ is

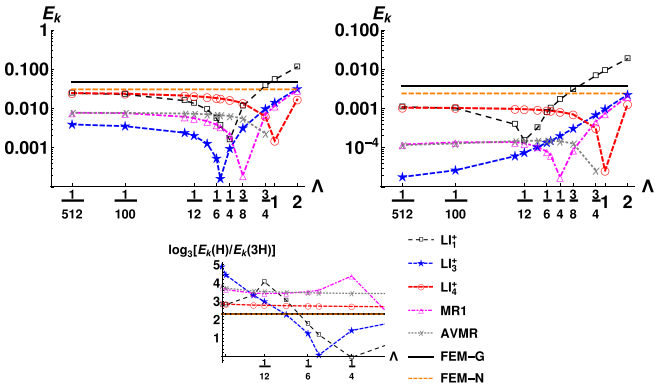

FIG. 30. The relative permeability error E_k when $c = 0.2$, $l \approx 8.17$ l.u., $k_{\rm th} = 0.2439\times10^{-1}$. (Left) $H = 33$, TRT: $N_l = 868$, $n_l = 8$, FEM-N: $E_l = 800$, FEM-G: $e_l = 8$; (right) $H = 99$, TRT: $N_l = 7860$, $n_l = 25$; FEM-N: $E_l = 7688$, FEM-G: $e_l = 25$; (middle) $r = \log_3[\frac{E_k(H)}{E_k(3H)}]$. FEM-N, FEM-G: $E_k(H = 33) \in [3.08, 4.88]\%$, $E_k(H = 99) \in [0.24, 0.37]\%$.

then not monotonous with Λ; when $\Lambda \geqslant \approx 1$, the truncation bulk terms dominate the parabolic boundary error and E_k grows with all schemes, and this half-interval is hence to be avoided. In contrast, LI_4^+ and AVMR show a Λ-independent convergence rate $r = 3$ and $r = 4$, respectively, although these rates are not (necessarily) asymptotic. Except LI_1^+ at large Λ, the TRT overpasses both P1 linear FEM-N and FEM-G in dilute arrays.

Figure 31 shows the results when $c = 0.6$ and the half-gap of $l \approx 2.078$ is resolved with 2 cells both in TRT and FEM-G. In TRT, E_k increases with all schemes; the LI_3^+ now monotonously increases E_k with Λ on the coarse grid and reduces it to the rate $r \approx 3$ on the finer one; the LI_4^+ rate reduces to $r = 2$ but AVMR maintains $r \approx 4$. The FEM-N overcomes TRT but when $H = 33$, all schemes, and especially the *p-flow* schemes, are between FEM-N and FEM-G; when $H = 99$ that is true only with the three *p-flow* schemes provided that $\Lambda < \approx \frac{1}{4}$.

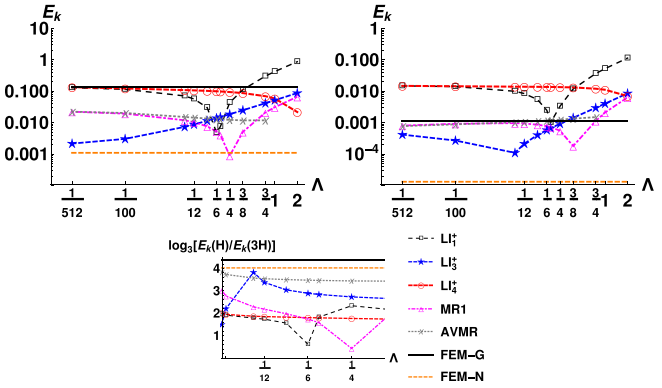

FIG. 31. Similar as in Fig. 30 but $c = 0.6$, $l \approx 2.078$ l.u, $k_{\rm th} = 7.128\times10^{-3}$. (Left) $H = 33$, TRT: $N_l = 432$, $n_l = 2$; FEM-N : $E_l = 392$; FEM-G: $e_l = 2$; (right) $H = 99$, TRT: $N_l = 3924$, $n_l = 7$; FEM-N: $E_l = 4232$; FEM-G: $e_l = 7$; (middle) $r = \log_3[\frac{E_k(H)}{E_k(3H)}]$. FEM-G, FEM-N: $E_k(H = 33) \in [0.11, 13.75]\%$, $E_k(H = 99) \in [0.001, 0.11]\%$.

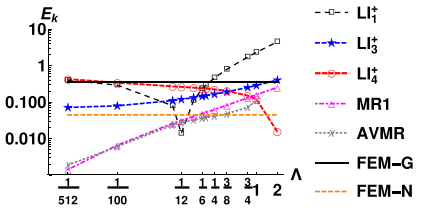

FIG. 32. Similar as in Figs. 30 and 31 but $H = 33$, $c = 0.7$, $l \approx 0.923$ l.u., $k_{\rm th} = 9.295\times10^{-4}$. TRT: $N_l = 328$, $n_l = 1$; FEM-N: $E_l = 288$; $E_k = 4.5\%$; FEM-G: $e_l = 2$, $E_k \approx 35.5\%$.

Figure 32 displays the results when $c = 0.7$ and the half-gap length $l = 0.92$ l.u becomes less than one fluid cell; the TRT resolves it with one grid node, $n_l = 1$, where the MR1 and AVMR are switched to CLI$_3$ using the previous step solution for $\beta f_q(\vec{r}_{\rm b}, t)$ or, simpler, to ELI-UQ$_3$. Since there no mass leakage in these simulations, all LI$_3^+$ substitutions produce the same steady state. The FEM-G needs here at least two elements per gap, $e_l = 2$, to produce nonzero velocity field. All directional schemes then increase E_k with Λ on the coarse grid except LI$_1^+$, which continues to display the optimal and most accurate solution when $\Lambda \in [\frac{1}{12}, \frac{1}{6}]$. As has been suggested, LI$_3^+$ loses the advantage over AVMR and MR1 in the presence of stronger local pressure gradients in the vicinity of the small flow aperture. The two parabolic schemes overpass both FEM-N and FEM-G when $\Lambda < \frac{1}{12}$; otherwise all schemes find their results in between, except for LI$_1^+$ with large Λ, similarly as in the two previous examples.

Figure 33 displays results when the solid fraction reaches $c = 0.75$ and the half-gap length reduces to $l = 0.376$ l.u, so that no TRT node is located inside the minimal gap, $n_l = 0$. The TRT numerical solution remains nevertheless consistent because all surrounding nodes properly account for the solid body position through their cut links. The FEM-G applies again with a finer resolution $e_l = 2$ but the TRT overpasses both FEM-N and FEM-G with LI$_4^+$, MR1 and AVMR in the most suitable interval $\Lambda \in [\frac{1}{12}, \frac{1}{4}]$. This result is interesting because LI$_4^+$, which removes the pressure gradient term $\beta^{(p)}\partial_q e_q^+$ from the closure relation, then competes with the parabolic schemes, whereas LI$_3^+$ behaves less accurately.

Figure 34 displays the pressure distribution $P - \bar{P}$, $\bar{P} = c_s^2\bar{\rho}$ (here $\bar{\rho} = \rho_0$ due to the mass conservation) on the symmetry axis inside the gap for the two fractions, $c = 0.6$ and $c = 0.75$. When $c = 0.6$, there are two nodes per half-gap and the displayed antisymmetric periodic pressure profile is

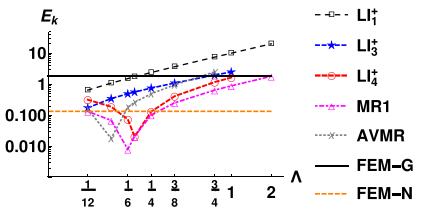

FIG. 33. Similar as in Figs. 30 and 32 but $c = 0.75$, $H = 33$, $l \approx 0.34$ l.u, $k_{\rm th} = 9.95\times10^{-5}$ [59]. TRT: $N_l = 284$, no one fluid node per gap, $n_l = 0$; FEM-N: $E_l = 288$, $E_k = 13.58$; FEM-G: $e_l = 2$, $E_k = 191.3\%$.

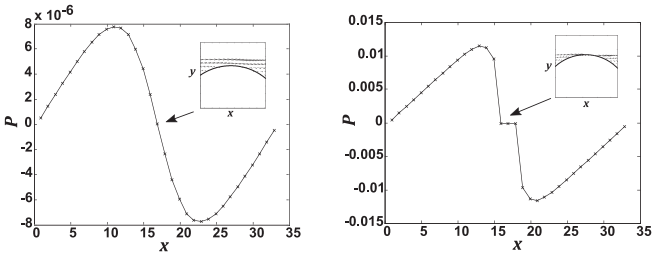

FIG. 34. The AVMR pressure distribution on the symmetry axis inside the gap, $c = 0.6$ (left) and $c = 0.75$ (right). Data: $H = 33$, $F_x = 10^{-3}$. See permeability error estimate in Figs. 31 and 33.

continuous, its maximum amplitude is about 8×10^{-6}. When $c = 0.75$, since there are no fluid nodes inside the gap, the zero pressure value is formally output in the three central nodes; the surrounding pressure variation is of order 10^{-2}. Hence, these numerical results confirm that the pressure gradient grows over about four orders and then the parabolic closure term $\beta^{(p)}\partial_q e_q^+$ prevails over the parabolic momentum term $\gamma^{(u)}\partial_q^2 e_q^-$. This explains why LI$_4$ shows a very similar accuracy to MR1 and AVMR, whereas LI$_3$ behaves less accurately.

To sum up, the parametrized linearly accurate family LI$_1^+$ is the least accurate with the small or large Λ but it holds its optimal values in the most suitable interval $\Lambda \in [\frac{1}{12}, \frac{1}{4}]$, in agreement with the previous studies. The *p-flow* LI$_3^+$ proves its advanced accuracy over all other schemes, including the formally more accurate two-node MR1 and AVMR when $\Lambda \leqslant \approx\frac{1}{6}$ (see $c = 0.2$ and $c = 0.6$). When $c = 0.7$ and the smallest gap is resolved with one node, MR1 and AVMR gain over LI$_3^+$ within the whole Λ interval. The same two schemes but also the LI$_4^+$ are the most accurate when $c = 0.75$, i.e when there is no TRT fluid node in the smallest gap. These results suggest that LI$_3^+$ efficiently replaces the two node parabolic VMR($\alpha^{(u)}, \hat{K}^{\pm}$) except when the solid walls are almost in touch. In such a case, LI$_4^+$ might appear to be preferable because the strong surrounding pressure drop dominates the boundary accuracy. Another attractive property of LI$_3$ and AVMR is that their convergence rate is mostly Λ-independent. All in all, the directional boundary rules show an advantage over the body fitted grids when close to realistic overlapping situations.

B. Circular Couette flow

The circumferential (tangential) radial velocity $u_\theta(r)$ of an incompressible fluid in the gap between two infinitely long concentric cylinders, "inner" (1) and "outer" (2), with at least one rotating, obeys [114]

$$u_\theta(r) = ar + br^{-1}, \quad u_\theta|_{r=R_1} = \Omega_1 r, \quad u_\theta|_{r=R_2} = \Omega_2 r,$$
$$a = \frac{R_1^2\Omega_1 - R_2^2\Omega_2}{R_1^2 - R_2^2}, \quad b = \frac{R_1^2R_2^2(\Omega_2 - \Omega_1)}{R_1^2 - R_2^2}. \tag{81}$$

Figure 35 examines the tangential momentum $j_\theta(r) = \rho_0 u_\theta(r)$ in the two configurations using the Stokes equilibrium: (1) the outer cylinder rotates and the inner one is at rest and (2) vice versa. The computations are conducted with the five parametrized boundary schemes: CLI$_1$, CLI$_3$, CLI$_4$ represent LI$_1^+$, LI$_3^+$ and LI$_4^+$, respectively, against the two parabolic

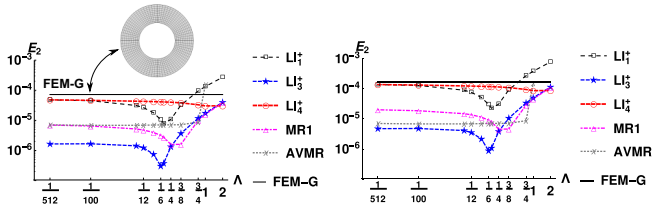

FIG. 35. The $E_2(j_\theta)$ with respect to Eq. (81) in circular Stokes Couette flow $j_\theta = \rho_0 u_\theta$, $\rho_0 = 1$, $\nu = \frac{3}{2}$. The FEM-G applies with $n_l = 10$ elements per gap between the inner cylinder $R_1 = 10$ l.u. and the outer cylinder $R_2 = 20$ l.u. Left: $\Omega_1 = 0$, $\Omega_2 = 10^{-3}\nu/R_2^2$; $E_2(\text{FEM-G}) = 7.22\times10^{-5}$; right: $\Omega_1 = 10^{-3}\nu/R_1^2$, $\Omega_2 = 0$, $E_2(\text{FEM-G}) = 1.69\times10^{-4}$.

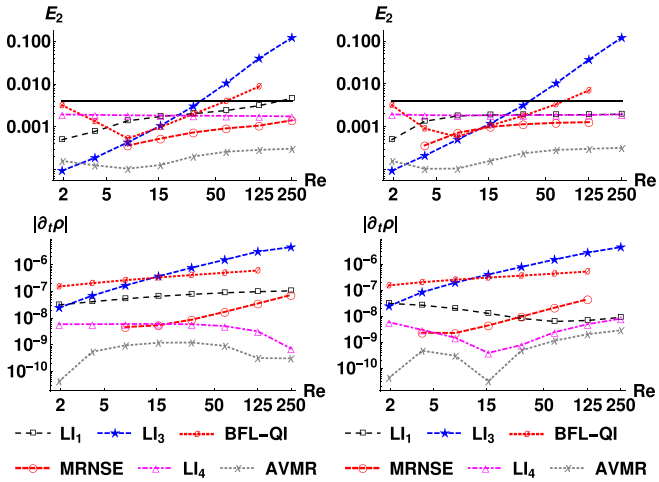

FIG. 36. The $E_2(j_\theta)$ with respect to Eq. (81) (top) and $|\partial_t\rho|$ (bottom) in circular Couette NSE flow. Left: linear decay $\Lambda_n(\text{Re}_n) = 2^{-n}\Lambda_0$. Right: square decay $\Lambda_n(\text{Re}_n) = 4^{-n}\Lambda_0$, $\Lambda_0 = \frac{1}{4}$. Data: $\text{Re}_n = 2^n\text{Re}_0 \in [1.95, 249.6]$, $n \in [0, 8]$, $\text{Re}_n = \frac{u_0 H}{\nu_n}$, $u_0 = 0.05$, $\nu_n = 2^{-n}\nu_0$, $\nu_0 = \frac{2}{3}$, $R_1 = 26$, $R_2 = 52$, $H = R_2 - R_1 = 26$, $\Omega_1 = u_0/R_1$, $\Omega_2 = 0$. The FEM-G: $E_2(\text{P1},\text{P1}) \approx 4\times10^{-3}$ (solid black on top diagrams). $E_2(\text{P2},\text{P1}) \approx 2.6\times10^{-4}$ and $E_2(\text{P2},\text{P2}) = 1.48\times10^{-7}$ using the linear (P1) and parabolic (P2) elements for velocity (first argument) and pressure (second argument).

schemes, MR1 and AVMR($\alpha^{(u)} = \frac{1}{2}$). In theory, the Stokes equation is then satisfied with a uniform pressure distribution $P(r) = p_0$. This condition is verified numerically: the density distribution is uniform and there is no mass leakage in the Stokes computations due to symmetry, the stationary solutions are then the same within a given class LI_k^+. Due to parametrization, $E_2(j_\theta)$ with respect to Eq. (81) is independent of Λ^+, and it is examined along $\Lambda \in [\frac{1}{512}, 2]$. The TRT results are also compared with the FEM-G simulations on body-fitted grid also using 10 elements along the radius between cylinders.

The error behavior is very similar between the two boundary configurations, although with a slightly larger error when the inner cylinder rotates, in both TRT and FEM, most likely because of the coarser resolution over the sharper velocity gradient. All schemes behave very similarly to the Stokes flow through a dilute array of cylinders in Fig. 31, where the open gap is about 8 l.u. The $\hat{K}_1^-$ and $\hat{K}_3^-$ clearly display the optimal precision around $\Lambda = \frac{1}{6}$; this particular value makes the fourth-order bulk (diffusion) error vanish. In turn, MR1 shifts its minimum error to larger Λ. The LI_4^+ and AVMR are almost Λ-independent, and in agreement with the predictions and other results, LI_4^+ and LI_1^+ behave very similarly at very small Λ, whereas MR1 displays the same property with respect to AVMR; AVMR($\alpha^{(u)} = \frac{1}{2}$) is typically unstable for the largest value $\Lambda = 2$ where it approaches its stability bound in Eq. (71). Remarkably, LI_3^+ gains over MR1 and AVMR as in the case of the dilute arrays in Fig. 31 and all TRT schemes gain over FEM, except LI_1^+ for unsuitable large Λ interval.

We consider now the standard NSE equilibrium in Eq. (3a). In theory, the NSE inertial term with velocity profile in Eq. (81) is exactly balanced by radial pressure gradient:

$$\partial_r P = \frac{\rho_0 u_\theta^2}{r}, \quad P(r) = p_0 + \frac{a^2 r^2}{2} + 2ab\log r - \frac{b^2}{2r^2}. \quad (82)$$

The "solid rotation" $\Omega_1 = \Omega_2$ ($b = 0$) is described by the linear profile $u_\theta = ar$ and parabolic pressure distribution $P(r)$ in Eq. (82). This solution is exact with all examined schemes, including the BB, because in this case $\vec{u}\cdot\vec{c}_q$, and so $e_q^\pm(x, y) = e_q^\pm(x + c_{qx}, y + c_{qy})$, is the same along any discrete velocity link, and hence $\hat{n}_q^\pm = 0$ (see Appendix A [58]). Otherwise, in our computations with $\Omega_1 \neq \Omega_2$, distinguished points are that the pressure (density) is not uniform and the space-time uniform mass leakage $\partial_t\rho$ in Eq. (11) accommodates the global mass conservation, such as when the NSE term causes this effect to happen even in a symmetric grid-inclined channel. Here we examine $E_2(j_\theta)$ and the mass leakage rate $|\partial_t\rho|$ when the Reynolds number $\text{Re}_n = 2^n\text{Re}_0$ varies between 2 and 250, whereas Λ_n reduces (1) linearly and (2) quadratically with Re_n. Figure 36 compares the two metrics for the five parametrized schemes: LI_1, the *p-flow* LI_3/IPLI, the *p-pressure* LI_4, the *c-nse-p-flow* AVMR and the *p-nse-flow* MR_{nse}; the LI_k is represented by YLI_k; YLI_3 is directionally switched either to $\text{LI}_3(\alpha_0^{(u)})$ according to Eq. (65) when $\Lambda(\text{Re}_n)$ becomes small (1) with the linear strategy ($n \geqslant 5$) or (2) the quadratic strategy ($n \geqslant 4$), or to IPLI in the limit $\Lambda \to 0$ ($n \geqslant 7$) according to Eq. (50).

All these schemes fix E_2 with Re_n and Λ_n for a given resolution. The BFL-QI results are also reported but, since this scheme is not parametrized, E_2 depends upon ν at fixed Re_n and Λ_n. The LI_3 shows the smallest $E_2(j_\theta)$ in the Stokes limit, but it grows $E_2(j_\theta)$ linearly with Re_n, almost independently of Λ_n. The LI_1 also increases $E_2(j_\theta)$ linearly with Re_n but using only the linear $\Lambda_n(\text{Re}_n)$ scaling, otherwise it approaches LI_4 as Re_n increases and $\Lambda_n(\text{Re}_n)$ becomes very small (quadratic scaling); but the LI_4 shows the smaller mass leakage. The BFL-QI increases its momentum error with Re_n and behaves less stably than other schemes in the two limits of the Λ_n interval. Although MR_{nse} is exact in the NSE inclined channels, it shows here less accurate results than AVMR, but their $E_2(\text{Re})$ dependencies show a similar shape. The MR_{nse} meets difficulties approaching its stability condition $\Lambda^+ > 2\Lambda$ in Table VII, but only when Λ_n is relatively large, such as $n = 0, 1$.

Figure 36 shows that the LI_3, BFL-QI and MR_{nse} increase $|\partial_t\rho|$ with Re_n using the two $\Lambda_n(\text{Re}_n)$ scalings, but LI_1 (quadratic scaling) reduces it with Re_n. In contrast, LI_4 and AVMR produce the two metrics which are almost

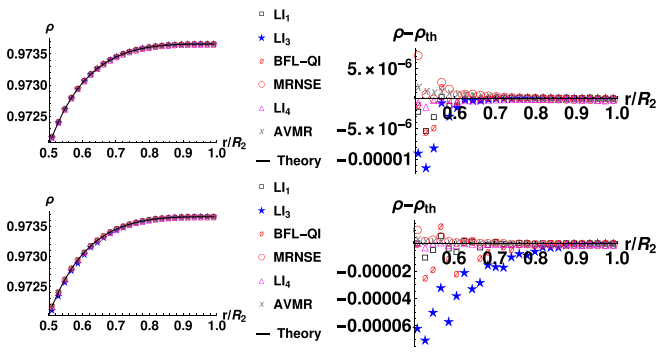

FIG. 37. The NSE solution for the density distribution (left) and difference with the analytical solution (right) vs r/R_2 when the inner cylinder $R_1 = \frac{1}{2}R_2 = 26$ rotates with $\Omega_1 = u_0/R_1$ and the outer is in rest, in the case of linear Λ scale in Fig. 36. Top: Re = 15.6, $n = 3$, $E_2(\rho_{\rm th}) = 10^{-6}\times\{1.39, 3.44, 1.58, 1.67, 0.315, 0.746\}$ following the order of the schemes presented in legend. Bottom: Re = 124.8, $n = 6$, $E_2(\rho_{\rm th}) = 10^{-6}\times\{3.09, 28.9, 8.95, 2.76, 0.702, 1.38\}$. Analytical density distribution corresponds to Eq. (82), $\rho_{\rm th}(r) = c_s^{-2}P_{\rm th}(r) + 1$; the center (0,0) is the common point of four central cells; the profiles are output along a coordinate axis, and all are fixed to the same ρ value at $r = \sqrt{0.5^2 + (R_2 - 0.5)^2} = 51.5024$.

Re-independent with the two strategies; the linear scaling produces a smoother behavior. Curiously, the linear-element-based body-fitted FEM-G shows a worse accuracy for the same discretization level, but it produces similar with the AVMR momentum error estimate using a (parabolic) P2 approximation of the velocity field, and slightly overpasses AVMR when the P2 discretization is used for both, pressure and velocity, variables.

Figure 37 compares the density distribution $\rho(r)$ to its prediction $\rho_{\rm th}(r) = c_s^{-2}P_{\rm th}(r)$ in Eq. (82) when Re = 15.6 and Re = 124.8 prescribing the same Ω_1 and Ω_2 in two cases, and hence the same solution $\rho_{\rm th}(r)$. On the whole, all schemes reproduce correctly $\rho_{\rm th}(r)$ but LI_3 rapidly increases its deviation from the prediction in the vicinity of the rotated cylinder, at least inversely with ν in agreement with $\beta^{(p)}\partial_q e_q^+$ scaling in Eq. (75a). In the case of these two Reynolds numbers, the mass leakage in Fig. 36 is the largest with the LI_3 and BFL-QI, and the smallest with LI_4 and AVMR, and the pressure deviation in Fig. 37 follows the same trend. Noticeably, the LI_4 delivers the best, twice smaller pressure error estimates than AVMR, although its momentum accuracy is worse than that of MR_{nse} and AVMR, and the mass leakage is larger than that with AVMR. The LI_1 is expected to behave like the LI_4 using the quadratic scaling $\Lambda \propto \nu^2$ when Λ becomes rapidly very small.

To sum up, the established momentum and density solutions of $\mathrm{LI}_k(\alpha^{(u)})$ and $\mathrm{AVMR}(\alpha^{(u)})$ are $\alpha^{(u)}$-independent; the higher $\alpha^{(u)}$ values converge faster. The single-node LI_4^+ and the two-node AVMR are the most suitable schemes to reduce the momentum and pressure error dependencies upon Re with the help of the specific, e.g., linear reduction of Λ with Re. The AVMR shows a one order magnitude smaller momentum error and the smallest mass-leakage, but LI_4 is even more accurate with respect to sharp radial pressure gradient in the vicinity of the rotated cylinder.

VIII. CONCLUDING DISCUSSION

We developed a unified analysis of directional Dirichlet boundary rules for Stokes and Navier-Stokes fluid flow, and applied it to the construction of a two- or three-population single-node LI^+ and a three- or five-population two-node EMR, which are suitable to describe grid-aligned or grid-rotated flat surfaces and curved walls. The two infinite-member classes operate with four freely selected functions: (1) $\alpha^{(u)}(\delta)$, which scales their directional Taylor closure approximation; (2) $\alpha^{(p)}(\delta)$, which sums the population coefficients subtracting 1; and (3) $\hat{K}^{\pm}$ coefficients of the local correction $\hat{K}^{\pm}\hat{n}_q^{\pm}$. All in all, we have shown that each commonly neglected closure term features a specific macroscopic characteristic, such as the curvature in the creeping flow, the pressure gradient and NSE equilibrium term gradient in the inertial flow; the closure relations become force-independent including the forcing term equally into the bulk and Dirichlet momentum equilibrium.

The three parametrized LI^+ subclasses are distinguished by $\hat{K}_k^-$: (1) LI_1^+, (2) the *p-flow* LI_3^+, and (3) the *p-pressure* LI_4^+; each subclass is then specified for (1) single-node three-population $\mathrm{LI}_k(\alpha^{(u)})$ with $\alpha^{(p)} = \hat{K}^+ = 0$ and (2) local-single-node two-population ELI_k^+ giving $K_{ELI}^+(\alpha^{(u)}, \alpha^{(p)}, \Lambda^+)$. The ELI_k^+ can be implemented very efficiently via a modified TRT postcollision, such as $\mathrm{ELI}_k^+ - \mathrm{UL}$ which operates with all zero population coefficients and applies most simply in any singular geometry. In turn, the *c-nse-p-flow* accurate EMR combines and extends the three LI_k^+ features, and it is specified by $\mathrm{AVMR}(\alpha^{(u)})$ family with $\alpha^{(p)} = \hat{K}^+ = 0$ and the three EMR subfamilies with only three nonzero population coefficients.

Typically, the stability improves when $\alpha^{(u)} \to 0$; however, very small $\alpha^{(u)}$ values worsen the transient accuracy and slow the convergence towards steady state. Our single-node linear symmetric-mode stability condition restricts $\alpha^{(u)}(\delta)$ to a viscosity-independent interval $]0, \delta^{-1}]$; this criterion is satisfied by the convex interpolations, such as BFL, YLI, and SSN, and their counterparts ELI-FL, ELI-UL, and ELI-ULT but also LLI and more generally $\mathrm{ZLI}(\alpha^{(u)})$ and $\mathrm{CHLI}(\alpha^{(u)})$ families. This unfortunately is not the case for the naturally parametrized but less stable "central" rules, such as CLI and CELI-UQ, where the population coefficients lie inside the interval $[-1, 1]$. At the same time, this last semiheuristic condition constrains rather reliably the suitable range $\Lambda^-(\alpha^{(u)})$ within AVMR/EMR, which tolerates well the $\Lambda(\mathrm{Re}_g)$ reduction with the kinematic viscosity, thus making their solutions the least Re-dependent. In contrast, the second nonequilibrium *antisymmetric mode* stability criterion restricts the low-viscosity range with the *p-flow* LI_3^+ where, complementary, its IPLI/CELI-IP members with $\hat{K}^- = 0$ help to stabilize the individual links. However, since it appears that the LI_3^+ shall be restricted to creeping flow, its low-viscosity stability constraint is not as penalizing.

The construction of the $\mathrm{FH}_3/\mathrm{MLS}_3$ counterparts of LI_3, not obeying the MR linear population combination, illustrates a more general closure formalism in the spirit of the S-TRT solver [69]. However, in contrast to the parabolic two-node schemes, they remain unparametrized in a general flow, and the same happens with the quadratic interpolation counterpart $\mathrm{BFL\text{-}QI}_3$ and their *p-pressure* corrections. Concerning the

extension to other collisions, first, all schemes apply easier with $\alpha^{(p)}=0$. Second, since the BGK/TRT/MRT and the regularized models give the same rate $\tau^-=\Lambda^-+\frac{1}{2}$ for all antisymmetric modes, the TRT boundary schemes adapt easier multiple symmetric rates when $\hat{K}^+=0$ and $\hat{K}^-(\alpha^{(u)},\Lambda^-)$ is Λ^+-independent; the LI_1, LI_4, and AVMR obey these three properties, where their steady-state momentum solutions are $\alpha^{(u)}$-independent due to two first conditions. On the other hand, those boundary algorithms which do not necessarily respect these conditions, like the original LLI and ELI, apply more easily in their undecomposed "population-based" forms beyond the TRT collision.

We have also shown that no scheme supports exactly the self-similarity of the analytical channel profiles *during the transient stage*. Also, although we have provided the formal time stepping estimate for the Dirichlet time-dependent boundary values, these predictions have not yet been explored but it is to notice that the nonequilibrium corrections destined for steady state might slightly worsen the transient behavior.

All in all, at steady state, the *p-flow* LI_3^+ reveals an improved accuracy in a porous array of cylindrical obstacles and circular Couette flow, where LI_3^+ overpasses all other schemes close to the Stokes limit. Alternatively, since the LI_4^+ relaxes the pressure and inertial gradients from its closure relation, it demonstrates its better suitability when these terms dominate the parabolic accuracy, such as in the most narrow gaps and increasing the Reynolds number. In turn, the AVMR not only combines the LI_3^+ and LI_4^+ accuracy but also liberates the Dirichlet closure from the second-order gradients of the pressure and inertial equilibrium terms; this family then enables an excellent (exact) benchmarking of a grid-rotated Couette NSE flow and largely overpass all other schemes in the grid-rotated Poiseuille NSE flow.

In the Stokes flow around circular obstacles, for both dilute and condensed porous configurations, all these parametrized schemes are more accurate than the body-fitted linear FEM under similar discretization levels. Moreover, the LBM is able to solve the touching limit due to its link-based neighborhood solid description, whereas FEM needs to "physically" discretize the interior flow path inside the minimal gaps. However, it shall be noted the good FEM convergence for an intermediate solid concentration, whereas the LBM convergence is Λ-dependent on the relatively coarse grids in agreement with the previous studies [17]; here the LI_4^+ and AVMR show the fastest and Λ-independent rates.

Switching to the inertial regime, we have first demonstrated that the simplest grid-rotated Poiseuille profile satisfies the bulk solvability conditions in a constant density field only when $\Lambda=\frac{1}{12}$ and, additionally, the standard incompressible NSE quadratic-velocity term [81] gets modified with the fourth-order projection $-\frac{||\vec{j}||^2}{\rho_0}a_\varepsilon\varepsilon_q$ giving a particular value $a_\varepsilon=-k_\varepsilon^{-1}$. Otherwise, *an unexpected* parabolic pressure distribution $\rho(y')$ adjusts the linear truncation dependency over y' in the wall-normal momentum equation, and when $a_\varepsilon\neq -k_\varepsilon^{-1}$, mass-conservation equation needs a space-time uniform density update, where $\mathcal{U}^{-1}\partial_t\rho$ scales in proportion to $\Lambda\mathrm{Re}_g h^{-4}$.

Indeed, in the NSE channel flow, all boundary schemes face the momentum error increase with Re_g when Λ and grid are fixed. However, the original interpolations and LI_1^+ delay this effect up to $\mathrm{Re}>\approx 50-100$ because their lack of parabolic momentum accuracy prevails over the inertial terms in slower regimes. In contrast, the LI_4^+ and parabolic VMR families follow the grid-rotated Poiseuille NSE flow truncation scale and then achieve a Re_g-independent mass-leakage rate, or even a Re_g-decaying behavior, when Λ reduces with Re_g linearly or quadratically, respectively; their momentum error-estimate then becomes Re_g-insensitive both in inclined channels and circular flows subject to the tangential wall motion.

Next, the truncation analysis of the grid-rotated Couette NSE flow subject to wall-normal injection reveals a much faster truncation Re dependency. Accordingly, the AVMR starts with much smaller errors than all other schemes in creeping flow regimes but it increases its error estimate much faster and joins them when the Reynolds number reaches some h-dependent critical value, similar to *p-flow* schemes in grid-rotated Poiseuille NSE flow at fixed Λ. We suggest that the boundary-scheme-independent accuracy level is principally defined by the discrete-exponential bulk and boundary accommodation modes [29], thus indicating that the higher Re range requires a finer resolution.

Concerning the Galilean invariance (GI) property, on the one side, it is reported [83] that, by using the "Galilean-invariant" momentum exchange [105] and the second-order refill, both CLI and PSM are more reliable than MR1 in terms of stability. On the other hand, the study [82] of the fluid-solid techniques for vortex-induced vibrations gives a preference to YLI over CLI for the Galilean invariance, and YLI over PSM at higher resolutions. This work explains why YLI is more stable than CLI, and shows that other LI_k^+ members, e.g., corresponding to convex interpolations or smaller Taylor prefactors $\alpha^{(u)}$, may become even more advantageous for that; moreover, the *p-pressure* LI_4 class clearly shows the best GI property among the single-node schemes. Further, AVMR surpasses the original MR1 scheme in stability and accuracy for finite Reynolds number simulations, also better respecting the GI property than single-node schemes on a static surface. We believe that these improved schemes, combined with the body-fitted reconstruction and momentum-exchange algorithms of equivalent accuracy will inspire fruitful moving surface and adaptive refinement techniques.

ACKNOWLEDGMENTS

The authors are grateful to the anonymous Reviewer for interesting questions. Goncalo Silva thanks the support of FCT, through IDMEC, under LAETA, project UIDB/50022/2020.

APPENDIX A: THE FOURTH-ORDER ANALYSIS

The fourth-order accurate Chapman-Enskog steady-state expansion around the equilibrium expresses the postcollision solution $\hat{n}_q^\pm=-n_q^\pm/\tau^\pm$ in Eq. (1) through the directional equilibrium gradients for $q\neq 0$:

$$\hat{n}_q^\pm=\partial_q e_q^\mp-\Lambda^\mp\partial_q^2 e_q^\pm+\left(\Lambda-\frac{1}{12}\right)\partial_q^3 e_q^\mp$$
$$-\Lambda^\mp\left(\Lambda-\frac{1}{6}\right)\partial_q^4 e_q^\pm,$$

where

$$-\Lambda^{\mp}=\frac{1}{2}-\tau^{\mp},\quad \Lambda-\frac{1}{12}=\frac{1}{6}-\frac{\tau^{\mp}}{2}+\Lambda^{\mp}\tau^{\pm},$$
$$-\Lambda^{\mp}\left(\Lambda-\frac{1}{6}\right)=\frac{1}{24}-\frac{\tau^{\mp}}{6}+\frac{\tau^{\pm}\Lambda^{\mp}}{2}-\tau^{\mp}\left(\Lambda-\frac{1}{12}\right). \tag{A1}$$

In principle, the steady-state solution shall produce $\hat{n}_0^+=0$. The two values, $\Lambda=\frac{1}{12}$ and $\Lambda=\frac{1}{6}$, make vanish, respectively, the TRT third- and fourth-order spatial errors for any equilibrium.

1. The *p-nse-flow* solvability conditions

The Poiseuille momentum profile obeying Eq. (15) is the exact bulk solution of the TRT grid-inclined system for Stokes equilibrium and constant density field. We derive its solvability conditions in Eqs. (16) and (17) in the presence of the nonzero NSE term in Eqs. (3a) and (3b). This analysis extends the solvability conditions [87] to the standard equilibrium and numerical validation with the help of our MR_{nse} Dirichlet boundary family.

We assume a channel profile $j_{x'}(y')$ that obeys Eq. (15) in a grid-rotated channel (x',y'), and either a constant, linear, or parabolic density distribution $\rho(y')$. Giving the discrete-velocity set $\{c_{q,x'}=\cos(\varphi)c_{qx}+\sin(\varphi)c_{qy},\ c_{q,y'}=\cos(\varphi)c_{qy}-\sin(\varphi)c_{qx}\}$, the inertial term $I_{nse}\mathcal{E}_q^{(u)}(y')$ becomes in Eq. (3b):

$$\mathcal{E}_q^{(u)}(y')=-\frac{j_{x'}^2(y')}{2\rho_0}\zeta_q,\quad \zeta_q=2a_\varepsilon\varepsilon_q+t_q^\star\left(1-3c_{q,x'}^2\right). \tag{A2}$$

Since a directional gradient $\partial_q^n e_q^{\pm}=(\partial_{x'}e_q^{\pm}c_{q,x'}+\partial_{y'}e_q^{\pm}c_{q,y'})^n$ reduces to $\partial_q^n e_q^{\pm}=(\partial_{y'}e_q^{\pm}c_{q,y'})^n$, Eq. (A1) then predicts the following nonequilibrium solution $n_q^{\pm}=-\tau^{\pm}\hat{n}_q^{\pm}$:

$$n_q^+(y')=-\tau^+t_q^\star\partial_{y'}j_{x'}(y')c_{q,x'}c_{q,y'} \tag{A3a}$$
$$-\frac{I_{nse}\tau^+\Lambda^-}{2\rho_0}\left[\partial_{y'}^2j_{x'}^2(y')\right]\zeta_q c_{q,y'}^2 \tag{A3b}$$
$$+\tau^+t_q^\star\Lambda^-c_s^2\partial_{y'}^2\rho(y')c_{q,y'}^2+T_q^{+(4)}(y'), \tag{A3c}$$
$$T_q^{+(4)}(y')=\frac{I_{nse}\tau^+\Lambda^-}{2\rho_0}\left(\Lambda-\frac{1}{6}\right)\left[\partial_{y'}^4j_{x'}^2(y')\right]\zeta_q c_{q,y'}^4, \tag{A3d}$$

and, accordingly,

$$n_q^-(y')=-\tau^-t_q^\star\left(c_s^2\partial_{y'}\rho c_{q,y'}-\Lambda^+\partial_{y'}^2j_{x'}c_{q,x'}c_{q,y'}^2\right) \tag{A4a}$$
$$+\frac{I_{nse}\tau^-}{2\rho_0}\partial_{y'}j_{x'}^2(y')\zeta_q c_{q,y'}+T_q^{-(3)}(y'), \tag{A4b}$$
$$T_q^{-(3)}=\frac{I_{nse}\tau^-}{2\rho_0}\left(\Lambda-\frac{1}{12}\right)\left[\partial_{y'}^3j_{x'}^2(y')\right]\zeta_q c_{q,y'}^3. \tag{A4c}$$

The Stokes equilibrium is expressed with Eqs. (A3a) and (A4a); the Couette NSE flow complements it with Eqs. (A3b) and (A4b). The pressure-gradient term in Eq. (A4a) corresponds in principle to the pressure-driven flow, and it is expected to vanish in a force-driven channel flow. However, we will see that *the parabolic pressure distribution* in Eqs. (A4a) and (A3c) ensures the solvability condition in grid-rotated Poiseuille NSE flow. The momentum equations in Eq. (6b) read

$$2\sum_{q=1}^{Q_m/2}\hat{n}_q^-c_{q,y'}=0,\quad 2\sum_{q=1}^{Q_m/2}\hat{n}_q^-c_{q,x'}=F_{x'}. \tag{A5}$$

Plugging Eq. (A4) into Eq. (A5), and summing Eq. (A3) in Eq. (6a), the corrective terms $E_{x'}(y')$ and $E_{y'}(y')$ in the l.h.s. of the x' and y' momentum equations, and a uniform l.h.s. contribution E_m in the mass-conservation equation, read, respectively, giving $j_{x'}=\rho_0u_{x'}$:

$$E_{x'}(y')=2\sum_{q=1}^{Q_m/2}T_q^{-(3)}c_{q,x'}=18I_{nse}\rho_0\left(\Lambda-\frac{1}{12}\right)a_\varepsilon$$
$$\times\sin(4\varphi)\partial_{y'}u_{x'}\partial_{y'}^2u_{x'}, \tag{A6a}$$
$$E_{y'}(y')=2\sum_{q=1}^{Q_m/2}T_q^{-(3)}c_{q,y'}=-\frac{3I_{nse}\rho_0}{2}\left(\Lambda-\frac{1}{12}\right)(1+k_\varepsilon a_\varepsilon)$$
$$\times\sin^2(2\varphi)\partial_{y'}u_{x'}\partial_{y'}^2u_{x'}, \tag{A6b}$$
$$E_m=2\sum_{q=1}^{Q_m/2}T_q^{+(4)}=\frac{3I_{nse}\Lambda^-\rho_0}{2}\left(\Lambda-\frac{1}{6}\right)(1+k_\varepsilon a_\varepsilon)$$
$$\times\sin^2(2\varphi)(\partial_{y'}^2u_{x'})^2. \tag{A6c}$$

These expressions are derived with the help of the (first) relation in Eq. (4) and the auxiliary relations in Eq. (A10); here it is considered that $\partial_{y'}^k u_{x'}(y')=0$ for $k\geqslant 3$ due to parabolic profile $u_{x'}(y')=j_{x'}(y')/\rho_0$. The corrections in Eqs. (A6a)–(A6c) all vanish for (1) Stokes flow ($I_{nse}=0$), (2) *c-nse-p-flow* ($\partial_{y'}^2j_{x'}=0$), but also (3) straight Poiseuille NSE flow ($\sin[2\varphi]=0$). Giving adimensional variables $t'=t/T$ with $T=h/\mathcal{U}$, $X'=x'/h$ and $Y'=y'/h$, we multiply the mass and momentum conservation equations by T and T/U, respectively; Eqs. (A6a)–(A6c) give then the following dimensionless corrections into the l.h.s. of conservation equations:

$$E'_{X'}(Y')=\frac{2592I_{nse}\left(\Lambda-\frac{1}{12}\right)a_\varepsilon\sin(4\varphi)\rho_0Y'}{h^2}, \tag{A7a}$$
$$E'_{Y'}(Y')=-\frac{216I_{nse}\left(\Lambda-\frac{1}{12}\right)(1+k_\varepsilon a_\varepsilon)\sin^2(2\varphi)\rho_0Y'}{h^2}, \tag{A7b}$$
$$E'_m=\frac{72I_{nse}\left(\Lambda-\frac{1}{6}\right)\Lambda\mathrm{Re}(1+k_\varepsilon a_\varepsilon)\sin^2(2\varphi)\rho_0}{h^4}. \tag{A7c}$$

These corrections are parametrized by Re and Λ on a fixed grid, and they vanish under the following conditions:

(1) Eq. (A7a): $E'_{X'}=0$ if $\Lambda=\frac{1}{12}$ or $a_\varepsilon=0$.
(2) Eq. (A7b): $E'_{Y'}=0$ if $\Lambda=\frac{1}{12}$ or $a_\varepsilon=-k_\varepsilon^{-1}$.
(3) Eq. (A7c): $E'_m=0$ if $\Lambda=\frac{1}{6}$ or $a_\varepsilon=-k_\varepsilon^{-1}$.

Here $k_\varepsilon=24$ due to Eq. (A10c) using ζ_q from Eq. (A2) with ε_q from Eq. (5). Hence, all three solvability conditions are satisfied with an uniform stationary density solution, or in a constant pressure-gradient-driven flow, only when $\Lambda=\frac{1}{12}$ and $a_\varepsilon=-k_\varepsilon^{-1}$. The two exceptions are (1) a coordinate-axis parallel flow $\sin[2\varphi]=0$ where Λ and a_ε remain free, and

(2) a diagonal flow $\sin[4\varphi]=0$ where Eq. (A7a) vanishes and $a_\varepsilon = k_\varepsilon^{-1}$ annihilates Eqs. (A7c) and (A7b) for any Λ. These findings are summarized in Eq. (16). In the case of an arbitrary inclination, $E'_{Y'} = E'_{X'} = 0$ when $\Lambda = \frac{1}{12}$, but the mass-conservation equation becomes adjusted with the help of the time/space uniform nonzero density update $\partial_t\rho$:

$$\Lambda = \tfrac{1}{12}\colon \partial_{y'}\rho(y',t) = 0, \quad \partial_t\rho = -E_m = \text{const}. \tag{A8}$$

When $a_\varepsilon = 0$, Eq. (A6a) vanishes but Eq. (A6b) becomes adjusted with the help of the *pressure gradient* in y'-momentum equation, and the mass equation then gets the Laplacian of the pressure term from Eq. (A3c):

$$\begin{aligned} &a_\varepsilon = 0, \quad \forall\,\Lambda\colon \partial_t\rho + E_m = \Lambda^- c_s^2\partial_{y'}^2\rho,\\ &c_s^2\partial_{y'}\rho(y') = -E_{y'}(y'), \quad E_{x'} = 0. \end{aligned} \tag{A9}$$

Since $E_{y'}(y')$ is linear, the density correction $\rho(y')$ is parabolic obeying $c_s^2\partial_{y'}^2\rho = -\partial_{y'}E_{y'}$, and Eq. (A9) then presents the exact solvability condition. Equation (17) summarizes the two principal cases: (1) $a_\varepsilon = 0$ (the standard NSE term) and (2) $\Lambda = \frac{1}{12}$; these developments are then exactly validated in Figs. 2 and 3 with the help of the MR_{nse} boundary scheme from Table VII.

Auxiliary relations:

$$\sum_{q=0}^{Q_m}\zeta_q = 0, \quad 2\sum_{q=1}^{Q_m/2}\zeta_q c_{q,x'}^2 = -2,$$

$$2\sum_{q=1}^{Q_m/2}\zeta_q c_{q,y'} = 0, \quad 2\sum_{q=1}^{Q_m/2}\zeta_q c_{q,y'}^2 = 0, \tag{A10a}$$

$$2\sum_{q=1}^{Q_m/2}\zeta_q c_{q,x'}c_{q,y'}^3 = -6\sin(4\varphi)a_\varepsilon, \tag{A10b}$$

$$2\sum_{q=1}^{Q_m/2}\zeta_q c_{q,y'}^4 = \frac{1}{2}\sin^2(2\varphi)(1+k_\varepsilon a_\varepsilon). \tag{A10c}$$

Errata [87]: After their Eq. (B.1), d2q9 should read with $\varepsilon_q^\star = \{-4, 2, -1\}$ (sign change); Eq. (B.9): the prefactor 3 is to be replaced by 6; Eq. (B.12): the prefactor -9 is to be replaced by 18.

2. The MR_{nse} *p-nse-flow* family

A *p-nse-flow* scheme in Eq. (39) obeys either four ($\beta^{(p)} = \gamma^{(p)} = \delta^{(p)} = \varepsilon^{(p)} = 0$), three ($\gamma^{(p)} = \delta^{(p)} = \varepsilon^{(p)} = 0$) or two ($\delta^{(p)} = \varepsilon^{(p)} = 0$) additional conditions with respect to *p-flow* LI_3^+, parabolic VMR or *c-nse-p-flow* AVMR/EMR. The MR_{nse} derivation does not rely on any particular $e_q^+(\vec{r})$; it follows Eq. (19) and applies the fourth-order accurate nonequilibrium solution (A1) and, accordingly, extends the Taylor expansion in Eq. (B3) to the fourth order and relates $\{e_q^\pm, n_q^\pm\}$ at two upstream neighbors $\{\vec{r}_\mathrm{b} - \vec{c}_q, \vec{r}_\mathrm{b} - 2\vec{c}_q\}$ to their values at boundary node $\vec{r}_\mathrm{b}$. The MR_{nse} then obeys Eq. (39) and supports exactly the parabolic pressure distribution and the quartic NSE term $\mathcal{E}_q^{(u)}(y')$. The MR_{nse} coefficients are expressed in Table VII with two free tunable parameters $\alpha^{(u)}$ and Λ, also specifying an optional distribution $\alpha^{(u)}(\delta,k)$ which holds all 7 population coefficients inside the interval $[-1,1]$ by reducing Λ with Λ^+, e.g., $\Lambda(k=2) < \frac{\Lambda^+}{2}$. The computations in Fig. 2 are run with $\Lambda = \frac{1}{8}$, $k=2$, $\Lambda^+ = \frac{3}{2}\times 2^{-n}$, and then they become unstable when $n \geqslant 4$ in agreement with this last condition. Figure 3 applies $\Lambda = 2^{-n}\Lambda_0$ and $\Lambda^+ = 2^{-n}\Lambda_0^+$, $\Lambda_0 < \frac{\Lambda_0^+}{2}$.

3. Truncation in rotated Couette flow with wall-normal injection

We assume the exponential momentum profile $j_{x'}(y') = \rho_0(a + be^{\frac{\mathrm{Re}y'}{h}})$, $j_{y'} = \rho_0 v_0$ from Eq. (78), substitute it into the NSE term $\mathcal{E}_q^{(u)}(y')$ in Eq. (3b), and build the d2q9 truncation corrections with Eq. (A1) following the rotated parabolic flow procedure in Eqs. (A3)–(A6). Giving adimensional variables $t' = t/T$, $X' = x'/h$ and $Y' = y'/h$, we then multiply the derived momentum equations by T/v_0 and the mass-conservation equation by $T = h/v_0$. Their dimensionless truncation corrections read, accordingly:

$$\begin{aligned} E'_{X'}(Y') = &-\frac{\rho_0 be^{\mathrm{Re}Y'}\left(\Lambda - \frac{1}{12}\right)\mathrm{Re}^3 r_{xy}}{4h^2}\\ &\times\{[3+\cos(4\varphi)] + a_\varepsilon k_\varepsilon(a + 4be^{\mathrm{Re}Y'})\\ &\times r_{xy}\sin(4\varphi)\}, \end{aligned} \tag{A11a}$$

$$\begin{aligned} E'_{Y'}(Y') = &-\frac{\rho_0 be^{\mathrm{Re}Y'}\left(\Lambda - \frac{1}{12}\right)\mathrm{Re}^3 r_{xy}\sin(4\varphi)}{2h^2}\\ &\times[2\cos(2\varphi) + (1+a_\varepsilon k_\varepsilon)(a + 4be^{\mathrm{Re}Y'})\\ &\times r_{xy}\sin(2\varphi)]. \end{aligned} \tag{A11b}$$

$$\begin{aligned} E'_m(Y') = &\frac{\rho_0 be^{\mathrm{Re}Y'}\left(\Lambda - \frac{1}{6}\right)\Lambda\mathrm{Re}^5 r_{xy}\sin(2\varphi)}{6h^4}\\ &\times[2\cos(2\varphi) + (1+a_\varepsilon k_\varepsilon)(a + 8be^{\mathrm{Re}Y'})\\ &\times r_{xy}\sin(2\varphi)]. \end{aligned} \tag{A11c}$$

We note that E'_m and $E'_{Y'}$ vanish in the straight channel but, in contrast with the polynomial profile, $E'_{X'} \neq 0$ when $\varphi = 0$; the discrete-exponential solution $u_x^{\mathrm{num}}(y)$ is then specified in Eq. (79). Giving Y' equation $v_0^{-2}c_s^2\partial_{Y'}\rho = -E'_{Y'}(y')$, and following Eq. (A9), we construct the dimensionless mass-leakage rate distribution $\partial_{t'}\rho(Y') = (hv_0)^{-1}\Lambda^- c_s^2\partial_{Y'}^2\rho - E'_m(\rho)$ and estimate its average value $\langle\partial_{t'}\rho\rangle = \int_{-1/2}^{1/2}\partial_{t'}\rho(Y')dY'$:

$$\begin{aligned} \langle\partial_{t'}\rho\rangle = &\frac{b\rho_0\Lambda\mathrm{Re}^4 r_{xy}\sin(2\varphi)\sinh\left(\frac{\mathrm{Re}}{2}\right)}{36h^4}\\ &\times\left\{2\cos(2\varphi) + (1+a_\varepsilon k_\varepsilon)\right.\\ &\left.\times[a + 8b\cosh\left(\frac{\mathrm{Re}}{2}\right)]r_{xy}\sin(2\varphi)\right\},\\ \langle\partial_t\rho\rangle = &\,T^{-1}\langle\partial_{t'}\rho\rangle, \quad T = h/v_0. \end{aligned} \tag{A12}$$

These results are discussed in Sec. VI F.

APPENDIX B: COLLISION AND CLOSURE RELATION

1. Extensions to (multirelaxation time) MRT

We discuss how to couple the MRT collision operator with the proposed boundary rules. The postcollision correction $\hat{F}_q$ in Eq. (22) becomes available for any collision due to the decomposition of the postcollision nonequilibrium on the symmetric (even-order) and antisymmetric (odd-order) basis vectors, and summing their contributions in $\hat{n}_q^+$ and $\hat{n}_q^-$, respectively. The MRT = MRT$^{(-)}$ ∪ MRT$^{(+)}$ hydrodynamic models [17,75] conserve the population momentum $\vec{J} = \vec{j} - \frac{1}{2}\vec{F}$ and typically apply the same (ghost) rate, say τ^-, for all third and higher order antisymmetric polynomial basis vectors in their MRT$^{(-)}$ collision component. Equivalently, the MRT$^{(-)}$ can be computed prescribing τ^- for all odd-order vectors, including $\vec{c}_q$, when the linear forcing term is incorporated into e_q^- with Eq. (3c):

$$e_q^-(\vec{r}) := t_q^\star \vec{j}\cdot\vec{c}_q + \mathcal{E}_q^{(f)} = t_q^\star(\vec{J}\cdot\vec{c}_q + \tau^-\vec{F}\cdot\vec{c}_q). \quad \text{(B1)}$$

This allows one to compute $\hat{n}_q^-$ with MRT$^{(-)}$ ∼ TRT$^{(-)}$, exactly as in the TRT$^{(-)}$ operator in Eq. (1). Conversely, when the standard (momentum conserving) equilibrium $e_q^- = t_q^\star \vec{J}\cdot\vec{c}_q$ applies adding the forcing term $t_q^\star\vec{F}\cdot\vec{c}_q$ directly to the postcollision populations, $\hat{n}_q^-$ shall sum the postcollision odd-order projections with this term [see Eq. (51) in Ref. [17]].

Next, the MRT$^{(+)}$ differs from the TRT$^{(+)}$ when some of the symmetric rates τ_i^+ are distinct from the kinematic viscosity rate τ^+; typically, these are the bulk viscosity and fourth-order polynomial modes, and their coefficients $\tau_i^+ - \frac{1}{2}$ shall scale in proportion to the kinematic viscosity for an exact steady-state parametrization, [17]. In principle, in the derivation of the two-node parabolic schemes, or in the presence of $\hat{K}^+\hat{n}_q^+$ correction in Eq. (22), the components $-\tau^+\hat{n}_q^+$ shall be replaced by the sum of the symmetric nonequilibrium projections on the basis vectors. However, as a first approximation, those *p-flow* and parabolic MR boundary schemes where the coefficients depend explicitly on Λ^+ may substitute $\Lambda^+ = 3\nu$, because the bulk viscosity modes are usually not relevant for boundary conditions in steady-state laminar flows [17].

2. Derivation of MR closure relation

We prescribe the TRT operator $\{\tau^\pm\}$ and decompose all populations into their equilibrium $\{e_q^\pm\}$ and nonequilibrium $\{-\tau^\pm\hat{n}_q^\pm\}$ components. We derive the closure coefficients in Eq. (19) assuming the diffusive timescale, $\delta t \sim \delta_x^2$, and retaining the time variation only for $e_q^\pm$. The local populations in Eq. (21) then read (here f_{+q} replaces f_q for all terms):

$$\begin{aligned}
f_{\pm q}|_{(\vec{r}_b,t)} &= (e_q^+ \pm e_q^- - \tau^+\hat{n}_q^+ \mp \tau^-\hat{n}_q^-)|_{(\vec{r}_b,t)},\\
f_{\pm q}|_{(\vec{r}_b,t+1)} &\approx (f_{\pm q} + \partial_t e_q^+ \pm \partial_t e_q^-)|_{(\vec{r}_b,t)},\\
\hat{f}_{\pm q}|_{(\vec{r}_b,t)} &= [e_q^+ \pm e_q^- + (1-\tau^+)\hat{n}_q^+ \pm (1-\tau^-)\hat{n}_q^-]|_{(\vec{r}_b,t)}.
\end{aligned} \quad \text{(B2)}$$

We substitute the Chapman-Enskog parabolic-accurate solution $\hat{n}_q^\pm$ from Eq. (18) where we reexpress the neighboring solution with the help of the directional second-order accurate Taylor expansion:

$$\begin{aligned}
e_q^\pm|_{(\vec{r}_b-\vec{c}_q,t)} &\approx (e_q^\pm - \partial_q e_q^\pm)|_{(\vec{r}_b,t)} + \tfrac{1}{2}\partial_q^2 e_q^\pm + O(\varepsilon^3),\\
\hat{n}_q^\pm|_{(\vec{r}_b-\vec{c}_q,t)} &\approx \big(\hat{n}_q^\pm - \partial_q^2 e_q^\mp\big)|_{(\vec{r}_b,t)} + O(\varepsilon^3).
\end{aligned} \quad \text{(B3)}$$

The neighboring populations in Eq. (21) then become expressed through the local solution, as

$$\begin{aligned}
f_q|_{(\vec{r}_b-\vec{c}_q,t)} \approx \big(&e_q^+ + e_q^- - \tau^+\hat{n}_q^+ - \tau^-\hat{n}_q^-\\
&- \partial_q e_q^+ - \partial_q e_q^- + \tfrac{1}{2}\partial_q^2 e_q^+ + \tfrac{1}{2}\partial_q^2 e_q^-\\
&+ \tau^+\partial_q^2 e_q^- + \tau^-\partial_q^2 e_q^+\big)|_{(\vec{r}_b,t)},\\
f_q|_{(\vec{r}_b-\vec{c}_q,t+1)} \approx\ & f_q|_{(\vec{r}_b-\vec{c}_q,t)} + \partial_t e_q^+ + \partial_t e_q^-|_{(\vec{r}_b,t)},\\
\widehat{f}_{-q}|_{(\vec{r}_b-\vec{c}_q,t)} \approx \big[&e_q^+ - e_q^- + (1-\tau^+)\hat{n}_q^+ - (1-\tau^-)\hat{n}_q^-\\
&- \partial_q e_q^+ + \partial_q e_q^- + \tfrac{1}{2}\partial_q^2 e_q^+ - \tfrac{1}{2}\partial_q^2 e_q^-\\
&- (1-\tau^+)\partial_q^2 e_q^- + (1-\tau^-)\partial_q^2 e_q^+\big]\big|_{(\vec{r}_b,t)}.
\end{aligned} \quad \text{(B4)}$$

We first substitute Eqs. (B2)–(B4) into Eq. (21), where Eqs. (24a) and (24b) then sum the coefficients of e_q^+ and e_q^-. Next, we substitute $\hat{F}_q = \hat{K}^+\hat{n}_q^+ + \hat{K}^-\hat{n}_q^-$ into Eq. (21), express $\hat{n}_q^\pm$ with Eq. (18), sum the coefficients of $\beta^{(p)}\partial_q e_q^+$ and $\beta^{(u)}\partial_q e_q^-$, and get with the help of Eq. (24):

$$\begin{aligned}
\beta^{(p)} &= -\tau^-\alpha^{(u)} + (\hat{\alpha} - \hat{\beta} - \hat{\gamma}) - (\hat{\gamma} + \gamma) + \hat{K}^-,\\
\beta^{(u)} &= -\tau^+\alpha^{(p)} + (\hat{\alpha} + \hat{\beta} + \hat{\gamma}) + (\hat{\gamma} - \gamma) + \hat{K}^+.
\end{aligned} \quad \text{(B5)}$$

Equation (25) then reexpresses Eq. (B5) through $\Lambda^\mp$. Accordingly, $\gamma^{(p)}\partial_q^2 e_q^+$ and $\gamma^{(u)}\partial_q^2 e_q^-$ come with

$$\begin{aligned}
\gamma^{(p)} &= -\beta^{(u)}\Lambda^-\\
&\quad + \Lambda^-(\hat{\gamma} - \gamma) + \big(\tfrac{1}{2} + \tau^-\big)\gamma + \big(\tfrac{3}{2} + \tau^-\big)\hat{\gamma},\\
\gamma^{(u)} &= -\beta^{(p)}\Lambda^+\\
&\quad - \Lambda^+(\hat{\gamma} + \gamma) + \big(\tfrac{1}{2} + \tau^+\big)\gamma - \big(\tfrac{3}{2} - \tau^+\big)\hat{\gamma}.
\end{aligned} \quad \text{(B6)}$$

Equation (26) reduces Eq. (B6). Finally, Eq. (41) sums the coefficients of $\partial_t e_q^\pm$. The derived spatial closure relation is the same as its solution [69] [see Eqs. (A.6) and (A.7) there with $\alpha^{(u)} = \alpha^{(m)}$], but here they are derived from the poststream two-node configuration and recursively expressed through the lower order coefficients.

3. The MR coefficient transform

For the sake of completeness we update an "equivalent" transform [59] of the MR in Eq. (21) giving an adjustable parameter k [Eq. (49) in Ref. [59]]:

$$\begin{aligned}
&\hat{\alpha} \to \frac{\hat{\alpha} - k}{1+k}, \quad \gamma \to \frac{\gamma - k}{1+k}, \quad \hat{\gamma} \to \frac{\gamma - k}{1+k}, \quad \beta \to \frac{\beta + 2k}{1+k},\\
&\hat{\beta} \to \frac{\hat{\beta} + 2k}{1+k}, \quad \mathcal{W}_q \to \frac{\mathcal{W}_q}{k+1}, \quad \hat{K}^\pm \to \frac{\hat{K}^\pm}{k+1}.
\end{aligned} \quad \text{(B7)}$$

The closure coefficients $\{\alpha^{(u)}, \beta^{(u)}, \gamma^{(u)}, \alpha^{(p)}, \beta^{(p)}\}$ in Eq. (21) then all get the prefactor $1/(k+1)$, except for $\gamma^{(p)}$. Since $\gamma^{(p)}$ is left free in the original parabolic MR and more generally in VMR($\alpha^{(u)}, \hat{K}^\pm$) family in Table VI, the k transform preserves the parabolic properties and can be useful to

bring all coefficients to the desired interval, e.g., MR1 was constructed giving condition $\hat{\alpha}=1$ [see Eqs. (51)–(56) in Ref. [59]]. However, the specific subclass PM [69], which includes the AVMR, and its extension EMR, both enforce an additional *c-nse-p-flow* condition $\gamma^{(p)}=0$. Therefore, this property is not preserved by the k transform and the presented parametrization of all schemes by the Taylor scale factor $\alpha^{(u)}$ is more suitable to retain all other coefficients properties.

4. Steady-state closure and parametrization

The exact steady-state closure relation drops the time in Eq. (21). A two-node directional TRT-based boundary rule can be then presented as a linear combination of the local and neighbor, equilibrium $\{e_q^{\pm}(\vec{r}), e_q^{\pm}(\vec{r}_{nb})\}$ and nonequilibrium components $\{\hat{n}_q^{\pm}(\vec{r}), \hat{n}_q^{\pm}(\vec{r}_{nb})\}$:

$$\begin{aligned} M_q\cdot X_q &= -w_q(\vec{r}_q),\\ M_q[8] &= \{m_1,m_2,m_3,m_4\}\\ &\quad\cup\{m_5,m_6,m_7,m_8\}_q,\\ X_q[8] &= \{e_q^+,e_q^-,\hat{n}_q^+,\hat{n}_q^-\}|_{\vec{r}_b}\\ &\quad\cup\{e_q^+,e_q^-,\hat{n}_q^+,\hat{n}_q^-\}|_{\vec{r}_{nb}},\\ \vec{r}_q &= \vec{r}_b+\delta\vec{c}_q,\ \vec{r}_{nb}=\vec{r}_b-\vec{c}_q. \end{aligned} \tag{B8}$$

The coefficients $\{m_i\}$ read with respect to Eq. (21)

$$\begin{aligned} m_1&=\hat{\alpha}+\beta+\hat{\beta}-1, & m_2&=(\hat{\alpha}+\beta-\hat{\beta}+1),\\ m_3&=-\tau^+m_1+\hat{\alpha}, & m_4&=-\tau^-m_2+\hat{\alpha}\\ &\quad+\hat{\beta}+\hat{K}^+, & &\quad-\hat{\beta}+\hat{K}^-,\\ m_5&=\gamma+\hat{\gamma}, & m_6&=\gamma-\hat{\gamma},\\ m_7&=-\tau^+m_5+\hat{\gamma}, & m_8&=-\tau^-m_6-\hat{\gamma}. \end{aligned}$$

The single-node LI$^+$ class operates with $\{m_5,m_6,m_7,m_8\}=0$ and $M_q[4]=\{m_1,m_2,m_3,m_4\}_q$ where according to Eq. (27), the coefficients are given in Eq. (32). The dimensionless form of Eq. (B8) is developed by Eqs. (36)–(40) in Ref. [69]. According to this result, the sufficient parametrization condition is fulfilled when the "rescaled" coefficients m_3', m_4' and m_7', m_8' depend upon $\Lambda^{\pm}$ only through Λ:

$$m_3'=\frac{m_3}{\alpha^{(u)}},\quad m_4'=\frac{m_4}{\alpha^{(u)}\Lambda^-},\qquad m_7'=\frac{m_7}{\alpha^{(u)}},\quad m_8'=\frac{m_8}{\alpha^{(u)}\Lambda^-}. \tag{B9}$$

Additionally, the dimensionless equilibrium Dirichlet value $e_q^-(\vec{r}_q)/\mathcal{U}$ shall remain fixed. A reduction of Eq. (B9) to single-node schemes is presented in Eq. (45).

APPENDIX C: THE SINGLE-NODE CLASS LI$^+$

1. The YLI [56], GLI [63], SSN [64], MSSN [65], ZLI [61], and CHLI [62] in LI

Following [59], we first fit YLI [56] to LI$_0$ in Eq. (21) with $I^{(t)}=1$, $\hat{K}^{\pm}=0$ in Eq. (22) and the coefficients obeying Eq. (46a), giving there $\alpha^{(p)}=0$ and $\alpha^{(u)}=\frac{2}{1+\delta}$ from Table III, then $\hat{\alpha}=\hat{\beta}=\frac{\delta}{1+\delta}$, $\beta=1-(\hat{\alpha}+\hat{\beta})$ and $\{\hat{\alpha},\beta,\hat{\beta}\}\in[0,1]$. The YLI applies locally by performing the streaming of $\beta\widehat{f_q}(\vec{r}_b-\vec{c}_q,t+1)$ prior to the boundary step. Alternatively, replacing $\beta f_q(\vec{r}_b,t+1)$ by the previous step solution when $I^{(t)}=0$ in Eq. (21), the YLI can be implemented as a single-node modified collision operator and it then coincides with the GLI [63]. As one example, YLI is presented [82] via a three-node linear interpolation [it is to note that the last term in their Eq. (14) should be the same as the first one ($i\to\bar{i}$ in their notation)]:

$$\begin{aligned} f_{-q}(\vec{r}_b,t+1) &= \frac{1}{1+\delta}f_{-q}(\vec{r}_q,t+1)\\ &\quad+\frac{\delta}{1+\delta}f_{-q}(\vec{r}_b-\vec{c}_q,t+1), \end{aligned} \tag{C1}$$

where the ghost population $f_{-q}(\vec{r}_q,t+1)=f_q(\vec{r}_q,t+1)-2e_q^-(\vec{r}_q)$ is obtained with the in-wall bounce-back from the upstream extrapolation: $f_q(\vec{r}_q,t+1)=f_q(\vec{r}_b,t+1)+\delta[f_q(\vec{r}_b+\vec{c}_q,t+1)-f_q(\vec{r}_b,t+1)]$. Assuming that $f_q(\vec{r}_q,t+1)$ contains the correct wall solution $e_q^-(\vec{r}_q)$, an involved approximation reduces to the nonequilibrium bounce-back: $n_{-q}=n_q$.

The most general among these schemes, the three-population interpolation ZLI is derived with the help of the two ghost nodes: $\vec{r}_1=\vec{r}_b+l\vec{c}_q$ and its wall-mirror image $\vec{r}_2=\vec{r}_q+(\delta-l)\vec{c}_q$, $\vec{r}_q=\vec{r}_b+\delta\vec{c}_q$, using (1) a linear interpolation between $f_q(\vec{r}_b,t+1)$ and $f_q(\vec{r}_b+\vec{c}_q,t+1)=\widehat{f_q}(\vec{r}_b,t)$ to define $f_q(\vec{r}_2,t+1)$; (2) the bounce-back between two ghost nodes, $f_{-q}(\vec{r}_1,t+1)=f_q(\vec{r}_2,t+1)-2e_q^-(\vec{r}_q)$; and (3) a linear interpolation between $f_{-q}(\vec{r}_b-\vec{c}_q,t+1)=\widehat{f}_{-q}(\vec{r}_b,t)$ and $f_{-q}(\vec{r}_1,t+1)$ for an unknown solution $f_{-q}(\vec{r}_b,t+1)$ [notations [61] apply with $f_q\to f_{\bar{i}}$, $f_{-q}\to f_i$, $l\to lh$, $\delta\to\gamma h$, $\vec{r}_b\to x_f$, $\vec{r}_q\to x_b$, $\vec{r}_b+\vec{c}_q\to x_r$, $\vec{r}_1\to x_1$, $\vec{r}_1\to x_2$, here $\delta_t\to 1$]. The final solutions in their Eqs. (3.7) and (3.8) match LI$_0$ in Eq. (21) with, respectively, $I^{(t)}=0$ and $I^{(t)}=1$, and Eq. (46a) with

$$\begin{aligned} &\text{ZLI}\in\text{LI}_0\text{: }\alpha^{(u)}=\frac{2}{1+l},\quad \alpha^{(p)}=0,\quad \hat{K}^{\pm}=0,\ \text{then}\\ &\hat{\alpha}=\frac{2\delta-l}{1+l},\\ &\hat{\beta}=\frac{l}{1+l},\quad \beta=1-(\hat{\alpha}+\hat{\beta}), \end{aligned} \tag{C2a}$$

$$\{\hat{\alpha},\beta,\hat{\beta}\}\in[0,1]\quad\text{if}\quad l\in[0,2\delta],\quad \delta\in\left[0,\frac{1}{2}\right],$$

$$\text{or}\quad l\in[2\delta-1,2\delta],\quad \delta\in\left[\frac{1}{2},1\right]. \tag{C2b}$$

Respecting conditions in Eq. (C2b), ZLI obeys the "convex" conditions: $\{\hat{\alpha},\beta,\hat{\beta}\}\in[0,1]$ and $\alpha^{(p)}=\hat{\alpha}+\hat{\beta}+\hat{\gamma}-1=0$. When $I^{(t)}=0$ in Eq. (21), these convex conditions combine the two time-step populations; otherwise, when $I^{(t)}=1$, they address the three outgoing populations; when $l=\delta$, ZLI($I^{(t)}=1$) and ZLI($I^{(t)}=0$) reduce respectively to YLI [56] and GLI [63]. Under conditions in Eq. (C2b), $\alpha^{(u)}\in[0,\delta^{-1}]$ and hence ZLI satisfies sufficient nonequilibrium stability condition to Eq. (40a) given in Eq. (61). The ZLI$_3$ is restricted to the common LI$_3^+$ condition in Eq. (63), which is less small-viscosity restrictive for smaller values of $\alpha^{(u)}(l)$. The second-order single-node SSN scheme [64] is the member of ZLI(l) in Eq. (C2a) with uniform solution $l=2\delta$, then $\alpha^{(u)}=\frac{2}{1+2\delta}$, $\hat{\alpha}=\gamma=\hat{\gamma}=0$, $\hat{\beta}=\frac{2\delta}{1+2\delta}$, $\beta=\frac{1}{1+2\delta}$, $\hat{K}^{\pm}=0$.

Since SSN operates with the smallest $\alpha^{(u)}$ value respecting Eq. (C2b), it is expected to be most the stable in ZLI(l); and it shares its stability boundaries with ELI-UL$_3$($\alpha^{(u)}=1$) when $\delta=\frac{1}{2}$, and with BFL-QI$_3$($\alpha^{(u)}=2/3$) in Table V when $\delta=1$. Accordingly, SSN$_0$ = SSN and SSN$_k$, $k=\{1,4\}$, satisfy the stability conditions in Eq. (40) with Eqs. (62a) and (62b). In turn, the parametrized (magic) scheme MSSN [65] then adopts the MGLI/LI$_1$ parametrization in Eq. (48) and it reads with $\hat{K}^-=\hat{K}_1^-=1-\hat{\alpha}=1$ in agreement with Eqs. (27) and (28) [65]; their optimal Λ solution is the MGLI solution [58] recalled in Eq. (49a).

Finally, the CHLI [62] is constructed very similarly with ZLI, and its solution coincides with ZLI when $l\geqslant 1$, which corresponds to $\delta\in]\frac{1}{2},1]$ in Eq. (C2b). Otherwise, the CHLI incoming solution is the same as in Eq. (C2) under the transformation $l=2\delta-\gamma$ when $\delta\in[0,\frac{1}{2}]$, $l\in[0,2\delta]$, $\gamma\in[0,2\delta]$ [with $\delta\to\Delta$ in [62]].

To sum up, ZLI$_0$ = ZLI belongs to LI$_0$($I^{(t)}=0$) where it prescribes $\alpha^{(p)}=0$ and the scale Taylor factor $\alpha^{(u)}(\delta,l)$ with a free parameter l, such that $\{\hat{\alpha},\beta,\hat{\beta}\}\in[0,1]$ when l obeys fractional conditions in Eq. (C2). Under these conditions, ZLI$_0$ also satisfies Eq. (40), and it reduces to uniform scheme SSN with the smallest $\alpha^{(u)}=\frac{2}{1+2\delta}$ when $l=2\delta$. In turn, the parametrized MSSN belongs to MGLI. The ZLI$_0$ can be extended for $I^{(t)}\in[0,1]$ where it reduces to GLI($I^{(t)}=0$) and YLI($I^{(t)}=1$) when $l=\delta$. Further, ZLI$_0$ = ZLI, its equivalent CHLI and their subclasses can be extended to ZLI$_k$ applying Eq. (44) where, respecting Eq. (C2b), {ZLI$_0$, ZLI$_1$, ZLI$_4$} satisfy the nonequilibrium stability conditions in Eq. (40).

2. The APLI($I_b=1$) against IPLI($I_b=0$), and WLI [70] in APLI

We follow the construction of the *p-flow* scheme IPLI in Eq. (50) but replace $I_b=0$ by $I_b=1$ in Eq. (33). A *p-flow* scheme then shall couple the term $\mathcal{E}_q^{(f)}=t_q^\star\Lambda^-\vec{F}\cdot\vec{c}_q$ from Eq. (3c) with the parabolic term $\gamma^{(u)}\partial_q^2 e_q^-$. Following [51,58], this is typically performed in the force-driven Stokes channel flow $j_{x'}(y')$:

$$-F_{x'}=\frac{\Lambda^+}{3}\partial_{y'}^2 j_{x'},\quad\text{then}$$

$$\Lambda^- t_q^\star\vec{F}\cdot\vec{c}_q=-\frac{\Lambda}{3\Theta_q^2}t_q^\star\partial_q^2(\vec{j}\cdot\vec{c}_q)=-\frac{\Lambda}{3\Theta_q^2}\partial_q^2 e_q^-,$$

$$\text{with}\quad\partial_q=\partial_{y'}c_{q,y'},\quad\Theta_q=c_{q,y'}=\vec{c}_q\cdot\vec{1}_{y'}. \tag{C3}$$

Substituting Eq. (C3) for $t_q^\star\Lambda^-\vec{F}\cdot\vec{c}_q$ and $\gamma^{(u)}$ from Eq. (47) [LI$_k$ with $\hat{K}^-=0$] we get

$$\text{APLI}\in\text{LI}_0\ \text{ with }\ I_b=1,\quad\text{and}$$

$$\gamma^{(u)}|_{\text{APLI}}=\gamma^{(u)}|_{\hat{K}^-=0}-\frac{\alpha^{(u)}\Lambda}{3\Theta_q^2},\quad\text{then} \tag{C4a}$$

$$\gamma^{(u)}|_{\text{APLI}}=\alpha^{(u)}\frac{\delta^2}{2}\quad\text{if }\alpha^{(u)}=\alpha^{(u)}_{APLI}, \tag{C4b}$$

$$\alpha^{(u)}_{APLI}=\frac{12\Lambda^+\Theta_q^2}{3\Theta_q^2[\delta^2+\Lambda^+(1+2\delta)]+2\Lambda\left(1-3\Theta_q^2\right)}. \tag{C4c}$$

In a straight channel $\Theta_q^2=1$ we define WLI scheme with

$$\text{WLI}:=\text{APLI}|_{\Theta_q^2=1}\ \text{ with}$$

$$\alpha^{(u)}=\alpha^{(u)}_{APLI}|_{\Theta_q^2=1}=\frac{12\Lambda^+}{3[\delta^2+\Lambda^+(1+2\delta)]-4\Lambda}. \tag{C5}$$

The APLI is parametrized with $m_4'=-\frac{\gamma^{(u)}}{\alpha^{(u)}\Lambda}|_{\text{APLI}}=-\frac{\delta^2}{2\Lambda}$, similarly with $m_4'(K_3^-)$ in Eq. (45). The coefficients $\{\hat{\alpha},\beta,\hat{\beta}\}$ are then defined with Eq. (46a):

$$\text{APLI:}\quad\{\hat{\alpha},\beta,\hat{\beta}\}\in[-1,1]\quad\text{if}$$

$$\Theta_q^2\in\left[0,\frac{1}{3}\right],\quad\forall\,\Lambda\ \text{ or }\ \Lambda\in\left[0,\frac{3\Theta_q^2\delta^2}{6\Theta_q^2-2}\right],\quad\text{then}$$

$$\text{WLI:}\quad\Lambda\in\left[0,\frac{3\delta^2}{4}\right]\quad\text{if}\quad\Theta_q^2\equiv 1. \tag{C6}$$

The APLI stability interval is slightly more favorable than $\Lambda\in]0,\frac{\delta^2}{2}]$ with IPLI in Eq. (50). However, in contrast to APLI, the IPLI coefficients are independent of the flow direction with respect to the grid and their derivation does not involve any macroscopic equation.

We show now that the scheme developed by Wang *et al.* [70] corresponds to Eq. (C5), and hence, it models exactly only the straight Poiseuille Stokes flow. In fact, the linear interpolation [70] given by their Eq. (15) fits LI$_0$ in Eq. (46a) with $\alpha^{(u)}=\gamma=\frac{2}{2+l}$ and $\alpha^{(p)}=0$, using their free parameters l and γ, and denoting the collision rates $\tau^+=\tau_s$ and $\tau^-=\tau_q$. The coefficients $\{\hat{\alpha},\beta,\hat{\beta}\}$ in Eq.(15) [70] then correspond to Eq. (46). If we replace $\alpha^{(u)}$ by $\frac{2}{2+l}$ in Eq. (C5), we get in the straight channel

$$l=\frac{-3\Lambda^++3\delta(\delta+2\Lambda^+)-4\Lambda}{6\Lambda^+}. \tag{C7}$$

Now, if we combine Eqs. (37) and (38) from [70] we get under the same notation convention

$$l=\frac{\delta^2+\delta(2\tau^+-1)}{2\tau^+-1}+C,\quad C=-\frac{4\tau^-+1}{6}. \tag{C8}$$

Plugging the second equation in the first one, and expressing $\tau^\pm$ through $\Lambda^\pm$ and then replacing Λ^- by Λ/Λ^+ we get Eq. (C7).

3. From XELI [66], ULT [67], and LLI [68] to ELI$^+\in$ LI$^+$

The XELI family [66] is introduced by their Eq. (13) as

$$f_{-q}(\vec{r}_{\rm b},t+1)=a_2[\widehat{f_q}(\vec{r}_{\rm b},t)+2e^-_{-q}(\vec{r}_q,t)]+a_3\widehat{f}_{-q}(\vec{r}_{\rm b},t)$$
$$+a_4 f_{-q}(\vec{r}_q,\tilde{t})+a_5\hat{f}_{-q}(\vec{r}_q,\tilde{t})-\hat{K}^-\frac{n_q^-}{\tau^-}, \tag{C9}$$

where the ghost wall population $f_{-q}(\vec{r}_q,\tilde{t})$ is built with the three options for its antisymmetric nonequilibrium approximation $\hat{n}^-_{-q}(\vec{r}_q,t)=-I_{ncs}\hat{n}_q^-(\vec{r}_{\rm b},t)$: XELI = {NELI, CELI, SELI} (*nonsymmetric*, *central*, and *symmetric*) with $I_{ncs}=\{-1,0,1\}$ respectively; the last term in Eq. (C9) is introduced for the parametrization following MGLI [57]. We first fit Eq. (C9) to Eq. (21) with the help of an additional

(ghost) term $\mathrm{ME}_q(\vec{r}_q)$ assuming the TRT nonequilibrium decomposition:

$$\begin{aligned}
\mathrm{ELI}_0 &= \text{XELI:}\\
f_{-q}(\vec{r}_\mathrm{b}, t+1) &= \mathrm{MR}_q(\vec{r}_\mathrm{b}) + \mathrm{ME}_q(\vec{r}_q) + \mathcal{W}_q(\vec{r}_q, \tilde{t}),\\
\hat{\alpha} &= a_2, \quad \hat{\beta} = a_3, \quad \beta = \gamma = \hat{\gamma} = 0,\\
\mathrm{ME}_q(\vec{r}_q) &= a_4 f_{-q}(\vec{r}_q, \tilde{t}) + a_5 \hat{f}_{-q}(\vec{r}_q, \tilde{t}),\\
f_{-q}(\vec{r}_q, \tilde{t}) &= e_q^+(\vec{r}_\mathrm{b}, t) - e_q^-(\vec{r}_q, \tilde{t})\\
&\quad - \tau^+ \hat{n}_q^+(\vec{r}_\mathrm{b}, t) + \tau^- I_{ncs} \hat{n}_q^-(\vec{r}_\mathrm{b}, t),\\
\hat{f}_{-q}(\vec{r}_q, \tilde{t}) &= f_{-q}(\vec{r}_q, \tilde{t}) + \hat{n}_q^+(\vec{r}_\mathrm{b}, t) - I_{ncs} \hat{n}_q^-(\vec{r}_\mathrm{b}, t),\\
\mathcal{W}_q &= -\mathcal{A}_w^{(p)} e_q^+(\vec{r}_\mathrm{b}, t) - \mathcal{A}_w^{(u)} e_q^-(\vec{r}_q, \tilde{t}),\\
\mathcal{A}_w^{(p)} &= 0, \quad \mathcal{A}_w^{(u)} = 2\hat{\alpha}.
\end{aligned} \tag{C10}$$

Equation (C10) accounts that $e_{-q}^+ = e_q^+$, $e_{-q}^- = -e_q^-$, $\hat{n}_{-q}^+ = \hat{n}_q^+$ and $\hat{n}_{-q}^- = -\hat{n}_q^-$, and involves approximation $\hat{n}_q^+(\vec{r}_\mathrm{b}) = \hat{n}_q^+(\vec{r}_q)$. We now fit ELI_0 to closure in Eq. (19) given $\beta = \gamma = \hat{\gamma} = 0$ with $\alpha^{(p)}$ and $\alpha^{(u)}$ defined in Eq. (24). Substituting $\mathcal{A}_w^{(p)} = 0$ and $\mathcal{A}_w^{(u)} = 2\hat{\alpha}$, the coefficients of e_q^+ and e_q^- give two closure conditions in Eq. (C10):

$$\begin{aligned}
&(1)\ \hat{\alpha} + \hat{\beta} + a_4 + a_5 - 1 = 0 \ \text{ then } \ a_4 + a_5 = -\alpha^{(p)},\\
&(2)\ \hat{\alpha} - \hat{\beta} + 1 - a_4 - a_5 = 2\hat{\alpha}, \ \text{ then}\\
&\qquad a_4 + a_5 + 2\hat{\alpha} = \alpha^{(u)},\\
&\qquad \text{with } \ \alpha^{(p)} = \hat{\alpha} + \hat{\beta} - 1, \quad \alpha^{(u)} = \hat{\alpha} - \hat{\beta} + 1.
\end{aligned} \tag{C11}$$

The term $\beta^{(u)} \hat{n}_q^+$ of the closure relation in Eq. (C10) determines the third necessary condition $\beta^{(u)} = \alpha^{(u)} \delta$ from Eq. (31):

$$\begin{aligned}
&(3)\ \beta^{(u)} = \alpha^{(u)} \delta, \ \text{ with}\\
&\qquad \beta^{(u)} = -\tau^+ (\hat{\alpha} + \hat{\beta} + a_4 + a_5 - 1) + \hat{\alpha} + \hat{\beta} + a_5.
\end{aligned} \tag{C12}$$

Since the coefficient of τ^+ vanishes due to condition (1) in Eq. (C11), conditions (1)–(3) express the four coefficients through $\alpha^{(p)}$ and $\alpha^{(u)}$:

$$\hat{\alpha} = \tfrac{1}{2}(\alpha^{(p)} + \alpha^{(u)}), \quad \hat{\beta} = 1 + \tfrac{1}{2}(\alpha^{(p)} - \alpha^{(u)}), \tag{C13a}$$

$$a_4 = 1 - \alpha^{(u)} \delta, \quad a_5 = \alpha^{(u)} \delta - 1 - \alpha^{(p)}. \tag{C13b}$$

The coefficients in Eq. (C13b) are the same as $a_4(a_2, a_3)$ and $a_5(a_2, a_3)$ in Eq. (34) [66]. By expressing ME_q through $\hat{F}_q$ and $\mathcal{W}_q$, XELI becomes reproduced by ELI_0^+:

$$\begin{aligned}
\mathrm{ELI}_0^+\text{:}\ \ & f_{-q}(\vec{r}_\mathrm{b}, t+1) = \mathrm{MR}_q(\vec{r}_\mathrm{b}) + \hat{F}_q(\vec{r}_\mathrm{b}) + \mathcal{W}_q(\vec{r}_q),\\
\hat{F}_q &= K_{ELI}^+ \hat{n}_q^+ + \hat{K}_0^- \hat{n}_q^-,\\
&\quad K_{ELI}^+(\alpha^{(u)}, \alpha^{(p)}, \tau^+) = (a_4 + a_5)(-\tau^+) + a_5,\\
&= \alpha^{(p)}(\tau^+ - 1) + \alpha^{(u)} \delta - 1,\\
\hat{K}_0^- &= -I_{ncs} K_{ELI_0}^-,\\
&\quad K_{ELI_0}^-(\alpha^{(u)}, \alpha^{(p)}, \tau^-) = (a_4 + a_5)(-\tau^-) + a_5,\\
&= \alpha^{(p)}(\tau^- - 1) + \alpha^{(u)} \delta - 1,\\
\mathcal{W}_q &= -\mathcal{A}_w^{(p)} e_q^+(\vec{r}_\mathrm{b}, t) - \mathcal{A}_w^{(u)} e_q^-(\vec{r}_q, \tilde{t}),\\
\mathcal{A}_w^{(p)} &= \alpha^{(p)}, \quad \mathcal{A}_w^{(u)} = \alpha^{(u)}.
\end{aligned} \tag{C14}$$

Here we substitute $\beta = \gamma = \hat{\gamma} = 0$, $\hat{\alpha}$ and $\hat{\beta}$ from Eq. (C13a) into MR_q, and a_4 and a_5 from Eq. (C13b) into $\hat{F}_q$. Table IV exemplifies $\alpha^{(p)}$ and $\alpha^{(u)}$ in the four XELI schemes [66]; in particular, ELI-ULT is defined with $a_2 = \hat{\alpha} = 0$, $a_5 = 0$, $a_4 = 1/(1+\delta)$, $a_3 = \delta/(1+\delta)$ and hence, $\alpha^{(u)} = -\alpha^{(p)} = 1/(1+\delta)$, where NELI then matches ULT [67].

We consider now the $\mathrm{LLI}(\gamma^-)$ scheme given in Eq. (15) [68]: it prescribes the unknown population through a linear combination of $\frac{1}{1+\delta} e_{-q}(\vec{r}_q)$, $\frac{\delta}{1+\delta} \widehat{f}_{-q}(\vec{r}_\mathrm{b}, t)$, $\frac{2-\gamma^-}{2(1+\delta)} n_q$, and $\frac{\gamma^-}{2(1+\delta)} n_{-q}$ (with their notation $q \to \delta$ and their adjustable coefficient $\gamma \in [0, 2] \to \gamma^-$). We apply the TRT decomposition $n_q = -\tau^+ \hat{n}_q^+ - \tau^- \hat{n}_q^-$ and recast this scheme into ELI^+ in Eqs. (53) and (54) as

$$\begin{aligned}
&\mathrm{LLI}(\gamma^-) \in \mathrm{ELI}^+\text{:}\ \hat{\beta} = \frac{\delta}{1+\delta} \in [0, 1], \quad \delta \in [0, 1],\\
&\hat{\alpha} = \beta = \gamma = \hat{\gamma} = 0, \quad \alpha^{(u)} = -\alpha^{(p)} = \frac{1}{1+\delta},\\
&\hat{K}^+ = \frac{-\tau^+}{1+\delta} = K_{ELI}^+(\alpha^{(u)}, \alpha^{(p)}, \tau^+),\\
&\hat{K}^- = \frac{(\gamma^- - 1)\tau^-}{1+\delta} = -(\gamma^- - 1) K_{ELI_0}^-, \quad \gamma^- \in [0, 2],\\
&\gamma^{(u)}(\gamma^-) = \frac{-\Lambda^+[-2\delta + (-2 + \gamma^-)(1 + 2\Lambda^-)]}{2(1+\delta)}.
\end{aligned} \tag{C15}$$

Thus, LLI extends ULT and XELI-ULT to adjustable coefficient $\gamma^- = 1 + I_{ncs}$ and reduces to its $\{N, C, S\}$ counterparts when $\gamma^- = \{0, 1, 2\}$, respectively. The LLI steady-state solutions depend upon γ^- and one may build its LLI_k counterparts by either equating $\gamma^{(u)}(\gamma^-)$ in Eq. (C15) to its solution $\gamma^{(u)}(\hat{K}_k^-)$ in Eq. (44) or, equivalently, replacing $\hat{K}^-$ from Eq. (C15) with its solutions in Eqs. (57c)–(57e); it is to note that LLI_k is equivalent to $\mathrm{ELI\text{-}ULT}_k$ when $k \neq 0$. The stability conditions in Eq. (40) are satisfied giving $\gamma^- \in [0, 2]$ with LLI, LLI_1 and LLI_4; however, Eq. (40) allows for a weaker condition. In particular, LLI_1 is parametrized with $\gamma^- = \frac{2(1+\delta+\Lambda^-)}{(1+2\Lambda^-)}$ satisfying Eq. (40) but $\gamma^- \in [0, 2]$ only when $\Lambda^- \geqslant \delta$, i.e., $\Lambda^- \geqslant 1 \ \forall \ \delta$.

Errata: Equations (13), (36), and (D1) in [66]: their last term shall change the sign.

APPENDIX D: THE TWO-NODE DIRECTIONAL SCHEMES

1. The *p-flow* BFL-QI_3 and FH_3

The quadratic interpolations [55] BFL-QI and the modified FH = {MLS, FH} [52,53] operate directionally over the two nodes $\vec{r}_\mathrm{b}$ and $\vec{r}_\mathrm{b} - \vec{c}_q$; we provide their closure coefficients in Eq. (19) and show that they ensure only linear accuracy. We then uniformly construct their *p-flow* $\hat{K}_3^-$ corrections and address parametrization and stability.

a. The BFL-QI and BFL-QI_3

The BFL-QI fits the MR structure in Eq. (21); its closure relation in Eq. (19) is built applying the procedure of Sec. B 2; the obtained closure coefficients are given in Table VIII. They confirm the BFL-QI linear accuracy due to $\beta^{(u)} = \alpha^{(u)} \delta$ but,

TABLE VIII. The "quadratic interpolation" BFL-QI scheme [55] is specified with respect to Eqs. (19) and (21); it reduces to BB when $\delta = \frac{1}{2}$ and operates with $\alpha^{(p)} = 0$ in Eq. (24a). The Dirichlet term is prescribed with Eqs. (23) and (28)–(29). The BFL-QI$_3$ complements the BFL-QI with $\hat{F}_q = \hat{K}_3^- \hat{n}_q^-$ from Eq. (D2). *Errata:* $\hat{\alpha}$ of BFL-QI(1) is erroneous in Table 2 of Ref. [59].

Directional closure relation in Eq. (19)		
Eq. (19)	BFL-QI(1), $\delta \in [0, \frac{1}{2}]$	BFL-QI(2), $\delta \in [\frac{1}{2}, 1]$
$\hat{\alpha}$	$\delta(2\delta+1)$	$\frac{1}{\delta(1+2\delta)}$
β	$1-4\delta^2$	0
$\hat{\beta}$	0	$\frac{2\delta-1}{\delta}$
γ	$\delta(2\delta-1)$	0
$\hat{\gamma}$	0	$\frac{1-2\delta}{1+2\delta}$
$\alpha^{(u)}$	2	$\frac{2}{\delta(1+2\delta)}$
$\beta^{(u)}/\alpha^{(u)}$	δ	δ
$\gamma^{(u)}/\alpha^{(u)}$	$\Lambda + (\delta - \frac{1}{2})(\delta - \Lambda^+)$	$\Lambda + (\delta - \frac{1}{2})(\delta + \Lambda^+)$
$\alpha^{(p)}$	0	0
$\beta^{(p)}/\alpha^{(u)}$	$\delta - (\Lambda^- + \frac{1}{2})$	$\frac{1}{2} - \delta - \Lambda^-$
$\gamma^{(p)}/\alpha^{(u)}$	$\delta\beta^{(p)}$	$\delta\beta^{(p)}$

since $\gamma^{(u)} \neq \frac{1}{2}\alpha^{(u)}\delta^2$, BFL-QI is not a *p-flow* scheme, and it does not model exactly even a straight parabolic profile. Moreover, since $\gamma^{(u)}$ in Table VIII depends upon Λ^+, BFL-QI cannot adjust the straight *p-flow* with Λ alone except when $\delta = \frac{1}{2}$ where it reduces to BB, or giving the same distance δ to the two walls when $\Lambda^+ \to 0$:

$$\text{BFL-QI}, \quad I_b = 0\text{: } \Lambda = \frac{\delta(1-\delta)}{2} \quad \text{when} \quad \Lambda^+ \to 0. \tag{D1}$$

This solution is valid only *asymptotically*, whereas a similar LI$_1$ solution in Eq. (49b) is valid for any viscosity value; these two solutions match the BB with $\Lambda|_{\delta=\frac{1}{2}} = \frac{1}{8}$; the original BFL-QI configuration $I_b = 1$ in Eq. (33) can be addressed following the derivation of Eq. (49a). Otherwise, plugging $\gamma^{(u)}|_{\text{BFL-QI}}$ from Table VIII into Eq. (26b), and summing $\gamma^{(u)}$ with $-\Lambda^+\hat{K}_3^-$ from Eq. (25a) due to $\hat{F}_q = \hat{K}_3^- \hat{n}_q^-$, BFL-QI$_3$ adjusts $\gamma^{(u)}$ to $\frac{1}{2}\alpha^{(u)}\delta^2$ similarly to LI$_3$ in Eq. (44):

$$\text{BFL-QI}_3\text{: } \gamma^{(u)}|_{\text{BFL-QI}} - \Lambda^+\hat{K}_3^- = \frac{\alpha^{(u)}\delta^2}{2}, \quad \text{then}$$
$$\hat{K}_3^- = \frac{\gamma^{(u)}|_{\text{BFL-QI}}}{\Lambda^+} - \frac{\alpha^{(u)}\delta^2}{2\Lambda^+}, \quad I_b = 0. \tag{D2}$$

The BFL-QI$_3$ then satisfies the *p-flow* condition in Eq. (34) provided that its default option $I_b = 1$ is replaced by $I_b = 0$. Table IX shows that neither BFL-QI nor BFL-QI$_3$ are parametrized according to Eq. (B9), that explains why these schemes produce a viscosity-dependent steady-state accuracy in Stokes flow and NSE flow at a given Re$_g$. On the positive side, the BFL-QI operates with the coefficient range $\{\hat{\alpha}, \beta, \hat{\beta}, \gamma, \hat{\gamma}\} \in [0, 1]$ and it remains stable in the examined Stokes flow close to stability limit $\Lambda^\pm > 0$. When $\delta = \frac{1}{2}$, BFL-QI$_3$ reduces to BB$_3$ and it behaves exactly as other interpolation-based LI$_3^+$ schemes with $\alpha^{(u)} = 2$. Moreover, although BFL-QI$_3$ is a two-node scheme, it obeys the

TABLE IX. Specification of the BFL-QI and BFL-QI$_3$ steady-state closure in Eq. (B9) giving $b = 2\delta - 1$. When $b(\delta = \frac{1}{2}) = 0$, BFL-QI reduces to BB, which is parametrized; otherwise BFL-QI does not satisfy the sufficient parametrization condition in Eq. (B9) because of Λ^+ dependency; $m_4'|_{\hat{K}_3^-}$ corresponds to BFL-QI$_3$; this rule is also not parametrized except when it reduces to $m_4'|_{\text{BB}_3(I_b=0)} = -\frac{1}{8\Lambda}$ for $\delta = \frac{1}{2}$.

	BFL-QI(1), $\delta \in [0, \frac{1}{2}]$	BFL-QI(2), $\delta \in [\frac{1}{2}, 1]$
m_3'	$\frac{\delta}{4}(1 + 6\delta + 2b\Lambda^+)$	$\frac{\delta}{4}(1 + 6\delta - 2b\Lambda^+)$
m_4'	$-1 + \frac{b\delta}{2} + \frac{b(2+3\delta)\Lambda^+}{4\Lambda}$	$-1 + \frac{b\delta}{2} + \frac{(2-\delta-6\delta^2)\Lambda^+}{4\Lambda}$
m_7'	$-\frac{b\delta}{4}(1 + 2\Lambda^+)$	$-\frac{b\delta}{4}(1 - 2\Lambda^+)$
m_8'	$-\frac{b\delta(\Lambda^+ + 2\Lambda)}{4\Lambda}$	$\frac{b\delta(\Lambda^+ - 2\Lambda)}{4\Lambda}$
$m_4'\|_{\hat{K}_3^-}$	$-\frac{1}{8\Lambda} - \frac{b[1-2\delta(1+3\Lambda^+ + 2\Lambda)]}{8\Lambda}$	$-\frac{1}{8\Lambda} - \frac{b[1+2\delta(-1+3\Lambda^+ - 2\Lambda)]}{8\Lambda}$

$\hat{K}_3^-$ stability condition in Eq. (63). This is demonstrated in Fig. 8, where BFL-QI$_3$ is more stable than the standard interpolation-based LI$_3^+$ schemes due to its smaller value $\alpha^{(u)}$ in Table V. Nevertheless, since LI$_3^+(\alpha^{(u)})$ operates with a freely adjustable $\alpha^{(u)}$, it improves stability when $\alpha^{(u)}$ diminishes. Two other noticeable advantages of LI$_3^+$ over BFL-QI$_3$ are its parametrization and single-node implementation.

b. The FH and FH$_3$

The original FH scheme [52] and its MLS modification [53] improve the bounce-back through a directional finite-difference equilibrium gradient. We apply the *local-single-node* FH for $\delta \geqslant \frac{1}{2}$ and the two-node MLS for $\delta \leqslant \frac{1}{2}$ (where original FH is not defined for $\tau^+ = 1$), and extend them to the symmetrized TRT formulation hereafter referred to as FH:

$$\begin{aligned} f_{-q}(\vec{r}_\text{b}, t+1) &= \text{FH}_q, \\ \text{FH}_q &= (1-\chi)\widehat{f_q}(\vec{r}_\text{b}, t) \\ &\quad + \chi[(e_q^+(\vec{r}_\text{b}, t) + e_q^-(\vec{r}_{bf}, t)] \\ &\quad - 2e_q^-(\vec{r}_q, t), \end{aligned} \tag{D3a}$$

$$\text{MLS}, \ \delta \in \left[0, \frac{1}{2}\right[\text{: } \chi = \frac{2\delta - 1}{\tau^+ - 2},$$
$$e_q^-(\vec{r}_{bf}, t) := e_q^-(\vec{r}_\text{b} - \vec{c}_q, t), \quad \tau^+ \neq 2, \tag{D3b}$$

$$\text{FH}, \ \delta \in \left[\frac{1}{2}, 1\right] \text{: } \chi = \frac{2\delta - 1}{\tau^+},$$
$$e_q^-(\vec{r}_{bf}, t) := \frac{\delta - 1}{\delta} e_q^-(\vec{r}_\text{b}, t) + \frac{1}{\delta} e_q^-(\vec{r}_q, t). \tag{D3c}$$

Since MLS is not defined for $\tau^+ = 2$, we prefer to define it numerically in $[0, \frac{1}{2}[$; the FH then reduces to BB when $\delta = \frac{1}{2}$ for any τ^+. Our "nonghost" formulation sums (the single-node) LI$_k^+$ in Eq. (21)–(23) with the two-node equilibrium

TABLE X. The FH = {MLS, FH} scheme (D3)–(D4) is specified according to Eqs. (19) and (21); here $\tau^{\pm}$ is expressed through $\Lambda^{\pm}$; the FH reduces to BB when $\delta = \frac{1}{2}$. The FH_3 complements FH with $\hat{F}_q = \hat{K}_3^- \hat{n}_q^-$ in Eq. (D6).

Directional closure relation in Eq. (19)		
Eq. (19)	MLS, Eq. (D3b), $\delta \in [0, \frac{1}{2}[$	FH, Eq. (D3c), $\delta \in [\frac{1}{2}, 1]$
χ	$\frac{2(1-2\delta)}{3-2\Lambda^+}$	$\frac{2(2\delta-1)}{1+2\Lambda^+}$
$\alpha^{(u)}$	2	2
$\beta^{(u)}$	2δ	2δ
$\gamma^{(u)}$	$\Lambda(2-\chi)+\frac{1}{2}\chi(1+\Lambda^+)$	$\Lambda(2-\chi)+\frac{1}{2}\chi(\delta+\Lambda^+)$
$\alpha^{(p)}$	0	0
$\beta^{(p)}$	$\Lambda^-(\chi-2)-\frac{1}{2}\chi$	$\Lambda^-(\chi-2)-\frac{1}{2}\chi$
$\gamma^{(p)}$	$\Lambda^-(\frac{1}{2}\chi-1)-\Lambda\chi$	$\Lambda^-(\frac{1}{2}\chi-1)-\Lambda\chi$

corrections giving χ from Eq. (D3):

$$\begin{aligned}
&\mathrm{FH}_q = \mathrm{LI}_q + \chi[\chi_- e_q^-(\vec{r}_b - \vec{c}_q, t) + \chi_0 e_q^-(\vec{r}_b, t)],\\
&\hat{\alpha} = 1-\chi, \quad \beta = \hat{\beta} = \gamma = \hat{\gamma} = 0, \quad \hat{K}^+ = 0,\\
&\mathcal{W}_q = -\alpha^{(p)} e_q^+(\vec{r}_b, t) - \alpha^{(u)} e_q^-(\vec{r}_q, \tilde{t})\\
&\qquad + \chi[e_q^+(\vec{r}_b, t) + \chi_+ e_q^-(\vec{r}_q, t)], \quad \alpha^{(p)}=0, \quad \alpha^{(u)}=2,\\
&\mathrm{MLS},\ \delta \in \left[0, \frac{1}{2}\right[: \chi_- = 1, \quad \chi_0 = \chi_+ = 0,\\
&\mathrm{FH},\ \delta \in \left[\frac{1}{2}, 1\right] : \chi_- = 0, \quad \chi_0 = 1-\chi_+, \quad \chi_+ = \delta^{-1}.
\end{aligned} \tag{D4}$$

The original schemes compute momentum in $e_q^-(\vec{r}_q, t)$ and $e_q^-(\vec{r}_b - \vec{c}_q, t)$ with their local velocity value and $\rho(\vec{r}_b, t)$; we account for the presence of the forcing term and apply them with Eq. (3) in bulk nodes, and with Eq. (33) in a (ghost) wall node $\vec{r}_q$. The second-order Taylor expansion and Chapman-Enskog approximation with Eq. (18) fit the FH to the closure relation in Eq. (21); its coefficients are provided in Table X. They confirm the linear accuracy due to $\beta^{(u)} = \alpha^{(u)}\delta$. As it happens with BFL-QI, $\gamma^{(u)}$ in Table X depends upon Λ^+ and then the straight symmetric *p-flow* solution can be adjusted only *asymptotically*:

$$\begin{aligned}
&\mathrm{FH},\ I_b = 0, \quad \Lambda^+ \to 0 : \Lambda = \frac{1}{4}(3\delta - 1), \quad \delta \in \left]\frac{1}{3}, \frac{1}{2}\right] \text{ or}\\
&\qquad \Lambda = \frac{\delta}{4}, \quad \delta \in \left[\frac{1}{2}, 1\right].
\end{aligned} \tag{D5}$$

When $\delta = \frac{1}{2}$ and $\mathrm{FH}(I_b = 0)$ reduces to $\mathrm{BB}(I_b = 0)$, this solution reduces to $\Lambda = \frac{1}{8}$, where it is valid for any Λ^+ in agreement with Eq. (49b), but no solution for $\Lambda > 0$ exists when $\delta \in [0, \frac{1}{3}]$. Otherwise, the FH_3 adjusts $\gamma^{(u)}$ to $\frac{\alpha^{(u)}\delta^2}{2}$ with the help of the $\hat{F}_q = \hat{K}_3^- \hat{n}_q^-$ giving $\gamma^{(u)}|_{\mathrm{FH}}$ from Table X, like the $\mathrm{BFL\text{-}QI}_3$ in Eq. (D2):

$$\mathrm{FH}_3: \quad \hat{K}_3^- = \frac{\gamma^{(u)}|_{\mathrm{FH}}}{\Lambda^+} - \frac{\alpha^{(u)}\delta^2}{2\Lambda^+}, \quad I_b = 0. \tag{D6}$$

The $\mathrm{FH}_3(I_b = 0)$ then satisfies the *p-flow* condition in Eq. (34) for any channel inclination. The most relevant coefficients of the steady-state closure equation are gathered in Table XI;

TABLE XI. Specification of m_3' and m_4' coefficients in FH and FH_3 steady-state closure in Eq. (B9) giving $m_3' = \frac{(1-\chi)(-\tau^+ +1)+\tau^+}{\alpha^{(u)}}$, $m_4' = \frac{(1-\chi)(-\tau^- +1)-\tau^-}{\Lambda^-\alpha^{(u)}}$, $\alpha^{(u)} = 2$, $m_7' = m_8' = 0$, $b = 2\delta - 1$; FH and FH_3 reduce to BB and $\mathrm{BB}_3(I_b = 0)$, respectively, when $b = 0$; otherwise these schemes are not parametrized.

	MLS, $\delta \in [0, \frac{1}{2}[$	FH, $\delta \in [\frac{1}{2}, 1]$
m_3'	$\frac{1}{2} + \frac{b(1-2\Lambda^+)}{2(3-2\Lambda^+)}$	$\delta - \frac{b}{1+2\Lambda^+}$
m_4'	$\frac{b\Lambda^+ - 4\Lambda(1+\delta-\Lambda^+)}{2\Lambda(3-2\Lambda^+)}$	$-\frac{b\Lambda^+ + 4\Lambda(1-\delta+\Lambda^+)}{2\Lambda(1+2\Lambda^+)}$
$m_4'\vert_{\hat{K}_3^-}$	$-\frac{1}{8\Lambda} + \frac{b[-7-6\delta+2\Lambda^+(1+2\delta)]}{8\Lambda(3-2\Lambda^+)}$	$-\frac{1}{8\Lambda} + \frac{b(b-2\Lambda^+(1+2\delta)}{8\Lambda(1+2\Lambda^+)}$

they do not obey the sufficient condition (B9) either with FH or FH_3 except when $\delta = \frac{1}{2}$. In agreement with these predictions, we will confirm that their Stokes and NSE solutions are not parametrized by the physical numbers except for their *c-flow* ($\mathrm{FH}/\mathrm{FH}_3$) and *p-flow* ($FH_3$) exact solutions, or their straight channel NSE equivalents. The heuristic stability condition $\hat{\alpha} \in [-1, 1]$ gives

$$\mathrm{MLS}: \hat{\alpha} = 1 - \chi \in [-1, 1] \quad \text{if} \quad \Lambda^+ \in]0, 1+\delta], \tag{D7a}$$

$$\mathrm{FH}: \hat{\alpha} = 1 - \chi \in [-1, 1], \quad \forall \Lambda^+ > 0. \tag{D7b}$$

Hence, the coefficient $1 - \chi$ of the outgoing bounce-back population forbids the large viscosity half-interval $\Lambda^+ \geqslant 1 + \delta$ with the MLS in Eq. (D7a), and then the most restrictive condition $\Lambda^+ \leqslant 1$ is set by $\delta = 0$. Numerical simulations in Fig. 7 confirm these predictions. Hence, the MLS component $\delta \in [0, \frac{1}{2}[$ shall be forbidden when $\Lambda^+ > 1$ and $\delta \to 0$; additionally, MLS_3 handles the viscosity range in the limit $\delta \to 0$ only for large enough Λ. In contrast, the single-node FH_3 component $\delta \in [\frac{1}{2}, 1]$ is stable when $\delta \to 1$, where both LI_3 and $\mathrm{BFL\text{-}QI}_3$ are limited for small viscosity and Λ ranges.

c. Summary

The BFL-QI and FH/MLS operate as two-node schemes but they are only linearly accurate and exact only in (rotated) Couette Stokes flow. The *p-flow* $\mathrm{BFL\text{-}QI}_3$ and FH_3 become exact for grid-aligned or inclined stationary Poiseuille Stokes flow, and Poiseuille NSE flow in a straight channel. However, neither FH, BFL-QI nor FH_3, $\mathrm{BFL\text{-}QI}_3$ are parametrized, and their steady-state error estimates are viscosity-dependent in Stokes flow and in NSE flow at given Re_g. Moreover, this property will remain with their $\hat{K}_1^-$ or *p-pressure* $\hat{K}_4^-$ parametrizations following Eqs. (44a) and (44c), respectively, because these are either two-node schemes, such as BFL-QI and MLS, or equilibrium-interpolation-based schemes, such as MLS and FH, where all of their relevant coefficients given in Tables IX and XI, and not only those of $\hat{n}_q^-$ as in single-node LI^+, do not obey the sufficient parametrization criteria in Eq. (B9). These conditions are, however, respected by the parabolic two-node families, as $\mathrm{MR1}^+$, AVMR, and EMR.

2. The *c-nse-p-flow* EMR

The two-node parabolic family EMR is introduced in Sec. V B with free tunable parameters $\alpha^{(p)}$, $\alpha^{(u)}$ and $\hat{K}^{\pm}$; EMR is subject to *c-nse-p-flow* conditions in Eq. (38), and it

includes the AVMR family from Table VI with $\alpha^{(p)} = \hat{K}^+ = 0$. We delineate the three families EMR-1, EMR-2, and EMR-3 with the common expressions for $\hat{K}^-$, γ and $\hat{\gamma}$:

$$\hat{K}^- = \tfrac{1}{2}[4 + 2\hat{K}^+ - \alpha^{(u)}(1+\delta)(1+\delta-2\Lambda^-) + \alpha^{(p)}(1-2\Lambda^+)], \quad \gamma = \tfrac{1}{4}\alpha^{(u)}\delta(\delta+2\Lambda^-),$$
$$\hat{\gamma} = -\tfrac{1}{4}\alpha^{(u)}\delta(\delta-2\Lambda^-). \tag{D8}$$

These three schemes operate with only one nonzero coefficient among $\{\hat{\alpha}, \beta, \hat{\beta}\}$:

$$\text{EMR-1:} \quad \beta = \hat{\beta} = 0, \quad \hat{\alpha} = -1 + \alpha^{(u)}\left(1 - \tfrac{1}{2}\delta^2\right),$$
$$\text{EMR-2:} \quad \hat{\alpha} = \beta = 0, \quad \hat{\beta} = 1 + \alpha^{(u)}\left(-1 + \tfrac{1}{2}\delta^2\right),$$
$$\text{EMR-3:} \quad \hat{\alpha} = \hat{\beta} = 0, \quad \beta = -1 + \alpha^{(u)}\left(1 - \tfrac{1}{2}\delta^2\right). \tag{D9}$$

Their coefficients $\hat{K}^+$ and $\alpha^{(p)}$ differ and read as

$$\text{EMR-1:}\alpha^{(p)} = -2 + \alpha^{(u)}\left(1 - \frac{\delta^2}{2} + \delta\Lambda^-\right), \quad \hat{K}^+ = -2\Lambda^+ + \frac{\alpha^{(u)}}{2}\{-1 + 2\Lambda^+ + \delta[2 - \delta(-2+\Lambda^+) + 2\Lambda]\},$$
$$\text{EMR-2: } \alpha^{(p)} = \alpha^{(u)}\left(-1 + \frac{1}{2}\delta^2 + \delta\Lambda^-\right), \quad \hat{K}^+ = -1 + \frac{\alpha^{(u)}}{2}\{1 - 2\Lambda^+ + \delta[2 + \delta(1+\Lambda^+) + 2\Lambda]\},$$
$$\text{EMR-3:}\alpha^{(p)} = 2 + \alpha^{(u)}\left(1 - \frac{1}{2}\delta^2 + \delta\Lambda^-\right), \quad \hat{K}^+ = -1 - 2\Lambda^+ + \frac{\alpha^{(u)}}{2}\{1 + 2\Lambda^+ + \delta[2 + \delta(1-\Lambda^+) + 2\Lambda]\}. \tag{D10}$$

These three schemes yield $\{\hat{\alpha}, \beta, \hat{\beta}, \gamma, \hat{\gamma}\} \in [-1, 1]$ under the simple sufficient condition in Eq. (71c). The numerical results suggest that this condition is sufficient with EMR-1 and EMR-2, whereas EMR-3 is less stable (see Fig. 12).

APPENDIX E: TO STABILITY OF XELI, CLI, AND LI$_3^+$

The LI$_k^+$ stability analysis is based on Eq. (40) where Eq. (40a) is satisfied when $\alpha^{(u)}(\delta) \in]0, \frac{1}{\delta}]$ in Eq. (61); this condition is respected by YLI/BFL, ELI-UL/ELI-FL, and ZLI. However, neither XELI-UQ$_k$, $X = \{N, C, S\}$ with $\alpha^{(u)} = 2$ nor CLI$_k$ with $\alpha^{(u)} = \frac{4}{1+2\delta}$, obeys Eq. (61) when $\delta \in]\frac{1}{2}, 1]$, and then they satisfy Eq. (40a) provided that

$$\text{XELI-UQ}_k\text{: } \delta \in \left[0, \tfrac{1}{2}\right] \text{ or } \Lambda^+ > \delta - \frac{1}{2}, \quad \delta \in \left]\frac{1}{2}, 1\right],$$
$$\text{then } \delta \in \left[0, \frac{1}{2}\right] \text{ or } \Lambda^+ > \frac{1}{2}, \ \forall\, \delta \in \left]\frac{1}{2}, 1\right], \tag{E1a}$$
$$\text{CLI}_k\text{:}\delta \in \left[0, \frac{1}{2}\right] \text{ or } \Lambda^+ > \frac{2\delta - 1}{2(1+2\delta)}, \quad \delta \in \left]\frac{1}{2}, 1\right],$$
$$\text{then } \delta \in \left[0, \frac{1}{2}\right] \text{ or } \Lambda^+ > \frac{1}{6}, \ \forall\, \delta \in \left]\frac{1}{2}, 1\right]. \tag{E1b}$$

In addition, Eq. (40b) restricts the free parameter Λ^- with CLI, SELI-UQ, and NELI-UQ:

$$\text{SELI-UQ: } \left(\Lambda^- \geqslant \frac{1}{2}\right)||\left(\frac{1}{2} - \delta \leqslant \Lambda^- \leqslant \frac{1}{2}\right), \quad \delta \in \left[0, \frac{1}{2}\right], \tag{E2a}$$
$$\text{NELI-UQ:}\left(\Lambda^- \geqslant \frac{1}{2}\right)||\left(\delta - \frac{1}{2} \leqslant \Lambda^- \leqslant \frac{1}{2}\right), \quad \delta \in \left]\frac{1}{2}, 1\right], \tag{E2b}$$
$$\text{CLI:}\left(\Lambda^- \leqslant \frac{1}{2}\right)||\left(\frac{1}{2} \leqslant \Lambda^- \leqslant \frac{1+2\delta}{2(1-2\delta)}\right), \quad \delta \in \left[0, \frac{1}{2}\right]. \tag{E2c}$$

Hence, Eq. (40b) is satisfied for any distance δ only when $\Lambda^- \geqslant \frac{1}{2}$ in SELI-UQ/NELI-UQ or $\Lambda^- \leqslant \frac{1}{2}$ in CLI. These conditions are coupled with Eq. (E1); they are numerically validated in Fig. 5 with XELI-UQ; CLI remains much more stable than predicted. Next, Eq. (62) specifies Eq. (40b) in the presence of correction $\hat{K}_k^-$. Equation (40) then gives *p-flow* $\hat{K}_3^-$ stability condition as

$$\forall\, \Lambda^\pm \quad \text{if } \delta = 0, \tag{E3a}$$
$$\Lambda^+ > \frac{\alpha^{(u)}\delta^2}{2(1+2\Lambda^-)} \quad \text{if } \alpha^{(u)} \in \left]0, \frac{1}{\delta} + \frac{1}{1-\delta+2\Lambda^-}\right], \tag{E3b}$$
$$\Lambda^+ > \frac{1}{2}(\alpha^{(u)}\delta - 1) \quad \text{if } \alpha^{(u)} > \frac{1}{\delta} + \frac{1}{1-\delta+2\Lambda^-}. \tag{E3c}$$

When Eq. (61) is satisfied, Eq. (40) reduces to Eq. (E3b) and the stable parameter space becomes described by Eqs. (63)–(65). These predictions are exemplified in Table V and are examined in Figs. 8 and 11.

[1] F. Higuera, S. Succi, and R. Benzi, Europhys. Lett. **9**, 345 (1989).

[2] C. K. Aidun and J. R. Clausen, Annu. Rev. Fluid Mech. **42**, 439 (2010).

[3] T. Krüger, H. Kusumaatmaja, A. Kuzmin, O. Shardt, G. Silva, and E. M. Viggen, *The Lattice Boltzmann Method: Principles and Practice* (Springer International Publishing, Switzerland, 2017).

[4] A. J. C. Ladd, J. Fluid Mech. **271**, 285 (1994).
[5] N. Q. Nguyen and A. J. C. Ladd, Phys. Rev. E **66**, 046708 (2002).
[6] Y. Thorimbert, F. Marson, A. Parmigiani, B. Chopard, and J. Latt, Comput. Fluids **166**, 286 (2018).
[7] C. Livi, G. Di Staso, H. J. H. Clercx, and F. Tosch, Phys. Rev. E **103**, 013303 (2021).
[8] L. Werner, C. Rettinger, and U. Rüde, Int. J. Numer. Methods Fluids **93**, 3280 (2021).
[9] V. Heidler, O. Bublík, A. Pecka, and J. Vimmr, J. Comput. Appl. Math. **398**, 113672 (2021).
[10] M. Wouters, O. Aouane, M. Sega, and J. Harting, Philos. Trans. R. Soc. London A **379**, 20200399 (2021).
[11] C. Kotsalos, J. Latt, and B. Chopard, J. Comput. Phys. **398**, 108905 (2019).
[12] Y. F. Lim, C. de Loubens, R. J. Love, R. G. Lentle, and P. W. M. Janssen, Food Function **6**, 1787 (2015).
[13] H. Yu, Xi Chen, Z. Wang, D. Deep, E. Lima, Y. Zhao, and S. D. Teague, Phys. Rev. E **89**, 063304 (2014).
[14] K. Mattila, T. Puurtinen, J. Hyväluoma, R. Surmas, M. Myllys, T. Turpeinen, F. Robertsén, J. Westerholm, and J. Timonen, J. Comput. Sci. **12**, 62 (2016).
[15] S. Bogner, S. Mohanty, and U. Rüde, Int. J. Multiphase Flow **68**, 71 (2015).
[16] Y. Chen, G. Jin, P. Zhang, S. A. Galindo-Torres, A. Scheuermann, and L. Li, Int. J. Numer. Methods Fluids **92**, 2009 (2020).
[17] S. Khirevich, I. Ginzburg, and U. Tallarek, J. Comput. Phys. **281**, 708 (2015).
[18] D. L. Koch and A. J. C. Ladd, J. Fluid Mech. **349**, 31 (1997).
[19] S. Khirevich and T. W. Patzek, Phys. Fluids **30**, 093604 (2018).
[20] C. Chukwudozie and M. Tyagi, Chem. Eng. Sci. **59**, 4858 (2013).
[21] L. Talon, D. Bauer, N. Gland, S. Youssef, H. Auradou, and I. Ginzburg, Water Resour. Res. **48**, W04526 (2012).
[22] X. Yang, Y. Mehmani, W. A. Perkins, A. Pasquali, M. Schönherr, K. Kim, M. Perego, M. L. Parks, N. Trask, M. T. Balhoff, and M. C. Richmond, Adv. Water Resour. **95**, 176 (2016).
[23] S. Liu, C. Zhang, and R. B. Ghahfarokhi, Energy Fuels **35**, 13535 (2021).
[24] C. Manwart, U. Aaltosalmi, A. Koponen, R. Hilfer, and J. Timonen, Phys. Rev. E **66**, 016702 (2002).
[25] D. Mierke, C. F. Janßen, and T. Rung, Comput. Math. Appl. **79**, 66 (2020).
[26] J. Latt, C. Coreixas, and J. Beny, PLoS ONE **16**, e0250306 (2021)
[27] R. Cornubert, D. d'Humières, and D. Levermore, Physica D **47**, 241 (1991).
[28] I. Ginzbourg and D. d'Humières, J. Stat. Phys. **84**, 927 (1996).
[29] I. Ginzburg, J. Comput. Phys. **431**, 109986 (2021).
[30] A. Sengupta, P. S. Hammond, D. Frenkel, and E. S. Boek, J. Comput. Phys. **231**, 2634 (2012).
[31] G. Silva, L. Talon, and I. Ginzburg, J. Comput. Phys. **335**, 50 (2017).
[32] P. A. Skordos, Phys. Rev. E **48**, 4823 (1993).
[33] J. Lätt, B. Chopard, O. Malaspinas, M. Deville, and A. Michler, Phys. Rev. E **77**, 056703 (2008).
[34] T. Inamuro, M. Yoshina, and F. Ogino, Phys. Fluids **7**, 2928 (1995).
[35] Q. Zou and X. He, Phys. Fluids **9**, 1591 (1997).
[36] I. Ginzbourg, Boundary conditions problems in lattice gas methods for single and multiple phases. Ph.D. thesis, University Paris VI, 1994.
[37] I. Krastins, A. Kao, K. Pericleous, and T. Reis, Int. J. Numer. Methods Fluids **92**, 1948 (2020).
[38] L. Zhang, Z. Zeng, H. Xie, X. Tao, Y. Zhang, Y. Lu, A. Yoshikawa, and Y. Kawazoe, Comput. Fluids **114**, 193 (2015).
[39] G. Silva and I. Ginzburg, Philos. Trans. R. Soc. London A **378**, 20190404 (2020).
[40] G. Silva and I. Ginzburg, Int. J. Numer. Methods Fluids **94**, 2104 (2022).
[41] L. Zhang, S. Yang, Z. Zeng, and J. W. Chew, Phys. Rev. E **97**, 023302 (2018).
[42] I. Ginzburg and G. Silva, Phys. Fluids **33**, 057104 (2021).
[43] M. Junk and Z. Yang, Phys. Rev. E **72**, 066701 (2005).
[44] A. Tiwari and S. P. Vanka, Int. J. Numer. Methods Fluids **69**, 481 (2012).
[45] D. R. Noble and J. R. Torczynski, Int. J. Mod. Phys. C **09**, 1189 (1998).
[46] S. A. Galindo-Torres, A. Scheuermann, and L. Li, Phys. Rev. E **86**, 046306 (2012).
[47] R. Trunk, J. Marquardt, G. Thäter, H. Nirschl, and M. J. Krause, Comput. Fluids **172**, 621 (2018).
[48] Z. G. Feng and E. E. Michaelides, J. Comput. Phys. **195**, 602 (2004).
[49] T. Seta, R. Rojas, K. Hayashi, and A. Tomiyama, Phys. Rev. E **89**, 023307 (2014).
[50] M. Pepona and J. Favier, J. Comput. Phys. **321**, 1170 (2016).
[51] I. Ginzbourg and P. M. Adler, J. Phys. II (France) **4**, 191 (1994).
[52] O. Filippova and D. Hänel, J. Comput. Phys. **147**, 219 (1998).
[53] R. Mei, L.-S. Luo, and W. Shyy, J. Comput. Phys. **155**, 307 (1999).
[54] B. Chun and A. J. C. Ladd, Phys. Rev. E **75**, 066705 (2007).
[55] M. Bouzidi, M. Firdaouss, and P. Lallemand, Phys. Fluids **13**, 3452 (2001).
[56] D. Yu, R. Mei, L.-S. Luo, and W. Shyy, Prog. Aeronaut. Sci. **39**, 329 (2003).
[57] I. Ginzburg, F. Verhaeghe, and D. d'Humières, Commun. Comput. Phys. **3**, 427 (2008).
[58] I. Ginzburg, F. Verhaeghe, and D. d'Humières, Commun. Comput. Phys. **3**, 519 (2008).
[59] I. Ginzburg and D. d'Humières, Phys. Rev. E **68**, 066614 (2003).
[60] I. Ginzburg, Adv. Water Resour. **28**, 1196 (2005).
[61] W. Zhao, J. Huang, and W.-A. Yong, Multiscale Model. Simul. **17**, 854 (2019).
[62] Y. Chen, X. Wang, and H. Zhu, Phys. Fluids **33**, 043317 (2021).
[63] M. Geier, M. Schönherr, A. Pasquali, and M. Krafczyk, Comput. Math. Appl. **70**, 507 (2015).
[64] W. Zhao and W.-A. Yong, J. Comput. Phys. **329**, 1 (2017).
[65] X. Meng, L. Wang, W. Zhao, and X. Yang, Adv. Water Resour. **141**, 103583 (2020).
[66] F. Marson, Y. Thorimbert, B. Chopard, I. Ginzburg, and J. Latt, Phys. Rev. E **103**, 053308 (2021).
[67] S. Tao, Q. He, B. Chen, X. Yang, and S. Huang, Comput. Math. Appl. **76**, 1593 (2018).

[68] S. Liu, T. Zhou, S. Tao, Z. Wu, and G. Yang, Int. J. Mod. Phys. C **30**, 1950041 (2019).
[69] I. Ginzburg, J. Comput. Sci. **54**, 101215 (2021).
[70] L. Wang, S. Tao, X. Meng, K. Zhang, and G. Lu, Phys. Rev. E **101**, 063307 (2020).
[71] B. Postma and G. Silva, Phys. Rev. E **102**, 063307 (2020).
[72] D. d'Humières and I. Ginzburg, Comput. Math. Appl. **58**, 823 (2009).
[73] I. Ginzburg, G. Silva, and L. Talon, Phys. Rev. E **91**, 023307 (2015).
[74] S. Gsell, U. d'Ortona and J. Favier, J. Comput. Phys. **429**, 109943 (2021).
[75] D. d'Humières, I. Ginzburg, M. Krafczyk, P. Lallemand, and L.-S. Luo, Philos. Trans. R. Soc. London A **360**, 437 (2002).
[76] J. Latt and B. Chopard, Math. Comput. Simul. **72**, 165 (2006).
[77] C. Coreixas, B. Chopard, and J. Latt, Phys. Rev. E **100**, 033305 (2019).
[78] C. Coreixas, G. Wissocq, B. Chopard, and J. Latt, Philos. Trans. R. Soc. London A **378**, 20190397 (2020).
[79] P. H. Kao and R. Y. Yang, J. Comput. Phys. **227**, 5671 (2008).
[80] C. Pan, L. Luo, and C. T. Miller, Comput. Fluids **35**, 898 (2006).
[81] Y. Qian, D. d'Humières, and P. Lallemand, Europhys. Lett. **17**, 479 (1992).
[82] M. Haussmann, N. Hafen, F. Raichle, R. Trunk, H. Nirschl, and M. J. Krause, Comput. Math. Appl. **80**, 671 (2020).
[83] C. Rettinger and U. Rüde, Comput. Fluids **154**, 74 (2017).
[84] X. Yin, G. Le, and J. Zhang, Phys. Rev. E **86**, 026701 (2012).
[85] R. Verberg and A. J. C. Ladd, Phys. Rev. Lett. **84**, 2148 (2000).
[86] B. Ahrenholz, J. Tölke, and M. Krafczyk, Int. J. Comput. Fluid Dyn. **20**, 369 (2006).
[87] I. Ginzburg, Phys. Rev. E **77**, 066704 (2008).
[88] Z. Chai and B. Shi, Phys. Rev. E **102**, 023306 (2020).
[89] F. Dubois and P. Lallemand, J. Stat. Mech. (2009) P06006.
[90] I. Ginzburg, Commun. Comput. Phys. **11**, 1439 (2012).
[91] G. Silva and V. Semiao, J. Comput. Phys. **269**, 259 (2014).
[92] I. Ginzburg and L. Roux, J. Comput. Phys. **299**, 974 (2015).
[93] M. Geier, A. Pasqualli, and M. Schnherr, J. Comput. Phys. **348**, 862 (2017).
[94] I. Ginzburg, Phys. Rev. E **95**, 013304 (2017).
[95] M. Bauer, G. Silva, and U. Rüde, J. Comput. Phys. **405**, 109111 (2020).
[96] F. Dubois, P. Lallemand, and M. Tekitek, Comput. Math. Appl. **59**, 2141 (2010).
[97] I. Ginzburg, Phys. Rev. E **95**, 013305 (2017).
[98] I. Ginzburg and K. Steiner, J. Comput. Phys. **185**, 61 (2003).
[99] P. J. Dellar, J. Comput. Phys. **190**, 351 (2003).
[100] P. Lallemand and L.-S. Luo, Phys. Rev. E **61**, 6546 (2000).
[101] P. J. Dellar, J. Comput. Phys. **259**, 270 (2014).
[102] F. Hajabdollahi and K. N. Premnath, Phys. Rev. E **97**, 053303 (2018).
[103] C. Peng, N. Geneva, Z. Guo, and L.-P. Wang, Phys. Rev. E **95**, 013301 (2017).
[104] C. Peng, Y. Teng, B. Hwang, Z. Guo, and L.-P. Wang, Comput. Math. Appl. **72**, 349 (2016).
[105] B. Wen, C. Zhang, Y. Tu, C. Wang, and H. Fang, J. Comput. Phys. **266**, 161 (2014).
[106] I. Christie, D. F. Griffiths, A. R. Mitchell, and O. C. Zienkiewicz, Int. J. Numer. Meth. Eng. **10**, 1389 (1976).
[107] L. Wang, S. Tao, X. Meng, K. Zhang, and G. Lu, Int. Commun. Heat Mass Transfer **122**, 105130 (2021).
[108] H. Hasimoto, J. Fluid Mech. **5**, 317 (1959).
[109] A. S. Sangani and A. Acrivos, Int. J. Multiphase Flow **8**, 193 (1982).
[110] P. Adler, *Porous Media: Geometry and Transport* (Butterworth-Heinemann, Stoneham, MA, 1992).
[111] G. Silva and I. Ginzburg, C. R. Mec. **343**, 545 (2015).
[112] G. Silva and I. Ginzburg, Transp. Porous Media **111**, 795 (2016).
[113] Comsol, Multiphysics Reference Guide for COMSOL 5.5, Burlington, MA (2019).
[114] J. Happel and H. Brenner, *Low Reynolds Number Hydrodynamics: With Special Applications to Particulate Media* (Prentice-Hall, New York, 1965).